Cold plasma initiated valorisation of triglyceride containing feedstocks

by

Jonathan Stuart Harris

A thesis submitted for the degree of

Doctor of Philosophy

School of Engineering,
Newcastle University, UK

September 2018

Abstract

This thesis reviewed current methodologies for producing liquid fuels from triglycerides. With ever increasing demands for sustainable liquid fuels compatible with modern engines, waste cooking oils (WCO) are an attractive source of glycerides. However, transesterification and thermochemical conversion of impure glycerides face significant challenges, including lower quality fuels; unwanted waste glycerol; poor selectivity and catalyst fouling via saponification. To overcome those challenges, a two phase dielectric barrier discharge plasma reactor was developed for the valorisation of oil rich biomass and waste oils by cold plasma with and without catalysts.

This thesis reports the valorisation of WCO and transesterification waste products via direct decomposition by cold plasma catalysis within a dielectric barrier discharge reactor. Non-catalytic cold plasma achieved 25% conversion of methanol to hydrogen, carbon oxides and hydrocarbons using a nitrogen carrier gas, and the use of a helium carrier gas notably generated propanal and methyl methanoate at trace yields (0.96 and 0.73wt.%). The synergistic effect of plasma catalysis has been demonstrated by the combination of cold plasma and various catalysts (Ni/Al_2O_3, HZSM-5, Y-Zeolite and zirconia). For example, 99% conversion of waste glycerol and 50wt.% yields of acetol can be obtained using a Ni/Al_2O_3 catalyst compared to 91% and 34wt.% with no catalyst. Triglyceride decomposition primarily produces gaseous and liquid hydrocarbons, fatty acid esters and hydrogen, with other products not observed thermochemically (e.g. acetol and formic acid). The two phase plasma system permits formation of thermally unfeasible liquid products as the liquid phase prevents electron induced reactions, stabilising high energy species and inhibiting decomposition of liquid phase products. Full reaction pathways were derived for all feedstocks.

Unlike conventional methods, the process is highly tolerant of poor feedstocks and selectivities are tunable to any product. For example, WCO decomposition produced over 50wt.% yields of fatty acid esters in under 11 seconds without requiring methanol, heating or high pressures. Use of hydrogen carrier gas permits high selectivities to low energy reactions, e.g. inducing esterification of free fatty acids with glycerides without a catalyst. Experimental decomposition of glucose and cellulose to valuable furan and pyran products suggests that cold plasma treatment of oil rich biomass for one-step generation of liquid fuels is feasible, offering cost and energy savings, expanding the range of potential sources and valorising waste. Similarly, two phase effects and the tunablity of

cold plasma presents significant research opportunities to utilise novel synthesis pathways to create value added products.

The current study demonstrated that two phase cold plasma could potentially utilise the by-products of commercial transesterification and waste oils to generate sustainable liquid fuels and negate the environmental impact of waste disposal. The findings could also be extended to other liquid feedstocks for applications such as pyrolysis oil upgrading.

Acknowledgements

I would like to express my sincere gratitude to my supervisors Dr Anh Phan and Dr Kui Zhang for their guidance, unstinting support and enthusiasm throughout this research project. Their immense knowledge and insight have been invaluable to my development as a researcher and their critical analysis and willingness to engage in rigorous scientific debate has aided my understanding considerably. I am indebted to them for their encouragement and commitment as my mentors throughout this work. My scientific writing in particular, has improved immeasurably thanks to their constructive criticism, patience and good humour.

I am grateful for the financial support provided by the EPSRC (grant no. OSR/0530/DT14/HARR), which enabled me to complete this work.

I would like to thank Dr Chris Ottley and Dr Emily Unsworth at Durham University for their assistance in performing ICP-OES analysis and Dr Nathan Skillen from Queens' University, Belfast for additional XRD analysis. Thanks are also due to Seal Sands Biodiesel Plant for supplying a sample of waste glycerol for experimental use and to various local restaurants for supplying samples of waste cooking oil.

I would like to formally thank staff within the School of Engineering, whose professionalism and expertise have made this work possible. I am particularly indebted to Rob Dixon, Paul Sterling, Ian Ditchburn, Kevin Brown and Ian Strong for their technical assistance and for producing bespoke equipment, which facilitated experimental progress considerably. My thanks go to the school office team, who have helped me so much throughout my time at Newcastle University.

I am grateful to faculty members and my fellow students for the many stimulating discussions and their words of encouragement. In particular, I would like to thank fellow members of the Process Intensification Group for broadening my scientific knowledge and improving my presenting skills.

Finally, I would like to thank my family: Stuart, Janet, Andrew and Julie for their amazing support and encouragement.

Table of Contents

List of publications and conferences

Conferences

Harris, J., Phan, A.N. and Zhang, K. "Upgrading Pyrolysis Bio-Oil"(2015) *Chem Eng Day UK 2015* Sheffield April 8-9

Harris, J., Phan, A.N. and Zhang, K."(2018) *3rd Green and Sustainable Chemistry Conference 2018* Berlin May 13-16

Publications

Harris, J., Phan, A.N. and Zhang, K. (2018) 'Cold plasma catalysis as a novel approach for valorisation of untreated waste glycerol', *Green Chemistry*, 20(11), pp. 2578-2587.

List of Figures:

List of Tables:

List of Equations and reactions

Acronyms

AC: Alternating Current

BET: Brunauer-Emmett-Teller (surface area analysis)

CHN: Carbon Hydrogen Nitrogen (elemental analysis)

DBD: Dielectric Barrier Discharge

EDS: Energy-Dispersive x-ray Spectroscopy

FAE: Fatty Acid Ester

FAME: Fatty Acid Methyl Ester

FCC: Fluid Cracking catalyst

FFA: Free Fatty Acid

FTIR: Fourier Transform Infra-red Spectroscopy

GC-MS: Gas Chromatography- Mass Spectroscopy

GC: Gas Chromatography

HDO: Hydrodeoxygenation

ICP-OES: Inductively Coupled Plasma- Optical Emission Spectroscopy

KF titration: Karl Fischer titration

LHSV: Liquid Hourly Space Velocity

NTP: Non-Thermal Plasma (generally referred to as cold plasma)

SEM: Scanning Electron Microscopy

UV: Ultraviolet

WCO: Waste Cooking Oil

WHSV: Weight Hourly Space Velocity

XPS: X-ray Photoelectron Spectroscopy

XRD: X-Ray powder Diffraction

5-HMF: 5-Hydroxy Methyl Furfural

Chapter 1. Introduction

Depleting fossil fuels reserves, increasing environmental concerns associated with the use of petroleum-based fuels and a highly industrialised society make sustainable and clean fuels highly desirable, as evidenced by a worldwide 10%/year increase in demand for sustainable fuels (U.S-National-Biodiesel-Board, 2017). Alongside other biofuels, biodiesel has been a key liquid fuel, accounting for 16% of current biofuel production (Figure 1.1) (BP, 2017). It is derived from triglyceride rich feedstocks such as fats, vegetable oil, waste cooking oil and algae.

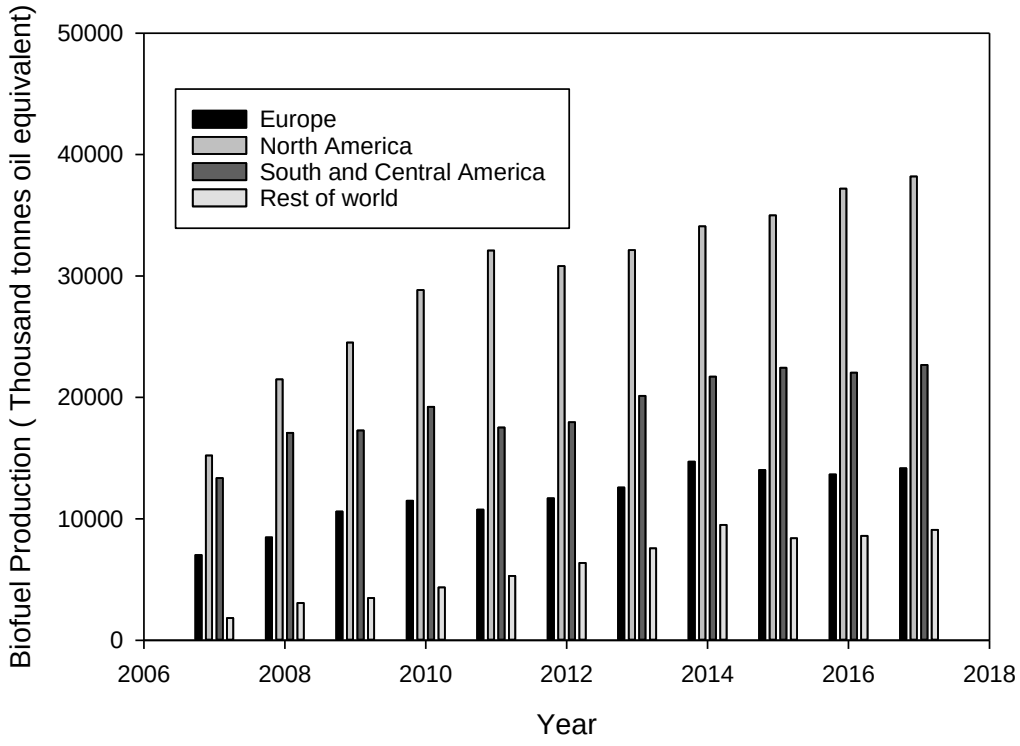

Figure 1.1: Recent biofuel production statistics by region

Direct use of triglycerides in diesel engines is impracticable due to high viscosities and difficulties with fouling deposits, pumping and atomisation. (Kulkarni and Dalai, 2006). Triglycerides are commonly converted to fatty acid methyl esters (FAME) via transesterification with methanol (Zhang *et al.*, 2003; Norjannah *et al.*, 2016) in the presence of a basic catalyst such as potassium hydroxide, sodium hydroxide or potassium methoxide. The water and free fatty acids in the feedstock must be below <0.1wt.% to avoid saponification, limiting the range of compatible feedstocks. Due to the high cost of these feedstocks for biodiesel production (i.e. 75% of the total cost of biodiesel production) (Atabani *et al.*, 2012) and concerns over land set aside for food being diverted

to energy crops, waste cooking oil, animal fat, algae and non-edible vegetable oil (such as rice bran and tobacco or rubber seeds) have increased their share as feedstock sources for biodiesel production. However, their contribution still remains less than 5% globally (Demirbas *et al.*, 2016).

1.1 Biodiesel challenges and drawbacks

Although pure biodiesel (100% FAME) is renewable, it has poorer low temperature flow properties than petroleum diesel, with a tendency to clog fuel lines or jam pumps. The cloud point and pour point of biodiesels are typically 15°C and 25°C, whereas diesel typically has values of -15°C and -27°C respectively (Wang *et al.*, 2005). Biodiesel also has lower mass and volumetric energy contents than petrodiesel, with biodiesel containing 10% less energy by mass, or 5% by volume (Krutof and Hawboldt, 2016). The larger proportion of straight chain molecules in biodiesel typically results in higher viscosities than that of diesel. To counter this, biodiesels are typically blended with petroleum diesel to produce fuels that meet the desired standards, but blends above 10% wt/wt biodiesel in diesel do not meet these standards as fouling deposits can result.

Transesterification produces waste glycerol (approximately 10wt.%) (Joshi *et al.*, 2017) which is contaminated by soaps, fatty acids, water and spent catalyst (30-75wt.% glycerol) (Wu *et al.*, 2013a). As a result, purification is not economically viable at small to medium scales, so it is generally considered as waste requiring disposal (Floyd *et al.*, 2007). Although there are several routes to convert glycerol to acetol (Chiu *et al.*, 2006), propenal, glycerol carbonate (Aresta *et al.*, 2007) or polyglyerols (Ayoub *et al.*, 2017), these require purified glycerol.

Current research into “drop-in” fuel development has considered other approaches such as hydrodeoxygenation to convert commercially produced FAME into long chain hydrocarbons (Yenumala *et al.*, 2017) to improve its cold flow properties, stability and viscosity (Dundich *et al.*, 2010; Jeczmionek and Porzycka-Semczuk, 2014a). However, this process requires large volumes and pressures of hydrogen gas (300 litres H_2 /litre FAME) (>10bar) (Jeczmionek and Porzycka-Semczuk, 2014b) at temperatures above 320°C and a 1 hour residence time in the presence of catalysts such as Rh, Pd or Ni. These catalysts are potentially susceptible to saponification, though catalyst degradation has not been

observed within a noticeable timeframe. These factors combine to make continuous operation challenging and expensive (Atadashi *et al.*, 2013).

Direct conversion of triglycerides to hydrocarbons without transesterification can be achieved via catalytic pyrolysis (Figure 1.2). However, research to date has been limited. It was reported (Wiggers *et al.*, 2013) that direct conversion of triglycerides to liquid hydrocarbons at pilot scale via conventional thermochemical conversion was unable to achieve liquid fuel yields above 55wt.% regardless of the operating conditions applied.

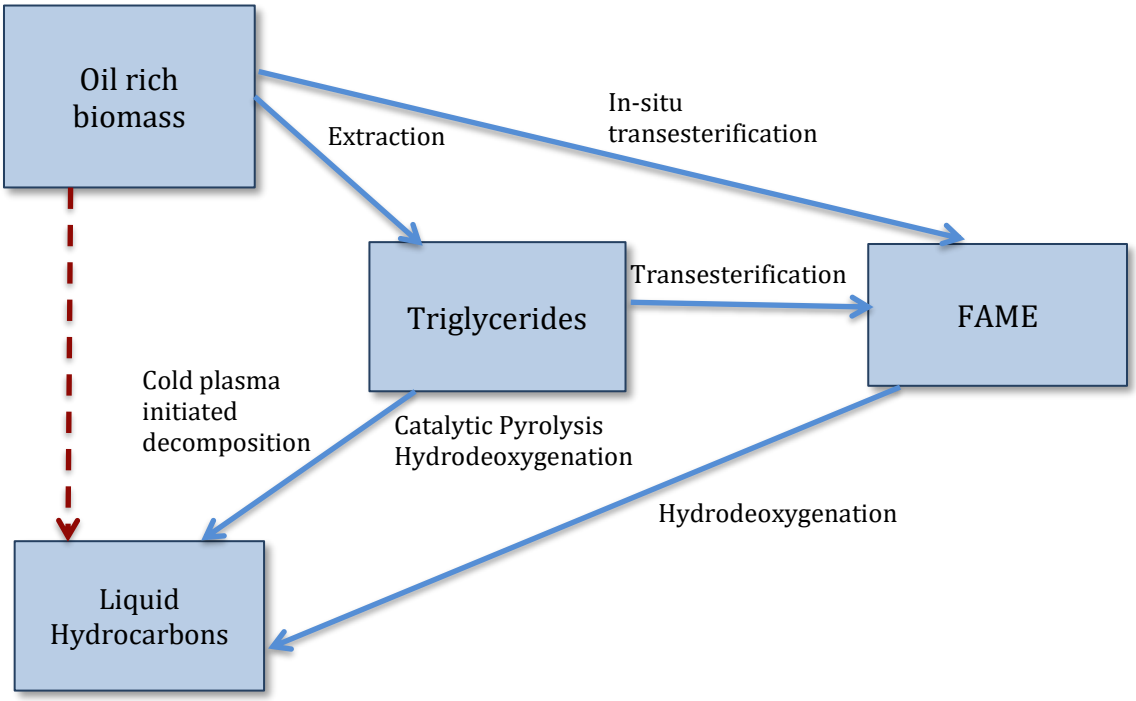

Figure 1.2: Routes for production of liquid hydrocarbons from triglycerides

1.2 Oil-rich biomass feedstocks for liquid fuel production

Currently, triglycerides have to be extracted from triglyceride rich biomass (Figure 1.2) via solvent extraction (typically with hexane/heptane) (Atabani *et al.*, 2012) and mechanical comminution. The triglycerides must then be separated from the solvent, leaving waste biomass and adding processing costs (Jiang *et al.*, 2013). Direct decomposition of triglycerides without prior extraction from the biomass is an attractive prospect that would improve the sustainability of the process and potentially generate valuable by-products.

Recent work has considered the possibility of transesterifying triglycerides to FAME and waste glycerol without prior separation from the biomass source. The process was found to be feasible but required very large quantities of methanol to extract the triglycerides in-situ. However, the waste biomass residue has to be removed at the end of the process (Go *et al.*, 2016). A possible alternative is the use of thermochemical methods, which have been utilised for valorising non-oil containing biomass previously (Agblevor *et al.*, 2010; Aysu, 2015) but no studies on oil-rich biomass can be found to date. If proved feasible, this could provide a method to directly convert oil-rich biomass to liquid hydrocarbons and potentially generate value added products from carbohydrates in the biomass, such as levoglucosan. However, thermochemical methods (300-700°C) (Balat, 2008) have been shown to generate highly acidic and water rich liquid products that required extensive further processing (Bi *et al.*, 2014). High yields of wastes, including both solid residues and gaseous by-products (Wildschut *et al.*, 2009; French and Czernik, 2010), and low yields of liquid hydrocarbons were produced, due to gasification reactions and the resultant low process selectivity (Greenhalf *et al.*, 2012; Eide and Neverdal, 2014). These challenges and the high downstream processing costs have prevented implementation of this direct conversion concept via thermochemical methods to date (Bridgwater, 2012).

Cold plasma assisted decomposition offers a potential solution that would overcome these challenges, allowing efficient direct conversion of biomass to higher quality liquid fuels. This could have many advantages over thermochemical conversion, including tunable process selectivities with and without catalysts, lower operating temperatures and a more robust reactor design. Catalysts could be used to improve process selectivity further, as they have synergistic effects with cold plasma due to the plasma temperature being highest near the catalyst surface. While cold plasma has been used previously for ozone generation, surface modification and gas phase radical reactions such as steam reforming of hydrocarbons, no studies utilising cold plasma for triglyceride valorisation or waste glycerol have been performed to date. This is because cold plasma primarily generates excited species in the gaseous phase and has a limited effect on the decomposition of liquid phase components such as triglycerides and FAME due to mass transfer resistances between phases (Locke *et al.*, 2006) and dissipation of incoming energy via intermolecular bonds in the liquid (Fridman, 2008).

A newer variant of cold plasma known as gas-liquid cold plasma could, in theory, be able to tolerate and decompose liquid feedstocks effectively (Di *et al.*, 2016), while maintaining the easily tunable process dynamics. The hypothesis of this work is that the tunable dynamics would make cold plasma highly appropriate for conversion of either triglycerides or oil-rich biomass to either FAME or liquid hydrocarbons directly, by permitting certain reaction pathways to be favoured over others.

1.3 Aims and objectives

The aim of this thesis was to study the feasibility and effectiveness of utilising cold plasma for valorisation of waste triglycerides and waste products from commercialised transesterification processes. The outcomes of this PhD study could also be applied for upgrading bio-oil derived from biomass or any processes involved in oxygen removal at atmospheric temperature.

The objectives were to:

- Study the feasibility of gas-liquid cold plasma decomposition using a methanol feedstock and establish a reaction pathway.
- Study cold plasma induced valorisation of purified glycerol and establish a complete reaction pathway and kinetic model.
- Study the robustness of cold plasma valorisation of glycerol using a waste glycerol feedstock
- Investigate the effectiveness of gas-liquid cold plasma for the conversion of pure triglycerides to liquid fuels
- Determine the resilience of the cold plasma decomposition process to a waste cooking oil feedstock.
- Investigate the feasibility of direct valorisation of oil-rich biomass via study of cold plasma promoted decomposition of glucose and cellulose

1.4 Thesis structure

This thesis reviewed prior work from literature (Chapter 2) on production of triglyceride derived biofuels and research relating to cold plasma and its potential applications. Chapter 3 detailed the experimental techniques and analysis procedures used within this work and the concepts behind the kinetic modelling utilised. The results and their analysis are included in Chapters 4-6. Chapters 4 (methanol) and 5 (glycerol) studied waste

products from transesterification to establish the feasibility of the technique and its resilience to highly fouling feedstocks. Chapter 6 analysed the direct decomposition of triglyceride feedstocks to liquid hydrocarbons. pure triglycerides were tested initially and extended to waste cooking oils to test the resilence of the process to fouling deposition. Triglycerides (Chapter 6) and cell membranes (from literature) can be decomposed using cold plasma, so decomposition of glucose and cellulose (to represent the cell walls within the biomass) via gas-liquid cold plasma (Chapter 7) were investigated to determine the feasibility of producing liquid hydrocarbons directly from oil containing biomass. Potential applications of the discoveries from this work were considered in Chapter 8. Conclusions and recommendations for future work were detailed in Chapter 9.

Chapter 2. Literature Review

This chapter reviewed literature relating to production of biofuels and pertaining to a novel approach employing cold plasma. The aim of this chapter was to take a wider look at literature concerning valorisation of triglycerides, their products and composition to enable informed consideration of the possibilities. Alternative methods of producing usable fuels from triglycerides including thermally induced deoxygenation, cracking and in-situ transesterification of inedible oils such as algal/seed oils were considered with their challenges and benefits. Reports on cellulose decomposition and modification were reviewed to predict the feasibility of in-situ decomposition of oil-containing biomass with cold plasma. Details of the waste product streams, notably waste glycerol, are included, with their current applications. Previous literature reports on cold plasma types, designs and applications were reviewed to establish the reactor design and baseline conditions within this study and to enable understanding of similar processes to establish reaction kinetics within the investigation.

2.1 Triglyceride feedstock

2.1.1. Transesterification

Biodiesel, a mixture containing ≥96.5vol% fatty acid esters (according to EU standard EN14214), is a key liquid fuel in the current biofuel industry, accounting for 16% of current biofuel production (BP, 2017). It is commonly produced via transesterification, a reaction between triglycerides and a short chain alcohol, e.g. methanol, to produce fatty

acid methyl esters (FAME) in the presence of a catalyst, as shown in Figure 2.1. Any FFA present is also converted to FAME via esterification (Figure 2.1).

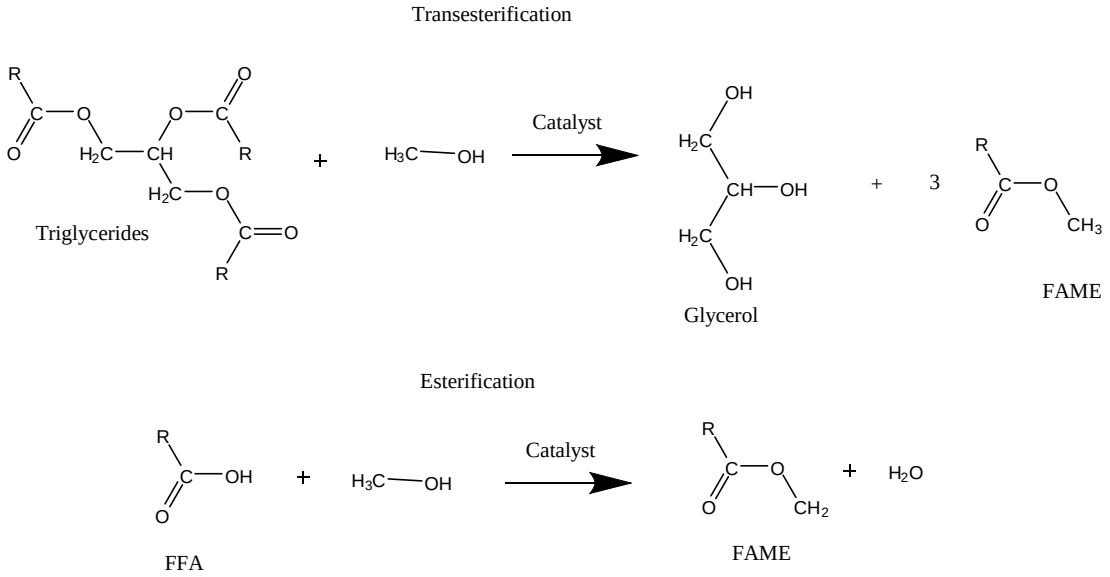

Figure 2.1: Transesterification and esterification reactions

Transesterification of triglycerides to produce FAME and by-product glycerol in the presence of a basic catalyst is performed commerically. However, the process requires a feedstock with low levels of free fatty acids and water (<1wt.%) (Hoydonckx *et al.*, 2004; Boey *et al.*, 2012) to minimise the saponification process and loss of product during separation (Festel *et al.*, 2014).

Currently, biodiesels are predominantly produced from edible vegetable oils (>70%) such as rapeseed, soybean and sunflower oils. These account for over 75% of the total cost of biodiesel production (Atabani *et al.*, 2012). Use of vegetable oils as feedstocks for biodiesel production is in direct competition with the food production industry, which leads to cost and availability implications (Bokade and Yadav, 2009). The environmental impact from deforestation and utilizing arable land which could otherwise be used for food crops, are also significant. A possible solution is the use of non-edible oils, especially from waste products or non-edible crops, such as algal oils, which can often be grown in areas unsuitable for edible crops. Animal fats and oils are readily available, but their high degree of saturation makes transesterification more challenging and produces a poorer quality biodiesel. Further processing by dehydrogenation can reduce the degree of saturation and improve the oil quality but is time consuming and energy inefficient, leading to increased costs (Maher and Bressler, 2007).

The use of waste oils (e.g. waste cooking oils) is attractive as it offers readily available, inexpensive feedstocks that would otherwise require environmentally sound disposal. However, such use presents challenges. Waste cooking oil (WCO) comprises oils that have typically been exposed to high temperatures of around 300°C. These temperatures cause decomposition of the ester bonds in the triglycerides, releasing water, fatty acids, monoglycerides and diglycerides. Impure oils produce lower quality biodiesels than virgin oils, with lower stability, higher viscosity, higher cloud and higher pour points, due to the presence of water, Free Fatty Acids (FFA) and additional salts (Utlu, 2007). Waste or recycled oils from cooking are problematic to transesterify due to their high free fatty acid content (>20wt.%) (Kouzu *et al.*, 2007; Jain *et al.*, 2011) which causes saponification in the basic catalysts, which are required to obtain rapid reaction rates.

While basic catalysts are significantly more effective at promoting transesterification of triglycerides than acidic catalysts, they are also vulnerable to saponification reactions, which simultaneously poison the catalyst active sites and deplete the catalyst. The presence of FFA causes the formation of soaps via saponification with the catalyst acting as the metal ion donor, as shown in Figure 2.2. Any water present promotes hydrolysis reactions, releasing FFA from both glycerides and fatty acid esters, and promoting further saponification (Eze *et al.*, 2015). The presence of soap increases the miscibility of the ester products in the generated waste glycerol phase, reducing the biodiesel yield and complicating the separation and purification of products (Klimmek, 1984). To overcome this, acid catalysts are generally used in pre-treatment steps to remove FFAs. The acid catalyst also induces some transesterification, though this is slower than basic catalysts (Chouhan and Sarma, 2011) and hence the basic catalyst should be introduced once the FFA is removed.

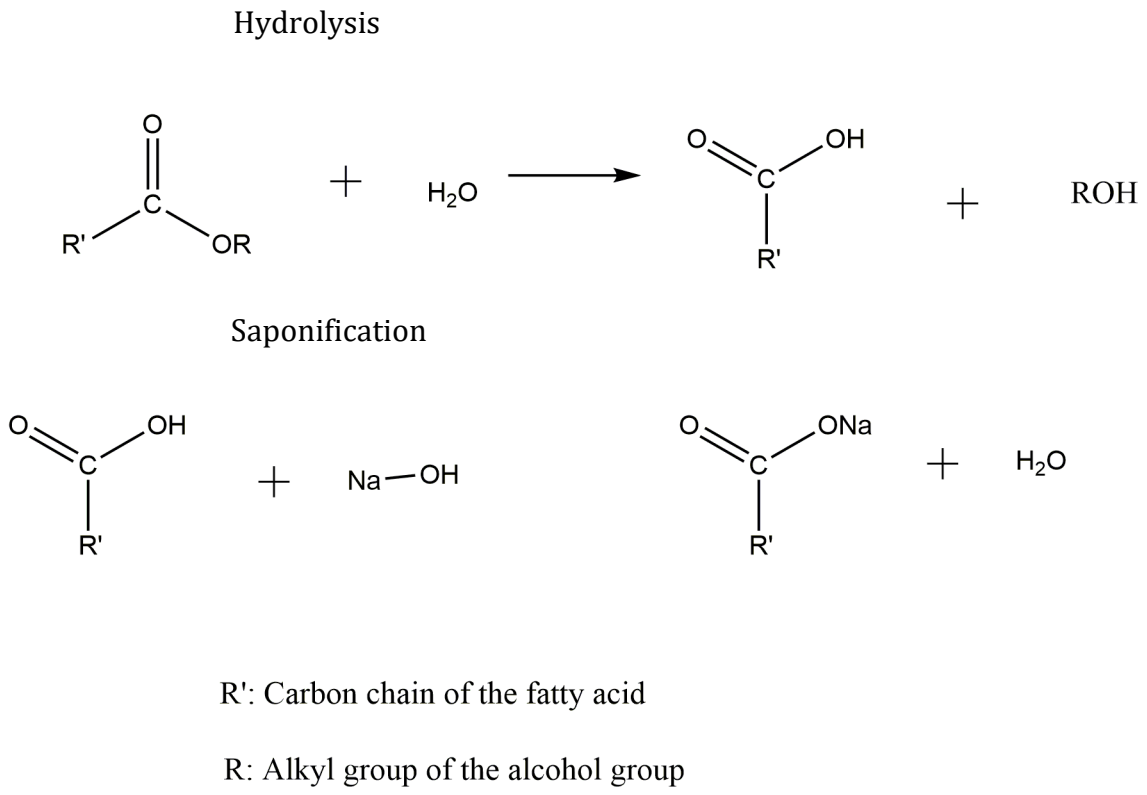

Figure 2.2: Saponification and hydrolysis reactions of FFA (Deng *et al.*, 2009)

2.2 Thermal decomposition of triglycerides

2.2.1 Triglyceride Pyrolysis

Triglycerides can be pyrolysed (Fortes and Baugh, 1999) with or without catalysts to produce hydrocarbons mostly in the diesel range (C9-C15) with ketones, fatty acids, hydrogen, carbon oxides and aromatics (Charusiri and Vitidsant, 2005). Temperatures in the range 400-500°C are typically used for producing liquid products as prior reactive distillation studies on triglycerides found maximum mass loss to hydrocarbon distillates occurs at 420°C, at 17.56wt.%/minute (Wako *et al.*, 2017).

Triglycerides and FAME decomposed at low temperatures (300°C) tended to favour decarbonylation/decarboxylation reactions due to their lower activation energies compared to cracking reactions (Mäki-Arvela *et al.*, 2007). These conditions produced high selectivity (up to 70%) to long chain hydrocarbons (C14-C18) but required 0.5g Pa/C catalyst per 0.035moles feedstock and 6 hour reaction time to achieve only 18% conversion. Temperatures above 500°C have also been used to produce hydrocarbons with a very short residence time i.e. <1 second (Fortes and Baugh, 1999) to avoid gasification to CO_2 and H_2O. The same products were identified throughout the tested temperature range of 400-1000°C but with increased yields of aromatic components (up

to 15wt.%) and gaseous products (up to 61wt.%) at higher temperatures (Wiggers *et al.*, 2013).

A pilot scale process for production of biofuel from triglycerides via non-catalytic fast pyrolysis with low levels of water (<10wt.%) at 525°C produced gasoline and diesel fractions at 23% and 43% yields respectively (Wiggers *et al.*, 2009).

2.2.2 Catalytic Pyrolysis

Catalytic pyrolysis has been extensively studied both for conversion of biomass and for the direct conversion of triglycerides to liquid hydrocarbons. Catalytic pyrolysis of triglycerides is performed between 380-500°C to allow cracking reactions to occur (Sadrameli *et al.*, 2009); (Demirbas, 2008). A range of catalysts have been successfully used, including zeolites (Charusiri *et al.*, 2006), alumina and silicates (Sadrameli *et al.*, 2009), sulfated zirconia (Charusiri and Vitidsant, 2005) and basic catalysts such as sodium carbonate (Demirbas, 2008). Charusiri *et al.* found that increasing temperature, pressure and residence time with a HZSM-5 or zirconium catalyst increased conversion, obtaining 24wt.% yield of gasoline after 90 minutes at 430°C (Charusiri and Vitidsant, 2005). HZSM-5 achieved a similar conversion but produced 40% higher yields of gases and gasoline length hydrocarbons (C_6-C_9) than zirconia, which produced 50% diesel length hydrocarbons. A kinetic model for the pyrolysis of triglycerides for several catalysts including HZSM-5, silicalite and alumina-silicate was developed, which indicated that pyrolysis primarily acts by cracking the C-C bonds in triglycerides to release hydrocarbons, hydrogen and carbon oxides. In terms of liquid production, the high surface area silicalite was effective, producing up to 50wt.% liquid hydrocarbons at 400°C, comparable to HZSM-5, whereas alumina-silicate produced only 9.8wt.%. This suggests that surface area is a key factor in the effectiveness of a pyrolysis catalyst, as the composition and acidity of these catalysts are very similar (Sadrameli *et al.*, 2009).

The presence and abundance of acid sites on each catalyst strongly affects the extent of cracking. Previous work studied three types of HZSM-5 with differing acidities, achieved by varying the Si:Al ratio from 50:1, 240:1 and 400:1 at 450°C with a palm oil feedstock (Sang, 2003). Microporous catalysts, such as zeolites, have been shown to be more active than mesoporous catalysts (Sadrameli *et al.*, 2009) but the latter have a higher adsorption capacity, which may indicate that the underlying material aids in adsorption of triglycerides. Combining two types of catalysts to combine their advantages has been

tested, achieving more than 90% conversion and 30% selectivity to gasoline hydrocarbons with 55wt.% yields of aromatics such as toluene and xylenes at 450°C and a WHSV of 2.5hr^{-1} (Twaiq *et al.*, 2004). However, catalyst preparation procedures and regeneration may be challenging due to the differing catalyst thermal stabilities.

Alkaline pyrolysis catalysts are also effective, producing up to 82.7% conversion and 47wt.% yields of liquid hydrocarbons (C_{10}-C_{18}) at 420°C for $NaCO_3$ catalyst with an approximate residence time of 65 minutes (Dandik and Aksoy, 1998). Using KOH at the same catalyst loading (5wt.%) produced a 54wt.% yield of hydrocarbons at 360°C at 30 minutes (Demirbas, 2008). Alkali catalysts have the added benefits of being relatively low cost and can rapidly remove any fatty acids from the oil, though this results in loss of catalyst from saponification in a 1:1 molar ratio with overall FFA content. These catalysts generally do not dissolve in the triglyceride, but as saponification occurs where the catalyst and triglycerides make contact, metal soaps are likely to be present in the output, which would require additional downstream processing. Catalytic pyrolysis has potential for producing biofuels from triglycerides without requiring an alkyl donor and produces liquid hydrocarbons that do not require blending with petrodiesels. However, as many reactions occur during catalytic pyrolysis, selectivity can be poor even with catalysts that selectively promote hydrodeoxygenation and the process generates carbon oxides, reducing atom economy.

2.2.3 Hydrodeoxygenation

An alternative to pyrolysis is hydrodeoxygenation/hydroprocessing, (Figure 2.3) which use hydrodeoxygenation (HDO) catalysts to remove all oxygen atoms from the triglycerides by elimination reactions as water, CO or CO_2 depending on the hydrogen availability.

Hydrodeoxygenation is the process of removing oxygen from the feedstock via decarbonylation, decarboxylation, hydrodeoxygenation and cracking reactions (Adjaye and Bakhshi, 1995; Wildschut *et al.*, 2009). If no hydrogen is present, hydrodeoxygenation reactions cannot occur so oxygen-containing groups could only be removed by catalytic cracking.

The optimum reaction time for hydrodeoxygenation depends on the reactor temperature and the feedstock. However, to date, the reaction time has not been studied systematically

under typical upgrading conditions. It was reported that pyrolysis oil upgrading in a $NiMo/Al_2O_3$ catalyst packed bed microreactor operating at low temperature and high pressure (180°C and 21bar) increased hydrocarbon yields from 30% at 0.43 second residence time to 52% with a 1.23 second residence time. However, fouling deposits were observed at operating temperatures ≥270°C due to coke formation, which rapidly plugged the reactor channels (Joshi and Lawal, 2012). Further study on the effects of reaction time on product yields and properties would be essential for scale up studies or commercial use.

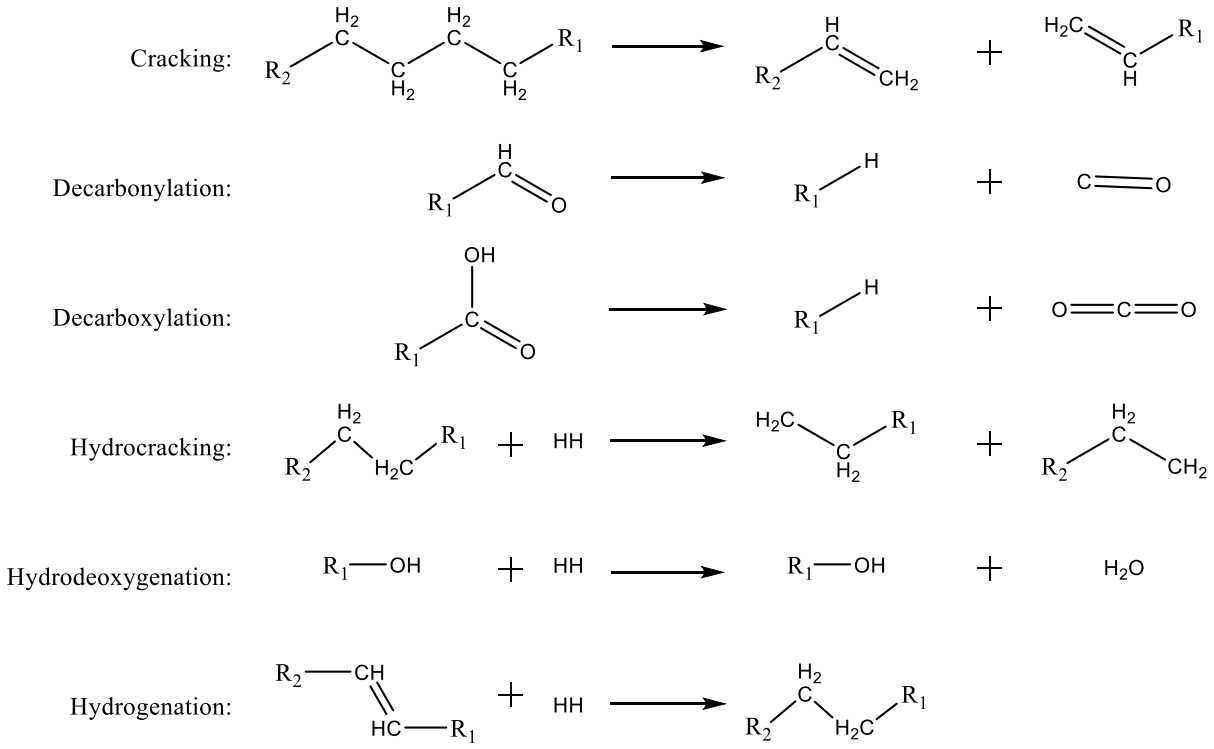

Figure 2.3: Mechanisms of HDO upgrading (Wildschut *et al.*, 2009)

Elimination and substitution reactions (decarbonylation, decarboxylation and hydrogenation) occur spontaneously at temperatures above 250°C, which is the lowest temperature viable for inducing HDO processing (Wildschut *et al.*, 2009). A full reaction pathway is extremely complex due to the large number of different bonds in the triglycerides and the large range of smaller fragments that can result, including FFA, hydrocarbons, acetol and propenal (Aresta *et al.*, 2007; Atong and Sricharoenchaikul, 2009; Rathnasingh *et al.*, 2009; Zuhaimi *et al.*, 2015)), which can further degrade to release CO, CO_2 and H_2O. Therefore, to obtain liquid products, the reaction time for HDO must be tightly controlled to prevent total conversion to low value coke solids, hydrocarbon vapour, water and carbon dioxide.

Due to the complexity of pyrolysis liquids and waste cooking oils, significant research has focused on various model compounds, i.e. phenol (Shafaghat *et al.*, 2015), guaiacol (Olcese *et al.*, 2012) and cresols (Li *et al.*, 2011b), which are considered to be representative of pyrolysis oil. HDO requires moderate temperatures (>250°C) and high pressures (>100bar) (Gutierrez *et al.*, 2009). Below these thresholds, the reaction rate and conversion are low. For example, at 150°C and 40bar H_2, diphenyl ether reaches 65% conversion after 3 hours (Yao *et al.*, 2015), while phenol reached 12% conversion after 3 hours at 300°C and 20 bar H_2 (Tan *et al.*, 2014). Previous studies with pyrolysis oil with a Ru/C catalyst indicated that HDO occurs at very slow rate when operated at ≤175°C (Tan *et al.*, 2014; Yao *et al.*, 2015). This could be due to the high activation enthalpy (above 200KJ/mol) of the reactions that occur during HDO (Venderbosch *et al.*, 2010; Ngo *et al.*, 2014). Further research could be done in this area to allow milder conditions to be utilised.

Theoretically, 50g (approximately 500litres) of hydrogen per kg of oil is required for complete deoxygenation (Mortensen *et al.*, 2011). However, experimental results indicated that at least 10%wt.% more hydrogen was actually required to reduce oxygen content to levels below <0.1mol% (Venderbosch *et al.*, 2010; Mortensen *et al.*, 2011), equivalent to 560 litres H_2/kg oil. HDO requires a long reaction time (4 hours) (Venderbosch *et al.*, 2010) in addition to the previously discussed high pressure, temperatures and hydrogen requirements. Fouling rates typically vary around 7wt.% of the catalyst per hour, giving a catalyst lifespan of around 8 hours. However, the catalyst lifespan can be increased to above 50 hours if a pre-treatment step, known as mild HDO, is used. For this, the oil is heated to the same conditions as the HDO reactor but without the catalyst present so the fouling precipitates and may be separated before the catalyst is introduced.

Due to poor cold properties and low thermal stability, biofuels rich in FAME must be blended with petroleum fuels to meet current standards for liquid fuels and to permit their use in engines and other controlled combustion applications without extensive modifications. The HDO of FAME to long chain hydrocarbons is therefore of great relevance as large amounts of FAME are already available from established commercial

production. FAME deoxygenation is often operated either as a HDO or decarboxylation process, depending on the hydrogen availability.

Decarboxylation also requires high temperatures (>300°C), high pressure hydrogen (>10bar) and an expensive catalyst (typically Pt/zeolite). It can achieve close to 100% conversion with a liquid hydrocarbon yield of 70wt.% with a relatively rapid throughput ($1hr^{-1}$) (Wang *et al.*, 2013a). A detailed study on this technique found that at 335°C with Pd catalyst, 13.8bar hydrogen and a 3-3.5 hour residence time, produced 71wt.% yield of hydrocarbons with an overall conversion of 98% (Wang *et al.*, 2013a). The decarboxylation process has many similarities to HDO, as the same 3 reactions (HDO, decarbonylation and decarboxylation) occur under both systems but in different ratios (Wang *et al.*, 2012a). The main difference between these reactions is the form in which the oxygen is removed i.e. HDO- water, decarbonylation-carbon monoxide and decarboxylation- carbon dioxide. HDO has higher carbon atom efficiency overall, as the methyl group is converted to methane instead of carbon oxides and hydrogen. However, HDO uses 100-300% more hydrogen than decarbonylation and decarboxylation, which has associated costs (Wang *et al.*, 2013b). Decarbonylation releases a combination of carbon monoxide and water and requires 100% more hydrogen than decarboxylation. Carbon monoxide is a potentially harmful by-product, (Jeczmionek and Porzycka-Semczuk, 2014a) but it could be used as a feedstock for other processes (An *et al.*, 2011). Decarboxylation removes 1 carbon atom per molecule as carbon dioxide, and consumes less hydrogen than HDO (Santillan-Jimenez and Crocker, 2012). The reaction conditions of each are chosen to favour one of these reactions over the others based on their relative product distributions. The 3 reactions are illustrated in Figure 2.4, showing the product distributions achieved per FAME molecule.

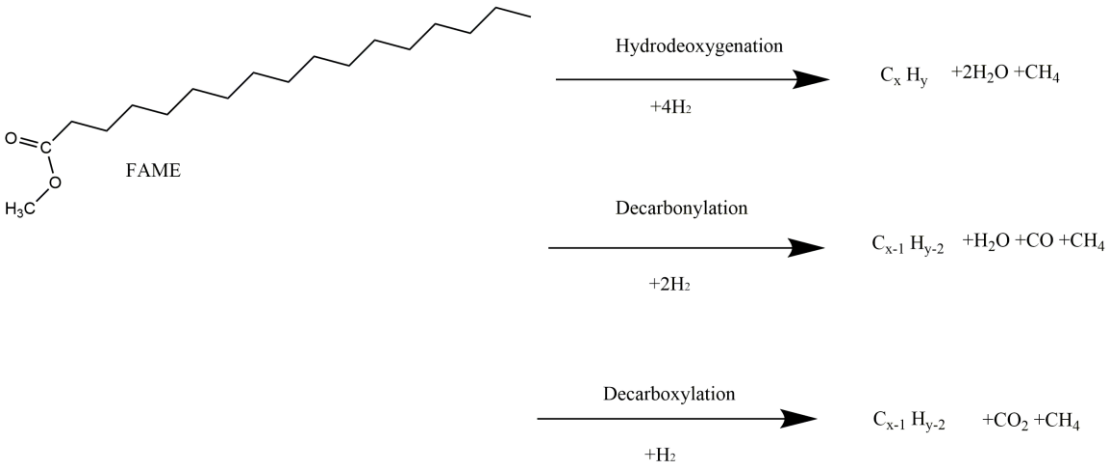

Figure 2.4: Deoxygenation pathways of FAME (An *et al.*, 2011)

Hydrodeoxygenation of FAME or triglycerides require significantly less hydrogen than for bio-oil feedstocks, due to their lower oxygen content (18wt.% vs >50wt.%) (McDonald and Kengne, 2014; Palanisamy and Gevert, 2016) and as the oxygen in FAME is within easily eliminated ester bonds (285KJ/mol vs >300KJ/mol) (Sang, 2003; Tanneru *et al.*, 2014). Therefore, hydrodeoxygenation of FAME or triglycerides is more viable and kinetically favourable (Dundich *et al.*, 2010) than that of bio-oils. However, the hydrodeoxygenation of triglycerides/FAME still requires unsustainably large amounts of hydrogen (>224 Litres H_2/ Litre oil) (>10bar H_2) and high temperatures (>300°C) (Joshi and Lawal, 2012).

Nickel based catalysts exhibited good selectivity to linear alkanes while achieving high conversion. Around 20bar hydrogen at 340°C with a NiP/SAPO-11 catalyst permited 97.8% conversion of FAME (Liu *et al.*, 2016) with a Weight Hourly Space Velocity (WHSV) of 2.5hr^{-1}, giving a yield of diesel length hydrocarbons of 82.4wt.%. Higher yields of hydrocarbons (91.5%) were achieved with 10bar hydrogen in the presence of a Ni/Hβ zeolite catalyst at 270°C after 8 hour reaction time (Chen *et al.*, 2014a). Catalyst support materials also have a significant effect on the catalyst activity (Tan *et al.*, 2014), though this has not been studied for triglycerides. To illustrate this, a conversion of phenol to cyclohexane of 65.6% was achieved by HDO with Pd/activated carbon compared to only 18.1% conversion using Pd/ Al_2O_3 under the same conditions (Tan *et al.*, 2014). This difference is due to activated carbon being a neutral surface that can support acid sites

which promote HDO reactions when in contact with a suitable catalyst such as palladium. This was also discussed in a review by (Mortensen *et al.*, 2011), with the same conclusions drawn. These findings were obtained for pyrolysis oil, but should still apply to HDO of triglycerides as ester bonds are also present in pyrolysis oil.

Noble metals such as Rh or Pd can be also used as catalysts but add significantly to costs as they are highly expensive (Janampelli and Darbha, 2018). An example of work on these catalysts was the conversion of FAME to heptadecane using a Pt-WOx/Al_2O_3 catalyst at 300-380°C with 5 bar hydrogen and a Liquid Hourly Space Velocity (LHSV) of $2hr^{-1}$. This achieved conversions above 95% with an alkane yield of up to 83wt.% at lower hydrogen pressures than utilised for the nickel based catalysts described above (Dundich *et al.*, 2010; Rodina *et al.*, 2017). Catalyst deactivation during FAME/triglyceride HDO was also reported by a single source (Dijkmans *et al.*, 2013) but the catalyst can be regenerated via heating to 400°C under nitrogen. However, the majority of sources did not observe any fouling or loss of activity over the duration of their experimental studies (Dundich *et al.*, 2010; Jeczmionek and Porzycka-Semczuk, 2014b; Yenumala *et al.*, 2017). This differs from HDO of bio-oil, which is susceptible to fouling due to reactions such as aldol polymerisation (Jeczmionek and Porzycka-Semczuk, 2014b; Kikhtyanin *et al.*, 2014).

Zeolites, such as HZSM-5, are alumnosilicate materials that are often used as catalysts for cracking reactions due to their abundant acid sites and highly expanded, uniform structures. These catalysts give similar conversion values to nickel catalysts but produce predominantly alkenes (olefins) instead of alkanes (Danuthai *et al.*, 2009). This reduces the energy content of the liquid fuel unless hydrogenation is performed subsequently. Zeolites can be used in conjunction with other catalysts, such as nickel, to improve conversion further (Liu *et al.*, 2016).

Oxygen can be removed from triglycerides/FAME in the absence of hydrogen via thermal or catalytic cracking, which can be catalysed by any HDO or cracking catalyst, including Pd/Al_2O_3, Ni/Hβ or HZSM-5. However, conversion is noticeably lower (<40%) and catalyst deactivation via solid carbon deposition occurs under these conditions within 5 hours of operation regardless of catalyst choice (Do *et al.*, 2009). Typical conversion of FAME from deoxygenation in the absence of hydrogen is approximately 12% over 3 hour reaction time, with 10% selectivity to long chain hydrocarbons, compared to almost 100%

conversion within 1 hour with a yield of long chain hydrocarbons close to the theoretical maximum (93%) for HDO (Immer *et al.*, 2010). A comparison of HDO to the other techniques detailed earlier in this chapter is shown in Table 2.1.

Table 2.1: Comparison of transesterification and thermal techniques for generating biofuels from triglycerides.

Catalyst	P (bar)	T_{max} (°C)	Time (hrs)	Conversion (%)	FAE/Hydrocarbon yield (%)	Solvent: oil ratio	Feedstock	Reference
Acid catalysed transesterification								
WO_3/ZrO_2 (esterification only)	1	150	2	96	93	9:1	Waste cooking oil (FFA content)	(Park *et al.*, 2010)
DTPA/K-10 clay	17	170	8	92	90	15:1	Vegetable oil	(Bokade and Yadav, 2009)
ZrO_2/SO_4^-	1	500	1	99.6	90.3	6:1	Palm kernel oil	(Hanif *et al.*, 2017)
Base catalysed transesterification								
Li doped $CaO–La_2O_3$	1	65	2.5	96.3	88	15:1	Canola oil	(Maleki *et al.*, 2017)
CaO	1	65	2	100	90	12:1	Waste cooking oil	(Kouzu *et al.*, 2007)
Mg/Al 2:1 hydrotalcites	1	60	4	97.1	89	9:1	Soybean oil	(Gomes *et al.*, 2011)
Supercritical transesterification								
None	65	260	<1 minute	85	76	3:1 methanol	Fresh cooking oil	(Poudel *et al.*, 2017)
None	75	260	<1 minute	95	83	3:1 ethanol	Fresh cooking oil	(Poudel *et al.*, 2017)
HDO								
Sulfated zirconia	10	400	0.5-1.5	80.13	27.53	0	Waste cooking oil	(Charusiri and Vitidsant, 2005)
HZSM-5	10	400	0.5-1.5	85.34	19.32	0	Waste cooking oil	(Charusiri *et al.*, 2006)
Pyrolysis								
No catalyst	1	550	1.5	72	32.1	0	Soybean oil	(Wiggers *et al.*, 2013)
No catalyst	1	330	6	94.9	69.0	0	Soybean oil	(Schwab *et al.*, 1988)
HZSM-5	1	500	0.25	61.72	38.2	0	Sunflower oil	(Chiaramonti *et al.*, 2016)
Decarboxylation								
Ni/C	40	360	6	99.3	77	0	Tristearin	(Santillan-Jimenez and Crocker, 2012)
Pd/C	40	360	6	98	84	0	Tristearin	(Santillan-Jimenez and Crocker, 2012)

As can be observed in Table 2.1, transesterification achieves the highest liquid fuel yields and only produces waste glycerol. However, FAME cannot be used in engines without blending it sparingly with other fuels due to its poor cold flow properties and instability. HDO and pyrolysis can achieve significant yields of liquid fuels (>25wt.%), but require hydrogen gas and liquid hydrocarbon yields are low (<5wt.%). The exception is some decarboxylation reactions, which do obtain a high yield of liquid hydrocarbons (77-84wt.%) but require high hydrogen partial pressures and a very long residence time (6 hours). The conventional methods reviewed above require abundant hydrogen and high pressures, or have low conversions and selectivity to hydrocarbons (Boocock *et al.*, 2008). Alternatives for conversion of FAME to hydrocarbons would be a significant advancement in producing more advanced and sustainable biofuels.

2.2.4 Current Challenges

The previous sections have shown that, unlike transesterification, thermal methods for triglyceride conversion are not prone to saponification and do not generate waste glycerol or waste water. However, thermal decomposition techniques require high temperatures (>400^{o}C) and often high pressures (>10bar) and their selectivity to liquid fuels is often much lower than transesterification (<55wt.% vs 90wt.%), as illustrated in Table 2.1.

The required temperature for triglyceride conversion can be reduced to approximately 260°C and the reaction time reduced from 0.5 - 3 hours (Foraita *et al.*, 2015) to less than 1 minute (Poudel *et al.*, 2017) by using supercritical treatment or hydroprocessing. However, this method requires high pressures (typically in excess of 70 bar) and large volumes of hydrogen (>300liters H_2/ litre triglycerides), and hydroprocessing requires >130bar hydrogen (Foraita *et al.*, 2015). Given the current value of liquid hydrocarbons and the cost of maintaining high pressures, hydroprocessing and supercritical treatments are not of significant interest for triglyceride conversion in industry (Saka and Kusdiana, 2001). However, hydroprocessing is of interest for stabilization of the oil mixtures from pyrolysis (Parapati *et al.*, 2014).

Compared to the typical 90wt.% liquid yield obtained from transesterification (Yang *et al.*, 2018), most thermal decomposition techniques produce low yields of desirable liquid

products. Catalytic pyrolysis, for example, only generated 36.4wt.% liquid (Dandik and Aksoy, 1998; Jeczmionek and Porzycka-Semczuk, 2014a). This is due to the thermal process occurring via non-specific radical decomposition reactions (Yenumala *et al.*, 2017), which result in many side pathways and further decomposition of the desired liquid products to gaseous by-products. The use of catalysts can increase the selectivity of the process to desirable products (Jeczmionek and Porzycka-Semczuk, 2014a; Kun-Asa *et al.*, 2017) but the maximum selectivity to liquid fuels achieved was 66%, which is much lower than that of transesterification (90wt.%) (Wiggers *et al.*, 2009). The applications of thermal methods for producing liquid fuels are therefore currently limited. However, techniques such as catalytic pyrolysis are considered as promising for producing liquid hydrocarbons if selectivities to liquid hydrocarbons can be improved.

2.3 Glycerol/ Waste Glycerol

Glycerol is a by-product of biodiesel production, with approximately 0.1kg of waste glycerol generated per kg of biodiesel produced (Leoneti *et al.*, 2012). As a result, more than 250 million barrels of glycerol are produced annually worldwide. This glycerol is typically 30-85wt.% pure, depending on the feedstock and biodiesel production conditions (Hu *et al.*, 2012; Apparao *et al.*, 2016; Tamošiūnas *et al.*, 2016). The remainder of the waste glycerol comprises impurities including methanol, catalyst, soaps and water. It therefore requires complex purification and separation in order for it to be suitable for commercial applications, e.g. the pharmaceutical and cosmetic industries require purity >99.5wt.%. The large surplus of by-product glycerol has led to market saturation, reducing the value of pure glycerol from £1300/ton in 2008 to £560/ton in 2012 and remaining relatively stable thereafter (Hu *et al.*, 2012). This low value makes the purification of by-product waste glycerol generally uneconomical, particularly for small and medium scaled plants. By-product glycerol is therefore generally considered to be waste requiring environmentally sound disposal (Wu *et al.*, 2013a). Energy recovery from the incineration of waste glycerol is possible but toxic compounds such as propenal may be released (Floyd *et al.*, 2007), leading to extra costs. If a cost effective use for large quantities of by product-glycerol, especially unpurified, could be identified, this waste could be used to produce valuable products whilst offering environmental benefits from reducing the need for its disposal. Almost all attempts to date to use conventional techniques to valorise waste glycerol have produced a wide range of unwanted by-products including fatty acids and soaps, with very rapid catalyst fouling.

Numerous investigations have produced value-added products from purified glycerol e.g. acetol, 3-hydroxypropanoic acid, glycerol carbonate or hydrocarbons (Manara and Zabaniotou, 2016) via either biological (Vlysidis *et al.*, 2011; Sarma *et al.*, 2013) or chemical processes (Aresta *et al.*, 2007; Atong and Sricharoenchaikul, 2009; Rathnasingh *et al.*, 2009; Zuhaimi *et al.*, 2015).

Gasification methods produce primarily hydrogen, carbon monoxide and carbon dioxide and short chain hydrocarbons (C_1-C_3) from glycerol (Van Bennekom *et al.*, 2011). The glycerol can be partially oxidised at 600-800°C with residence times of 2-4 seconds over Ni/Al_2O_3 to form methane, hydrogen and carbon dioxide (Atong and Sricharoenchaikul, 2009). Over 90% conversion of pure glycerol to hydrogen and carbon monoxide (Zhu *et al.*, 2009) was achieved thermally. These gasification methods can tolerate waste glycerol but require high temperatures and their products are less valuable than most other glycerol derivatives e.g. acetol/propenal. At lower temperatures (240-500°C), propenal (acrolein), acetol and propanal can be produced (Mohamad *et al.*, 2011). For example, purified glycerol was dehydrated to form 29-59% propenal and 3-5% acetol at 325°C after 4 hours using Bronsted acidic ionic liquids (Munshi *et al.*, 2010). The remaining products mostly comprised water and unreacted glycerol. Up to 92.71% conversion of glycerol with an acetol selectivity of 90.62% was obtained using semi batch operated reactive distillation and a copper chromate catalyst (Chiu *et al.*, 2006). This process required a temperature of 240°C and pressure of 1 bar with a 5 hour reaction time. Without a catalyst at 300°C, a 40% conversion of glycerol was achieved but the selectivity to acetol was very low (0.5%) (Yamaguchi *et al.*, 2008). The use of supercritical water at the same temperature has also been studied, but had no significant effect on conversion or selectivity without a catalyst (Yamaguchi *et al.*, 2008).

Glycerol carbonate can be produced by reacting pure glycerol with 5MPa carbon dioxide at 277°C in the presence of a tin based catalyst for 15 hours (Aresta et al., 2007). However, this only achieved 2-7% conversion. A higher conversion of glycerol was achieved using urea as a co-reactant, with a 83.6% yield of glycerol carbonate after 4 hours (Zuhaimi *et al.*, 2015). However, the robustness of these processes to unpurified glycerol has not been tested.

All the above methods for generating acetol, propenal and glycerol carbonate are generally incapable of tolerating impurities in the glycerol feedstock, as the catalysts and reactors are vulnerable to fouling. The methods detailed also generally require relatively high pressures, temperatures and catalysts. Low selectivity and low conversions are common when pure glycerol is used as a feedstock without specialised catalysts such as supported copper chromate, due to the many different pathways with similar kinetic constants that occur in parallel.

Thermo-chemical conversion (i.e. pyrolysis at 500-700°C in the presence of Fluid Catalytic Cracking (FCC) catalysts) of waste glycerol was also investigated with the aim of producing acetol or propenal (Corma *et al.*, 2007). A lower propenal yield (20wt.%) was obtained from waste glycerol compared to pure glycerol (30-60wt.%). The acetol yield was low i.e. around 3wt.%. Generation of acetol and propenal was successfully induced with the use of FCC catalysts such as ZSM5, but these were vulnerable to fouling when operated at lower temperatures (<500°C), which limited the possible propenal and acetol yields (Corma *et al.*, 2007).

Little work has been done on plasma assisted glycerol decomposition. Around 57% yields of H_2 were obtained at 45KW cold plasma power with an unrecorded residence time alongside other products including CO (35%), CH_4 (5%) and C_2H_6 (0.9%) (Hoang *et al.*, 2008). Although lower plasma powers can be used without external heating (i.e. 20W), low flowrates of glycerol (0.08ml/min) were required to achieve conversions above 80% (Zhu *et al.*, 2009).

Waste glycerol can be partially oxidised at a higher temperature to prevent fouling, but this can only be employed for gasification processes. For example, at 600-800°C with residence times of 2-4 seconds over a nickel catalyst, up to 60% conversion of waste glycerol was achieved to produce hydrogen and carbon dioxide (Atong and Sricharoenchaikul, 2009). This method successfully avoided the general fouling that typically occurs on all surfaces.

Biological processes typically require the glycerol feedstock to be very pure (around 99%) due to the poisoning effects of alkaline species such as NaOH (Estrela, 2001) and soap (Aresta et al., 2007). Extensive pre-processing would be needed before waste glycerol

from biodiesel production could be used in biological processes, increasing the costs significantly. Converting glycerol to succinic acid using biological processing (Vlysidis et al., 2011) achieved a yield of 1.21g succinic acid/g glycerol when using pure glycerol as the only carbon source. Small additions (<5wt.%) of waste glycerol could be tolerated due to the dissolved carbon dioxide neutralising the alkaline species, though higher levels cause cell lysis in the biomass. Production of 3-hydroxypropanoic acid from glycerol has been performed biologically, but achieved a relatively low product yield, of up to 35wt.% at 100ml scale (Rathnasingh et al., 2009). Other potentially desirable products from biological glycerol decomposition include 1, 3 propandiol and polyhydroxyalkanoates, although limited work on these has been performed to date (Apparao et al., 2016). Gaseous products, such as hydrogen, can also be generated biologically from glycerol. Sarma *et al.* used a biological process to convert waste glycerol to hydrogen at 2.05 litres H_2/litre reaction medium (Sarma *et al.*, 2013). This hydrogen yield corresponds to 31.5mol.%, which is comparable to waste glycerol pyrolysis. However, it should be noted that the biological process required the dilution of the waste glycerol to 10g/litre, sterilisation of the waste glycerol and a residence time of 168 hours compared to 3 hours for pyrolysis, which is unlikely to be economically viable.

2.4 Direct conversion of biomass to liquid fuels

Recently, direct transesterification of oil-containing biomass has become of interest due to the potential to obtain increased yields with fewer processing steps (Figure 1.2). Heterogenous catalysts are generally preferred due to the ease of separation from the oil phase. However, when transesterifying biomass such as lipid rich algae directly, homogeneous catalysts are preferred due to difficulties in separating solid catalysts from the spent biomass (Wyatt and Haas, 2009; Zeng *et al.*, 2009; Kasim *et al.*, 2010). Direct transesterification of oil-rich seeds has been reported to be more efficient than transesterification of extracted triglycerides due to the additional conversion of non-extractable triglycerides (Harrington and D'Arcy-Evans, 1985). Transesterification of meal and seed hull feedstocks also yields FAME from non-extractable triglycerides, though typically only 5% of the hulls can be retrieved as FAME (Harrington and D'Arcy-Evans, 1985).

Work on this topic has found that a catalyst is required to help extract triglycerides by transesterifying the phospholipids within the cell membrane (Bi and He, 2016; Salam *et*

al., 2016) and to tranesterify the extracted triglycerides. Triglyceride extraction can be performed without catalysts using appropriate solvents such as n-hexane, but the methanol and other short chain alcohols typically used as alkyl donors are largely immiscible with triglycerides (Zeng *et al.*, 2009). Methanol was only capable of extracting 4.5wt.% of the soybean as triglycerides, compared to 45wt.% from n-hexane (Zeng *et al.*, 2009). Hexane is an effective co-solvent, which helps to extract the triglycerides from biomass feedstocks. However, the ratio of co-solvent to the alkyl donor is critical. Too little co-solvent and the triglycerides are not extracted effectively, and too much co-solvent reduces activity via dilution of the reactants (Caetano *et al.*, 2017).

Co-solvents (such as CO_2 or n-hexane) can improve extraction significantly but longer reaction times (>2 hours) are still required to achieve triglyceride conversions to FAME and glycerol close to 100% (Wyatt and Haas, 2009; Kasim *et al.*, 2010). These processes are typically restricted to temperatures below the boiling point of methanol (≤65°C), as pressurisation would otherwise be required to maintain a liquid phase (Harrington and D'Arcy-Evans, 1985). Reducing the particle size of the biomass improves conversion signficantly, e.g. 43% conversion to FAME with 1mm particles but 86% with 0.3-0.5mm particles (Kildiran *et al.*, 1996). Further reductions in particle size can further increase conversion but have little further effect on the reaction rate once conversion approaches 100%.

Compared to conventional glyceride oil transesterification, the amounts of solvent, catalyst and alkyl donor required for in-situ transesterification are typically much higher due to the water content of oil-rich biomass, which dilutes the acid and can induce hydrolysis of glycerides to FFA (Atadashi *et al.*, 2013). Haas et al reported that the solvent dilution ratio had to be increased by 150% compared to transesterification of thoroughly dried algal biomass, to achieve similar conversions to FAME. Catalyst depletion due to saponficiation was observed to increase by 127% with wet biomass sources (Haas *et al.*, 2004). A similar result was observed for in-situ transesterification of microalgae biomass using an SrO/SiO_2 catalyst. This found that moisture completely inhibited the transesterification reaction but in the absence of moisture, 95% conversion was achieved within 10 minutes (Tran *et al.*, 2013).

2.4.1 Current Challenges

The main barrier to direct conversion of low value oil seeds or algal biomass using basic catalysts is their high FFA content, similar to that of waste cooking oils. This can be countered by using a high alcohol: oil ratio, but increases operating costs. For example, chlorella vulgaris biomass (3.4wt.% FFA) was successfully converted to FAME at conversions of 78% using basic NaOH catalyst over 75 minutes, but required a methanol: lipid molar ratio of 600:1 (Velasquez-Orta *et al.*, 2012). Acid catalysts under the same conditions can achieve 97% conversion but typically require a 20 hour reaction time due to the lower catalyst activity of acid catalysts (Demirbas *et al.*, 2016). The extraction of the liquid products could be performed using a Soxhlet extractor, which can extract the products from the reactor into an appropriate solvent where they can be processed without complicated separation (Li *et al.*, 2011c). The solid catalysts would also need to be separated out from the residual biomass and waste streams.

Three potential solutions have been proposed to date for simplifying separation of heterogenous catalysts from residual biomass (Jiang *et al.*, 2013). The first uses indigenous lipases from germinating seeds instead of the catalyst; the second uses a catalyst basket to keep the catalyst separate. The final alternative uses a magnetic catalyst support such as Fe_3O_4-SiO_2, allowing magnetic removal of the catalyst for reuse (Tran *et al.*, 2012).

The use of indigenous lipases from germinating seeds was judged to be promising but required a germination period of about 4 days to allow high activity, which is undesirable due to sizing implications (Jiang *et al.*, 2013). Immobilized lipases work well for liquid oils but their application for direct in situ transesterification is hindered by the need to separate immobilized lipase from the residual biomass (Tran *et al.*, 2012). The use of a catalyst basket to contain the catalyst is more practicable but reduces reaction rates due to separation of the reactant and catalyst. Magnetic supports (e.g. Fe_3O_4) were initially successful and tolerated moisture well but catalytic activity rapidly decreased, dropping below 80% after only 3 uses, limiting the catalyst lifespan. Further research into other magnetic catalysts, such as $S_2O_8^{2-}/ZrO_2–TiO_2–Fe_3O_4$, demonstrated they could be extracted 8 times after use and maintain 85% yields, which could be a potential solution to the separation of solid catalysts from residual biomass (Wu *et al.*, 2014).

For in situ transesterification to be effective, the reaction conditions must facilitate the breakdown of the biomass (typically algae or seed biomass) cell walls. The cell walls are primarily composed of cellulose with a membrane of glycerides and proteins for active and passive diffusion into and out of the cells (Oasmaa *et al.*, 2003; Huber *et al.*, 2006; Choudhury *et al.*, 2014). Therefore, the properties of cellulose are key in developing methods for performing in situ transesterification.

2.4.2 Cellulose Properties and Separation

Cellulose (Figure 2.5) is a linear polymer of D-glucose. Many hydrogen bonds link the molecules together, giving cellulose high tensile strength (Huber *et al.*, 2006).

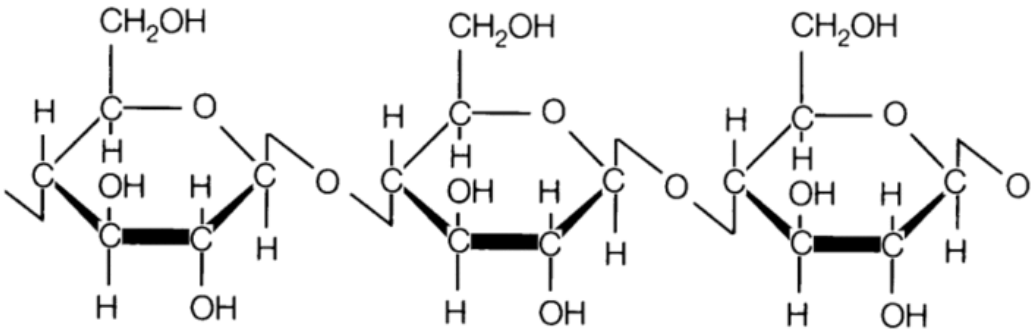

Figure 2.5: Structure of cellulose (Klemm *et al.*, 2005)

Most current methods of valorising cellulose employ acid catalysed hydrolysis of the cellulose polymer to its monomer, glucose, before further conversion to liquid products. Various pre-treatment methods are employed to enhance conversion, including steam explosion, dilute acid treatment and mechanical comminution. The conditions used for cellulose hydrolysis are heating to 150°C at >5bar pressures in the presence of acids (e.g. sulfuric acid, nitric acids or solid acids such as amberlyst-15) (VandeVyver *et al.*, 2011). The resulting glucose can be purified easily and is typically used for chemical or biological processes, or thermally decomposed to furanic or pyranic products.

Once glucose is produced, decomposition to more valuable products can be performed by thermal treatment at 500-600°C under a nitrogen atmosphere. The kinetics of this process were investigated during investigations into pyrolysis, which established that complete conversion of glucose to furans, pyrans, gaseous products and solid residues, occurs within 2-3 seconds at 500°C under a 1 bar nitrogen atmosphere (Vinu and Broadbelt,

2012). Thermal treatment of glucose and mannose achieved 94.6% conversion with yields of 5-hydroxymethylfurfural and furfural of 16wt.% and 7wt.% respectively, with up to 3wt.% yields of levoglucosan and other furan based materials (Hu *et al.*, 2018). It was also reported (Seshadri and Westmoreland, 2012) that gaseous and non-furan products can also be produced from glucose during thermal decomposition, including glyceraldehyde, ethendiol and glycolaldehyde.

Thermal decomposition studies on cellulose without hydrolysis have also been performed (Henrique *et al.*, 2015). These indicate that the cellulose purification method affects the optimum temperature for cellulose pyrolysis, but that in general, 600°C was required to achieve decomposition above 20wt.%, while 800°C obtains complete conversion to gaseous products (gasification).

It has been proposed that cellulose decomposition operates via four possible pyrolysis reaction pathways which occur in parallel, as shown in Table 2.2 (Wang *et al.*, 2012b). The C-O bonds are the least resistant to degradation, with their decomposition producing pyrans, furans and water (Wang *et al.*, 2012b).

Table 2.2: Cellulose degradation pathways(Wang *et al.*, 2012b).

Pathway	Product	Reaction	Reaction location
1	Levoglucosan	Dehydrogenation	C1 and C6
2	3,4 anhydroaltose	Dehydrogenation	C3 and C4
3	Furfural	Repeated hydrogenation and isomerisation	C1, C2 and C5, with loss of C6
4	Hydrocarbon chains (C8 or less)	Ring opening reactions	Non-specific

According to kinetic studies, cellulose pyrolysis generated a similar range of products (furans, pyrans and cyclic ketones) to glucose pyrolysis with a marginally faster reaction rate (Wang *et al.*, 2012b). However, a larger proportion of the feedstock (>25wt.%) was converted into a solid carbon based material instead of liquid products, which reduces conversion and liquid yields. The liquid products from cellulose pyrolysis are mostly furans and pyrans such as levoglucosan but also include short chain carboxylic acids, which were not detected experimentally for glucose (Seshadri and Westmoreland, 2012). A carbonaceous solid results, as well as a tar coating from polymerisation of the degradation products that form a fouling layer on all reactor surfaces.

The fouling deposits can be removed by steam desorption using pressurised steam (>5bar) at temperatures above 800°C for approximately 2 hours, a method which has mostly been used for removing lignocellulosic biomass pyrolysis derived fouling. Increasing the pressure could decrease the removal time (Tian *et al.*, 2013) but there is a trade-off between energy requirements, equipment costs and the extent of catalyst regeneration required. Thermal decomposition of the fouling products produces synthesis gas (Chan and Tanksale, 2014), which is a moderately valuable product.

Combustion (≥700°C) can also be used to remove coke deposits from the reactor. Coke deposits are oxidised to carbon dioxide, carbon monoxide and water, but the catalysts can potentially be damaged by sintering, so this technique is not widely used (Garcia *et al.*, 2000; Zhang *et al.*, 2014).

Cellulose can be used for a wide variety of applications directly, e.g. filler in tablets, resins and plastics, due to its strength, flexibility and low cost. However, cellulose is highly hydrophilic which prevents its dispersion in non-polar solvents which limits the range of potential applications. Surface modification, for example with amine or amide groups, could reduce the hydrophilicity (Li *et al.*, 2015) and permit additional uses if a method could be developed. Surface modification with ester or acetyl groups can be performed chemically and surfactants employed, which is useful for some applications such as in composite materials (Missoum *et al.*, 2013). However, the limited range of surface modifications prevents the wider use of cellulose. The substitution of amine or amide groups could alter the material properties to permit use as bacterial supports for biochemical processes or grafted onto other polymers to produce assorted composites.

Currently, cold plasma is used to add nitrogenous groups to cellulose using ammonia as a nitrogen source (Deslandes *et al.*, 1998; Pertile *et al.*, 2010). Nitrogen has been used directly (instead of ammonia) at low powers (33W) and pressures (20-100Pa) (Deslandes *et al.*, 1998; Pertile *et al.*, 2010). This successfully introduced nitrogenous groups and increased porosity but did not affect wettability or other surface parameters. Further development of this technique may allow amine group substitution without ammonia, which would help with making sustainable cellulose based composites.

2.5 Cold Plasma and its applications to chemical and bio-refining processes

Plasma, the 4th state of matter, is defined as an ionised gaseous state with electrical conductivity due to the presence of free electrons, ions and radicals. Plasma is generated by inducing decomposition of the gaseous molecules, thermally, electrically or via application of microwaves or ultraviolet radiation. Due to its high concentrations of reactive species such as radicals and free electrons, plasma is an effective reaction initiator (Sato *et al.*, 2014). There are two main types of plasma, cold (non-thermal) plasma and thermal plasma. Both types can be found in nature. Examples of thermal plasma are stars and lightning. Fire and the Aurora Borealis are examples of cold plasma (Fridman, 2008).

Thermal plasma occurs when there is a thermal equilibrium between the electrons and ions/molecules in the bulk of the phase. This is often achieved by heating the gas to very high temperatures using fuels such as acetylene, though thermal plasma can also be induced via microwaves and electrically (Khani *et al.*, 2014). For the gas phase to transition to a plasma, the temperature has to be high enough to break down the molecules in the gas, generally ≥3000°C. As the mean electron temperature determines the reactivity of the plasma, most thermal plasmas are operated at ≥3500°C (Mostaghimi and Boulos, 2015). However, this extreme temperature means that any feedstock input is rapidly decomposed to the most thermodynamically stable form possible so reactions with unstable products are not viable in thermal plasma (Tamošiūnas *et al.*, 2016).

The temperature of the electrons in cold plasma is much higher than the bulk temperature (non-equilibrium). As plasma has a high electron temperature except when the power available is very low, cold plasma can be of ambient temperature or below and still retain its ability to initiate reactions (Di *et al.*, 2017). This offers significant advantages for inducing reactions that produce unstable products as the bulk temperature can be low enough to allow the products to accumulate. Some theoretically proposed reactions are not observed thermally at any temperature, as their activation energy is high and the rate constant of the reaction is inversely proportional to the temperature. The product may also be unstable at high temperatures. The presence of high energy species in cold plasma, coupled with the low temperature of the bulk, can allow these otherwise unachievable reactions to be performed at acceptable conversions (Aerts *et al.*, 2015).

2.5.1 Cold Plasma Mechanics

Electrically derived cold plasma initially consists of only the externally imposed electric field. This electric field prompts excitation of electrons from the carrier gas and the reactor walls. These electrons then generate other excited species via electron impact dissociation and other interactions with stable molecules, generating the radicals and ions known to be present in cold plasma.

Cold plasma induces reactions through three pathways: electron driven, ion driven and radical driven mechanisms, which occur in parallel (Fridman, 2008). These pathways are all initiated by the electric field, and hence the overall activity of the plasma depends on the field strength. The electric field depends on the gas pressure, voltage difference and the width of the discharge gap (Hu *et al.*, 2002). Control of these variables hence allows tight control over the process dynamics, and allows flexibility in reactor design provided these parameters are maintained. Catalysts and packing materials synergise well with cold plasma as these reduce the effective discharge gap locally and hence focus the electric field in the vicinity of the packing.

The electrons required for electron driven reactions are generated via excitation of gas phase compounds by the electric field. These electrons interact with the gases in the cold plasma to generate both ions and radicals via the mechanisms shown in Table 2.3 (Hu *et al.*, 2002).

Table 2.3: Range of electron driven reactions under cold plasma (Hu *et al.*, 2002)

Excitation	$e + A_2 = A_2^* + e$
Dissociation	$e + A_2 = 2A + e$
Attachment	$e + A_2 = A_2^-$
Dissociative Attachment	$e + A_2 = A^- + A$
Ionization	$e + A_2 = A_2^+ + 2e$
Dissociative Ionization	$e + A_2 = A^+ + A + 2e$
Recombination	$e + A_2^+ = A_2$
Detachment	$e + A_2^- = A_2 + 2e$

Radicals are generated from electron impact dissociation reactions, displayed in Table 2.3, and induce their own set of reactions in the gas phase. Ions can also form, which share the same range of reactions as radicals, which are shown in Table 2.4. Ions and radicals

can induce different reactions from electrons, including charge transfer and recombination reactions (Zhang *et al.*, 2017).

Table 2.4: Range of radical driven reactions under cold plasma (Hu *et al.*, 2002)

Penning Dissociation	$M^* + A_2 = 2A + M$
Penning Ionization	$M^* + A_2 = A_2^+ + M + e$
Charge Transfer	$A^{\pm} + B = B^{\pm} + A$
Ion Recombination	$A^- + B^+ = AB$
Neutral Recombination	$A + B + M = AB + M$
Collisional Detachment	$M + A_2^- = A_2 + M + e$
Associative Attachment	$A^- + A = A_2 + e$
Synthesis (electronic)	$A^* + B = AB$
Synthesis (Atomic)	$A + B = AB$
Decomposition (electronic)	$e + AB = A + B + e$
Decomposition (Atomic)	$A^* + B_2 = AB + B$

Application of cold plasma for chemical processes is a relatively novel development, though the use of cold plasma for ozone generation is well established (Hartmann *et al.*, 2007). Most studies used cold plasma for reactions with gaseous and solid feedstocks. Examples include conversion of carbon dioxide to carbon monoxide and oxygen (Zhang *et al.*, 2017), hydrocarbon reforming and surface modification of cellulose and other polymers (Deslandes *et al.*, 1998).

Cold plasma is not generally utilised for liquid processes as the excited electrons are not effective of initiating decomposition of liquids directly, as the intermolecular forces dissipate the incoming energy. The main applications of gas-liquid cold plasma currently are water treatment (Locke *et al.*, 2006; Malik, 2010; Sein *et al.*, 2012) and various medical applications, most notably disinfection of wounds and sterilisation of medical equipment (Uhm *et al.*, 2012). Use of cold plasma for decomposition of liquid wastes such as glycerol,

glycerides or biomass has not previously been investigated and forms the basis of this thesis.

Cold plasmas have been used in certain bio-refining applications, such as electroporation of biomass to enhance drying (Babaeva and Naidis, 2018). Cold plasma introduces additional pores into the cell walls and membranes of cells by producing excited species that repel the non-polar chains of the phospholipids in the cell membrane. This typically aims of either extract the cell contents or degrade infectious biomass (Kuznetsova *et al.*, 2016). Electroporation acts by degrading bilayer components in the external membrane, which become fragmented and polar (Sowers, 2012). These distort the local bilayer, causing the formation of small holes, which vary in size depending on the plasma power and other factors such as biomass size distribution.

A higher power cold plasma (Approx 500-1000W) is utilised to generate pores for injecting plasmids and other DNA samples into cells and is the current method of choice for genetic modification of mammalian cells (Beebe, 2013). Apart from its applications in electroporation, cold plasma is not used in biological processes due to the relatively poor selectivities compared to the demands of bio-refinery processes and the higher risk of cell damage (Wang *et al.*, 2011).

2.5.2 Plasma Arcs

Plasma arcs are a type of thermal plasma that form in cold plasma when the voltage across electrically induced plasma becomes sufficiently high. At lower voltages, the excitation and breakdown of gas molecules occurs relatively evenly between the electrodes and on their surfaces. However, as the voltage increases, the increased degree of ionisation decreases the electrical resistance of the plasma, increasing the current (Zhang *et al.*, 2016). The increased current on lower energy paths between the electrodes means that the lowest energy path becomes more electrically conductive rapidly and hence more electricity is discharged along that path (Malik, 2010). The strong discharge ensures this path remains the most conductive path, focussing further discharges along it, producing a plasma arc. The plasma arc causes an increase in temperature from electrical resistance, increasing continually until the electron and bulk temperatures match (i.e. thermal plasma). This arc will be focussed on a very small area of the ground electrode and can easily cause damage to the electrode and reactor contents (Locke *et al.*, 2006). Visible light

is also emitted from the high temperature plasma arc. The point at which plasma arcs form for a given gas pressure and voltage is described in Paschen curves. These are graphical illustrations that can be used to predict maximum plasma powers for a given reactor design. Plasma arcs are generally unpredicatable and undesirable but can be useful for inducing reactions, which is achieved through reactor design and control of experimental conditions.

The positive feedback loop between the conductivity of the arc and the current flowing through it means that shut off systems have to be included in the system or the current would continually increase until the reactor was destroyed. When properly controlled by preventing exponential current increases, plasma arcs can be used for various purposes and are the basis of gliding arc plasma reactors (Burlica *et al.*, 2010). Other applications of plasma arcs include spark plugs for electrical ignition of fuel/air mixtures, arc welders that use the resulting thermal plasma for welding metal and electric arc furnaces that use the thermal plasma to melt down metals.

2.5.3 Cold plasma reactor configurations

Most applications generate cold plasma electrically, though induction via microwaves is also widely utilised. Cold plasma generation methods include: dielectric barrier discharge, corona discharge, gliding arc and plasma jets. Other techniques for electrical cold plasma generation exist, which mostly are variations on the above methods and are generally categorised by the spacing distance between the electrodes.

2.5.4 Dielectric Barrier Discharge (DBD)

Dielectric barrier discharge (DBD) reactors use a pair of electrodes separated by either one or two insulating barriers with dielectric properties, typically with a spacing of approximately 1cm between the electrodes. The insulating layers prevent electrical discharges or plasma arcs but their dielectric properties allow the electrical potential energy between the electrodes to produce columns of plasma, as illustrated in Figure 2.6. These columns contain higher levels of radicals and excited species (Neretti *et al.*, 2017) than the rest of the reactor. The position of the insulating layers between the electrodes does not affect the effectiveness of cold plasma, with some work utilising a single barrier

mounted equidistant between the electrodes to obtain two separate reactor volumes (Kogelschatz *et al.*, 1997).

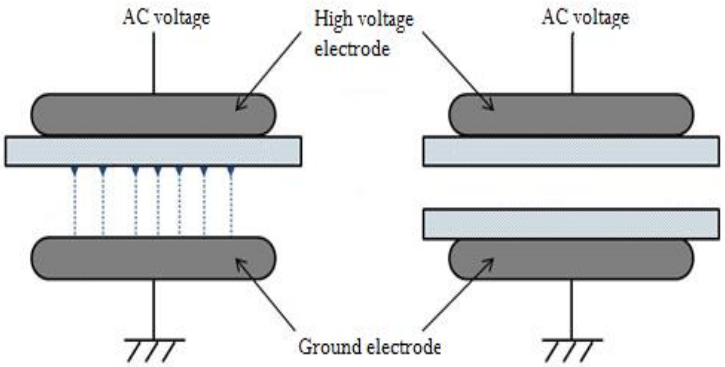

Figure 2.6.: Example dielectric barrier discharge reactor cross sections with one (left) and two (right) insulating layers

DBD reactors produce UV light through relaxation of excited species in the plasma. This feature is used commercially for the production of ozone and early attempts at commercial production of nitric acid and ammonia. It is also possible to use the resulting UV radiation for medical applications such as disinfecting skin (Liu *et al.*, 2010; Uhm *et al.*, 2012) or surfaces (Wolf *et al.*, 2007).

DBD reactors require a supply of high voltage AC electricity (Tian *et al.*, 2016), which is most effective with microwave to radio frequency AC. Power can be supplied from a typical wall socket with a transformer and a frequency converter to increase the voltage and the frequency to the desired values.

A variant of DBD is called resistive barrier discharge (Uhm *et al.*, 2012). This utilises an electrode with a highly resistive cover, which allows much lower frequency electricity to be used. It is also possible to replace the resistive cover with a semi-conductive layer, such as gallium arsenide, which allows DC electricity to be used under specific conditions (580-740 V) (Fridman, 2008). DBD reactors, unlike many other types of plasma generation, can tolerate relatively high pressures (up to 1 bar) compared to many other plasma reactors, which require partial vacuums, and produce little heating relative to the energy present in the plasma. The DBD plasma field is highly energetic compared to other plasma reactors, allowing high-energy reactions to occur more quickly but wastes energy when the plasma is shut off unless energy recovery is performed.

Dielectric barrier discharge reactors can be any shape, with the restriction that the electrodes must be a constant distance apart throughout the reactor to prevent plasma arcs. Most DBD reactors are either plate type or cylindrical: plate type has two plates spaced less than 1cm apart with a dielectric layer between; cylindrical types have one electrode inside the other.

The disadvantages of DBD are the low power number/ electrical efficiency, often in the range 0.1-0.3, the limited range of discharge gap widths and high ignition voltages. The combination of a small gap between the electrodes and the high voltage means plasma arcs are possible at higher electrical currents (Ge *et al.*, 2015).

DBD reactors with two dielectric barriers are resistant to fouling due to the insulated electrodes (Khani *et al.*, 2015), and generally no catalyst is required. The most electrically active zone of the reactor is at the reactor inner surfaces, which can act to degrade any fouling (Karuppiah *et al.*, 2012), making DBD reactors effective for fouling prevention. Using cold plasma to remove oxygen from bio-oil has been tested previously by decomposing raw pyrolysis oils with ethane in a DBD reactor to produce hydrocarbons and hydrogen (Khani *et al.*, 2015). This obtained conversions of 30-70%, depending on plasma power, to gaseous hydrocarbons (C_1-C_3) and hydrogen at selectivities of 24 and 72% respectively. This is effective for producing gaseous fuels but is comparable to the results of gasification studies (Hlina *et al.*, 2014). Other work using cold plasma achieved pure glycerol conversion of 70% to hydrogen and carbon monoxide at 80% selectivities, using a gliding arc plasma reactor (Zhu *et al.*, 2009). 80W cold plasma was used for dry reforming of methane (Wang *et al.*, 2009) using a fluidised bed of Ni/Al_2O_3 catalyst, obtaining 11% conversion of methane to longer hydrocarbons at 25°C, increasing to 47% at 500°C .

The ability of cold plasma to remove fouling from catalysts such as HZSM-5 has been successfully demonstrated (Fan *et al.*, 2015) in the presence of oxygen, rapidly converting coke to carbon oxides and restoring full catalytic activity within 5 minutes. The prerequisite for oxygen to be present to prevent fouling accumulation may not apply if other oxygenated compounds are present. This has not yet been proven, and more work would be needed to determine if cold plasma can prevent fouling during operation.

2.5.5 Gliding Arc Plasma Reactors

Gliding arc plasma reactors use the arc discharge phenomenon to produce a stream of cold plasma by passing a stream of the desired gas through plasma arcs (Derakhshesh *et al.*, 2010). The rapidly moving gas pulls the highly conductive plasma arc along the electrodes towards the outlet, which transitions from thermal to cold plasma as the arc dissipates, and a stream of cold plasma leaves at the gas outlet. The electrodes can be any shape, such as conical, diverging or straight. Diverging is the most common type, often knife shaped, with the closest approach between the electrodes near the gas inlet and diverging after that (Du *et al.*, 2007). Figure 2.7 shows a cross section with a diverging plasma stream being generated. The result is that the arc forms at the closest approach and the plasma is pulled away with the gas stream.

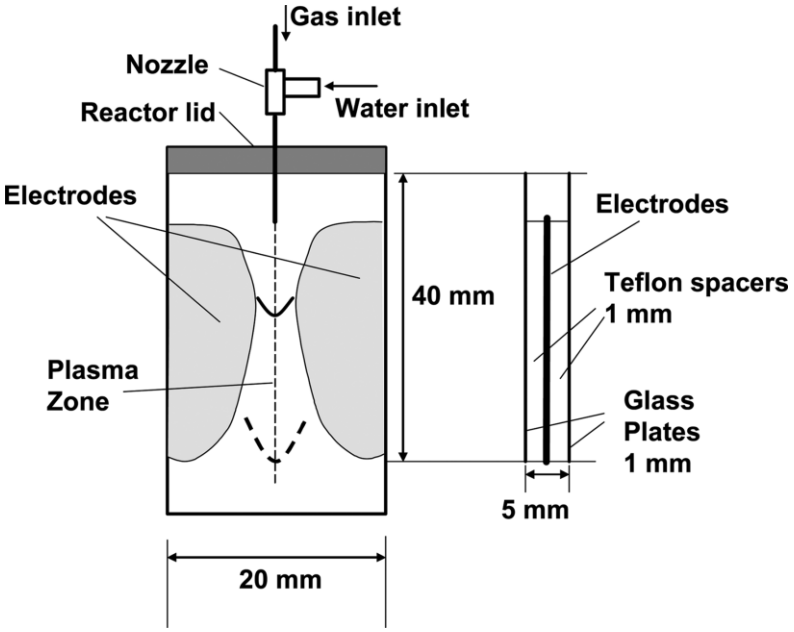

Figure 2.7: Cross section of a gliding arc plasma reactor (Zhang *et al.*, 2016)

The electrodes are aligned to the direction of flow, which causes the arc to move along the electrodes with the gas, stopping when it reaches the end then reforming at the closest approach. Gliding arc plasma reactors are relatively simple to build and are mostly used for gas conversion reactions such as steam reforming (Khani *et al.*, 2014). Liquids can also be introduced provided they are finely dispersed, in which case the reaction occurs on the surface of the gas–liquid interfaces (Burlica *et al.*, 2010). The process can also be used for solids by situating the solid in the path of the plasma stream. However, process control is significantly more complicated than other plasma reactors due to the continuously changing plasma arcs and the plasma generated is less energetic than DBD plasma.

2.5.6 Corona Discharge Reactors

Corona discharges are relatively weak discharges compared to the other reactor designs and only occur below atmospheric pressure in close proximity to a strong magnetic field and an electrode with a small radius of curvature. The original design featured two cylindrical electrodes inside an insulating reactor, with one mounted inside the other with a short separation distance. This design is very similar to a cylindrical DBD reactor, except no insulating dielectric layers are used (Hartmann *et al.*, 2007). The electrode separation is chosen in the range of 0.5-2cm to achieve discharges while maximising energy efficiency. Compared to DBD reactors, the voltage needed and the discharge strength are much lower, but the process is significantly more energy efficient (90% vs 50%) (Malik, 2010). However, pressures below atmospheric and low voltages are required to prevent plasma arcs (Hu *et al.*, 2002). An alternative configuration is a multi-electrode arrangement with multiple needle like anode electrodes in a grid around a central electrode that acts as the cathode. This is an alternative for scaling up, as it maintains the small radius of curvature for the electrodes and allows the diameter of the reactor to be increased. However, corona plasma reactors are typically scaled out by utilising multiple reactors in parallel (Feng *et al.*, 2009).

2.5.7 Microwave plasma reactors

Cold plasma can also be generated using microwaves. Microwave plasmas have been used for hydrogen generation from solid wastes (Lupa *et al.*, 2012) or methane (Czylkowski *et al.*, 2016) and for production of nanocrystalline diamond (An *et al.*, 2015) and silicon carbide (Menser *et al.*, 2016).

This method of cold plasma generation is highly energy efficient (up to almost 100%) and does not require electrodes (Czylkowski *et al.*, 2016). However, the reactor has to be enclosed to prevent loss of microwave energy and the power systems are signficiantly more complex. Additionally, all forms of microwave plasma have significantly increased bulk temperatures (from microwave heating) compared to electrical methods (Chang, 2001). Therefore, microwave plasmas often generate thermal plasma and are not well suited to applications where low temperature operation is desirable (Chang, 2001).

DBD was chosen for this work due to its resistance to fouling and plasma arcing, compatibility with liquid inputs and its relatively uniform plasma distribution. Gliding arc

plasma reactors would be a feasible alternative but the resulting stream of plasma would be harder to isolate from the air and the plasma distribution would likely be less uniform (Burlica *et al.*, 2010).

2.5.8 Gas-Liquid Cold Plasma

In theory, radicals and ions can diffuse into the liquid phase to allow radical driven reactions to occur, but in practice the rate of diffusion into the liquid is very low. This leads to significantly reduced performance with non-gas phase feedstocks (Du *et al.*, 2007). However, recent work has determined a method for using cold plasma in two phase systems, known as gas-liquid cold plasma (Malik, 2010).

Gas-liquid cold plasma exposes both a gas and the liquid feedstock to an electric field to generate plasma, predominantly along the phase boundary. Radicals forming at the interface can escape into the gas phase or diffuse into the liquid to induce liquid phase radical reactions, which generally do not occur in thermal processes. This is illustrated in Figure 2.8. As cold plasma has a combination of low bulk temperature and high energy species (Zhang *et al.*, 2017) and its properties are altered by operating conditions and reactor configuration (Flynn *et al.*, 2013; Park *et al.*, 2017), the process can be easily tuned to select for any given desired product.

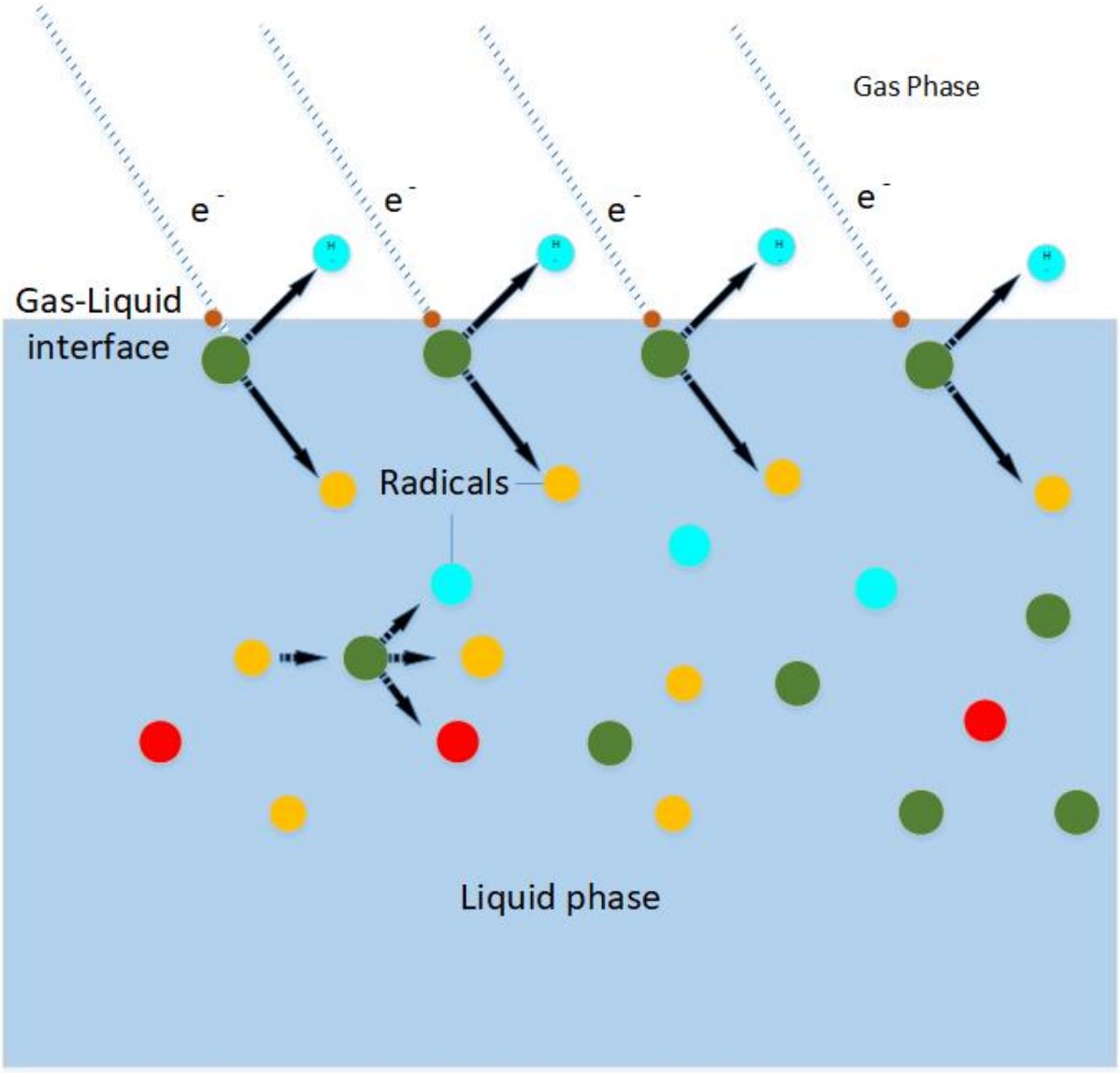

Figure 2.8: Gas-liquid cold plasma mechanism showing liquid phase radical generation and propagation (Di *et al.*, 2016)

This technique has been used for waste water treatment (Malik, 2010), one step ammonia production from nitrogen and water (Haruyama *et al.*, 2016), along with facile preparation of copper hydroxynitrate nanosheets (Di *et al.*, 2016) from an aqueous solution of copper hydroxynitrate. Under these conditions, the heterogenous catalyst was found to attract the liquid phase radicals and excited species due to the presence of acid sites on the catalyst surfaces and the dielectric properties of the solid. This enhances the catalyst activity and could potentially be used for other processes. As the investigation undertaken in this thesis aims to upgrade a liquid product, this behaviour may be useful at decomposing specific compounds in an energy efficient and clean manner. These studies on gas-liquid cold plasma also showed that heterogeneous catalysts can be effective for promoting reactions under gas-liquid cold plasma conditions (Di *et al.*, 2016),

which is of significant interest for improving the dynamics of the liquid phase decomposition of non-volatile feedstocks such as glycerol.

A similar technique to convert methanol to carbon monoxide and hydrogen (Zhang *et al.*, 2016) used two phase gliding arc plasma to induce the decomposition of liquid methanol. However, the process was operated with a gas temperature of 80°C, which is sufficient to evaporate methanol without producing noticeable levels of liquid phase radicals. This achieved conversions up to 95.6%, but further work at lower operating temperatures would be required to establish the ability of gas-liquid cold plasma to decompose liquid methanol.

2.5.9 Plasma modelling

Modelling of cold plasma kinetics was studied previously for hydrocarbon polymerisation (Yang, 2003) and for carbon monoxide reformation to carbon dioxide (Feng *et al.*, 2009). In these studies, the extended Arrhenius equation was assumed to be applicable, and the three constants required for each reaction were obtained by fitting the process to the data using the ELENDIF kinetics solver (Feng *et al.*, 2009). The ELENDIF solver was designed to calculate the rate of change of concentration for all expected excited states from the corresponding neutral species. Boltzmann differential equations were solved iteratively for each excited species present for each time step, which are derived from the predicted reaction pathway. The cold plasma itself was modelled as two separate fluids that are not in thermal equilibrium, namely excited species (represented by electron temperature) and neutral species (represented by bulk temperature). The bulk temperature can be measured experimentally via conventional methods, but the electron temperature must be calculated separately, as described below.

In previous works (Thomas and Jen-Shih, 1997; Zhu and Pu, 2010; Shrestha, 2012), the electron temperature was calculated using the line intensity ratio method. The line intensity ratio method is a technique based on the Stark broadening effect, which dictates that the optical emission lines of the gas in the plasma zone are broadened and shifted from their regular locations due to the presence of an electric field, with increased electric fields shifting the emission lines towards higher values in a linear relationship. To derive the electron temperature, two emission lines corresponding to the carrier gas are observed via optical emission spectroscopy (OES) on the plasma zone (Fridman, 2008). The ratio between the intensities of the emission lines and the intensities of the

corresponding emission lines in the unexcited gas is recorded and used to calculate the electron temperature according to equation 2.1.

$$\frac{R_1}{R_2} = \frac{I_1}{I_2} \div \frac{I_3}{I_4} = \left(\frac{A_{pq}}{A_{rs}}\right)\left(\frac{g_p}{g_r}\right)\left(\frac{\lambda_{rs}}{\lambda_{pq}}\right)\left(\frac{g_u}{g_x}\right)\left(\frac{\lambda_{xy}}{\lambda_{uv}}\right)e^{\left[-\frac{E_p - E_r - E_x + E_u}{KT_e}\right]} \quad (2.1)$$

Where:

R is the intensity ratio between two lines,

I is the intensity of a given spectral line

A_{pq} is the transition probability of p→q

g_i is the statistical weight of state i

λ is the wavelength of the emitted electromagnetic radiation (nm)

E_i is the energy of state I (KJ)

K is the Boltzmann constant (m^2 kg s^{-2} K^{-1})

T_e is the electron temperature (K)

This is the only established method for finding the electron temperature used in models to date.

2.6 Summary

As the use of pure oils for producing biodiesel is costly and raises enivronmental concerns due to competition between land for fuel and land for food, waste cooking oils (WCO), non-edible oils and algae are promising alternatives. Production of biodiesel from waste cooking oils is currently performed via transesterification and is hindered by the the presence of FFA and/or water, which leads to rapid catalyst depletion via saponificiation. To avoid this, extensive pre-treatment is required to reduce water and FFA contents to below 0.1wt.% before use. Even with pre-treatment, the product stream would contain soaps, which generates more waste water from washing and methanol recovery is more challenging due to increased miscibility between the two liquid phases.

Transesterification requires large amounts of methanol, which is unsustainable. Other alkyl donors could be used instead but these are costly due to the low water content requirements. Biodiesel is also primarily composed of FAME, which requires blending with petrodiesel to be usable in unmodified engines due to its poor cold flow properties, volatility and tendency to polymerise. Another challenge is that oils are generally expensive to extract from the original biomass in large volumes. The biodiesel production

process could be optimised to require less unit operations using in situ transesterification. However, this requires an extremely large proportion of methanol compared to the oil volume (600:1 ratio), which offsets any savings from reducing unit operations. Thermal methods which do not require methanol are under consideration but the product is rich in FFA and the liquid fuel yields (25-55wt.%) are much lower than transesterification.

To address these issues, the biodiesel production process would require a reactor design that can easily tolerate fouling and solids, and preferably not require large amounts of methanol. Avoiding methanol usage would require cracking of the glycerol backbone in the triglycerides, which implies a radical based process and would require high selectivity to cracking reactions to avoid by-products.

Most techniques that tolerate solids and fouling utilise high temperatures to decompose any fouling deposits as they form, and most reactors with improved process dynamics are highly susceptible to fouling. However, microwave and plasma based reactors are capable of processing both solids and liquids and can continuously remove or decompose fouling over time, so appear to be suitable for low temperature biofuel production from triglycerides. However, neither of these techniques have been utilised for triglyceride utilisation to date.

Cold plasma could have potential for decomposing triglycerides. Almost all work with cold plasma is performed on a gas phase feedstock as the excited electrons can only exist within the gas phase. However, triglycerides cannot be evaporated, as they thermally decompose before their boiling point. As a result, the use of cold plasma for initiating decomposition of glycerol has not been studied to date, despite the far larger potential throughput achieved when using a liquid feedstock (factor of ≥100). To enable a decomposition reaction to occur in the liquid phase, a high power active plasma would be required to produce decomposition products at the gas-liquid interfaces due to mass transfer resistances, and the electrodes would have to be protected from the triglyceride decomposition products. This suggests the use of dielectric barrier discharge plasma reactors, as these include the dual barrier configuration that protects both electrodes. And generates the required radicals, ions and excited species at high concentrations. In dielectric barrier discharge, the highest energy plasma is located close to the electrodes, which would act to reduce fouling build-up and formation, and the barriers would prevent

plasma arcing at high powers. The liquid phase radicals that are created in gas-liquid plasma systems would help to prevent fouling and could potentially allow selectivities that would otherwise be unfeasible. Two phase cold plasma may be tunable towards cracking reactions, which would preferentially generate FAME and particularly liquid hydrocarbons from triglycerides, to create higher quality fuels that do not require blending.

In this work, a selection of feedstocks from the biodiesel production process are used to determine the effectiveness of gas-liquid cold plasma for decomposition of triglycerides. These feedstocks are methanol, glycerol, waste glycerol, rapeseed oil and waste cooking oil. The mechanism by which each feedstock decomposes was determined to facilitate later process tuning. Finally, glucose and cellulose plasma decomposition were investigated to extend the applicability of the findings and determine the feasibility of producing biofuels directly from oil containing biomass.

Chapter 3. Methodology

This chapter describes materials, catalyst preparation, the methodologies and techniques used to identify, quantify and analyse the feedstocks, catalysts and products. Experimental procedure for the decomposition process with and without the assistance of cold plasma was described along with data analysis methodologies. Numerical methods used in developing process models are also described.

3.1 Materials and chemicals

Three different carrier gases, namely nitrogen, helium and hydrogen, (BOC, 99.999% purity) were used in cold plasma assisted decomposition. Nitrogen is commonly used as a carrier gas in conventional thermal decomposition processes due to its kinetic stability and therefore it allows comparison to this research. Additionally, nitrogen has a large number of excited states ≥12.96eV (125.1 KJ/mol), which means that it can potentially create a range of reactions (Park *et al.*, 2017). Helium is a noble gas and thus has a highly stable atomic structure, and hence a high energy initial excited state at 19.2eV (Altshuler, 1953). Therefore helium allows extremely high energy reactions to occur that would be unfeasible under other gases (Altshuler, 1953). Hydrogen, with its low energy excited state (3.7eV) (Dieke, 1958), was used to identify the effect of hydrogen and hydrogen radicals on the cold plasma assisted decomposition process of feedstocks. This also enabled comparison to HDO processes and determined if these deoxygenation reactions can be initiated under cold plasma conditions.

Waste glycerol was kindly donated by Harvest Energy at Seal Sands, Teesside, UK. The sample contained more than 20 inorganic elements of which potassium, sodium and calcium contributed a large percentage, 4.06wt.%, 0.21wt.%, and 0.03wt.% respectively, while the others were at ppm levels (Table 3.1) determined by ICP-OES.

Table 3.1: Composition of inorganic elements in the waste glycerol sample (errors:± 1ng/g)

Element	**Content (µg/g)**	**Element**	**ng/g**	**Element**	**ng/g**
Potassium	4063.1	Rubidium	878.27	Molybdenum	41.764
Sodium	208.99	Lithium	641.00	Selenium	36.923
Calcium	28.068	Aluminium	454.27	Astatine	26.027
Silicon	4.8347	Zinc	295.68	Germanium	11.501
Iron	4.3363	Chromium	264.81	Cobalt	11.199
Phosphorus	2.5380	Titanium	161.01	Scandium	6.6575
Magnesium	1.3661	Nickel	128.02	Zirconium	2.7235
		Copper	85.346	Gallium	1.8157
		Manganese	72.937	Vanadium	1.5131
		Strontium	53.871	Yttrium	0.3026

Ultimate analysis (CHN analysis) of the waste glycerol sample was carried out using a Carlo Erba 1108 Elemental Analyser (error: ±0.1wt.%) based on the standard BS ISO 29541. The sample was found to have an empirical formula of $CH_{2.89}O_{1.14}$. Higher H/C and O/C ratios in waste glycerol than in pure glycerol (H/C=2.67 and O/C=1) were due to high water content (9.45wt.%) and the presence of other oxygenated compounds from biodiesel production. The composition of the waste glycerol comprised glycerol (58.96wt.%), free fatty acids (FFA, 33.38wt.%), glycerides (2.13wt.%) and traces of methanol and some metal salts as shown in Table 3.2.

Table 3.2: Waste glycerol composition (dry basis) (errors:±0.05wt.%)

Compound	Composition (wt.%)
Glycerol	58.96
FFA	33.38
Glycerides	2.13
Methanol	1.18
Inorganics	4.35

Waste cooking oil (WCO) was kindly donated by local restaurants in Newcastle Upon Tyne. WCO was characterised in terms of its chemical composition and properties. Table 3.3 illustrates the composition of WCO, which comprised mainly glycerides (70.73wt.% of

comprising 43.09wt.% triglycerides, 21.24wt.% diglycerides, 6.40wt.% monoglycerides), FFA (12.43wt.%) and other compounds (glycerol, acetol and aldehydes). The sample did not contain any metals above 1ppm levels with traces of sodium and potassium at 100ppb levels.

Table 3.3: Composition of the WCO sample (errors: ±0.03wt.%)

Compound	Composition (wt.%)
Water	0.12
Acetol	0.23
FFA	12.43
Glycerol	1.80
FAME	3.31
Other fatty acid esters	9.18
C14-18 Hydrocarbons	1.47
C14-18 Aldehydes	0.73
Monoglycerides	6.40
Diglycerides	21.24
Triglycerides	43.09

Compared to rapeseed oil (99%), WCO had reduced levels of triglycerides (43.09%) in favour of triglyceride decomposition products, predominantly diglycerides and FFA. Tests on the two feedstocks showed that the WCO chain length distribution was similar to that of the pure rapeseed oil (average chain length of 16.39 carbons for WCO vs 16.68 carbons for the rapeseed oil) except with a greater prevalence of shorter chain fatty acids, reflecting limited cracking reactions occurring during cooking. The fatty acid chain lengths were only tested for a subsection of experimental runs in this work, as the slight differences in fatty acid chain length observed should have little effect on the decomposition pathway (Abbot and Dunstan, 1997).

Several of the components in the WCO sample, such as FAME and other fatty acid esters (e.g. 2-oxopropyl fatty acid esters), were not reported in other WCO characterisation studies (Jain *et al.*, 2011). However, FAME is known to be present in WCO at low levels due to the induction of limited pyrolysis during cooking, which produces traces of FAME

(Kulkarni and Dalai, 2006). Oxopropyl fatty acid esters are a dominant product of triglycerides pyrolysis, along with FFA (Lien and Nawar, 1973).

The water content of the WCO sample was low (0.12wt.%) because water is largely immiscible with triglycerides and has a higher density. During cooking, the water would form a layer below the triglycerides and thus be subjected to high temperatures well above its boiling point and therefore be lost as vapour.

From ultimate analysis (CHN analysis) using an Carlo Erba 1108 Elemental Analyser (error: ±0.1wt.%), the WCO had an oxygen content of 9.38wt.% compared to 10.31wt.% for rapeseed oil. The difference in oxygen content is due to the condensation reaction that occurs during use for cooking and the resulting evaporation of water. A slightly lower H/C ratio in WCO, 1.91:1 (12.37wt.% H) than that of fresh rapeseed oils, 1.92:1 (12.44wt.% H) was also observed, and is due to hydrolysis, decomposition and oxidation occurring at high temperature and evaporation of water from the cooking process.

In order to establish reaction mechanisms/pathways, pure chemicals such as fresh rapeseed oil (obtained from Marks & Spencer, 99% pure triglycerides) and glycerol (99.5% purity from Thermo Fischer Scientific) were purchased. As methanol is a potentially valuable decomposition product of glycerol and is a common contaminant in waste glycerol, the decomposition of methanol was also studied, giving insight into glycerol decomposition due to the similarity in structure and enabling clear reaction pathways to be developed.

3.2 Catalyst preparation and characterisation

The catalysts / packing materials, barium titanate beads ($BaTiO_3$) (99.5% purity, Alfa Aesar), HZSM-5 (99.95% purity, surface area: 410m^2/g), zirconium (IV) oxide (99% trace metals basis, 5μm, Sigma Aldrich) and γ-zeolite (99.9%, surface area: 660m^2/g, Alfa Aesar) were prepared to a 0.5-1mm size by pelletizing, crushing and screening.

Ni/Al_2O_3 was synthesized from high surface area alumina (surface area: 180m^2/g particle size: 0.5mm 99.95% purity, Alfa Aesar) and nickel nitrate hexahydrate (99.9% purity, Sigma Aldrich) via a wet impregnation method proposed by Bartholemew and Farrauto (Bartholomew and Farrauto, 1976). Al_2O_3 (100g, 99.9% purity) pellets were added to

nickel nitrate hexahydrate (1M, 100mL). The mixture was stirred vigorously at ambient temperature for 1 hour to remove air bubbles from within the particles. The pellets were extracted from the solution and dried in an oven set at 105-110°C for 24 hours, to remove unbound water molecules. The dried sample was then calcinated at 550°C in air for 5 hours to convert all nickel nitrate hexahydrate to nickel oxide. This was then hydrogenated using a hydrogen flow (20mL/min) and 500°C for 24 hours to reduce nickel oxide to nickel, which produces a more stable structure than obtained with lower calcination temperatures (Bartholomew and Farrauto, 1976). The sample was then reduced to the correct size range (0.5-1mm), which is the maximium particle size able to fit into the plasma zone, which minimizes pressure drop.

The packing materials were characterized in terms of surface area, elemental distribution, structure and crystallinity, to ensure consistency throughout this research and simplify comparison with other works.

3.2.1 Scanning electron microscopy (SEM) with Energy-Dispersive x-ray Spectroscopy (EDS) analysis

SEM is a method of using a beam of electrons to view the surface morphology of materials at higher magnifications than conventional microscopes (x35-x100,000 magnification range). An XL30 ESEM was used in combination with EDS to determine surface topology and elemental distribution. The sample was prepared in a clean fume cupboard with the venting turned off to prevent loss of sample to the air and possible contamination of the stub or samples. Preparing the sample entailed attaching a disk of double sided carbon tape to the top of a stub in a clean environment, followed by introducing a small amount of sample to the top of the carbon tape. The stub was then tapped on a clean surface to remove any material that was not firmly stuck down.

The stubs were then mounted inside the vacuum chamber, which was then closed. The vacuum was then turned on to extract the air and then the x-ray beam was turned on. Three x-ray beam power settings were used throughout for different functions. The 5KV beam is lower resolution but updates faster and was used first to find areas of interest. The 10KV beam was used to take images once an area of interest was found, while the 25KV beam was used after this to perform EDS on the area (Goldstein *et al.*, 2017). To ensure the image was focused correctly, the magnification was increased beyond the desired magnification until detail was lost. The focus and contrast were then adjusted to

regain as much detail as possible, and the magnification was pulled back to the desired value and the images taken (Mikmeková *et al.*, 2011). Images were taken at x30, x500, x1000 and x8000 magnification for all samples to show the structures at a variety of scales and allow the catalysts to be compared accurately.

3.2.2 X-ray Photoelectron Spectroscopy (XPS)

XPS is a technique for determine the elemental composition of the surface of a material and the chemical groups these elements are contained within. This technique is very similar to EDX as described above, except that EDX measures the characteristic x-rays generated from the material while XPS measures the kinetic energy and number of electrons lost. The same sample preparation methods used for SEM were also used for XPS and the experiments were performed in a k-alpha XPS analyser with a aluminium Kα x-ray source. 7 repeats were performed for each sample and the signal was averaged for each sample before full analysis.

3.2.3 Brunauer–Emmett–Teller (BET) analysis

Surface area and other parameters such as the pore diameter profile and pore area distributions of catalysts were determined using a Thermo Scientific Surfer gas adsorption porosimeter.

100mg ±0.1mg of the sample was placed inside the bulb of a burette. The burette was then plugged with a rod and sealed by adding a closable valve section on top. This was then hooked onto the degasser, and the burette valve opened to let air out. The burette was then evacuated of any residual gases over 12-24 hours depending on the sample and simultaneously heated to 120°C to extract air to achieve the minimum possible pressure obtainable by the degassing pump. Degassing was performed at 120°C for all catalysts for consistency and to avoid any surface deformation in the more fragile catalysts such as zirconium oxide. After degassing, the burette was switched to a secondary vacuum for a further 2 hours. As the secondary vacuum did not output additional gases, complete degassing was confirmed to occur. After degassing was complete, the valve was closed and the burette moved to the BET machine.

Once the burette had cooled, it was placed in a liquid nitrogen dewar, which cools the sample and maintains its temperature to allow measurable amounts of nitrogen to adsorb

during analysis. A Thermo Fischer Scientific gas adsorption porosimeter was used for the sample cooling and regassing steps.

The first step was to determine the dead space inside the sample cell. This was performed by injecting a known amount of helium to the cell and measuring the resulting internal pressure. Helium was used as it does not adsorb noticeably to any sample at the experimental temperatures used. The next step was to introduce nitrogen at low pressures, corresponding to 0.05 of the expected number of moles of N_2 required to create a monolayer on the material (Sing, 2001), based off the mass of the sample and its expected surface area. Since the method used is single point, only the surface area was calculated, by plotting the gas re-introduction isotherm and using the gradient and intercept to find the monolayer capacity and hence surface area (Li *et al.*, 2004).

3.2.4 X-Ray powder Diffraction (XRD) analysis

To characterise the structure of the material further, a SToe STADI/P powder diffractometer was used to provide insight into the crystal structures of the material and a measure of its crystallinity.

The incident x-ray radiation was generated using a Cu k_α source, which generates wavelengths of precisely 1.54056 Å. The samples of catalyst were ground to as fine a powder as possible, less than 10μm, in liquid to reduce damage to the structure which could affect the results. The sample was then removed from the liquid, immobilised on a glass slide and loaded into the XRD central chamber. The aperture to the radiation source was then opened and the angle from the immobilised sample to the source changed to detect which angles refract the incoming radiation.

The reflected radiation was detected on a JASCO-V550 UV–vis spectrophotometer and the results plotted based on the signal and the angle. Bragg's law was then used to find the atomic spacing and arrangement.

3.2.5 CHN analysis

To confirm the findings of FTIR and GC analysis, CHN analysis was performed on the solid products of glucose and cellulose decomposition and during characterisation of waste glycerol and triglyceride feedstocks. This analysis was performed in an Elementar Vario MACRO cube, where a 0.1g sample of the sample was loaded into a vessel and placed on

the sample carousel. A pre-run was conducted on a standard sample with a known CHNO ratio to check calibration, and the results confirmed against literature. Once the calibration was tested, the solid sample in the vessel was loaded into the machine, filled with excess oxygen and combusted at 1400°C. This converted all the carbon, hydrogen and nitrogen in the sample to carbon dioxide, water and nitrogen dioxide. A scrubber was used to reduce the nitrogen oxides back to nitrogen, catalysed by tightly packed copper granules in a silica tube maintained at 500°C.

Gas chromatography was used to separate the output gases, with a thermal conductivity detector to find the quantity of each gas. The total mass of each gas and the mass of the sample were then compared to find the CHNO ratio. This assumed that all the remaining mass in the sample not detected as carbon, hydrogen or nitrogen was oxygen. This is generally accurate as the samples are organic and contain very low levels of inorganic elements. For waste glycerol, where this is not the case, ICP-OES was also performed to find the inorganic ion content.

3.2.6 Fourier Transform Infra-red spectroscopy

Fourier transform infrared spectroscopy (FTIR) was used to identify the functional groups present in the solid samples and support the results of CHN analysis. This was carried out using an Agilent Cary 630 FTIR spectrophotometer for powdered samples. The diamond crystal plate below the probe is first cleaned with acetone and wiped dry with clean laboratory tissue. Then the probe was lowered and a contrast test was taken. On successful completion of this test, the background signal was taken. The probe tip was then raised and a 1mm covering of the sample was placed on the plate below the probe. The covering was adjusted with a clean spatula to evenly cover the plate where the probe fits with no gaps. The probe was then lowered again and the spectrum from 4000-600nm was taken 3 times. The background signal was then subtracted from the average spectrum to get the results for that solid. The solid can then be removed and the probe cleaned again with acetone before any further runs were performed.

This technique was also used for liquid analysis to identify functional groups. A ReactIR4000 FTIR machine with a 16mm diameter Dicomp type probe was used with a wavelength region of 2400 to 2000 nanometres where the probe tip absorbs light. As the liquid is not expected to be highly nitrogenous, this was judged unlikely to affect results.

The absence of nitrogen was confirmed separately with CHN and gas chromatography, and would have been retested with a different probe should nitrogen have been identified. Before use, the detector is filled with liquid nitrogen and the probe head cleaned thoroughly with acetone, then arranged with the probe facing down. A contrast test was then performed to check the gain on the probe was within acceptable limits and the probe lowered into acetone for calibration purposes. The performance, signal to noise ratio and signal stability were tested by running the probe in the acetone, and compared to manufacturer specifications to check the accuracy of the technique.

Following calibration, a further contrast test was done to check the purge and probe cleanliness status and the water background was taken to correct for the water content in the air around the probe.

The sample for FTIR analysis was placed in a 10ml glass sample jar and the probe tip lowered into the sample and gently agitated to remove any bubbles. The probe was set to run one spectrum from 4000 to 600nm every minute and repeated 6 times. The spectra were then averaged once outliers were removed to give a spectra for that sample. This was repeated for the other liquid samples from the same conditions, which gives 3-4 spectra to represent that experiment. The FTIR probe, detector and sample jar configuration is shown in Figure 3.5.2.1. The sample is then removed and the equipment cleaned with acetone and the contrast test re-run after cleaning. This cleaning was repeated until the contrast test confirms probe cleanliness.

3.3 Experimental setup

Cross sections and images of the experimental set up used for cold plasma assisted decomposition are shown in Figure 3.1. The reactor consisted of two co-axial quartz tubes with one centred inside the other. The outer quartz tube was 30 cm long and had a 2 cm inner diameter. The inner tube was 15 cm long with a diameter of 1.8cm, and was closed at one end to protect the inner electrode. The inner electrode was mounted inside the inner quartz tube while the outer electrode was on the outside of the outer tube, as shown in Figure 3.1(b). These dimensions gave the plasma zone a cross sectional area of 0.597cm^2. The electrodes were 12cm long, giving a total plasma volume of 7.16cm^3. To illustrate this, a cross sectional views of the reactor are shown in Figure 3.1 (a, b) and a side view in Figure 3.1(c).

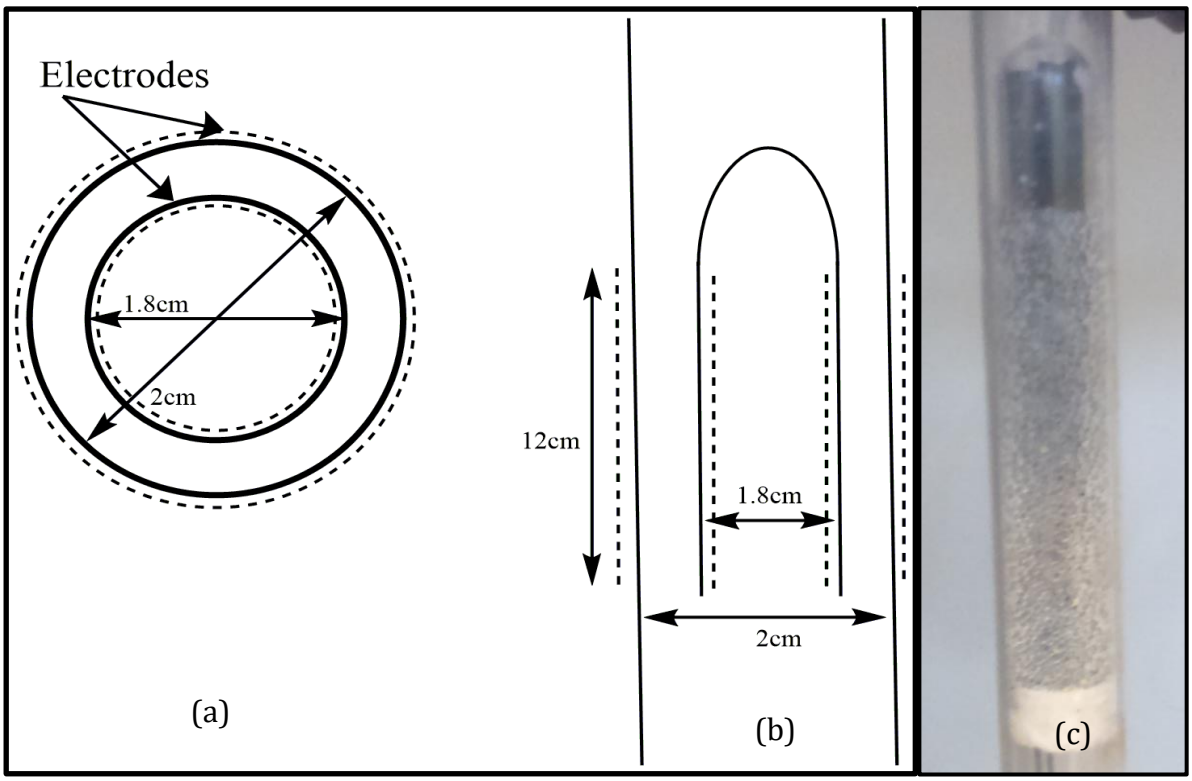

Figure 3.1: (a) cross section view of cold plasma reactor, (b) side view of cold plasma reactor, (c) image of packed bed with ceramic wool band

Prior to each experiment, the system was continuously purged with the desired carrier gas, i.e. hydrogen, nitrogen or helium (>99.999% purity, BOC Ltd.) for 30 minutes at a flow rate of 50ml/min using a Bronkhorst El-flow mass flow controller (error: ±0.03 ml/min). When the system was air-free, which was confirmed by gas chromatography (GC), the flow rate of the carrier gas was adjusted to 40ml/min. A known flow rate of reactant was continuously fed into the reactor at a T-junction (Figure 3.2) to maintain a ratio of carrier gas to liquid of 40:1 (vol/vol) using a WPI Al-4000 syringe pump (error: ±0.01ml/min) to prevent reactor flooding and maintain a consistent phase distribution.

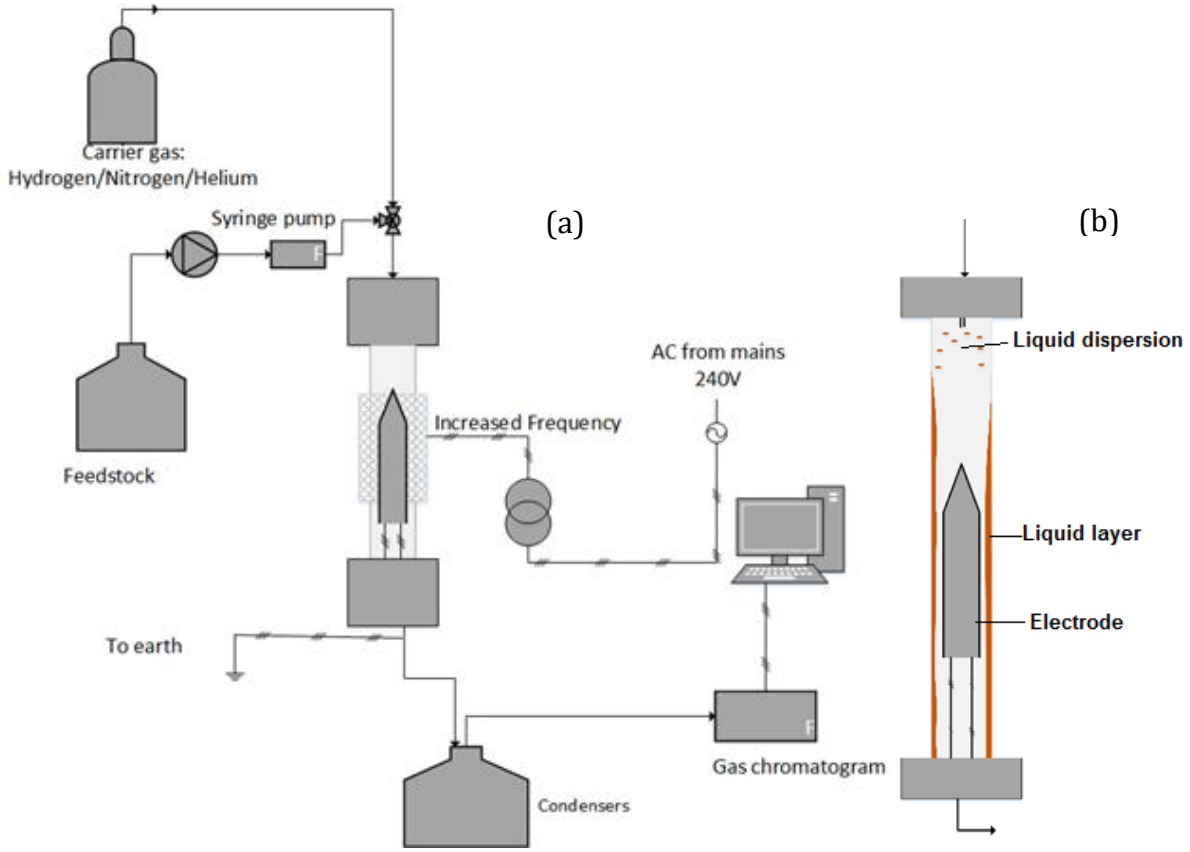

Figure 3.2: Experimental set-up for cold plasma induced decomposition operating at atmospheric pressure and temperature (a) and the gas/liquid distribution (b)

Under these conditions, the inlet feed was under the slug flow regime for all liquid feedstocks, with the liquid forming pulses in the inlet line separated by gas bubbles (Neretti *et al.*, 2017). An image of the inlet feed with slug flow is shown in Figure 3.3, with 3 liquid slugs visible in the line. This feed connects directly to the reactor, where the slug flow causes bubbles to rapidly grow and break at the inlet, distributing the liquid over the outer walls of the reactor. A constant stratified liquid distribution was observed to consistently form under the liquid and gas flowrates used in the reactor matching the pattern shown in Figure 3.2(b).

Figure 3.3: Image of liquid-gas slug flow in reactor inlet

When a packing material was used in the cold plasma reactor, the material was mounted in the plasma zone with 1mm width ceramic wool placed at the base of the plasma zone to hold the packing material in place. This is illustrated in Figure 3.1 (c). Blank tests with only ceramic wool were also performed for all feedstocks. These found that the presence of the ceramic wool had no effect on the process compared to when no packing was applied. The plasma zone was filled with spherical particles of the chosen packing material up to a depth of 8cm from the base of the plasma zone, reducing the plasma volume from 7.16cm^3 to 4.48cm^3. The packing material and ceramic wool disrupted the flow so that turbulence was generated, ensuring that the liquid was uniformly distributed on the material. Evenly coating the packing particles with feedstock is desirable due to the dielectric effect (Zhang *et al.*, 2016) because plasma discharges occur between particles, so an even coverage over all surfaces prevents arcing and the associated wasted energy.

The liquid and gas flow controllers were started at the same time as the plasma system was switched on and adjusted to the desired power (e.g. 10, 30 or 50W). The reaction was typically carried out at atmospheric temperature and pressure, though some later experiments used external heating via a temperature controlled tubular furnace. The outlet of the reactor was fitted to a quench system comprising 2 sequential bottles maintained at 60°C and 0°C to collect liquid products, using a water bath and an ice water bath. The experiments were run for 45 minutes, with longer 2 hour runs performed when characterising fouling. A 45 minute run was chosen to allow three gas samples to be analysed, to confirm steady state was obtained. A longer run was also performed if the two gas samples differed significantly. Non-condensable products were analysed online using a GC. At the end of the 45 minute run, the flow of liquid was stopped and the gas flow continued for 10 minutes with the plasma still active to convert residual material in the reactor. The plasma and gas were then turned off and the liquid samples were collected for off-line analysis. Each set of experiments was repeated at least three times to ensure repeatability.

The liquid yield was calculated based on the mass of liquid collected in the condensers and the liquid remaining in the reactor. The liquid remaining in the reactor was determined by weighing the reactor before and after the experiment to determine the mass attributed to remaining liquids.

When fouling or other solids were observed, the remaining liquids had to be quantified separately. To do this, the reactor was weighed after completion of the experiment. The reactor was then dried in an oven at 105°C for 4 hours to remove any volatiles in the reactor and re-weighed with the difference representing trapped liquids. Some non-volatile liquids, such as glycerol, may remain after drying so the fouling mass measurement may also represent some of these components. The gas yields were determined by difference.

3.4 Analysis

3.4.1. Gas analysis

Non-condensable gas was analysed on-line by a Varian 450-GC. Runs were performed at a frequency of 15 minutes on-line. If more frequent analysis was required, tedlar bags were used to collect gas with an additional valve before the bag to reduce leakage to the atmosphere. A Varian 450-GC consisting of 2 ovens equipped with one thermal conductivity detector and 2 flame ionisation detectors previously calibrated with reference gas mixtures was used. One oven housed 3 columns (Hayesep T0.5mx1/8" ultimetal, Hayesep Q0.5mx1/8" ultimetal and Molsieve 13X1.5mx1/8" ultimetal) in sequence to detect atmospheric gases. The second oven housed two columns: a CP-SIL 5CB FS 25X.25 (0.4mm ID) for hydrocarbon analysis and a CP-WAX 52CB FS 25X.32 (1.2mm ID) for alcohols. The permanent gas columns were set at a temperature of 100°C for the full 13.25 minute run time. The hydrocarbon and alcohol columns used a separate heating profile, which started at 40°C, heating by 2°C/minute to 50°C, then by 8°C/minute up to 90°C, then 10°C/minute to 120°C. The GC was calibrated for all hydrocarbons, alcohols and permanent gases before any runs.

3.4.2. Liquid analysis

The liquid feedstocks and the liquid collected from the condensers were characterised in terms of their chemical composition and properties. The methods required depended on the liquid origins, as glycerol, triglycerides and FFA require specific methods and separation. The water content was determined by coulometric Karl-Fischer titration (error: ±0.03wt.%). A Perkin-Elmer Clarus 500 GC equipped with a 30m x 0.32mmID x 0.25μm BPX-BD20 column and a 540C MS detector was used to identify compounds in the liquid phase. An undiluted sample was used for enhanced sensitivity for the methanol samples due to the low boiling nature of the liquids. This was compensated for by using a

smaller injection volume of 0.5µl and a split ratio of 20:1, to prevent the detector from being overloaded. 1ml of the sample and the feedstock were injected into 2ml vials using a 1ml disposable microsyringe and loaded into the autosampler. The column used during GC-MS analysis was a 30m x 0.32mmID x 0.25µm BPX-BD20 column as the components are low boiling and are appropriate for polar liquids. A HP 6890 GC also equipped with a 30m x 0.32mmID x 0.25µm BPX-BD20 column was used to quantify compounds. The heating profile for both GC methods was 40°C initially, heating by 2°C/minute to 50°C, then by 8°C/minute up to 90°C, then 10°C/minute to 120°C. Functional groups were identified using a ReactIR4000 with a 16mm diameter Dicomp type probe.

For glycerol and waste glycerol GC analysis, a selection of initial samples were diluted 20:1 in dicholoromethane and analysed in a GC-MS with an elite-5 HP capillary column for qualitative analysis purposes, using the temperature profile: initially 50°C held for 4 minutes, increased to 180°C at 15°C/min, then 7°C/min to 230°C, then 10°C/min to 340°C and held for 25 minutes. The high temperatures ensured that the glycerol present could not remain in the column past the end of the run, necessitating a cleaning run between samples. The identified compounds were quantified using a HP6890 GC with an elite-5 HP 30 m x 0.25 mm, 0.50 µm capillary column with helium as the carrier gas and the same heating profile, calibrated separately using stock solutions of the products detected by GC-MS. Glycerol and glycerides contents were determined according to BS EN 14105-2011 and calibrated with glycerol and butan-1,2,4-triol stock solutions.

For the glucose and cellulose derived liquid products, the complex products (such as levoglucosan, 5-HMF and furans) were analysed through GC-MS analysis only, as obtaining calibration samples for all of the detected products was cost prohibitive and many rquired calibration samples were unavailable. GC-MS analysis was performed with an elite-5 HP capillary column, using the temperature profile: 50°C held for 4 minutes, increased to 180°C at 15 °C/min, then 7°C/min to 230°C, then 10°C/min to 340°C and held for 25 minutes. Each peak was analysed based on their relative peak area; hence the results are defined as area% instead of wt.% as used throughout this work.

Triglyceride derived samples required a more extensive procedure for GC analysis, covering analysis of FFA and glycerides content. The FFA content of waste glycerol was determined by titration of 0.05 ml of waste glycerol diluted to 2 ml in chloroform

containing a pH indicator solution. This solution was titrated to pH 7, as shown by the indicator colour change, with aqueous 0.05M NaOH. NaOH/ chloroform solutions were prepared directly before use, to prevent changes in concentration from evaporation.

ICP-OES data was also collected for the raw waste glycerol to determine the residual catalyst content from biodiesel production. As the most common catalysts for biodiesel production are potassium, sodium and calcium hydroxide, the run focussed on these elements primarily. A broad spectrum test was also performed to detect any other elements, which were not present at 1mg/L levels or above. This was also performed for waste cooking oil to detect dissolved inorganic elements. Waste glycerol was extensively diluted in water to address the high sample viscosity before ICP-OES, which would otherwise interfere with the operation of the nebuliser.

To fully analyse triglyceride derived samples, 5 analyte samples of 1ml volume were collected: 3 for analysis of fatty acids, FAME, acetol and propanal/propanone and the fourth for analysis of glycerol and glycerides. FTIR and Karl Fischer titration were performed on the final sample.

Sample 1:

Hexane extraction

The first sample had the FAME, other fatty acid esters, and liquid hydrocarbons /aldehydes extracted from the analyte via mixing with 10ml hexane and agitating for 10 minutes. FAME, other fatty acid esters and liquid hydrocarbons are soluble in hexane, but FFA (approx. 0.3g/100g solubility) and other products are not.

Liquid/liquid separation from hexane

Liquid/liquid separation with acetonitrile (1:1 hexane to acetonitrile volumetric ratio) was performed on the hexane fraction, to separate esters (e.g. FAME, 2-oxopropyl fatty acid esters) from C14-18 hydrocarbons and aldehydes.

Acetonitrile soluble fraction

The acetonitrile soluble fraction was analysed according to the standard BS EN ISO 5508 in a HP6890 gas chromatogram with a CP-Wax column to detect and quantify FAME and other fatty acid esters. The analysis was repeated 3 times and the results averaged

(outliers removed and an extra repeat performed). Triglycerides from the initial sample were also contained in this sample, but were not eluted as a sharp peak. Column conditioning via a pure acetonitrile sample injection and temperature hold at 240°C for 20 minutes was performed to remove triglycerides from the column in between runs.

Acetonitrile insoluble fraction

The hexane fraction was also analysed using a HP6890 GC using helium as the carrier gas. The heating profile was 150°C for 1 minute, heating at a rate of 10°C/minute up to 210°C and maintained for 10 minutes. The liquid hydrocarbons and aldehydes were calibrated for using a stock solution of liquid hydrocarbons and GC-MS analysis with an identical column to the HP6890 and identical run parameters. The analysis was repeated 3 times and the results averaged (outliers removed and an extra repeat performed).

Methanol dilution of hexane insoluble fraction

The hexane insoluble analyte was separated from the hexane surface and diluted in methanol. This was then analysed using gas chromatography using the same heating profile and column to measure acetol, propanal/propanone and FFA content. The analysis was repeated 3 times and the results averaged (outliers removed and an extra repeat performed). Glycerol and monoglycerides/diglycerides were also present, and were eluted during the run as extremely broad peaks. These peaks were ignored as the content of these components was analysed separately. Column conditioning was performed at 240°C for 20 minutes with a pure methanol injection after every 3rd run to ensure no contamination from glycerides was allowed to accumulate.

GC-MS analysis was also performed for a selection of the above GC runs to confirm the identity of the peaks found. No inconsistencies were observed.

Sample 2: Methanol dilution

Further tests were needed to ensure that no loss of FFA or FAME was incurred when performing the separation with hexane and methanol of sample 1. To address this, sample 2 was also used to analyse acetol, FFA and propanal/propanone content.

The analyte mixture was diluted at a 1:19 ratio in methanol, and analysed using a HP6890 GC. The carrier gas used was 2ml/min helium, and the heating profile was: 150°C for 1 minute, followed by heating by 10°C/minute up to 210°C then maintained for 10 minutes.

Standard samples of acetol, propanal/propanone and FFA were also run for calibration purposes. The GC runs were repeated 3 times and the results averaged (outliers removed and an extra repeat performed). Column conditioning was performed at 240°C for 20 minutes with a pure methanol injection after every 2nd run to ensure no contamination from glycerides occurred.

Sample 3: Titration with NaOH

The FFA content was confirmed by titration of the 3rd sample, diluted 40:1 in chloroform, with aqueous NaOH according to the method below.

The triglyceride derived sample was accurately weighed (±1mg) and placed into a suitable Erlenmeyer flask containing chloroform at a 1:40 volume ratio of analyte: chloroform. A pH indicator solution was then introduced, and the solution was titrated to pH 7, as shown by the indicator colour change, with 0.05M NaOH in chloroform. NaOH/ chloroform solutions were prepared directly before use, to prevent changes in concentration from evaporation.

The FFA concentration is calculated using the standard formula:

$$\text{FFA concentration (mmol FFA/g sample)} = \frac{N \times V}{W}.$$

Where N, V, and W denote the molarity of the titrant (mmol/ml), the volume (ml) of titrant, and weight (g) of sample, respectively.

This titration was performed 5 times for each sample, discounting outliers before averaging.

Sample 4: Glycerol and glyceride content determination

Sample 4 was used to determine glycerol and glycerides content. The initial drying was performed by introducing 3Å molecular sieves equal to 15% of the total sample volume for 24 hours in a tightly sealed container, followed by Coulometric Karl-Fischer titration to confirm the water content was below 0.1wt.%

A 0.1ml sample of the dried waste glycerol was then analysed for glycerides according to the 2011 BS EN ISO 14105 standard for glycerides analysis. This was compared to reference samples of butan-1,2,4-triol, triglycerides and glycerol to calculate the resulting yield of glycerol and glycerides. To confirm the results, 2 repeats of each derivatized sample were performed, and a third if the results were inconsistent.

3.4.3 Solids analysis

The only solid products observed in this work were the residue detected on the reactor and catalyst after triglyceride decomposition runs and the solid residue from glucose and cellulose. The solid residues were first tested for solubility in polar and non-polar solvents (methanol and hexane). The solid mass fraction, comprised of soluble components, was measured by reweighing after dissolution then compared to the original solid weight. The soluble solid was analysed by GC/GC-MS using the same procedure as the corresponding liquid fraction. For triglyceride derived solids, none of the deposits contained insoluble components. However, the glucose and cellulose solid residues were largely insoluble and were analysed further using SEM, BET and CHN analysis, as detailed in sections 3.2.1, 3.2.2 and 3.2.4 respectively.

3.5 Numerical methods

The cold plasma itself was modelled as two separate fluids that are not in thermal equilibrium, namely excited species and neutral species, representing the electron and bulk temperatures respectively, as used in previous works. This work models reactions in both phases using the modified Arrhenius equation as shown in equation 3.1, with plasma initiated reactions using the electron temperature and other reactions using the bulk temperature.

$$k = AT^{n}e^{-\frac{Ea}{RT}} \qquad (3.1)$$

Where k is the rate constant of the reaction

A is the pre-exponential factor

T is the temperature in Kelvin (electron temperature if the reaction is plasma initiated, bulk temperature otherwise)

n is the temperature dependence (Vinu and Broadbelt, 2012)

Ea is the reaction activation energy in KJ/mol

R is the universal gas constant (R=8.314 KJ/mol K)

To develop a plasma model based on the modified Arrhenius equation, it is necessary to determine the electron temperature, in addition to other constants specific to individual reactions.

3.5.1 Electron temperature

In previous works (Thomas and Jen-Shih, 1997; Zhu and Pu, 2010; Shrestha, 2012), the electron temperature was calculated using the line intensity ratio method. The line intensity ratio method is a technique based on the Stark broadening effect, which dictates that the optical emission lines of the gas in the plasma zone are broadened and shifted from their regular locations due to the presence of an electric field, with increased electric fields shifting the emission lines towards higher values in a linear relationship. To derive the electron temperature, two emission lines corresponding to the carrier gas are observed via optical emission spectroscopy (OES) on the plasma zone (Fridman, 2008). The ratio between the intensities of the emission lines and the intensities of the corresponding emission lines in the unexcited gas is recorded and used to calculate the electron temperature according to equation 2.1 (Section 2.5.9).

To determine the electron temperature using this method, optical data for the plasma during operation is required to quantify the intensity of the optical emissions. This method has been demonstrated to be effective at approximating the electron temperatures for corona discharge plasmas (Shrestha, 2012). With a DBD reactor, the plasma zone is hidden within the reactor so no locations were available to mount the optical probe to permit this method of calculating the electron temperature (Thomas and Jen-Shih, 1997; Zhu and Pu, 2010). Therefore, an alternate method for calculating the electron temperature was employed, which uses the power input to the reactor as a means of approximating the electron temperature.

The energy introduced to the reactor over the residence time was calculated directly using equation 3.2:

$$Energy\ In = \frac{Power \times Plasma\ reactor\ residence\ time}{Power\ factor} \tag{3.2}$$

Where the power factor is the efficiency of the type of plasma reactor, which is determined experimentally. The plasma power is accurately determined for the process from a wall mounted power meter, while the residence time can be measured based on reactor volume and input flowrates.

The electron temperature (T_e) was approximated from this based on the assumption that the ratio between the electron temperature and the temperature of gaseous ions is 1.0 which is a typical value for DBD plasma (Xi-Ming and Yi-Kang, 2008; Isoardi *et al.*, 2011). Using this ratio allows an approximate electron temperature to be derived by calculating the temperature of the ions, primarily either nitrogen or hydrogen. The number of molecules of nitrogen/hydrogen in the reactor was calculated from the gas density and molecular weight, and the energy per molecule was calculated by dividing Energy in by the number of molecules. This gives a value for the ion temperature, which is then used as the electron temperature. This can then be converted to eV to obtain an approximation of the electron temperature.

The validity of this approximation was tested by comparison with experimental data for electron temperatures in dielectric barrier discharge reactors (Zhu and Pu, 2010; Gangwar *et al.*, 2015) at 30W, 50W and 100W plasma power input in a nitrogen environment. At 100W plasma power, the calculation used in this work gave T_e = 4.099eV, compared to 3.9eV measured (Zhu and Pu, 2010). At 50W, T_e is approximated as 2.188eV, compared to 2.4eV (Gangwar *et al.*, 2015) while T_e =1.409eV at 30W, measured as 1-1.4eV (Naz *et al.*, 2012; Gangwar *et al.*, 2015). As the values obtained from the approximation are sufficiently similar to literature (given the range of sources), to within ±10% of actual values, this approximation was used in model development.

3.5.2 Model design

Based on experimental data and the parameters described in section 3.5.1, a simulation-based model of cold plasma decomposition was produced for methanol and glycerol to aid understanding of the process and enable comparison to other studies.

The liquid phase reaction and interphase mass transfer effects were assumed to affect only the observed activation energy of the process, based on the liquid being observed to prevent decomposition of liquid products except at high powers. The simulation was simplified by assuming that the process was equivalent to a batch process of duration equal to the residence time of 11 seconds with an additional 10 seconds with no power input to simulate the effect of liquid condensation and termination reactions between radicals. This is a reasonable assumption since the residence time is constant for the liquid and the conversion is too low for annular mixing to have a significant effect.

Each component that is expected to be generated or otherwise be present during plasma decomposition has a differential equation in the computational model. This equation (equation 3.3) is derived from each reaction that forms or depletes that component and is of the form:

$$\frac{dm_i}{dt} = \sum_j [(a_{ij}{}^F - a_{ij}{}^R) K_{jt} \prod_j N_i^F \qquad (3.3)$$

Where:

Π indicates the product of all terms inside the operator

m_i is the number of moles of component i

K_{jt} is the derived rate constant of reaction J at time t

$N_i{}^F$ is the concentration of component i in the forward side of reaction j

a_{ij} is the stoichiometric coefficient of the reactant i in reaction j,
where $a_{ij}{}^F$ represents reactions that generate component i
$a_{ij}{}^R$ represents reactions that consume component i

The plasma models developed in this thesis for methanol and glycerol decomposition use the modified Arrhenius equation to determine the rate of all predicted reactions and utilise thermal kinetics data for the reactions between the radicals, while the constants were developed using prior plasma kinetic data from literature sources for plasma initiated reactions. The fitting process for the plasma initiated constants was performed numerically due to the network of reactions making graphical methods impracticable. The modified Arrhenius equation is very commonly used as a basis for chemical models, which should allow easy comparison with other kinetic data and models. The thermal kinetics used for non-plasma initiated reactions were obtained from literature and used without modification to determine the values of K_{jt} for each reaction.

The initial kinetic data for the methanol model was obtained from previous plasma kinetic studies, where carbon monoxide reformation (Thomas and Jen-Shih, 1997) and hydrocarbon conversion were investigated (Yang, 2003). Initial kinetic values for 7 of the 12 proposed initiation reactions under cold plasma conditions are available in these sources. The remaining 5 utilise thermal kinetic values (Ing *et al.*, 2003) for the initial values.

For the glycerol model, the values derived during the methanol model were used directly as initial values where appropriate, with additional plasma kinetic values obtained from

(Hemings *et al.*, 2012). Data for the remaining reactions was unavailable so thermal kinetic data was utilised as initial values.

The methodology for improving the fit of the kinetic values to effectively model the decomposition process was to iteratively fit the kinetics to the data available, which is illustrated in Figure 3.4 below. The model was run at all three powers with the initial kinetic constants and the rate constants at each power recorded. The pre-activation constants of the methanol/glycerol decomposition reactions were scaled in proportion to each other to obtain acceptable estimates of the conversion at 50W as the greatest conversion was achieved at this power. The activation energy and temperature dependence were then tuned proportionally to fit the process to the conversion at all three power values. The modelling approach was tailored for the two feedstocks, as methanol produced only unstable initial products while glycerol produced acetol directly. For methanol, the distribution between the generation of dominant products (e.g. CO, CH_4) was fitted for by modifying the parameters of the initial decomposition reactions to reflect the relative yields of these products. The glycerol model kinetic parameters were fitted for using the intermediate products (e.g. acetol, methanol) as well as dominant products, using the relative yields of each to tune the model. Once this was achieved, fitting for products that required multiple reactions to form (i.e. CO_2 and C_2+ hydrocarbons) was performed on the relevant reactions using the relative yields of each at all powers. This produced a broadly accurate simulation, which was then optimised using an iterative least sum of squares method on the individual products, weighted according to their yield at 50W.

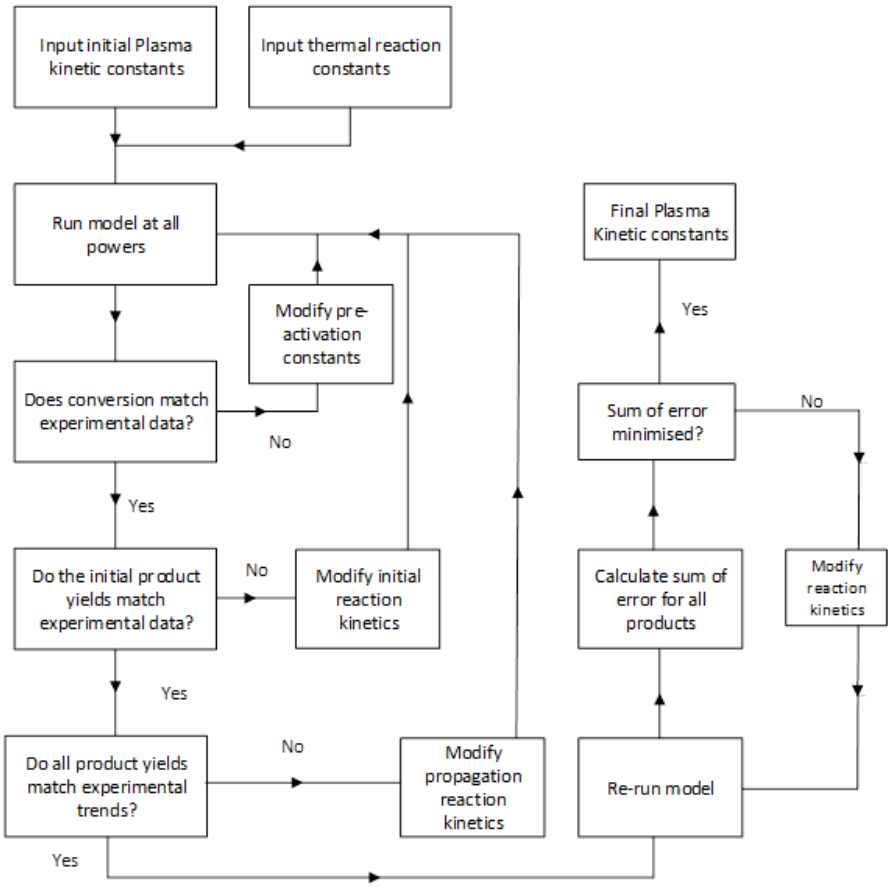

Figure 3.4: Procedure for fitting kinetic model constants to experimental data

3.6 Definitions

The selectivity of the process relates to the proportion of the converted material that becomes the desired product. This is defined in the mass% form as:

$$S_{P/K} = \frac{N_{p,out} - N_{p,in}}{N_{k,in} - N_{k,out}} \quad (3.4)$$

Where: $S_{p/k}$ is the selectivity to product P from reactant K

$N_{p,in}$ is the total mass of component p entering the reactor

$N_{k,in}$ is the total mass of component k entering the reactor

$N_{p,out}$ is the total mass of component p leaving the reactor

$N_{k,out}$ is the total mass of component k leaving the reactor

This equation is also used for molar selectivity, where $N_{k,in}$ and $N_{k,out}$ are replaced by the total moles entering and leaving the reactor.

The process yield is also defined, which is the mass proportion of the input that is converted to a desired product. This differs from selectivity in that it depends on the total mass input instead of the proportion of the input that is converted. The yield is defined as:

$$Y_P = \frac{N_{p,out} - N_{p,in}}{N_{s,in}} \quad (3.5)$$

Where: Y_p is the yield of product P

$N_{p,in}$ is the total mass of component p entering the reactor

$N_{s,in}$ is the total mass entering the reactor

$N_{p,out}$ is the total mass of component p leaving the reactor

The final definition for the product distribution is the conversion, which is used here as the proportion of the material input that is converted to another compound. This is written as:

$$X = \frac{N_{r,in} - N_{r,out}}{N_{r,in}} \quad (3.6)$$

Where: X is the conversion

$N_{r,in}$ is the mass of reactants entering the reactor

$N_{r,out}$ is the mass of reactants leaving the reactor

For pure feedstocks, this definition is sufficient, as there is only one component of interest in the inlet stream. However, for waste glycerol and waste cooking oil, the desired products are also present in the raw material, so defining the conversion and selectivities is problematic. For waste glycerol, this is done by treating glycerol, FFA and glycerides as the reactants, as these comprise over 95wt.% of the feedstock and are not useful products. For waste cooking oil, monoglycerides, diglycerides and triglycerides are counted as the feedstock, as nothing decomposes to them except other glycerides, which releases other products. This only accounts for around 80% of the feedstock, but FFA for this feedstock is a significant product due to the high yields possible.

Chapter 4. Cold plasma assisted liquid methanol decomposition

This chapter describes the establishment of the feasibility of two phase gas-liquid cold plasma assisted decomposition. Methanol was used as a model compound to enable understanding of the mechanisms and the effects of cold plasma operating conditions on deoxygenation because it is the simplest alcohol and shares many chemical bonds with other model compounds such as glycerol and triglycerides. The effects of plasma power and carrier gas (also known as purge gas) on the methanol decomposition pathway and products were studied, with a focus on the range of products that can be derived without catalysts/packing materials or additional reagents. From the range of products at the outlet of a reactor, the full mechanism of the cold plasma assisted decomposition of methanol was established and compared to thermal processes in terms of radical products and kinetics. A kinetic model of the process was developed based on the product distribution and used to derive appropriate activation energy and pre-exponential constants for the cold plasma initiated reactions.

Although cold plasma initiated methanol decomposition has been studied previously, this was performed in the gas phase at very low methanol contents (20ppm methanol in N_2) (Hsiao *et al.*, 1995; Derakhshesh *et al.*, 2010) compared to this work or exclusively studies hydrogen evolution rates (Zhang *et al.*, 2016). In this chapter, liquid methanol was used to study whether cold plasma promoted alternative reactions in a multiple-phase system and if the presence of a bulk liquid phase has any novel effects on the plasma activity and the composition of the outputs. Based on experimental data recorded in Section 4.1, a full mechanism of liquid-phase methanol decomposition was developed and validated via comparison of the model outputs to literature data under identical conditions. The proposed mechanism successfully explained the presence of the unexpected liquid products.

Analysis of experimental results and the kinetic model informed later studies on glycerol decomposition due to its structural similarities to methanol. Comparison of derived kinetic data to thermal kinetics demonstrated that cold plasma is a viable alternative in terms of conversion and selectivity.

4.1 Effects of plasma power and carrier gas on methanol decomposition pathways

Table 4.1 shows that methanol conversion increased with increasing plasma power for all

three tested carrier gases (H_2, N_2 and He). This is because increasing the plasma power increases the rate of formation of excited species, which induce the decomposition process (Du *et al.*, 2007; Bahri *et al.*, 2016). The carrier gas had a significant effect on the conversion of methanol. For example, 25.92% conversion was achieved in H_2 environment but only 13.75% in N_2 at the same plasma power of 50W. The conversion was in the order H_2> He > N_2 with very different product distributions, except for the case at low plasma power i.e. 10W. CO_2 was only produced under N_2 and He whereas high yields of CO (9.69wt.%) and gaseous hydrocarbons (C_1-C_3) (14.44wt.%) were obtained in a H_2 environment. In contrast, He environment at 50W produced similarly high levels of CO (7.90wt.%) with moderate hydrocarbon yields (5.54wt.%), H_2 yields (1.46wt.%) and traces of propanal (0.96wt.%) and methyl methanoate (0.73wt.%) whereas N_2 environment at 50W produced high yields of ethanol (1.80wt.%) with moderate hydrocarbon yields (5.89wt.%). These differences suggest that different pathways are favoured for each carrier gas.

Table 4.1: Cold plasma assisted decomposition of methanol at atmospheric conditions (temperature and pressure) at a ratio of liquid to gas of 40:1 (vol/vol) and residence time of 11 seconds in the absence of a catalyst (Error: ±2%)

Carrier gas	**H_2**			**N_2**			**He**		
Plasma power (W)	10	30	50	10	30	50	10	30	50
Gas yield (wt. %)	2.96	12.07	24.13	4.20	8.46	10.20	4.63	7.41	15.87
Conversion of methanol (%)	3.81	13.15	25.92	5.15	10.83	13.75	5.54	11.42	18.17
Yield of gaseous products (wt.%)									
CO_2	-	-	-	0.41	1.27	0.92	0.38	1.59	0.96
H_2	-	-	-	0.45	0.67	0.81	-	0.53	1.46
CO	1.23	4.87	9.69	2.85	2.67	2.58	2.24	2.36	7.90
CH_4	1.21	1.61	2.89	0.41	0.80	3.94	0.89	0.59	2.04
C_2H_6	0.52	5.56	11.33	0.09	2.87	1.67	1.07	2.32	3.05
C_3H_8	-	0.03	0.22	-	0.17	0.28	0.05	0.02	0.45
Liquid product yields (wt. %)									
Ethanol	0.06	0.44	1.21	0.45	0.75	1.80	-	0.54	0.14
Propanal	-	-	-	-	-	-	-	-	0.96
Methyl methanoate	-	-	-	-	-	-	-	-	0.73
Water	0.79	0.64	0.59	0.50	1.62	1.75	0.91	3.47	0.47
pH	6.31	4.94	4.72	5.55	6.08	5.34	5.98	4.76	5.91

The main products obtained from liquid methanol decomposition in cold plasma were gaseous (total gas yields comprise 64-93% of the total conversion) and comprised primarily CO_2, CO, H_2 and light hydrocarbons (C_1-C_3). The product yield distribution was very different from that obtained from conventional thermal processes and other cold plasma work, where H_2 (15.1%) and CO (35.4%) yields dominate, and only traces of hydrocarbons (C_1-C_2) (1.1%) and CO_2 (0.5%) were detected (Derakhshesh *et al.*, 2010; Zhang *et al.*, 2016). All of these indicate the product distribution is significantly affected by reactor designs (Bichon *et al.*, 2007), multi-phase reactions (Bichon *et al.*, 2007;

Derakhshesh *et al.*, 2010), feedstock concentration and power inputs (Zhang *et al.*, 2016).

Prior studies (Bichon *et al.*, 2007; Derakhshesh *et al.*, 2010) demonstrated that gas phase methanol could decompose in the presence of cold plasma to produce hydrocarbons (C_1-C_3), water and CO via two dominant pathways (Reaction 4.1): decomposition to methyl and hydroxyl radicals via C-O bond splitting (Ge *et al.*, 2015) and decomposition to methoxy and hydrogen radicals via O-H bond splitting (Bichon *et al.*, 2007; Derakhshesh *et al.*, 2010; Ge *et al.*, 2015; Zhang *et al.*, 2016).

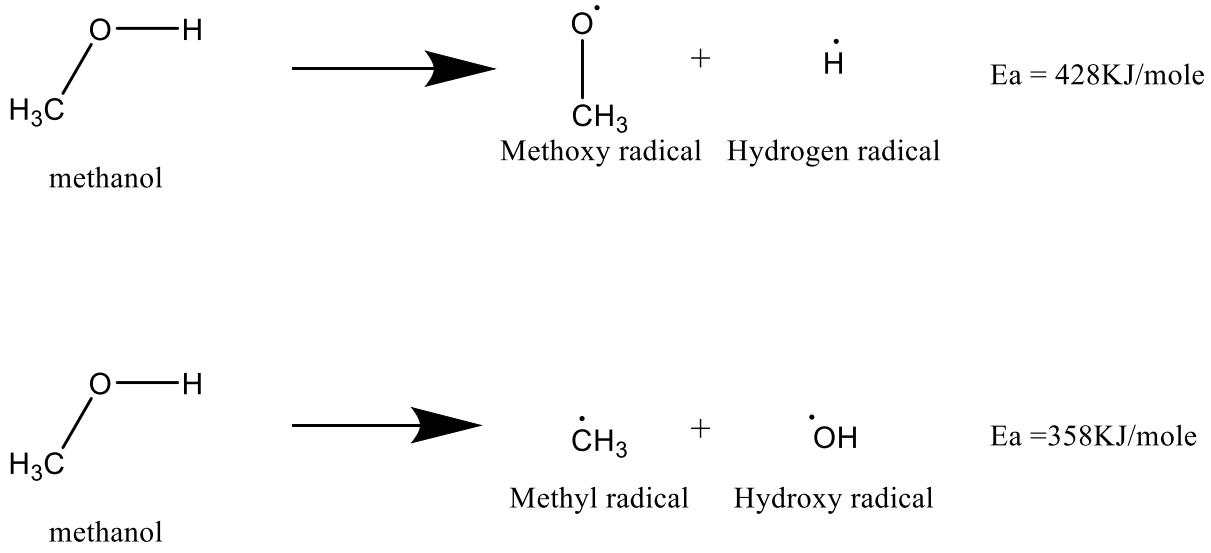

Reaction 4.1: Primary initiation reactions for methanol decomposition

Of these two pathways, the formation of methyl and hydroxyl radicals would dominate due to lower C-O bond energy (358KJ/mol) than the O-H bond (428KJ/mol). The formation of methanol cation radicals ($CH_2OH.$) also occurs, which further decompose to CO and H_2. Derakhshesh et al. reported that the two dominant initiation reactions in DBD plasma for gas phase methanol (400ppm methanol) decomposition in N_2 environment are formation of methyl and methanol cation radicals, of which the formation of methoxy radicals was less favoured (Derakhshesh *et al.*, 2010). The theorised initation reactions above are supported by the observation of their derivatives (H_2, C_2H_6 and ethanol) in Table 4.1. As these initiation reactions are included in the mechanism proposed in this work (Reaction 4.1 and 4.2), the reaction kinetics approximated by this source are utilised in the modelling section (Section 4.2) below.

Another study (Hsiao *et al.*, 1995) on methanol decomposition with cold plasma achieved 73% conversion. This is a much higher conversion than was obtained in this study (25.92%) (Table 4.1), likely to be due to the methanol in previous work being gas phase

which facilitates plasma decomposition (Koeta *et al.*, 2012). Additionally, the presence of abundant oxygen is likely to affect the reaction pathway, so a full comparison of kinetics is not practicable. Therefore, only limited comparison can be made between this and earlier work, which generally are in accord with respect to products and likely mechanisms. The primary decomposition pathway was confirmed to be the formation of methyl and methanol cation radicals and their further decomposition to mostly H_2 and carbon oxides (Hsiao *et al.*, 1995).

The methoxy radicals can reform into methanal via isomerisation when in the presence of hydroxyl radicals, releasing water as a by-product (Reaction 4.2) (Tsang and Hampson, 1986; Di *et al.*, 2016).

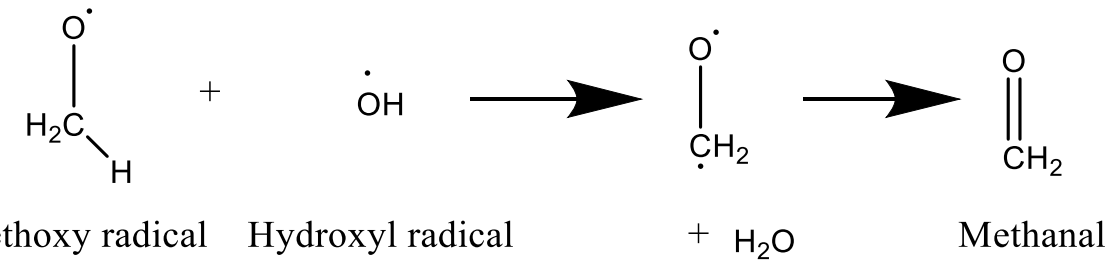

Reaction 4.2 Reformation pathway for methoxy radicals to methanal

It is known (San Fabián and Pastor-Abia, 2007) that in a N_2 plasma environment, excited nitrogen atoms and molecules (N* (^{4}S, ^{2}D, ^{2}P) and N_2*(A $^3\Sigma_u^+$)) are generated, with the lowest excited energy state at 6.1eV. These excited states were generally quenched rapidly at atmospheric pressure and were unlikely to contribute significantly to the reaction, with the possible exception of the triplet meta-stable state of nitrogen, N_2 *(A $^3\Sigma_u^+$) and excited nitrogen atoms, N* (^{2}D), which could initiate the decomposition of methanol. The wide range of excited states offers a wide range of available energies, permitting a greater variety of reactions (Harling *et al.*, 2005). He, with its very high energy excited state (>19 eV (Ding and Chen, 2011)), the highest first excited state possible, produces some extremely energetic species that can allow reactions that are otherwise impossible. H_2 has a low energy excited state (around 3.7 eV (Baulch *et al.*, 1992; Fridman, 2008)) and is easily converted into hydrogen radicals, allowing rapid hydrogenation. These excited states are illustrated in Figure 4.1, with the exception of He, which is on the scale at 19eV. As can be seen, while H_2 has the lowest energy excited states, the concentration of electrons capable of exciting H_2 is greater than the proportion capable of exciting N_2. Electrons below the excitation energy of the carrier gas are capable

of inducing gas phase reactions but are unable to diffuse into the liquid phase, unlike the excited species and decomposition products.

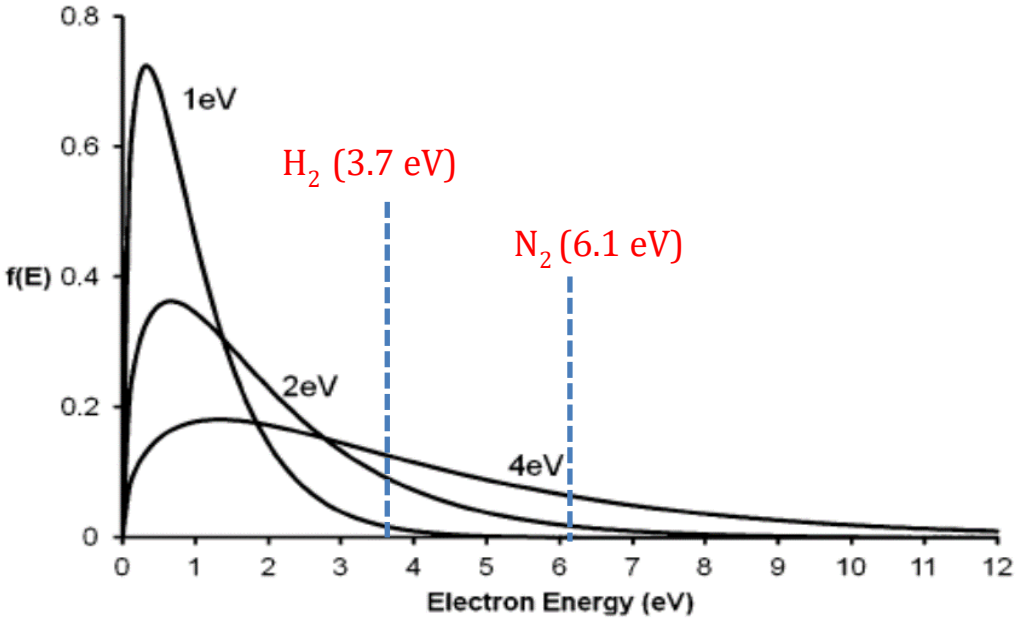

Figure 4.1: Electron energy distribution showing carrier gas excited states (Michelmore *et al.*, 2013)

Theoretically, based on activation energies, the formation of methane would be the dominant pathway at low powers via the methyl radical route (288KJ/mole). Methane will be formed ($CH_{3}\cdot + H\cdot = CH_4$) as well as longer chain hydrocarbons due to the propagation steps (e.g. $CH_{3}\cdot + CH_{3}\cdot = C_2H_6$). As shown in Table 4.1 the highest methane yield was observed in the H_2 environment, except at 50W plasma power. However, from Table 4.1, CO was formed at low plasma power i.e. 10W under all carrier gases (1.2-2.9 wt.%) despite the dissociation of the O-H bond requiring a high activation energy (428KJ/mole) (4.43eV), which is higher than the electron energy under H_2 (3.7eV). The generation of CO under H_2 can be explained by generation of $CH_2OH\cdot$ radicals via C-H bond breakage followed by isomerisation to methanal (160KJ/mol or 1.65eV) (Wiest, 1996) and dehydrogenation to CO(296KJ/mol or 3.06eV) (Koeta *et al.*, 2012), which require much lower activation energies and are lower than the electron energy under H_2 (3.7eV).

The yield of methane was higher than that of ethane in H_2 and N_2 at 10W and N_2 at 50W. However, at other powers, the ethane yield was at least 10% higher than that of methane (0.89 vs 1.07wt.%) in a He environment and 300% higher in a H_2 environment at 50W

(2.89 vs 11.33wt.%). This is unexpected as ethane is expected to form from reactions between two methyl radicals, but in the presence of hydrogen radicals (>0.45wt.% H_2) (Table 4.1), methyl and hydrogen radicals react to generate methane more rapidly than ethane (Tsang and Hampson, 1986). This is because the reaction between 2 methyl radicals has a much lower rate constant ($6x10^{-11}cm^3mole^{-1}s^{-1}$) than the reaction between methyl radicals and hydrogen radicals ($3.5x10^{-10}cm^3mole^{-1}s^{-1}$) (NIST). This suggests an alternative pathway to ethane exists. It was reported (Yetter et al., 1989; Ing et al., 2003) that methoxy radicals could be converted to methoxymethane via reactions with methyl radicals, then reform to ethane by hydrogen radical attack (Reaction 4.3). This reaction pathway provides an explanation for the unexpectedly high ethane yields.

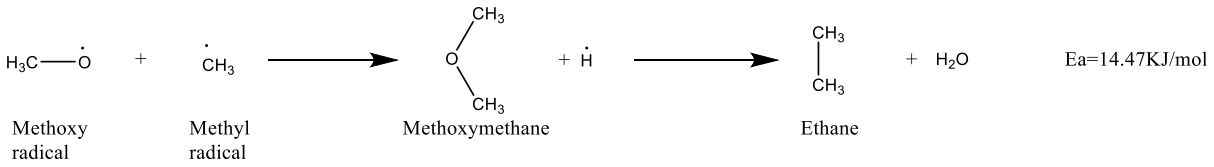

Reaction 4.3: Formation of ethane via methoxymethane decomposition

The reduction in ethane content (from 2.87wt.% at 30W to 1.67wt.% at 50W) in N_2 environment is most likely due to the decomposition of ethane to methyl radicals via cracking reactions, which are known to occur under cold plasma (Ouni *et al.*, 2009) and have high rate constants at typical cold plasma electron temperatures ($2.3x10^{-7}$ $cm^3mole^{-1}s^{-1}$) (NIST).

The extra methyl radicals formed from ethane cracking would be consumed by the formation of ethanol in the liquid phase (predominantly CH_3 radical attack on methanol cation radicals (Reaction 4.4) due to the increased methane yield at 50W).

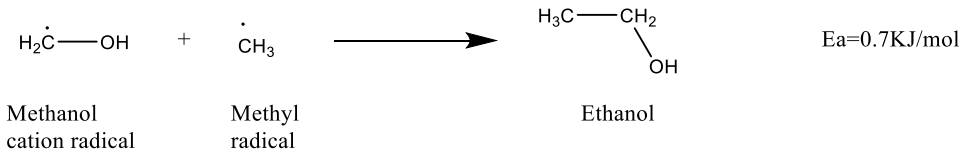

Reaction 4.4: Proposed route for formation of ethanol

The highest conversion (25.92%) and hydrocarbon (C_1-C_3) yields (14.44wt.%) were obtained in the H_2 carrier gas, which is unexpected due to its low energy excited state (3.7eV). This implies that the conversion of methanol requires a lower electron temperature, which is likely due to the greater proportion of electrons that can excite H_2

to generate liquid phase radicals (Figure 4.1). As radicals and other excited species can diffuse into the liquid phase but electrons cannot (Di *et al.*, 2016), this results in H_2 introducing more radicals to the liquid phase at any given power and hence increasing the rate of decomposition reactions. However, as hydrogen radicals typically decompose molecules by substitution, C-H and O-H bonds are less likely to be affected under H_2 (Neretti *et al.*, 2017). This would increase selectivity to hydrocarbons through decomposition of the C-O bond, as observed. It was found that H_2 carrier gas flowrate at the outlet was less than at the inlet, indicating its consumption during radical attack and stabilizing other radicals. The consumption of H_2 during cold plasma treatment was determined by the use of a make-up gas, i.e. N_2. The amount of H_2 consumed during the decomposition process increased with plasma power, for example 3.67 cm^3/min at 10W, 15.12 cm^3/min at 30W and up to 25.67cm^3/min at 50W. These termination reactions do not require additional energy as both reactants are radicals and will therefore occur under all conditions ($k=1.5x10^{-10}cm^3mole^{-1}s^{-1}$) (NIST) when H_2 is abundant (Derakhshesh *et al.*, 2009). Hydrogen radicals would also prevent dehydrogenation via excited species interactions, such as conversion of methanol to methoxy and methanol cation radicals. The formation of methyl and methoxy radicals from initial methanol decomposition (Reaction 4.1) is expected to occur under H_2 and thus permits the formation of methoxymethane under H_2 carrier gas ($k= 5.5x10^{-11}cm^3mole^{-1}s^{-1}$) (Reaction 4.3). The increased hydrogen radical concentration would promote hydrogen radical attack on methoxymethane due to increased reactant concentrations (Yetter *et al.*, 1989), explaining the increased ethane yields.

The formation of CO_2 in N_2 and He environments is most likely from the reforming of methoxy radicals to CO, which in turn reacts with a hydroxyl radical to produce formate radicals, which then reform to CO_2 (Reaction 4.5) (Yetter *et al.*, 1989; Troe, 2007). Theoretically, formic acid could form from hydrogenation of the formate radicals, but no formic acid was detected during analysis under any conditions, indicating dehydrogenation to CO_2 dominates.

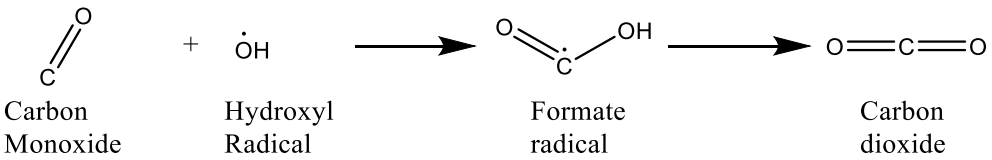

Reaction 4.5: Formation pathway for carbon dioxide via formate radicals

The formation of methoxy and hydrogen radicals (Reaction 4.1) has the highest energy pathway at 428KJ/mole and requires decomposition of an O-H bond. As a result, the reactions of the methoxy decomposition pathway do not occur in a H_2 environment, as evidenced by the lack of CO_2 detected under H_2 (formate radical to CO_2 requires O-H bond splitting). The prevalence of this pathway is also limited under N_2 and He, with products such as methyl methanoate and CO_2 at low yields due to the higher activation energy. In a H_2 environment, the abundant hydrogen radicals would react with hydroxyl radicals to form water with a 5.06KJ/mole exotherm, competing with formation of formate radicals by removing hydroxyl radicals from solution through both elimination and evaporation. This would also occur under the other carrier gases from hydrogen radicals released via dehydrogenation of methanol.

Although methanal (HCHO) and other aldehydes were observed in conventional thermal decomposition processes (Table 4.2) (Bichon *et al.*, 2007), methanal was not detected in this study. This could be due to the instability of methanal in the presence of highly energetic electrons causing its rapid decomposition to CO and H_2 (Koeta *et al.*, 2012), which is an explanation for the relatively high CO yields (9.69wt.%). In a He environment, a small amount of propanal (0.96wt.%) was detected at 50W plasma power. This indicates that aldehdyes can be generated but are decomposed by the plasma if they are in gas phase.

Unlike conventional thermal decomposition studies of methanol (Ing *et al.*, 2003; Balat, 2008; Brudnik *et al.*, 2009; Van Bennekom *et al.*, 2011), ethanol and methyl methanoate were generated in the presence of cold plasma. Ethanol could be generated via a reaction between methyl radicals and methanol cation radicals (initial methanol decomposition products) (Reaction 4.4), or from ethyl radicals and hydroxyl radicals (secondary decomposition products). Previous cold plasma work utilised lower methanol concentration (10ppm) in the gas phase (Derakhshesh *et al.*, 2010). In this source, ethanol was not detected at 22W cold plasma in N_2 environment. This thesis detected traces of ethanol (0.45wt.% at 10W) at similar conditions (Table 4.1). This may indicate that the presence of a liquid phase under cold plasma conditions increases selectivity towards liquid products. As shown in Table 4.2, in conventional thermal processes CO + H_2 or CO_2+ H_2 were the main products. The pyrolysis studies by (Ing *et al.*, 2003) do not comment on H_2 formation, but its generation is strongly suggested by performing an elemental mass balance on the results (Table 4.2).

Table 4.2: Comparison of methanol thermal decomposition methods from literature

Thermal decomposition methods	Conventional (Ing *et al.*, 2003)	Conventional (Ing *et al.*, 2003)	Supercritical conditions (Van Bennekom *et al.*, 2011)	Catalytic steam reforming (Bichon *et al.*, 2007)
Temperature (°C)	800	600	514	255
Liquid flow rate (moles/second)	0.04	0.008	0.0133	0.0941
Carrier gas/solvent	Methane	Methane	Water	Steam
Pressure (bar)	5	5	260	1
Catalyst	N/A	N/A	N/A	$CuZn/Al_2O_3$
Residence time	1	2	15	300
Conversion (mol%)	43	98	55	39
Product Yields (mol%)				
CH_2O	7.4	1.2	-	-
CO	31.8	87.3	14.4	0.1
CH_4	3.8	9.4	4	-
CO_2	-	0.02	25.5	14.2
H_2	-	-	56.1	85.7
C_2H_6	-	0.01	-	-

A methanol/water mixture decomposition was performed using gliding arc plasma preheated to 80°C where the liquid phase methanol was exposed to an indirect plasma stream (Zhang *et al.*, 2016) with 92% conversion to produce H_2 (63mol% yield) and CO (26mol% yield). Gliding arc plasma often induces a combination of thermal and cold plasma effects, but the arc was not used for conversion directly and the pre-heating temperature was too low for methanol decomposition. This means the decomposition would be predominantly due to cold plasma effects. The selectivities to carbon oxides and hydrocarbons closely resemble that of methanol pyrolysis at 600°C (Hsiao *et al.*, 1995; Ing *et al.*, 2003), except that the required residence time is longer and conversion is less extensive, indicating that the thermal decomposition mechanism is likely to be similar to cold plasma decomposition.

The use of catalytic (Cu/Al_2O_3) plasma reactors for liquid phase plasma decomposition of methanol have been studied previously (Ge *et al.*, 2015). Adding steam enhanced the conversion due to catalytic stream reforming, increasing the yield of H_2. For example, at a

carbon: steam molar ratio of 1:1, more than 80% conversion was achieved with a long residence time (12 minutes vs 11 seconds) and comparable gas flow rate (25ml/min N_2). The study reported that the thermal decomposition onset temperature was largely unaffected by cold plasma, but the conversion was markedly increased in the presence of plasma (Ge *et al.*, 2015). This indicates that the increased temperature increases the effects of the cold plasma. Increased H_2 yield, decreased CO yield and the presence of CO_2 under cold plasma at thermal decomposition temperatures appears to indicate that the plasma primarily promotes steam decomposition, which lines up well with gas-liquid cold plasma theory (Di *et al.*, 2016).

Methyl methanoate can be produced from esterification of formic acid and methanol in the presence of a catalyst such as H_2SO_4 at ambient conditions (Mendow *et al.*, 2011; Chen *et al.*, 2014b). Typical acidic esterification (Reaction 4.6) occurs via the addition of a hydrogen atom from an oxonium ion (H_3O^+) to the carbonyl oxygen to produce a diol group and an electropositive carbon atom. The alkyl molecule attaches to the electropositive carbon, transferring the electropositive zone as the ester bond forms (Bender, 1960). This electropositive area is stabilised by releasing an oxonium ion (H_3O^+), which reforms the original carboxylic acid oxygen to a carbonyl group, leaving an ester (Huber *et al.*, 2006). This is known as Fischer esterification, and requires an acid catalyst to supply oxonium ions (Sobkowicz *et al.*, 2009). In the He environment at 50W plasma power, around 0.73wt.% methyl methanoate (Table 4.1) was produced in the absence of a catalyst. This could be due to interactions between formate radicals and methanol (Reaction 4.6), but this has been previously shown to require residence times in excess of 10 hours without a catalyst due to high activation energies (246KJ/mole) (Sobkowicz *et al.*, 2009). In cold plasma, hydrogen radicals would have to be substituted onto the carbonyl oxygen of formate radicals in the presence of methanol. This is energetically unfavourable, which would explain why it only happens under He at 50W, as He has the highest excitation energy of the three carrier gases (19eV or 1833 KJ/mol), which is much higher than the activation energy required for these reactions (200-450KJ/mol). The excitation energy has to be significantly larger than the activation energy due to the liquid phase preventing excited electrons from decomposing the liquid components. This limits decomposition to the liquid surface and formation of liquid radicals is required to induce bulk liquid decomposition. As the liquid is electrically conductive, a proportion of the incoming energy is dispersed as heat (Fridman, 2008). These factors combined mean that significantly higher excitation energy is required for this reaction to be observed.

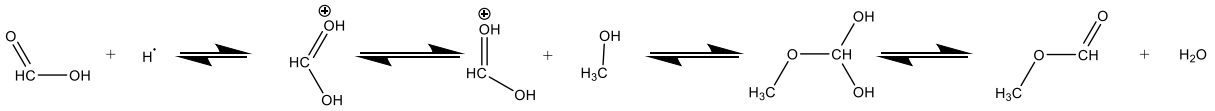

Reaction 4.6: Typical acidic esterification reaction mechanism

As shown in Table 4.1, the yields of water and hydrocarbons were comparable to those obtained in conventional thermal decomposition (Tsang, 1987; Iwasa *et al.*, 2000; Bichon *et al.*, 2007). The conversion of methanol in cold plasma assisted decomposition (maximum 26% in H_2 at 50W) (Table 4.1) was lower than that in thermal decomposition (39-95%) (Table 4.2). These indicate that cold plasma assisted decomposition follows the reaction pathway of the conventional thermal processes. In addition, polymerization of methyl radicals to form long chain hydrocarbons (Tsang, 1987), and formation of methoxy radicals (Derakhshesh *et al.*, 2010) (Reaction 4.3) occur, which require high activation energies and do not occur under thermal conditions without a catalyst (Bichon *et al.*, 2007). These reactions can occur in cold plasma due to initiatiation via radicals and energetic electrons instead of high temperatures (Tsang and Hampson, 1986). As the energetic electrons are unable to decompose liquid phase products rapidly (Di *et al.*, 2016), products of these reactions can accumulate.

The residence time used in this work was around 11 seconds, similar to most thermal processes (performed at 800°C). Cold plasma produces high energy radicals at lower operating temperatures (60°C) than pyrolysis (600°C), which permits accumulation of products that would be unstable under pyrolysis conditions (Ing *et al.*, 2003; Kongpatpanich *et al.*, 2011). This was observed experimentally, as methyl methanoate, propanal and ethanol were generated under cold plasma (Table 4.1).

The reaction mechanism developed from experimental data for cold plasma decomposition of methanol is illustrated in Figure 4.2. The reactions are shown with their kinetic activation energies (Ea) to provide evidence of their feasibility and to support earlier arguments on which reactions occur at low powers (i.e. 10W). In addition to plasma initiated reactions, Figure 4.2 shows propagation and termination reactions between excited species. These reactions between excited species have activation energies below 10KJ/mol and occur spontaneously even in the absence of a plasma field.

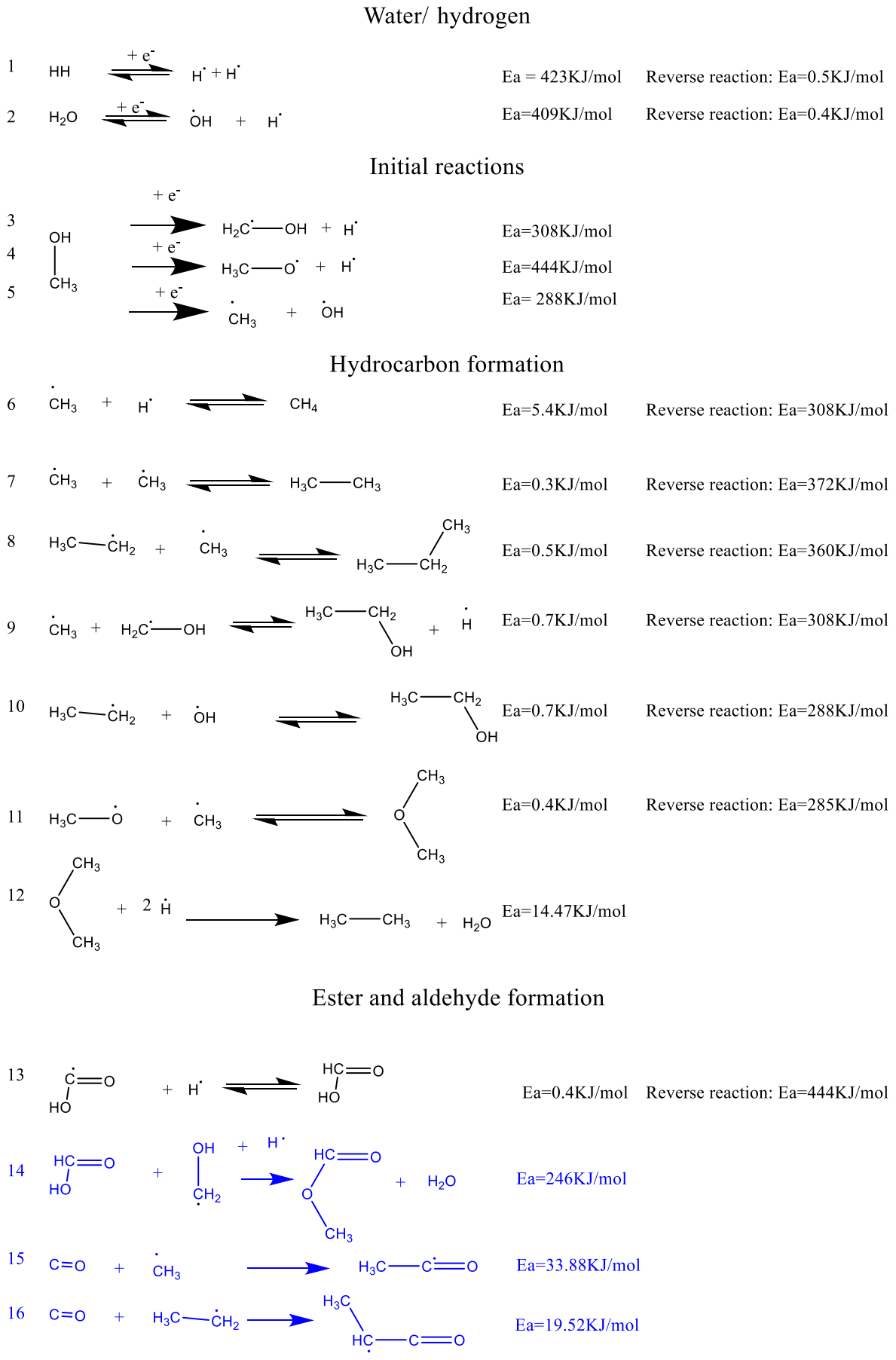

Figure 4.2: Proposed mechanisms of cold plasma assisted methanol decomposition- Continued overleaf

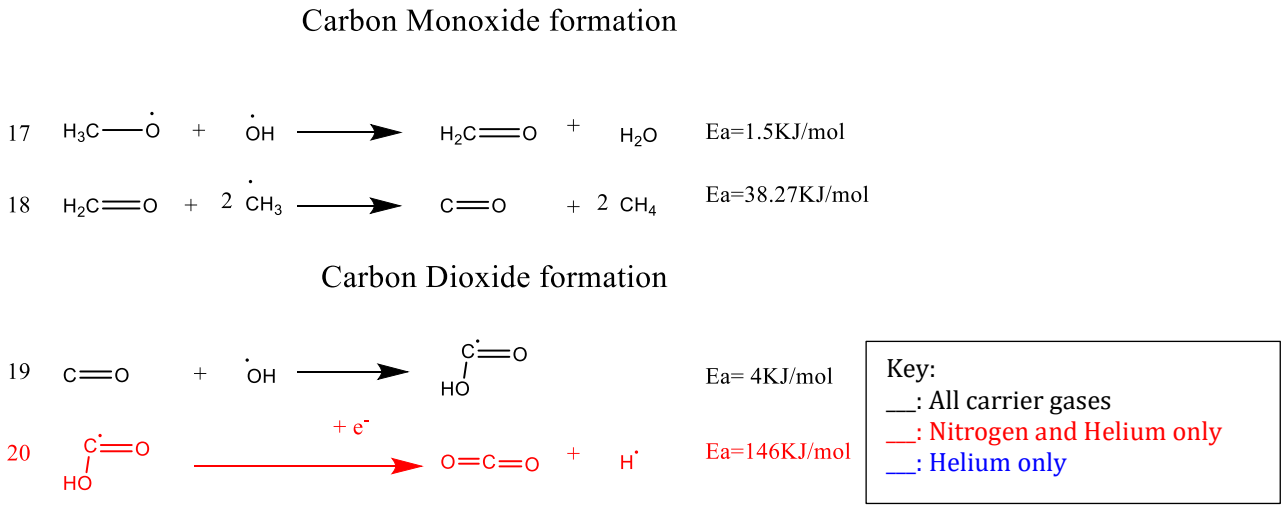

Figure 4.2: Proposed mechanisms of cold plasma assisted methanol decomposition

4.2 Computational modelling of methanol decomposition and validation

A mechanistic two phase plasma model was prohibitively complex to develop with the software and data available due to the requirement for mass transfer resistances, multiple types of energetic species with different mass transfer characteristics and an unpredictable fluid distribution profile. To approximate for the presence of two phases, these electron generation reactions and mass transfer resistances were lumped into the activation energies to account for generation of excited species and their transfer into the liquid phase.

Modifications to the activation energy were found to provide an acceptable approximation of the dual phase behaviour, due to the excited species generation having a separate defined activation energy (Fridman, 2008) and mass transfer between phases being considered as a single mass transfer resistance. This meant that changes to the pre-exponential constant and temperature dependance could not be used to model liquid phase reactions effectively. However, the use of this assumption does mean that the model would be inaccurate if used for gaseous methanol, as the activation energies would be significantly overestimated.

The initial content of methanol and water was defined in the model at a concentration corresponding to the methanol: N_2 flowrate ratio of 1:40 and the plasma zone volume of 7.16cm^3 as defined in chapter 3.3.

Cold plasma assisted methanol decomposition was modelled by inducing 12 initiation reactions, with initial kinetic parameters derived from previous plasma decomposition studies (Yetter *et al.*, 1989; Thomas and Jen-Shih, 1997; Yang, 2003; Derakhshesh *et al.*,

2010) or from NIST where unavailable. These initial parameters are shown in Table 4.3 below.

Table 4.3: Initial model constants from literature

Reactions	**A (Pre-exponential constant) (s^{-1})**	**N (Temperature dependence)**	**Ea (Activation energy) (KJ/mole)**	**Reference**
H_2 ⟶ 2 H.	1.7 x10^{-8}	0	119.94	(Yang, 2003)
CH_3OH⟶ $CH_2OH.$ + H.	1.64 x10^{7}	2.55	384.7	(Derakhshesh *et al.*, 2010)
CH_3OH⟶ $CH_3.$ + OH.	3.26 x10^{10}	2.05	378	(Derakhshesh *et al.*, 2010)
CH_3OH⟶ $CH_3O.$ + H.	1.19 x10^{7}	2.39	416.7	(Derakhshesh *et al.*, 2010)
CH_3OH⟶ CHOH.. + H_2	2.03 x10^{-10}	1.22	361.5	(Derakhshesh *et al.*, 2010)
C_2H_6 ⟶ $C_2H_5.$ + H.	1.53 x10^{-7}	-0.06	121.4	(Yang, 2003)
C_2H_6 ⟶ $CH_3.$ + $CH_3.$	2.17X10^{13}	-17.6	298.0	(Yang, 2003)
C_3H_8⟶ $C_3H_7.$ + H.	4.0X10^{-7}	-0.05	119.8	(Yang, 2003)
C_4H_{10}⟶ $C_4H_9.$ + H.	5.0X10^{-7}	-0.07	119.2	(Yang, 2003)
CH_2O ⟶ CO + H_2	2.11X10^{-7}	-1.1	296.0	(Thomas and Jen-Shih, 1997)
CH_4 ⟶ $CH_3.$ + H.	5.16x10^{-5}	-0.642	169.9	(Yang, 2003)

These kinetic parameters were then modified using the experimental data obtained from this study. In addition to cold plasma induced reactions, radical propagation and termination reactions detailed in the mechanism shown in Figure 4.2 were also modelled using kinetic data obtained through NIST (Tsang and Hampson, 1986; Ing *et al.*, 2003). A script was set up to calculate the rate constants and was solved using ODE45 over an 11 second residence time obtained from this study.

The interval time step with this method and solver is variable and responds to the rate of change of reactants to maintain consistent accuracy using the Newton-Raphson method

with a pre-defined tolerance value. The interval size is determined as the interval where the errors in the component values between the projected next step and two steps of halved interval are below the specified tolerance value. This is derived iteratively, starting with a time step of 0.5 seconds. If the sum of the error for all reactants is below the tolerance, the larger step was used, while if the error was too large, the smaller step was selected and the process re-run until the error was within tolerances. A scalar tolerance of 10^{-3} was used, as reducing the tolerance further was found to have no effects on the process outcome, defined as the sum of the modulus of the difference between the predicted values of the small and large step sizes. Once this process is complete, a matrix of the concentrations with time of each component is output. This records radical components at significant yields. These concentrations are then used as inputs for a second pass with a plasma temperature of zero to simulate the gas bottle at the outlet quenching radical species. The same matrix of outputs was then converted into wt. % using their molecular weights.

The derived plasma initiated reactions are shown in Table 4.4, with kinetic constants derived from fitting to experimental results under N_2 environment. The reactions listed in Table 4.3 only included the initiation reactions, which are not shown as reversible as the reverse reactions are reactions between already excited species and thus are assumed to have rate constants independent of plasma power. The full range of propagation and termination reactions included in the model are shown in Figure 4.2 above.

Table 4.4: Cold plasma initiated reaction kinetics

Reactions	**Plasma kinetics (experimentally derived)**			**Thermal kinetics (NIST)**		
	A (pre-exponential constant) (s^{-1})	N (Temperature dependence)	Ea (Activation energy) (KJ/mole)	A (pre-exponential constant) (s^{-1})	N (Temperature dependence)	Ea (Activation energy) (KJ/mole)
H_2 ⟶ 2 H.	5.40E-07	0	119	6.12E-9	-0.2	426
CH_3OH ⟶ $CH_2OH.$ + H.	5.67E-05	-0.681	923	2.16E-8	0	280
CH_3OH ⟶ $CH_3.$ + OH.	7.44E-04	-0.612	2488	1.97E-7	-0.4	285
CH_3OH ⟶ $CH_3O.$ + H.	9.62E-05	0.781	2833	9.62E-6	0.76	376
CH_3OH ⟶ CHOH.. + H_2	1.67E-07	-0.681	6309	2.12E13	1.2	362
C_2H_6 ⟶ $C_2H_5.$ + H.	1.53E-05	-0.06	122	8.47E18	-2.7	432
C_2H_6 ⟶ $CH_3.$ + $CH_3.$	1.53E-05	-0.06	122	2.57E-5	-0.2	296
C_3H_8 ⟶ $C_3H_7.$ + H.	2.30E-06	0	121	1.58E16	0	408
C_4H_{10} ⟶ $C_4H_9.$ + H.	2.80E-06	0	121	1.58E16	0	410
CH_2O ⟶ CO + H_2	1.67E-04	-0.681	18.3	2.11E-7	-1.1	296
CH_4 ⟶ $CH_3.$ + H.	5.16E-07	-0.642	170	1.39E-1	-4.5	435

In comparison to thermal data shown in Table 4.3, the pre-exponential constants (A) for plasma initiated reactions were around 100 times higher than those from the thermal processes. This can be explained by the high levels of electrically charged particles such as radicals and ions in the gas and liquid phases. Many of the excited species, including radicals, are electrically charged by the electron collision, and will strongly attract other charged species of the opposite polarity. This enhances the likelihood of a collision and hence increases the rate of collisions in both phases. In theory, catalysts should also have increased rates of collisions, as catalysts would also become charged as a result of exposure to plasma and hence attract molecules from the gas phase of the opposite charge. The simulated pre-exponential constants would also increase to mirror the increased activation energies identified under cold plasma.

However, the simulated activation energies of the reaction are often significantly higher than those of the thermal decomposition reactions, which greatly reduces the overall reaction rate. This is unique to the methanol decomposition reactions and is due to the model accounting for the mass transfer between phases and radical propagation behaviours. The order of magnitude increase in the activation energy suggests that the liquid phase is very effective in preventing decomposition of liquid phase components.

Some reactions, however, have greatly decreased rate constants compared to the thermal reaction. For example, ethane dehydrogenation had a thermal pre-exponential constant of 8.47×10^{18} $cm^3 mole^{-1} s^{-1}$ compared to 1.53×10^{-5} $cm^3 mole^{-1} s^{-1}$ with cold plasma. This is partially offset by the higher activation energy (432 KJ/mol thermally vs 122KJ/mol for cold plasma) and temperature dependence (-2.7 thermally vs -0.06 for cold plasma). These differences indicate that plasma can effectively dehydrogenate hydrocarbons at relatively slow rates at all powers but that the plasma power has much less effect on the hydrogen yield than predicted by thermal kinetics. This may explain the increased abundance of hydrocarbons other than methane in this study. These were not reported in thermal decomposition studies (Van Bennekom *et al.*, 2011) and only traces were detected in previous plasma induced decomposition works (Raju *et al.*, 2013; Ge *et al.*, 2015).

Another significant difference is the decomposition of methanal, where the pre-exponential constant is increased from $2.11 \times 10^{-7} cm^3 mole^{-1} s^{-1}$ to 1.67×10^{-4} $cm^3 mole^{-1} s^{-1}$ by employing cold plasma. This difference is amplified by the activation energy, which drops sharply from 296KJ/mol to 18.3KJ/mol with cold plasma decomposition. This

reflects the extremely rapid decomposition of aldehydes in cold plasma discovered prior to this work (Koeta *et al.*, 2012).

The results from the model were compared to experimental data for validation purposes and to determine any other effects that may be occurring in the reactor. The comparison data is tabulated below in Table 4.5.

Table 4.5: Comparison of experimental data and simulation results for N_2 purged plasma.

	Experimental data			**Simulation data**		
	10W	30W	50W	10W	30W	50W
Methanol Conversion **(%)**	5.15	10.83	13.75	2.16	10.64	14.85
H_2 (wt. %)	0.45	0.67	0.81	0.41	0.51	0.53
CH_4 (wt. %)	0.41	0.80	3.94	0.14	2.09	2.99
C_2H_6(wt. %)	0.09	2.87	1.67	-	0.57	1.20
C_3H_8 (wt. %)	-	0.17	0.28	-	0.01	0.03
CO (wt. %)	2.85	2.67	2.58	1.07	2.07	1.70
CO_2 (wt. %)	0.41	1.27	0.92	0.09	1.12	1.23
CH_2O (wt. %)	-	-	-	0.04	0.19	0.25
Ethanol (wt. %)	0.45	0.75	1.80	0.19	1.15	1.28
Water (wt. %)	0.50	1.62	1.75	0.22	2.91	4.55

Comparison of model and experimental data showed strong correlation in terms of conversion and product distribution, which remained consistent regardless of plasma power and effectively followed trends in product distribution and yields. Ratios between products were also predicted effectively. However, inconsistencies exist, some of which could potentially be addressed through further modification of the model design and kinetic parameters, such as accumulation of CO_2. Others, however, may provide insight into the existence of additional interactions and reactions, requiring further study and subsequent modelling efforts.

The model correctly predicted an increased conversion with increasing plasma power. More accurate results were obtained at 30 and 50W, with up to 162% more water and methane predicted than found experimentally. CO, ethane and propane were under predicted up to 1.8wt.%, 2.3wt.% and 0.25wt.% respectively, observed at 30W. Despite the yield of CO being under predicted at all powers, the CO: CO_2 ratio is close to the experimental ratio e.g. 1.85 simulated compared to 2.10 experimentally. At 50W, CO_2 can

be decomposed into O_2 and CO (Aerts *et al.*, 2015; Zhang *et al.*, 2017), which was not included in the simulation due to its slow rate and the rapid depletion of O_2, resulting in little effect on the model outcomes from preliminary model designs.

The experimental profile of methane yields (0.41wt.%, 0.8wt.%, 3.94wt.%) cannot be accurately fitted for with kinetic values given these reaction pathways. This is because the profiles of methane and water yields (0.5wt.%, 1.62wt.%, 1.75wt.%) were inconsistent relative to each other, due to water being formed from OH radicals, which are produced from the same reaction as the CH_3 radicals which generate methane. Experimental data indicated the formation of methoxymethane from methoxy radicals and methyl radicals was the dominant mechanism for ethane formation (Pan *et al.*, 2007). This was assumed to be unaffected by plasma in the model as it is a reaction between already excited species (Thomas and Jen-Shih, 1997). At higher powers, ethane from methoxymethane reformation can decompose to methane readily ($k= 2.3x10^{-7} cm^3 mole^{-1} s^{-1}$) (NIST). The inability to achieve a close fit for methane yields may indicate that the kinetics of methoxymethane formation are increased by the presence of cold plasma, which would increase ethane and hence methane yields, particularly at high powers. This would reduce the discrepancy significantly and likely enable close kinetic fitting for methane. The yields of all longer chain hydrocarbons are lower in the model than observed experimentally (by >29%), which may also indicate that methyl and ethyl radicals are more active in cold plasma than predicted.

The water content in the model is significantly elevated at powers ≥ 30W (by 80- 162%) compared to the experimental data (Table 4.1). This may be an indication that generated ethanol decomposes to hydroxyl radicals and hydrocarbons, which has been found to be kinetically viable in previous work (Auprêtre *et al.*, 2002) ($k=6.35 \times 10^{-5} cm^3 mole^{-1} s^{-1}$).

Minor discrepancies between the model and the actual data can be explained by the assumptions that were used in producing the model, detailed in Chapter 3.5. In particular, it was assumed the gas: liquid distribution was constant. However, the temperature of the cold plasma reactor increases while in operation due to plasma heating, potentially reaching temperatures where methanol boils (68°C). It is also likely that the two phase system, with methanol in both phases due to evaporation and with turbulent liquid: gas mixing, had very different dynamics to plasma and methanol without heating (Fridman, 2008).

The electron temperature was assumed to be constant throughout the reactor, which is unlikely to be true as electron temperature is known to depend on distance from the electrodes (Shrestha, 2012), and the presence of liquid may also influence it. This could explain why the model was less accurate at low powers. At low powers, the uneven electron temperature distribution means that methanol decomposition can only occur in certain regions. At higher powers, electron temperatures are sufficient thoughout and thus the overall reaction rate would likely be unaffected by the uneven temperature distribution.

Overall, the model and actual data agreed as to conversion and yields at all powers, with some unexpected differences that suggest additional reactions that were not captured. For example, the differences between the model and experimental data suggest that decomposition of water to hydroxyl and hydrogen radicals is possible at higher powers (Burlica *et al.*, 2010). The yields of long chain hydrocarbons were also underestimated, which may be an indicator that either methyl-methyl or methyl-methoxy radical reactions are more rapid than predicted by literature (Yang, 2003). As the differences are relatively minor, this suggests that the process was well represented by the proposed reaction mechanism.

The derived kinetics were also applied to the H_2 and He runs, with corrections for the energetic state and relative abundance of H_2.

Table 4.6 Comparison of simulation results and experimental data for cold plasma decomposition of methanol in H_2 and He over a range of plasma powers (10-50W)

	H_2						**He**					
	Experimental data			Simulation data			Experimental data			Simulation data		
	10W	30W	50W	10W	30W	50W	10W	30W	50W	10W	30W	50W
Conversion (%)	3.81	13.15	25.92	6.88	13.88	16.81	5.54	11.42	18.17	7.14	14.74	17.10
H_2 (wt. %)	-	-	-	1.81	6.44	6.27	-	0.53	1.46	0.09	0.26	1.87
CH_4 (wt. %)	1.21	1.61	2.89	0.10	2.28	3.48	0.89	0.59	2.04	0.74	4.39	7.38
C_2H_6 (wt. %)	0.52	5.56	11.33	-	0.18	0.43	1.07	2.32	3.05	0.01	0.40	0.96
C_3H_8 (wt. %)	-	0.03	0.22	-	-	-	0.05	0.02	0.45	-	-	0.01
CO (wt. %)	1.23	4.87	9.69	1.07	1.63	1.46	2.24	2.36	7.90	4.75	2.70	2.76
CO_2 (wt. %)	-	-	-	-	0.10	0.14	0.38	1.59	0.96	0.02	0.19	0.28
CH_2O(wt. %)	-	-	-	0.05	0.14	0.17	-	-	-	0.25	0.25	0.35
Ethanol (wt. %)	-	-	-	0.03	0.45	0.47	-	0.54	0.14	0.28	0.77	0.93
Water (wt. %)	0.79	0.64	0.59	0.13	2.99	0.98	0.91	3.47	0.47	1.01	5.78	2.57
Propanal (wt.%)	-	-	-	-	-	-	-	-	0.96	-	-	-
Methyl methanoate (wt.%)	-	-	-	-	-	-	-	-	0.73	-	-	-

In general, the kinetics derived for the N_2 carrier gas provided a good fit for the He environment, with conversions matching up well and product yields following similar trends. However, the yields of carbon oxides under He were significantly under-predicted (2.76wt.% vs 7.9wt.% CO at 50W). This suggests an increased rate of dehydrogenation reactions under He, which would also explain the over-prediction of water (2.57wt.% vs 0.47wt.% at 50W). Predicted conversion for He was too high at 10-30W (14.7 vs 11.4%) and too low at 50W (17.1 vs 18.2%), which was the inverse of what happened for N_2. This appears to be due to an over-prediction of methane yield at high plasma powers (7.38wt.% vs 2.04wt.%), which could be because He favours dehydrogenation reactions over cracking and deoxygenation reactions, as discussed in Section 4.1.

Under a H_2 carrier gas, the conversion was well represented at lower powers (13.88 vs 13.15% at 30W) but was significantly underpredicted at 50W (16.8 vs 25.9%). This is due to very large yields of ethane recorded experimentally that are not explained by the model (11.33wt.% vs 0.43wt.%). As the N_2 model did not consider the formation of methoxymethane as a plasma induced reaction due to it being between already excited species, predicted yields of ethane will be lower than experimentally observed. This pathway is therefore a likely method for the formation of the missing ethane. Ethane formation via methoxymethane was also discussed as a potential reaction under N_2, but the discrepancy in ethane content was much less significant for N_2 than H_2. This further supports the methoxymethane pathway as the explanation, as abundant hydrogen is required to reduce methoxymethane to ethane. Methane yields were slightly over-predicted (3.48wt.% vs 2.89wt.%), suggesting that formation of methyl radicals is limited under H_2.

Predicted CO yields were much lower in the H_2 environment than in He (1.46 vs 2.76wt.% for He at 50W) which was opposite to that observed experimentally (9.69 vs 7.90wt.% for He at 50W). This could be due to the decomposition of methoxymethane to ethane and O_2 as detailed in Section 4.1 (Figure 4.2, Reaction 12).

In general, the model developed for cold plasma assisted methanol decomposition in a N_2 environment produces a good fit for the H_2 and He carrier gas environments, except for the yields of ethane and CO for H_2, and the carbon oxides yields for He. These discrepancies can be attributed to additional reactions that do not occur under N_2, such as formation of methyl methanoate, or could be due to changes in reactant concentrations due to the different carrier gas excited states. These need to be investigated further.

The model and mechanism were also applied to predict the results of other cold plasma assisted decomposition studies. Table 4.7 summarises the modelling results derived from the proposed mechanism in this study for the experimental conditions of other studies. A good agreement between modelling and experimental results was observed in gliding arc plasma decomposition in terms of conversion, with similar yields of hydrocarbons and water. However, the CO yield was underestimated by 56% whereas the CO_2 yield was over-predicted. These discrepancies may be partially due to the gliding arc plasma study utilising a co-feed of water and methanol at a 1:1 ratio while this simulation model is based on a pure methanol feedstock equal to the methanol flowrate. This would explain the higher H_2 yields, as water decomposes to hydrogen and hydroxyl radicals, where hydroxyl radicals often reform to water via attack on C-H bonds (Derakhshesh *et al.*, 2010). However, this contradicts the yields of CO, which would be further converted to CO_2 if an abundance of hydroxyl radicals were present. Of note is that the summed carbon oxide yields only differ by 1.2mol%, which indicates that the difference is that gliding arc plasma does not induce the conversion of CO to CO_2 as rapidly as DBD plasma..

For the corona discharge studies, the CO: CO_2 ratio was predicted well for the 300°C run (4:1 ratio) but not individual yields, (around 93-95% difference, shown in Table 4.7). No other gaseous products were reported for this work. The discrepancies can be explained as the work used filtered air as the carrier gas instead of N_2, therefore oxidation reactions were part of the process. A good agreement in the conversion was achieved at the lower temperature (120°C) corona discharge run. However, the yields of carbon oxides are still under-predicted by 80-85% (Table 4.7). This may indicate that temperature effects are highly significant.

Table 4.7: Predicted product distribution and conversion using the model proposed in this study for other plasma studies.

	Gliding arc plasma		**Corona discharge plasma**		**Corona discharge plasma**	
	Experiment	Simulation	Experiment	Simulation	Experiment	Simulation
Plasma power	300W	300W	62W	62W	62W	62W
Temperature (°C)	120	25	300	25	120	25
Methanol flow rate (mol/min)	0.5	0.5	0.026	0.026	0.026	0.026
Methanol Conversion (%)	75.2	68.62	52.1	16.80	15.0	16.80
H_2 (mol %)	41.6	33.34	-	3.70	-	3.70
CH_4 (mol %)	1.8	2.22	-	3.93	-	3.93
C_2H_6 (mol %)	1.7	1.17	-	0.55	-	0.55
C_3H_8 (mol %)	-	0.50	-	0.01	-	0.01
CO (mol %)	23.1	9.70	42.5	2.29	13.75	2.29
CO_2 (mol %)	0.2	12.39	9.6	0.65	3.75	0.65
CH_2O (mol %)	-	0.42	-	0.14	-	0.14
Ethanol (mol %)	-	4.95	-	0.24	-	0.24
Water (mol %)	6.9	3.93	-	5.30	-	5.30
Reference	(Zhang *et al.*, 2016)		(Hsiao *et al.*, 1995)		(Hsiao *et al.*, 1995)	

4.3 Summary

In summary, gas-liquid cold plasma initiated methanol decomposition at atmospheric pressure and temperature produced up to 14.44wt.% of hydrocarbons, comparable to thermal processes at >300°C. The carrier gas had a significant effect on the process dynamics, indicating that product distributions can be tuned effectively via choice of plasma power and carrier gas. Methanal was not detected in the cold plasma but ethanol, propanal and methyl methanoate (only in He environment) were recorded at trace levels (up to 1wt.%), which would be a topic for further investigation. The interactions between the liquid and gas phases are likely to be the cause of the differences from other studies in the gas phase, such as the CO/CO_2 ratio, in the presence of cold plasma. Gas-liquid cold plasma is unique in that plasma induced radicals diffuse into the liquid phase and liquid phase products from radical reactions are protected from plasma decomposition by the

bulk liquid, allowing them to accumulate. This may have potential for inducing thermally unfeasible reactions such as esterification or hydrogenation of CO_2.

In terms of carrier gas, H_2 promoted the formation of CO and longer chain hydrocarbons, N_2 increased ethanol and H_2 yields, while He produced more CO and unique liquid phase products such as propanal and methyl methanoate.

A complete mechanism has been developed for methanol decomposition and validated using experimental results and other data available in literature.. The simulation predicted trends and values in product composition effectively for N_2 carrier gas. The discrepancies between the modelling and experimental results appear to indicate that both water and CO_2 decompose under >30W cold plasma and the standard kinetic data for radical interactions underestimates the actual process under gas liquid cold plasma.

Chapter 5. Glycerol decomposition

In this chapter, the effects of plasma power and carrier gas i.e. H_2 and N_2 on the decomposition of glycerol were studied. The full reaction pathway of glycerol, representing poly-alcohols, under cold plasma was established. He was not chosen as a carrier gas, as discussed previously in Chapter 4, as it had little improvement in terms of conversion and product selectivity compared to N_2. This first section of this chapter covered pure glycerol decomposition via gas-liquid cold plasma. From experimental data, the mechanism was determined. The glycerol decomposition process was then simulated using numerical methods to determine rate constants and other kinetic data. Finally, decomposition of waste glycerol was performed to determine the feasibility of using gas-liquid cold plasma for valorising waste glycerol. The work demonstrated the potential advantages of direct cold plasma treatment of waste glycerol within commercial processes, as refining waste glycerol is unfeasible in small and medium biodiesel plants.

5.1 Glycerol decomposition

5.1.1 Effect of plasma power and carrier gas on process performance

Table 5.1 illustrates the results obtained from cold plasma assisted decomposition of pure glycerol over a range of plasma power of 10-50W in two different types of carrier gas (H_2 and N_2). The conversion increased with plasma power under both carrier gases, similar to the case of methanol decomposition as described in Chapter 4, though maximum glycerol conversion (53%) is noticably higher than the maximum methanol conversion (25.9%) . In a N_2 environment, the conversion of pure glycerol was found to be 4-4.5 times higher than in a H_2 environment for all tested plasma powers. A possible explanation for the lower conversion under H_2 could be because abundant hydrogen radicals terminate other radicals through rapid hydrogenation, thereby stabilising the decomposing glycerol (Kongpatpanich *et al.*, 2011; Salciccioli and Vlachos, 2012) due to its low energy excited state (3.7eV) (Baulch *et al.*, 1992; Fridman, 2008) compared to N_2 (12.97eV).

As discussed in Chapter 4, N_2 has a wide variety of high energy excited states, several of which are capable of initiating decomposition of alcohols such as methanol or glycerol. The wide range of excited states offers a wide range of available energies, permitting a greater variety of reactions (Harling *et al.*, 2005). Glycerol decomposition requires more reactions than methanol (Van Bennekom *et al.*, 2011) due to its larger size so the presence of higher energy species from N_2 could have a significant effect on conversion.

Furthermore, it was reported (Hoang *et al.*, 2008; Valliyappan *et al.*, 2008a; Hemings *et al.*, 2012; 'Waste glycerol gasified to make hydrogen,' 2016) that in the presence of either cold plasma or high temperature, H_2 was the dominant product (70-85mol% selectivity) from glycerol decomposition. The formation of hydrogen was via dehydrogenation reactions on the kinetically favoured C-H bond ($k=1.97x10^{-7}$ cm^3/molecule s^{-1}) compared to the O-H bond ($k= 7.52x10^{-14}$ cm^3/molecule s^{-1}) in the glycerol (Hemings *et al.*, 2012). Inhibition of this pathway due to the abundance of the product hydrogen and the reverse reaction being kinetically feasible ($k=5.12x10^{-9}$ cm^3/molecule s^{-1}) (Le Chateliers principle). The significant differences in conversion between the two carrier gases indicate that dehydrogenation via the decomposition of C-H or O-H bonds is the primary initiation reaction for glycerol as observed in literature (Hoang *et al.*, 2008).

Table 5.1: Product yields and properties derived from cold plasma assisted pure glycerol decomposition at a liquid to gas volume ratio of 1:40, residence time of 11 seconds without packing/catalyst (errors±5%)

Carrier gas	H_2			N_2		
Plasma power (W)	**10**	**30**	**50**	**10**	**30**	**50**
Conversion (%)	2.89	6.41	11.72	12.10	28.86	52.99
Unreacted glycerol (wt.%)	97.11	93.59	88.28	87.90	71.14	47.01
Total gas yield (wt.%)	0.1	0.7	2.4	0.4	5.1	16.3
Gaseous product yields (wt.%)						
CO_2	-	-	0.25	0.17	1.04	1.51
H_2	-	-	-	0.22	2.42	7.39
CO	-	0.44	1.64	-	1.33	6.20
CH_4	0.06	0.08	0.23	-	0.22	0.52
C_2H_4/C_2H_6	0.04	0.18	0.25	0.01	0.07	0.58
C_3H_8	-	0.01	0.03	-	0.01	0.09
Liquid product yields (wt.%)						
Methanol	0.83	0.60	-	2.10	0.79	8.93
Ethanol	-	-	-	-	-	0.03
Propanol	-	-	1.25	0.15	0.21	0.01
Propenal	-	-	0.21	-	-	-
Acetol	1.27	3.67	4.51	7.97	17.18	15.48
Water	0.60	0.78	1.17	1.13	1.77	2.26
Methyl Methanoate	-	-	-	-	-	0.84
pH	4.98	4.85	4.18	5.52	4.90	4.34

Conventional thermal decomposition of glycerol has been widely studied and shown to produce gaseous hydrocarbons (C_1-C_4), propenal and acetol depending on the choice of temperature, pressure and catalyst (Atong and Sricharoenchaikul, 2009). Partial oxidation of glycerol at 600-800°C using Ni/Al_2O_3 catalyst produced gaseous hydrocarbons as the main products with H_2 and CO as by-products (Atong and Sricharoenchaikul, 2009). In contrast, more than 90% H_2 and CO were produced in a 2:1 molar ratio in an inert environment without a catalyst at 600-800°C (Zhu *et al.*, 2009). Low temperatures (300-400°C) favoured the formation of propenal and acetol (Mohamad *et al.*, 2011) regardless of catalyst choice. 29-59% propenal and 3-5% acetol yields were obtained over 2-4 hours at 275°C using Bronsted acidic ionic liquid catalysts (Munshi *et al.*, 2010). Reactive distillation with a copper chromate catalyst (Chiu *et al.*, 2006),

achieved yields of up to 85% acetol at 240°C. In comparison to non-catalytic methods, cold plasma is effective at generating acetol, but not compared to selective catalysts such as copper chromate.

The carrier gas had significant effects on the product distribution. As shown in Table 5.1, the decomposition of glycerol in the liquid phase produced mainly acetol, e.g. 4.51wt.% in the H_2 environment and 15.48wt.% in the N_2 environment (equivalent to 29-38% selectivity to acetol). More CO was produced in the N_2 environment (6.20wt.%) than in the H_2 environment (1.64wt.%) at the same power input i.e. 50W, but the selectivity to CO (yield increases proportionally with conversion) was unchanged, indicating that hydrogenation of CO does not occur under these conditions.

The generation of both C_2H_4 and C_2H_6 can be observed via GC analysis, but poor separation between the two reveals a bifuricated GC peak, which prevents these from being quantified separately. The relative peak heights indicate the yields of C_2H_6 dominate under all conditions (60-80% C_2H_6 by peak height) but C_2H_4 is present under all conditions. In contrast, no propene was detetced, as addition of a methyl radical to ethene generates a propane radical, which is unlikely to dehydrogenate to propene under the hydrogen concentrations (>1wt.%) observed.

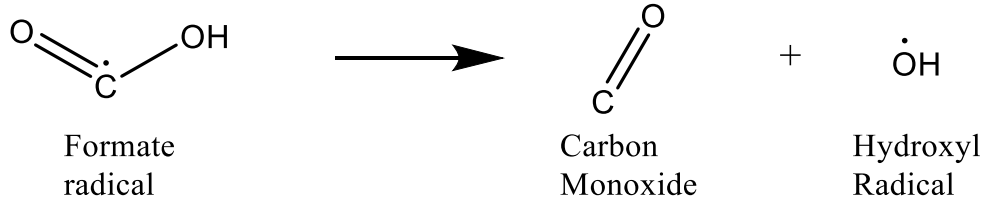

Reaction 5.1: Formate radical dehydration (Koeta *et al.*, 2012)

CO_2 was produced at all tested powers in the N_2 environment but only at 50W in the H_2 environment at low level (0.25wt.%), which indicates that H_2 inhibits the formation of CO_2, likely via dehydration of formate radicals to CO as shown in Reaction 5.1 (Majewski *et al.*, 2010), instead of dehydrogenation to CO_2. Zhu et al (Zhu *et al.*, 2009) recorded that a low level of CO_2 (1.4mol%) was obtained under all temperatures for liquid glycerol pyrolysis but higher yields of CO_2 (14.9mol%) were observed when using glycerol diluted in water (32wt.% glycerol) which would support the formation of CO_2 from CO and hydroxyl radicals without additional heating. The work of Hoang et al (Hoang *et al.*, 2008) also showed the water-gas shift reaction as the cause of CO_2 formation, which means that

CO_2 formation should be favoured by lower temperature operation and occurs in the gaseous phase generated during pyrolysis. Additionally, a low yield of water detected (<3wt.% compared to a predicted 8wt.% given the degree of glycerol dehydration) despite being a decomposition product for one of the initiation reactions, indicating its consumption via another reaction, which would likely be CO_2 formation.

For conventional decomposition of glycerol (Mohamad *et al.*, 2011), the primary pathway is via the degradation of a C-O bond to generate acetol and water (Reaction 5.2) due to C-O being the lowest energy bond (358KJ/mol). Isolation of acetol is challenging due to its rapid decomposition to propenal (acrolein) under thermal decomposition conditions (>270°C) (Reaction 6, Figure 5.1), with more favourable kinetics than acetol formation (k= $3.13x10^9$ vs $5.64x10^8$ cm^3/molecule s^{-1}) (Hemings *et al.*, 2012).

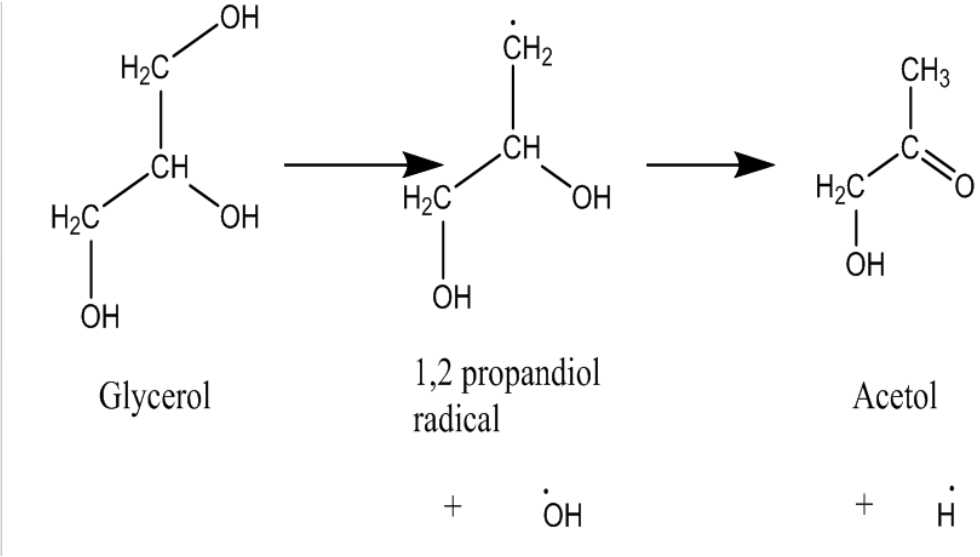

Reaction 5.2: Primary glycerol decomposition pathway

From Table 5.1, it can be seen thatacetol and water yield increased with plasma power but only a small amount of propenal (0.21wt.%) was detected at 50W in H_2 environment. The presence of high yields of C_2H_4/C_2H_6 and CO (up to 0.58wt.% and 6.20wt.% at 50W under N_2 respectively) confirms the hypothesis that propenal forms from acetol but decomposes further to CO and C_2H_4, as opposed to acetol being stable under plasma. As discussed in Chapter 4 (Section 4.1), volatile aldehydes are known to be susceptible to decomposition in cold plasma from literature, so it is likely that propenal decomposes further in the gas phase in these experiments (Koeta *et al.*, 2012). This suggests that gas-liquid cold plasma could be used for the removal of toxic propenal from waste streams at low temperatures. Propenal is abundantly produced during waste glycerol incineration

and requires high temperatures (1000-1300°C) to remove completely due to its continual formation from acetol/glycerol during combustion despite its relative instability (Floyd *et al.*, 2007). Cold plasma could be utilised to decompose the propenal to less harmful products, allowing lower temperature operation and hence reducing costs.

Propenal is unstable and thermally decomposes to C_2H_4 and CO with or without a catalyst at above 250°C (Floyd *et al.*, 2007; Kongpatpanich *et al.*, 2011; Hemings *et al.*, 2012), of which CO was observed at significant yields (6.2wt.%) in both carrier gases compared to other gaseous products. This also explains much higher yields of C_2H_4 produced than CH_4 (Kongpatpanich *et al.*, 2011; Hemings *et al.*, 2012) as propenal decomposition generates C_2H_4 directly from without requiring methyl radicals.

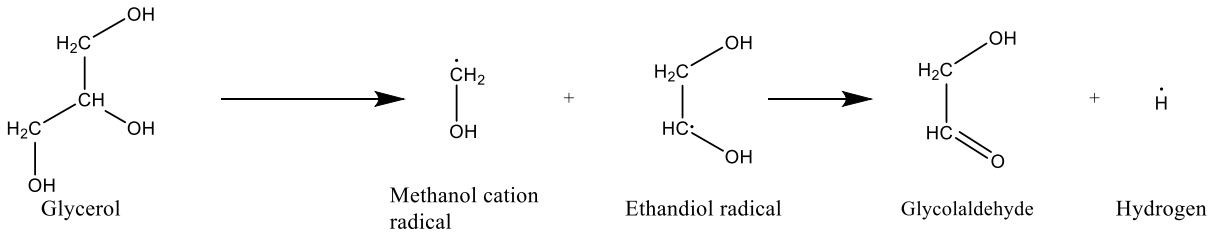

Reaction 5.3: Initial decomposition pathway from glycerol to glycolaldehyde

In parallel to decomposition to acetol via C-O (346KJ/mol) or C-H bond splitting (358KJ/mol), C-C bonds (348KJ/mol) can also be broken to generate methanol cation radicals and ethendiol radicals, shown in Reaction 5.3. The ethendiol radicals could decompose further to two methanol cation radicals but are more likely to isomerise to glycolaldehyde (Reaction 5.3) (Ye *et al.*, 2012) as the ethendiol radical is an unstable intermediate (Joe Chong and Curthoys, 1981). Glycolaldehyde is also unstable at room temperature (Salciccioli and Vlachos, 2012) and easily decomposes to CO and CH_4 (Cui and Fang, 2011). This pathway would indicate that high yields of both CH_4 and methanol would be observed. This was confirmed by experimental data shown in Table 5.1, i.e. 0.52wt.% and 8.93wt.% respectively at 50W N_2. However, the yield of methanol was much higher than that of CH_4 (300% higher except for the 50W in H_2 environment, as shown in Table 5.1). This can be explained by abundant hydroxyl radicals from glycerol and acetol decomposition reforming a significant amount of CH_4 to methanol. Methanol was then decomposed into CO through dehydrogenation as explained by the pathways detailed in Chapter 4 (Figure 4.2).

In contrast to the generation of radicals and ions, gas-liquid cold plasma can only generate free electrons in the gas phase despite the electron temperature and density being highest near the liquid surface (Zhu and Pu, 2010). These electrons cannot readily attack the liquid components as the energy is easily dissipated through intermolecular bonds but are effective in the gas phase (Burlica *et al.*, 2010). Therefore, volatile components are likely to be affected than the less volatile components. At 10W, methanol can accumulate as the temperature generated from cold plasma heating was well below its boiling point (42°C). As the plasma power increased from 10 to 30W, the reactor temperature rose to 56°C, sufficient to evaporate a slight portion of the methanol. This exposes it to excited electrons in the gas phase resulting in rapid decomposition and hence a reduction in methanol yield from 2.1wt.% to 0.79wt.% from 10W to 30W (Table 5.1). At 50W, the C-C bond decomposition becomes more favourable due to rapid dehydration /dehydrogenation and methanol can accumulate (8.93wt.%). The more rapid formation of methanol with 50W in N_2 environment (Table 5.1) was reflected by a 280% increase in the total yield of CH_4, C_2H_4 and C_3H_8, along with formation of traces of ethanol.

In summary, glycerol decomposition to acetol and water, and to ethandiol and methanol radicals, are the dominant initiation reactions via either thermal or cold plasma initiation in the absence of a catalyst. Splitting of a C-C bond (346KJ/mol) generates methanol cation and ethandiol radicals while splitting of C-O (358KJ/mol) or C-H (411KJ/mol) bonds initiates dehydration of glycerol to acetol (Hemings *et al.*, 2012). The other plausible pathways that can result from bond splitting are formation of 1,3 propandiol from C-O bond decomposition followed by hydrogenation, and formation of glyceraldehyde (2, 3-Dihydroxypropanal) via O-H (459KJ/mol) bond splitting. Splitting an O-H bond is likely to have little effect on the process both due to its high activation energy and the dominant feasible reformation products of glyceraldehyde (Wu *et al.*, 2013b) are glycolaldehyde, CO and water, which are also generated in the 2 main pathways.

These pathways explain the presence of most of the products detected with an exception of CO_2. CO_2 was noted to form under H_2 at low levels (0.25wt.%) at 50W, but was generated under the N_2 environment at all tested plasma powers. This trend was also observed for methanol (Chapter 4), which proposed a reaction between hydroxyl radicals and CO to produce formate radicals followed by reformation to CO_2 as the source of the CO_2. This reaction was also noted to occur under thermal conditions with a catalyst (Zhao

et al., 2014), suggesting decomposition of formate radicals as the source of CO_2 from glycerol. The formation of methyl methanoate (as detected under He in Chapter 4) also provides evidence of formate radicals generation, as does the significantly reduced pH of plasma treated glycerol compared to untreated (pH 7.1 untreated vs 4.2-5.5 after cold plasma). The formation of methyl methanote in N_2 for glycerol despite high energy He being required for methanol may be due to to a higher levels of formate radicals present in glycerol, which is supported by lower pH values for glycerol than methanol.

Propanol formation is not predicted by the proposed pathways. However, the intermediate between glycerol and acetol can potentially be stablised by hydrogen radicals, (Figure 5.1, Reaction 2) as discussed previously. This produces 1,3 propandiol and propanol, and ethendiol radicals from C-C bond splitting can be similarly stabilised to form ethendiol. This would produce increased yields of propanol in the presence of abundant H_2, which is observed when comparing the H_2 and N_2 carrier gases. Propandiol and ethendiol are not detectable in the liquid outputs, which is most likely due to the low prevalence of this pathway detailed in literature (max 1.25wt.%), resulting in yields below the detection limits of analytical instrument.

Comparison of the final decomposition product yields for glycerol (Section 5.1) and methanol (Section 4.1) reveals details on the hydrocarbon production pathway, which will enable future process optimisation towards specific products. The relative yields of hydrocarbons and CO for methanol decomposition are approximately 1:1 but for glycerol the ratio is approximately 1:5. This is because glycerol primarily decomposes to ketones and aldehydes via dehydration reactions after any C-H or C-O bond is broken, which do not occur for methanol. These ketones/aldehydes then decompose to release CO, resulting in an increased CO yield (Chiu *et al.*, 2006). Another factor is that the formation of hydrocarbons from glycerol requires at least two bonds to be broken (e.g. a C-O and a C-C to release CH_2 from glycerol), as opposed to one bond (C-O) for methanol (Li *et al.*, 2009).

5.1.2 Mechanism

There were three possible routes for glycerol decomposition, of which two dominant initial reactions produce either methanol cation radicals and glycolaldehyde (Reaction 5.3) or acetol and water (Reaction 5.2), which are shown above. In the final pathway,

methanol cation radicals form if a carbon-carbon bond is broken, whereas acetol forms if a C-H or O-H bond is broken. Splitting a C-C bond directly releases a methanol cation radical and leaves an unstable ethandiol radical. This ethendiol radical spontaneously reforms to glycolaldyde (Hemings *et al.*, 2012), releasing a hydrogen radical (Reaction 5.3).

The removal of a hydroxyl radical from glycerol causes the alcohol group on the adjacent carbon to react with the destabilised area, prompting refomation to acetol (Reaction 5.2). A hydrogen radical is also released, resulting in a net release of water from this reaction. The process is illustrated in Figure 5.1.

Further decomposition of acetol yields propenal (Figure 5.1, Reaction 6), methanol, CH_4, CO (Figure 5.1, Reaction 8), ethene and formate radicals (Figure 5.1, Reaction 7). The glycolaldehyde formed typically decomposes into methanol cation radicals and methanal (Figure 5.1, Reaction 11) (Cui and Fang, 2011), which are converted to methanol (Ge *et al.*, 2015) and formate radicals respectively via Reactions 14 and 12 in Figure 5.1.

Reaction pathways were established for conventional pyrolysis of glycerol (Valliyappan *et al.*, 2008a; Fernández *et al.*, 2009; Hemings *et al.*, 2012). Based on the similarities between the product distributions in literature and shown experimentally in Table 5.1, most thermally induced reactions also occur during the gas-liquid cold plasma decomposition process.

However, aldehydes were detected in the conventional thermal process up to 48% (Yamaguchi *et al.*, 2010; Kongpatpanich *et al.*, 2011; Hemings *et al.*, 2012) but were not detected under cold plasma. The absence of ketones/aldehydes is linked to the instability of aldehydes in the plasma phase as short chain aldehydes can evaporate and be rapidly decomposed by plasma to form CO and hydrogen radicals. Although aldehydes are resistant to attack by hydrogen radicals due to the lack of low energy bonds other than C-H (Troe, 2007; Koeta *et al.*, 2012), they are prone to attack by free electrons in cold plasma, leading to the removal of hydrogen atoms to form CO (Wiest, 1996; Buszek *et al.*, 2011). The formation of CO from methanol (Chapter 4) provides evidence of rapid aldehyde decomposition due to its similar structure.

However, the presence of propanol in cold plasma treated glycerol but not in conventional pyrolysis indicates that either hydroxyl radicals can attack C_3H_8 /propyl radicals in the

gas phase or hydroxyl radicals are removed from glycerol without inducing reformation of the remaining OH groups to C=O groups (Figure 5.1, Reaction 2). Hydrogen radicals cannot induce these reactions due to the very high bond energy of C=O bonds (799KJ/mol, 8.28eV), which prevents radical attacks from occurring.

The low yields of ethanol under both carrier gases suggest that ethanol formation is via removal of hydroxyl radicals from glycerol, as hydroxyl radical attacks would occur on both C_2H_4/C_2H_6 and C_3H_8, which would also generate propanol. As propanol was not detected, this indicates that hydroxyl radical attack is not the dominant mechanism. However, ethanol was not formed except at 50W plasma power in N_2 environment despite the high concentration of C_2H_4/C_2H_6 compared to C_3H_8 (0.58wt.% vs 0.09wt.%). Hydrogenation of the reaction intermediates during acetol generation from glycerol would permit removal of hydroxyl radicals without producing acetol. This would be more prevalent under H_2, which was observed in the propanol yields with and without H_2 (1.25wt.% vs 0.01wt.%).

The presence of propenal in the liquid product stream suggests that the propenal decomposition reaction acts primarily in the gas phase, supported by the fact that aldehydes are unstable in cold plasma (Koeta *et al.*, 2012). This may also be due to energetic electrons not being able to enter the liquid phase to induce decomposition of propenal in that phase, while gaseous products can be decomposed by these energetic electrons (Chiu *et al.*, 2006). The more rapid decomposition in the gas phase would enhance the rate of acetol decomposition relative to glycerol decomposition, reducing the acetol yield as plasma power increased (Hu *et al.*, 2012).

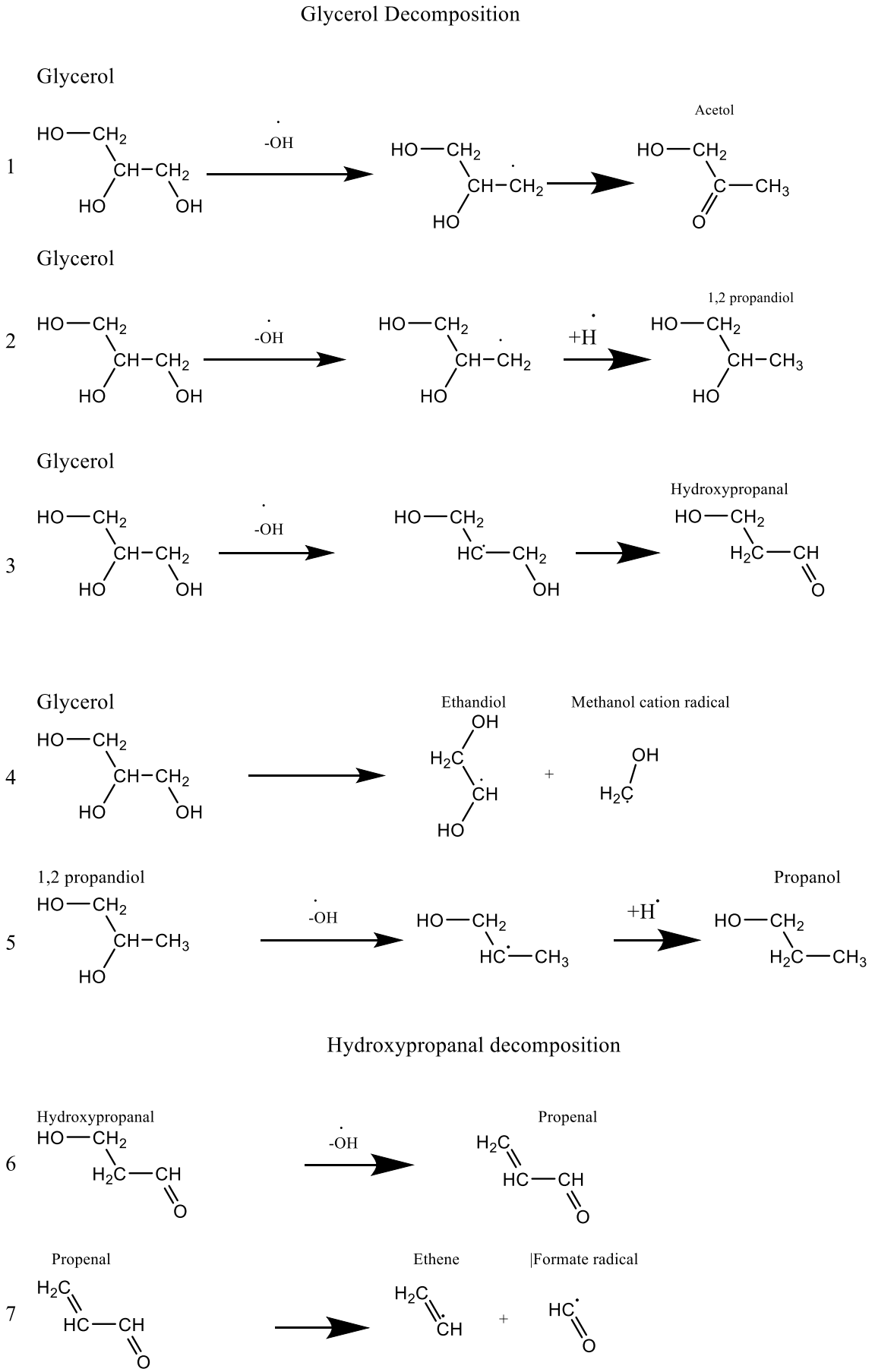

Figure 5.1: Proposed Reaction pathways for glycerol decomposition- Continued overleaf

8 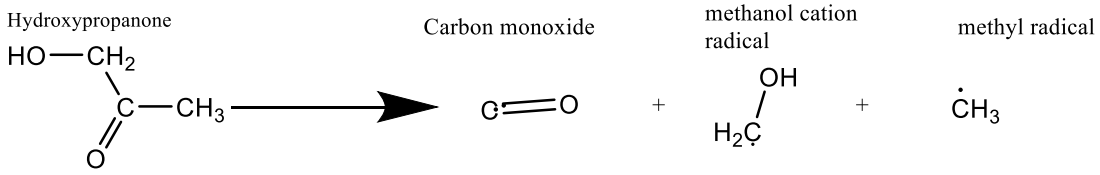

Ethandiol decomposition

9 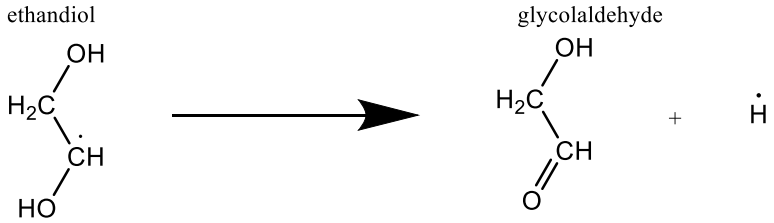

10 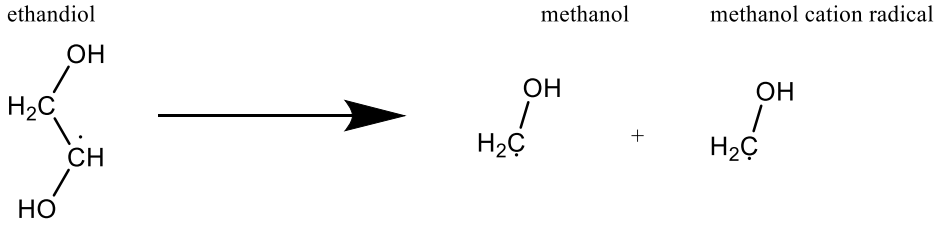

11 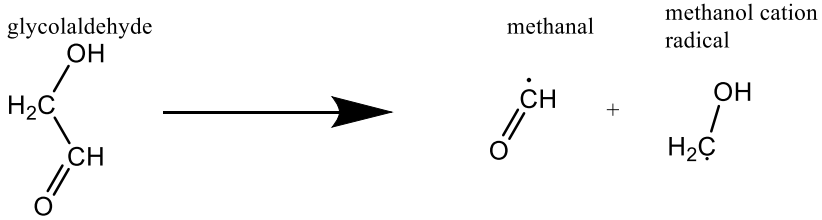

Formate radical and Carbon dioxide formation

12 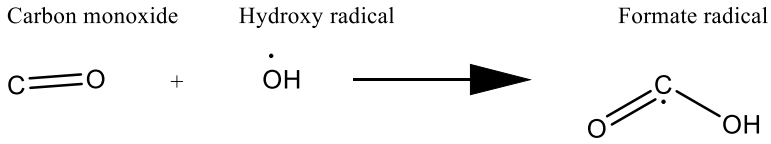

13 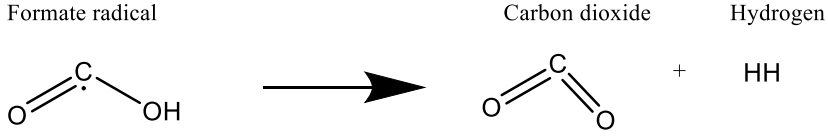

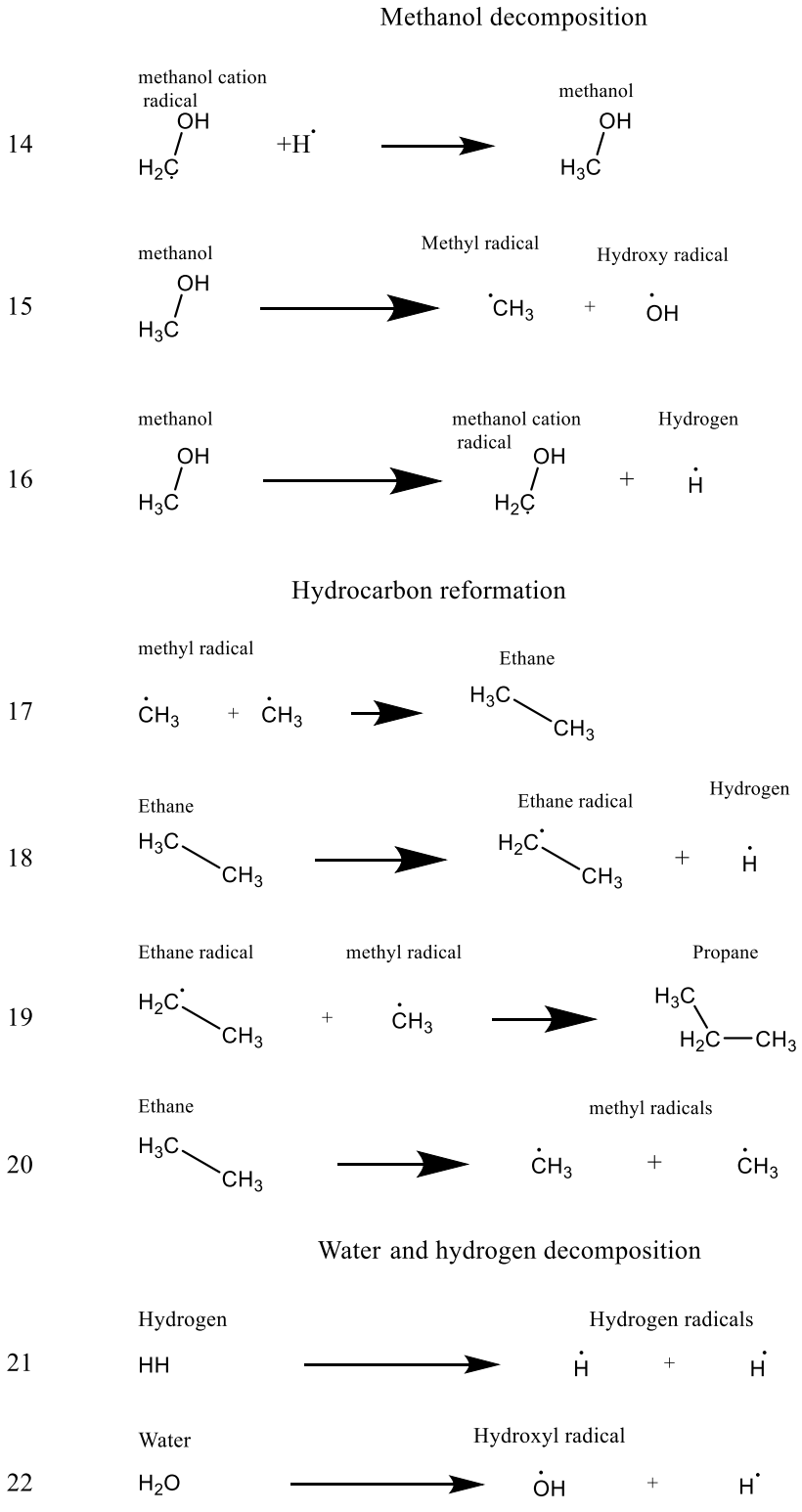

Figure 5.1: Proposed reaction pathways for glycerol decomposition

In summary, gas-liquid cold plasma decomposition of glycerol produced more hydrocarbons and alcohols and less aldehydes than conventional thermal decomposition. This is because gas-liquid cold plasma primarily converts alcohol groups to hydroxyl radicals, while thermal decomposition results in predominantly aldehyde groups and

hydrogen radicals. The dual phase allows heavier products such as methanol, ethanol, propenal and methyl methanoate, to be isolated. However, the rapid decomposition of volatile and gaseous components observed under cold plasma allows acetol production without generating significant yields of the potentially harmful by-product, propenal.

5.2 Kinetic studies of glycerol decomposition

The initial content of glycerol was defined in the simulation based on the experimental glycerol: gas flowrate ratio of 1:40 and the plasma zone volume of 7.16cm^3. The model was based on the principles discussed in Chapter 3.5.

The proposed reactions initiated by cold plasma assisted glycerol decomposition are summarised in Figure 5.2. The kinetic parameters used for these proposed plasma initiated reactions were initially derived from thermal data (Kongpatpanich *et al.*, 2011; Hemings *et al.*, 2012). Without modification, these initial unmodified values predict complete conversion to gaseous products as the electron temperature was significantly higher than the bulk temperature used in thermal kinetic studies. These kinetic parameters were then modified to predict cold plasma behaviour based on the experimental results which are shown in Table 5.2 along with initial values from literature.

In addition to plasma-induced reactions, radical propagation and termination reactions detailed in the mechanism in Figure 5.1 were modelled using kinetic data obtained through NIST. These propagation and termination reactions are not considered plasma initiated and so the model utilises thermal reaction constant data for them without modification (Tsang and Hampson, 1986; Ing *et al.*, 2003).

The simulation utilised the rate co-efficient to derive rate constants for each reaction at each time step and integrated the results using ODE45 over the 11 second residence time utilised experimentally. Once this finished, a matrix of the concentrations with time of each component was output, which still contained abundant radicals. These concentrations were used as inputs for a second iteration to simulate reactions occurring upon exiting the plasma reactor and before detection. The same matrix of outputs was then converted into wt. % as shown in Table 5.3.

For process optimisation, this model also aimed to clarify the range of radical reactions that occur via fitting simulated data to the experimental process, increasing confidence in the proposed mechanisms.

1 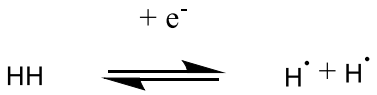

2 

3 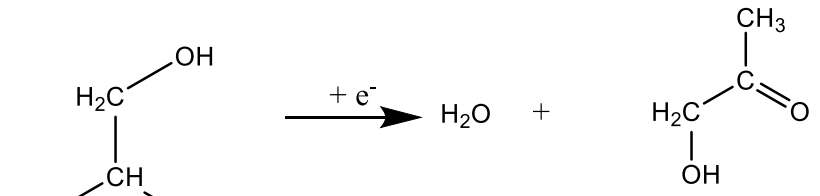

4 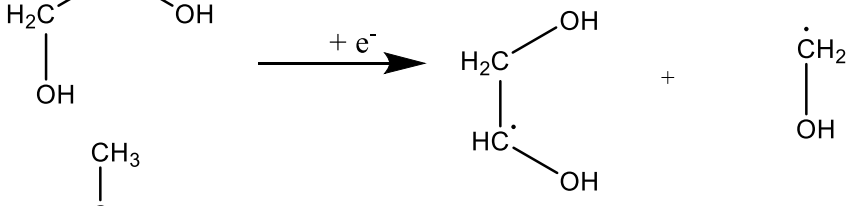

5 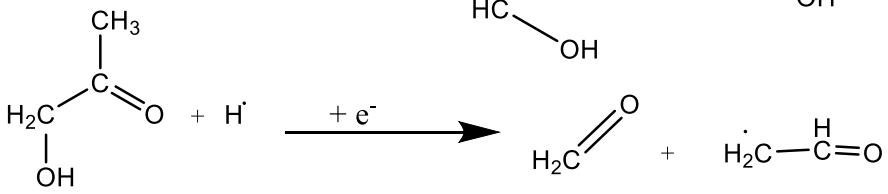

6 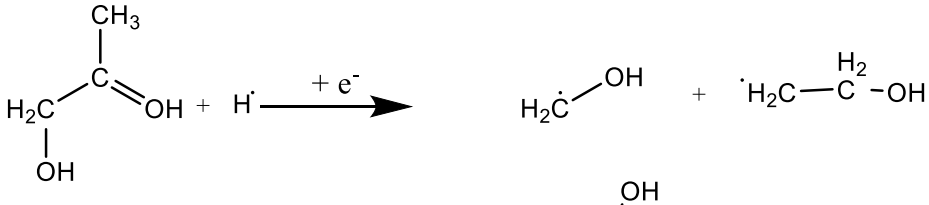

7 

8 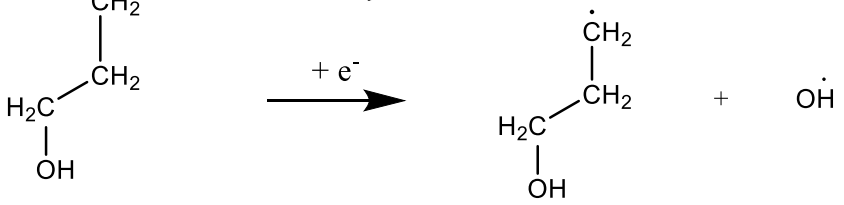

9 

10 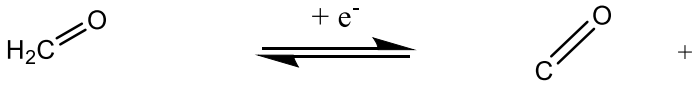

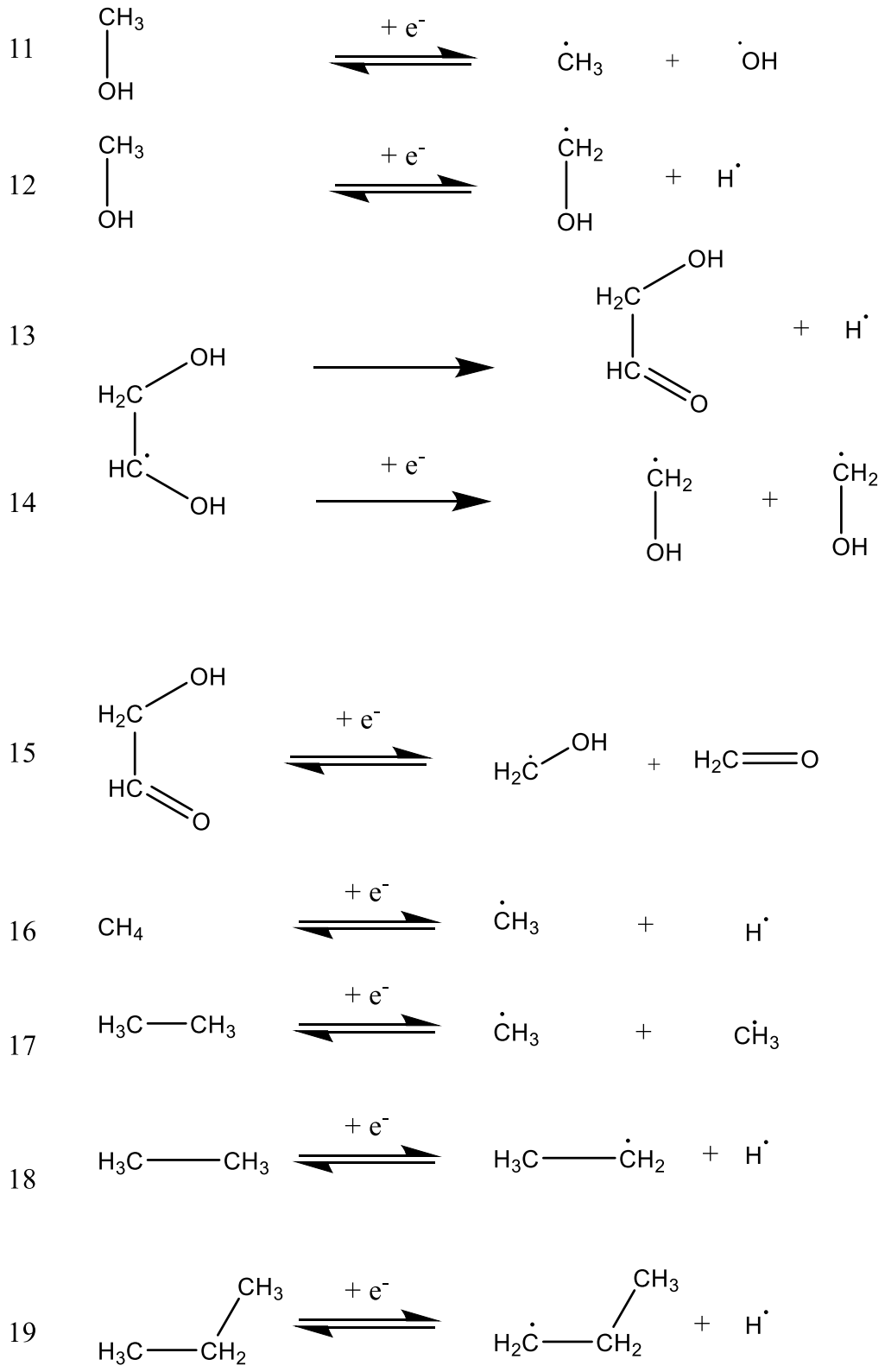

Figure 5.2: Proposed plasma induced reactions of glycerol decomposition

Combining the reactions in Figure 5.2 with the set of radical reactions determined experimentally (Figure 5.1) allows the product distribution at the outlet to be predicted. Some of the initiation reactions have pre-determined constants from previous sources, such as oxidation of methyl radicals (Pratt and Wood, 1984) and production of formate radicals (Yetter *et al.*, 1989). The remainder were either derived in Chapter 4, derived from literature data for thermal decomposition or through comparison to reactions with known parameters when no kinetic data was available. These kinetic values were used as starting values and modified to fit the data more accurately according to the procedure in Figure 3.4.

Table 5.2 Cold plasma and thermally initiated reaction kinetic data for glycerol decomposition

		Plasma kinetics (experimental)			**Thermal kinetics (Hemings *et al.*, 2012) (NIST)**		
Reaction number (Figure 5.2)	Reaction	A (pre-exponential constant)	N (Temperature dependence)	Ea. (Activation energy) (KJ/mole)	A (pre-exponential constant)	N (Temperature dependence)	Ea. (Activation energy) (KJ/mole)
1	H_2 2 H.	1.70E-03	0	99.7	6.12E-9	-0.2	426
2	H_2O H. + OH.	3.62E-01	-0.781	152.1	2.56E-12	1.9	360
3	Glycerol Acetol + H. + OH.	2.87E-02	-0.681	385.2	6.64E-11	0	65
4	Glycerol Ethendiol + CH_2OH.	5.54E-04	-0.612	416	-	-	-
5	Acetol Ethenol + CH_2O	6.53E-03	-0.08	609.3	3.32E-11	0	53
6	Acetol CH_2OH. + ethanal	4.43E-04	-0.12	425.3	1.66E-8	0	80
7	1,3propandiol Propenal + H_2O	5.94E-04	-0.612	353.7	8.3E-12	0	167
8	1,3propandiol + H. Propanol + OH	7.53E-08	0	241.3	-	-	-
9	Ethanal CO + CH_3. +H.	1.53E-01	-0.06	100.6	3.02E-10	0.9	322
10	CH_2O CO + H_2	6.67E+03	-0.081	15.0	2.11E-7	-1.1	296
11	Methanol OH. + CH_3.	7.94E-03	-0.612	150.2	1.97E-7	-0.4	285
12	Methanol CH_2OH. + H.	4.94E-03	-0.612	141.5	2.16E-8	0	280
13	Ethendiol Glycolaldehyde + H.	1.62E-03	-0.781	150.6	-	-	-
14	Ethendiol 2*CH_2OH.	1.53E-01	-0.12	925.3	1.34E-8	0.3	157
15	Glycolaldehyde CHO. + CH_2OH.	1.67E-01	-0.062	10.0	7.21E-6	0.1	166
16	CH_4 CH_3. + H.	5.16E-01	-0.642	141.3	1.39E-1	-4.5	435
17	C_2H_4 2 CH_3.	1.53E-01	-0.06	100.6	2.51E-7	1.5	282
18	C_2H_4 C_2H_5. + H.	8.53E-01	-0.06	100.6	1.41E-5	-2.7	432
19	C_3H_8 C_3H_7. + H.	7.52E-02	-0.03	141.3	2.62E-8	0	408

5.2.1 Modelling results and validation

The pre-exponential constants of cold plasma assisted decomposition could be up to 6 orders of magnitude higher than those in a thermal process. This is partially offset by the increased activation energies implemented to account for the mass transfer limitations between the gas in liquid phases and the inability of electrons to induce liquid phase reactions directly. The increased pre-exponential constants are supported by the difference in reaction time between cold plasma and thermal decomposition being 1:1000 given the same conversion. This ratio is known for glycerol initiation reactions, which have typical reaction times of 10-60 minutes when pyrolysed without a catalyst at 650-800°C (Floyd *et al.*, 2007; Valliyappan *et al.*, 2008a; Valliyappan *et al.*, 2008b). These differences between the thermal and plasma kinetic parameters imply that plasma induces many more collisions between reactant and excited species than in thermal processes. This is reasonable based on plasma theory (Fridman, 2008; Di *et al.*, 2016), as the two phase system limits the reaction to the gas-liquid interface, which has a relatively high surface area compared to the reactor volume. Additionally, up to 90% of the incoming energy is converted into heat, which was observed as an increase in temperature from 18°C to 45-70°C over 11 seconds in the plasma zone.

Table 5.3: Comparison of simulation results and actual data for glycerol decomposition in N_2 over a range of plasma powers (10-50W)

	Experimental data			**Simulation data**		
	10W	30W	50W	10W	30W	50W
Conversion (%)	11.74	25.03	43.85	10.14	21.17	43.96
H_2 (wt. %)	0.22	2.42	7.39	2.80	5.37	9.47
Acetol (wt. %)	7.97	17.18	15.48	5.98	12.17	11.68
Water (wt. %)	1.13	1.77	2.26	0.41	2.85	2.02
Methanol (wt. %)	2.10	0.79	8.93	0.88	0.34	10.04
Ethanol (wt. %)	-	-	0.03	-	-	-
CH_2O (wt. %)	-	-	-	0.02	0.02	0.07
Methyl methanoate (wt.%)	-	-	0.84	-	0.01	0.52
Propanol (wt. %)	0.15	0.21	0.01	-	-	0.01
Diols (wt. %)	-	-	-	0.06	0.08	0.20
CH_4 (wt. %)	-	0.22	0.52	-	0.15	1.79
C_2H_4 (wt. %)	0.01	0.07	0.58	-	0.01	2.24
C_3H_8 (wt. %)	-	0.01	0.09	-	-	0.01
CO_2 (wt. %)	0.17	1.04	1.51	-	-	0.24
CO (wt. %)	-	1.33	6.20	-	0.17	5.68

As shown in Table 5.3, the trends in product yields and conversion versus plasma power were similar in both modelling and experimental data. However, modelled conversions were around 15% lower than the experimental values. The yields of some products were underestimated i.e. 25-30% for acetol, 60% except at 50W for methanol, 10% for CO and 85% for CO_2. In contrast, hydrocarbons and water yields were overestimated by 40-130%.

The discrepancies between modelling and experimental data could be due to the assumption of constant electron temperature, as discussed in Section 4.2. Prior work with dielectric barrier discharge (Ráhel and Sherman, 2005; Zaima and Sasaki, 2014) has shown that the highest electron temperature was near the inner wall and lowest at the midpoint between the two walls and can vary by more than 0.6 eV (7,000°K) from the average within a 2mm discharge gap (Gangwar *et al.*, 2015), which is an indicator that the electron distribution is non-constant. If the even electron temperature assumed by the model was correct, the high electron temperature throughout would ensure even

exposure to high energy species and hence the extent of conversion would be independent of position (Ráhel and Sherman, 2005). An uneven distribution at higher powers would cause conversion to be location dependant, resulting in more fully decomposed products from high conversion areas (CO, CH_4) and lower yields of intermediates such as acetol (Thomas and Jen-Shih, 1997). However, the conversion would become less location dependant as the power increased due to a greater proportion of the reaction volume having sufficient energy to initiate reactions. The predicted conversion would hence become more accurate as the power increased as observed in Table 5.3.

The inconsistent energy density theorised experimentally would mean material near the walls is more likely to be decomposed to hydrocarbons and water, while material near the middle of the reactor would be less affected than predicted. As a result, yields of intermediates such as acetol and methanol would likely be higher in the actual system than predicted by the model. The CO deficit could be explained by the uneven electron distribution (Zaima and Sasaki, 2014) as the reactions that form CO require high energy (>400KJ/mol) and require multiple dehydrogenation reactions (Hemings *et al.*, 2012).

The absence of propanol in the modelling results (experimental values 0.01- 0.21wt.%) at lower powers can also be attributed to propanol formation requiring high levels of hydrogen radicals to hydrogenate acetol or propenal. Propanol is known to form during thermal processing (Atong and Sricharoenchaikul, 2009; Hemings *et al.*, 2012) but has not been observed to form in plasma decomposition processes except in the presence of abundant H_2, which supports this theoretical pathway (Zhu *et al.*, 2009). This is reflected in the model results as it is predicted at high powers, where hydrogen radicals are more abundant. The absence of diols (ethendiol or 1,3 propandiol) from the experimental data (Table 5.1 and Table 5.3) is only partially explained by this effect, as diols should still be recorded experimentally, just at lower levels. However, this may be due to being unable to identify them with the low yields of diols present, as discussed in Section 5.1. Diols have been encountered in thermal decomposition of glycerol (Ye *et al.*, 2012; Tamošiūnas *et al.*, 2016) but not in cold plasma (Zhu *et al.*, 2009). However, the cold plasma literature sources focus on gas phase products and do not analyse the liquid, so diols may be present below the minimum detection limits but unrecorded given the variety of diol-derived products that are present after cold plasma processing.

To address these discrepancies, a new model simulating two phase fluid flow in the reactor would be required, which would incorporate an electron temperature distribution that takes account of the varying fluid distribution. Simulating two phase flow effectively would require producing a mesh for the plasma zone, generating a fluid dynamics model and producing discrete reaction pathways for each phase. This was not feasible as part of this thesis, but would be very useful if performed as further work.

These factors can also explain the differences in conversion predicted by the model and observed experimentally. At low plasma powers, the higher electron temperature near the walls permits conversion of reactants when the overall conversion would otherwise be low (Thomas and Jen-Shih, 1997; Ráhel and Sherman, 2005; Derakhshesh *et al.*, 2010). Elsewhere, conversion is largely unaffected as the electron temperature elsewhere is too low for decomposition to occur at a noticeable rate (Zhu and Pu, 2010). Comparing the results at 10W to 30W and 50W follows this trend, as the selectivity to intermediates is reliably lower than observed in thermal processes.

As no literature data exists for glycerol decomposition under hydrogen either thermally or under cold plasma, this model was developed to reveal additional effects on the data introduced by the presence of H_2 using the experimental data obtained only within this study. The kinetic parameters derived from experiments in a N_2 environment were also used to model glycerol decomposition under H_2, with the results shown in Table 5.4 below. To account for the absence of excited nitrogenous species, a secondary set of initiation reactions were included that utilise hydrogen radicals as an initiator in addition to the originals. This was done only for the initial reactions as the observed activation energy for these reactions were the highest observed. These additional reactions are plasma propagation/ termination reactions and hence utilise thermal kinetic data directly. The differences in the electron temperature for a given plasma power between the carrier gases were accounted for by modifying the electron temperature calculation by using the physical constants (e.g. molecular mass) for the new carrier gas. Beyond these, changes to the reaction kinetics should not be required as the same species are available under both carrier gases except for excited nitrogen species, which exclusively act as a reaction initiator. Any differences between the carrier gases would hence be due to differences in the particle/electron energy distribution for the two carrier gases, which this model aims to investigate.

Table 5.4: Comparison of simulation and experimental results for decomposition of pure glycerol under H_2 environment at all powers

	Experimental data			**Simulation data**				
	10W	30W	50W	10W	20W	25W	30W	50W
Conversion (%)	2.95	5.97	9.33	2.16	5.83	10.35	21.16	43.44
Acetol (wt.%)	1.27	3.67	4.51	1.21	3.42	6.12	12.17	11.68
Water (wt.%)	0.60	0.78	1.17	0.81	2.28	3.78	2.85	2.02
Methanol (wt.%)	0.83	0.60	-	0.07	0.07	0.37	0.34	10.04
Ethanol (wt.%)	-	-	-	-	-	-	-	-
CH_2O (wt.%)	-	-	-	0.01	0.01	0.01	0.02	0.07
Propanol (wt.%)	0.15	0.21	1.25	-	-	-	-	0.01
Diols (wt.%)	-	-	-	0.05	0.05	0.05	0.08	0.20
CH_4 (wt.%)	0.06	0.08	0.23	-	-	0.01	0.15	1.79
C_2H_4 (wt.%)	0.04	0.18	0.25	-	-	-	0.01	2.24
C_3H_8 (wt.%)	-	0.01	0.03	-	-	-	-	0.01
C_4H_{10} (wt.%)	-	-	-	-	-	-	-	-
CO_2 (wt.%)	-	-	0.25	-	-	-	-	0.24
CO (wt.%)	-	0.44	1.64	-	-	0.01	0.17	5.68

The results in Table 5.4 showed significant differences between modelling and experimental data, except at 10W where the predicted conversion and yield of acetol agreed well with experimental data (conversion: 2.16wt.% vs 2.96wt.%) (yield: 1.21wt.% vs 1.27wt.%). The predicted conversion was around 300% higher at 30 and 50W with inconsistent selectivity of products. This could be due to differences in reaction kinetics between N_2 and H_2. However, there were many similarities in trends between model and experimental data. Acetol was the dominant product and carbon oxide yields were well represented, though formation of methanol was underestimated at lower powers (0.83wt.% vs 0.07wt.% at 10W). The model predicted hydrocarbon yields relatively well, except at 50W (e.g. 0.23wt.% vs 1.79wt.% CH_4 at 50W). Propanol however, was not predicted by the model except as traces at 50W, whereas it was present at moderate yields experimentally.

Modification of the plasma power profile provides a significant improvement in the fit between model and experimental data. This can be observed in Table 5.4, showing that the model data for a plasma power of 20W produced a product distribution and conversion that matched well with the experimental data at 30W. Similarly, a simulated run for a plasma power of 25W matched well with the experimental data at 50W.

As the model converts plasma power to electron temperature, this apparent reduction in effective plasma power suggests that the presence of H_2 is lowering the mean electron temperature in the reactor relative to the equivalent N_2 experiment. This is likely to be related to the energetic states of H_2 and N_2. The ionised state of H_2 is at 13.6eV, so electrons cannot generate hydrogen radicals with energies above that, limiting the effectiveness of radical induced decomposition (Crance, 1988; Das and Bhattacharyya, 1992). Electrons can exist above the 13.6eV threshold, but are generally incapable of decomposing liquid phase components due to dissipation of the energy via intermolecular bonds. N_2 has much higher energetic states (>12.96eV), so the range of excited states does not limit radical induced decomposition for N_2. This would not be significant for methanol. However, glycerol cannot evaporate (boiling point: 285°C) so is not affected by electrons directly. This explains the reduced conversions under H_2 compared to N_2 observed experimentally and also the over-prediction by the kinetic model as these effects were not included within the model. The 20W and 25W model data significantly underestimated the experimental gas phase yields at 30W and 50W for the same reason (e.g. 0.01 vs 0.23wt.% CH_4), as decomposition of the volatile products to gases can be initiated by electrons (Du *et al.*, 2007). Hence, these reactions would be underestimated by the model as the maximum energetic state of electrons was not constrained.

In summary, the cold plasma assisted decomposition of glycerol under N_2 can be accurately simulated with the kinetics derived, validating the model under the range of conditions studied. The model provided a good fit for both conversion and most components, and accurately described the trend in product yields compared to experimental data. There were some significant discrepancies between predicted and experimental data, primarily in CO_2 yield (Table 5.3). These appear to indicate that reactions that are not initiated by plasma may still be affected by it, possibly through electromagnetic radiation or free electrons, though this has not been studied to date. Any

further discrepancies can be attributed to gas-liquid plasma effects or mass transfer limitations that would require a sophisticated model beyond the scope of this work.

The kinetic constants should not be affected by the choice of carrier gas, as N_2 does not participate in the reaction other than as a reaction initiator, although the relative reaction rates will change due to differences in the electron energy distribution and the relative concentrations of reactants and intermediates. Despite this, the model does not represent the H_2 data effectively at higher powers (Table 5.4), causing significant underprediction. It was, however, found that setting the plasma power within the model to a lower value (i.e. 25W and 20W instead of 50W and 30W respectively) provided a much better fit. This is likely to be due to the H_2 limiting the maximum energy of a given radical/ion given its energetic states, which would distort the Paschen curve and reduce the proportion of excited species capable of inducing a reaction.

5.3 Waste glycerol

Waste glycerol, a by-product of alkaline catalysed biodiesel production, was decomposed under cold plasma with the aim of testing the plasma reactor's resistance to fouling, the obtainable product selectivity and conversions. Later stages of experimentation utilised packing materials ($BaTiO_3$ or Ni/Al_2O_3) to focus plasma or act as a catalyst respectively, and were also tested for fouling resistance.

5.3.1 Effect of operating conditions on waste glycerol conversion in the presence of cold plasma

Table 5.5 shows that increasing plasma power increased the conversion of waste glycerol. This is due to high energy level electrons contributing to the collisions with gas molecules, creating different energy level excited species (Park *et al.*, 2017). However, the degree of conversion and product yields strongly depends on the carrier gas. The degree of decomposition was in the order: He> $H_2 \sim N_2$ for FFA but N_2>>He>H_2 for glycerol. Therefore, if acetol is the desired product, the process should be operated in N_2 environment whereas H_2 and He are the preferred choice of carrier gas if hydrocarbon gases are desired.

Purification of liquid products such as acetol and other products (formate radicals and propenal) from treated feedstock would be straightforward due to the large differences in boiling points of the compounds (Mohamad *et al.*, 2011). Other methods such as solvent extraction (Li *et al.*, 2011d) and membranes (Wang *et al.*, 2015) can be also applied.

Table 5.5 shows that up to 91 % waste glycerol was converted in N_2 plasma at 50 W and the yield of acetol was high at all tested powers. The glycerol content in waste glycerol was mainly converted into acetol at 50W in N_2 plasma, which was also observed for pure glycerol. The 22 % reduction in acetol yield observed when increasing power from 10W to 30W could be due to the instability of this compound (Chiu *et al.*, 2006), which decomposed further to form formate radicals (5.67wt.% at 30W), CH_4 and CO. At 50W, no formic acid was observed but a significant amount of CO_2 was formed. This can be explained due to formic acid decomposing further to CO_2 at higher powers, as observed in Chapters 4 and 5. It can be also concluded that the rate of acetol formation is faster than its decomposition at high powers. This is in contrast to the results of Section 5.1, where acetol yields equilibrate at high powers. The difference can be attributed to the other compounds in waste glycerol that consume energy when they decompose, which would reduce the energy available for glycerol conversion. The use of waste glycerol is known to reduce glycerol conversion for thermal processes (Valliyappan *et al.*, 2008b), which supports this argument. It was also observed that in the N_2 environment, H_2 production increased with increasing power. This could be explained by the coupling effect of small hydrocarbons i.e. C_1-C_2 into C_3-C_4.

Significant amounts of CO and hydrocarbons (mainly C_2) were formed in He plasma (Table 5.5). Acetol yield decreased with plasma power from 24.63wt.% at 10W to 6.3wt.% at 50W. The lower yield of acetol in He than that in the N_2 environment could be because the high energy level of excited He cleaves strong chemical bonds. Acetol decomposition generates CO, resulting in at least 145 % more CO produced than the other carrier gases under any conditions. However, a low conversion of glycerol molecules was observed because only a small fraction of excited He is formed due to the distribution of electron energy (Zhang *et al.*, 2017).

In contrast, in a H_2 environment, the conversion was mainly from the decomposition of FFA in raw waste glycerol to form mainly hydrocarbons and oxygenated compounds of

which more than 60 % of the gaseous products were C_1-C_2. This can be explained by the low energy level of excited H_2 and abundant hydrogen radicals in the system. A high yield of formic acid obtained at 50 W (21wt.%) could be the result of stabilising COOH radicals derived from FFA decomposition, and is supported by the absence of formic acid detected for pure glycerol (Table 5.1) under the same conditions. No CO_2 and only a small amount of CO (4.7wt.%) was observed at 50W due to limited decomposition of acetol in a hydrogenating environment (Li *et al.*, 2009; Tamošiūnas *et al.*, 2016).

Table 5.5: Yields and product distribution obtained from liquid waste glycerol decomposition in the presence of cold plasma at atmospheric temperature and pressure without catalysts under different carrier gases with a residence time of 11 seconds

Power, W	**10**			**20**	**30**			**50**		
Carrier gas	H_2	N_2	He	N_2	H_2	N_2	He	H_2	N_2	He
Conversion, %	28.91 ±2.3	65.91 ±4.6	54.62 ±3.2	65.12 ±4.5	29.77 ±2.7	67.91 ±4.4	50.37 ±4.1	35.04 ±3.1	91.11 ±4.4	52.74 ±4.7
Total gas yield, wt.%	22.9 ±1.0	21.1 ±0.81	30.0 ±0.97	24.4 ±0.93	26.3 ±1.31	25.5 ±0.91	38.2 ±1.71	12.8 ±0.62	38.2 ±1.01	46.7 ±2.29
CO_2	-	-	-	1.87	-	3.46	-	-	10.79	-
H_2	-	0.91	-	0.96	-	1.01	-	-	2.72	0.46
CH_4	9.33	7.14	1.60	5.19	8.17	3.25	2.75	1.63	4.44	1.37
CO	-	2.14	15.01	6.81	-	8.56	17.32	4.70	9.90	23.51
C_2H_4	13.57	10.91	12.54	9.37	7.32	7.82	16.50	2.80	6.36	19.28
C_3H_8	-	-	0.52	0.21	5.73	0.88	1.17	1.86	2.40	1.25
C_4H_{10}	-	-	0.33	0.03	5.05	0.56	0.46	1.84	1.58	0.83
Liquid products yield, wt.%	6.01 ±1.39	43.91 ±3.84	24.63 ±2.19	42.38 ±3.52	3.5 ±1.46	40.59 ±3.61	12.16 ±2.44	22.21 ±2.55	52.2 ±3.45	6.3 ±2.42
Formic acid	-	-	-	1.17	3.13	5.67	-	21.48	-	-
Propenal	0.59	-	-	-	-	-	-	0.73	-	-
Acetol	5.42	44.91	24.63	41.21	0.37	34.92	12.16	-	52.20	6.30
Unreacted feedstock, wt.%										
Glycerol	62.01	14.00	42.82	22.86	62.70	23.19	48.68	59.70	2.00	46.80
FFA	7.59	7.54	1.18	6.89	5.71	5.46	0.05	4.96	3.81	0.02
Glycerides	1.49	3.55	1.39	3.43	1.82	3.44	0.90	0.29	3.08	0.44

FTIR analysis (Figure 5.3) shows that OH groups in the liquid phase were mostly converted to ketones instead of to water as reflected by the trend of water content presented in Figure 5.4 below. This can be seen from the significant changes in the O-H, C-H and C=O peaks at 3300cm^{-1}, 2900 cm^{-1} and 1700 cm^{-1} respectively. A slight increase in the C-H peak (Figure 5.3(a)) could be a result of hydrogenation. The hydrogenation of glycerol would require the replacement of a hydroxyl radical with hydrogen or hydrogenation of C=C bonds formed from removal of alcohol groups to other oxygenated groups. All the peaks in the range 700-1500 cm^{-1} decreased after plasma treatment, which is an indicator of shorter chain hydrocarbons in the products. This is supported by the formation of hydrocarbons in the gas phase. The same behaviour was observed in N_2 and He plasma as shown in Figures 5.3 (b & c) respectively.

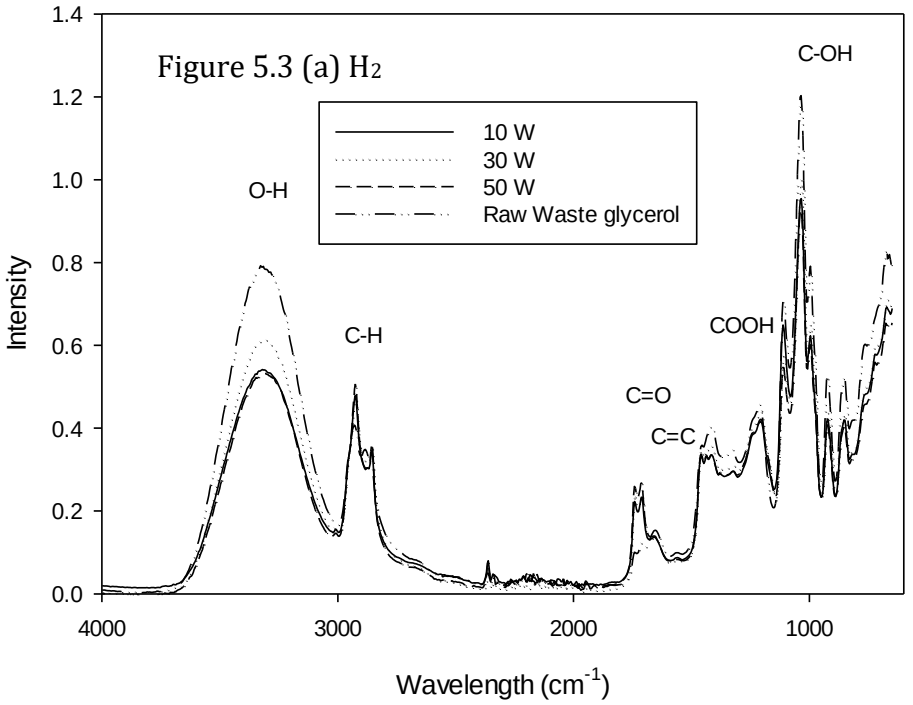

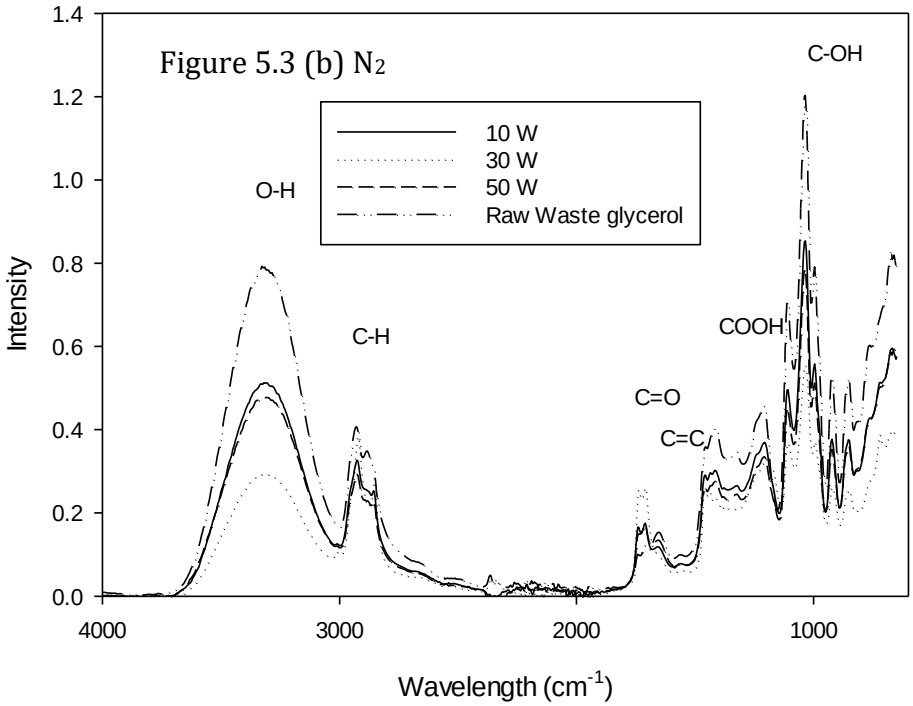

Figure 5.3: FTIR spectra of the liquid phase before (raw waste glycerol) and after (a) H_2 (b) N_2 carrier gas cold plasma - continued overleaf

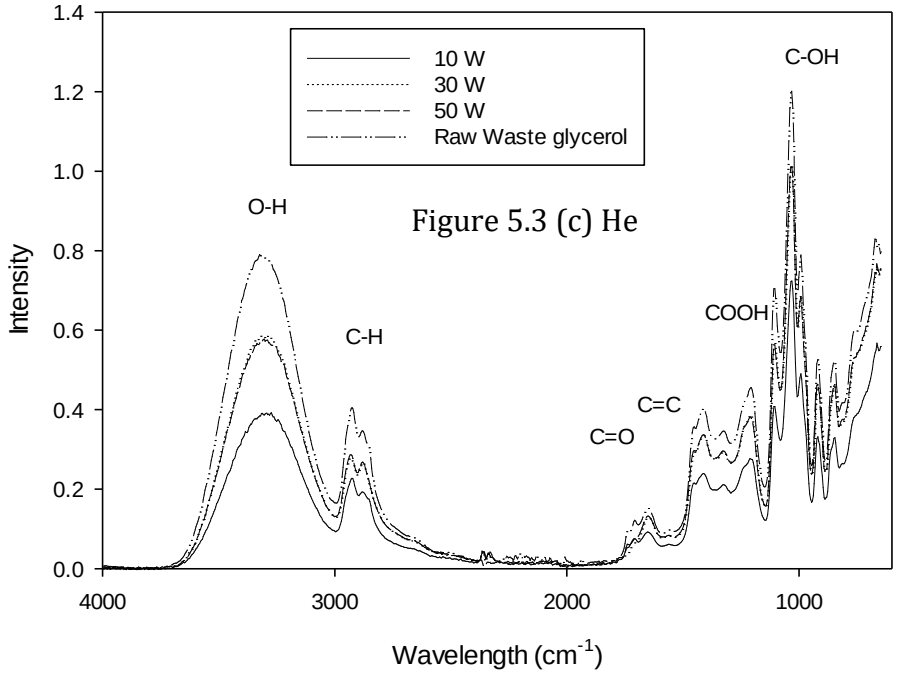

Figure 5.3: FTIR spectra of the liquid phase before (raw waste glycerol) and after (a) H_2 (b) N_2 and (c) He carrier gas cold plasma

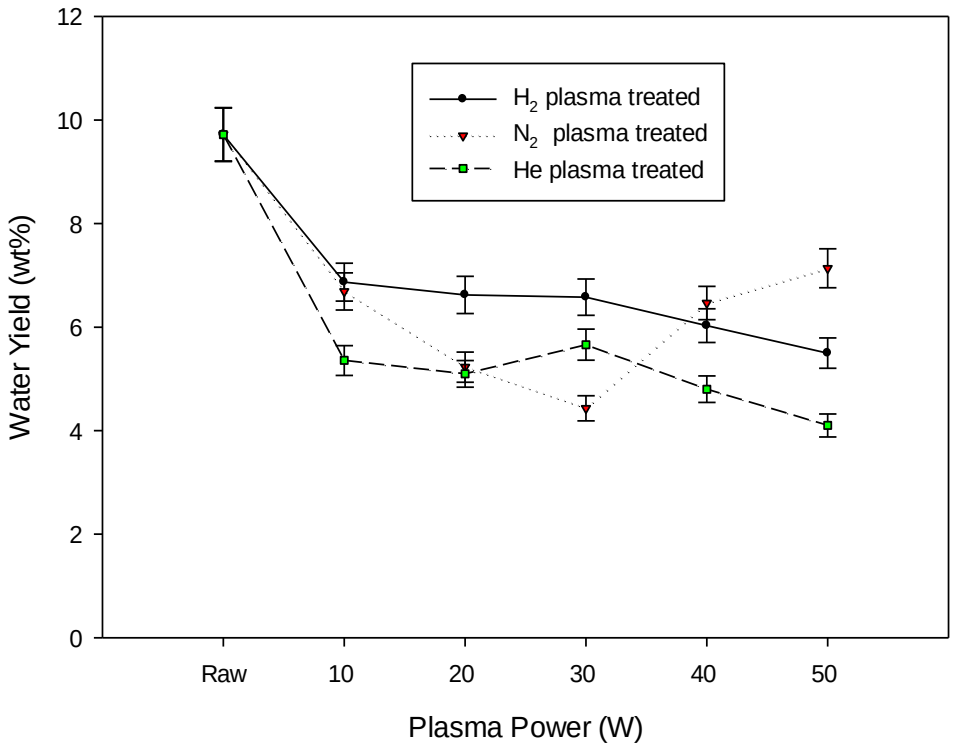

Figure 5.4: Water content of waste glycerol feedstock and liquid products obtained at various treatment conditions without catalysts at atmospheric temperature and pressure with a 16 second residence time

To date, direct conversion of waste glycerol to high value added liquid products has not been reported. However, conversion of waste glycerol into gases at high temperatures (650-800^{o}C) has been studied (Valliyappan *et al.*, 2008a; Dianningrum *et al.*, 2014). Dehydration of pure glycerol under high temperature water and CO_2 via catalytic reactive distillation was reported (Chiu *et al.*, 2006; Yamaguchi *et al.*, 2008), with the yield of acetol varying from 26-60wt.% depending on catalysts over >1 hour reaction time. By using cold plasma in this study, without a catalyst and at ambient conditions, 52wt.% acetol from waste glycerol was obtained at around 16 second residence time alongside 14.78wt.% hydrocarbon gas (C_1-C_4), 2.72wt.% H_2 and 9.90wt.% CO. The selectivities to acetol, CO and propenal are within the error range of the results obtained for glycerol, but the conversions obtained for waste glycerol were greatly increased relative to pure glycerol (92.1wt.% vs. 52.99wt.%). This has not been observed for other processes (Dianningrum *et al.*, 2014), and may be linked to the gas-liquid cold plasma mechanics. Cold plasma is established to be incapable of exciting reactions in the liquid except at the phase boundaries with excited electrons (Di *et al.*, 2016), but radicals are capable of diffusing into the bulk and inducing reactions there (Burlica *et al.*, 2010). Waste glycerol contains more volatiles than pure glycerol such as methanol, water and formic acid (Table 3.2), which can be decomposed to radicals more easily than glycerol, increasing the rate of liquid bulk reactions and hence conversion.

Based on the trend of acetol and gaseous (hydrocarbons and CO) yields with cold plasma power, it can be concluded that the acetol formation pathway in cold plasma is similar to that observed in thermal processing, where glycerol dehydrates at the secondary OH to form acetol. Propenal is the product of the dehydration of the primary OH group (Kongpatpanich *et al.*, 2011). Propenal could decompose to ethene and formate radicals (Munshi *et al.*, 2010; Hemings *et al.*, 2012), of which the latter can dehydrogenate further to CO (Troe, 2007; Van Bennekom *et al.*, 2011). In this study, propenal was not detected except in the presence of H_2, which is due to the instability of aldehydes in cold plasma (Koeta *et al.*, 2012). It was also noted that the water content decreased in the presence of plasma, which suggests that OH radicals are formed from the water and maintain an equilibrium.

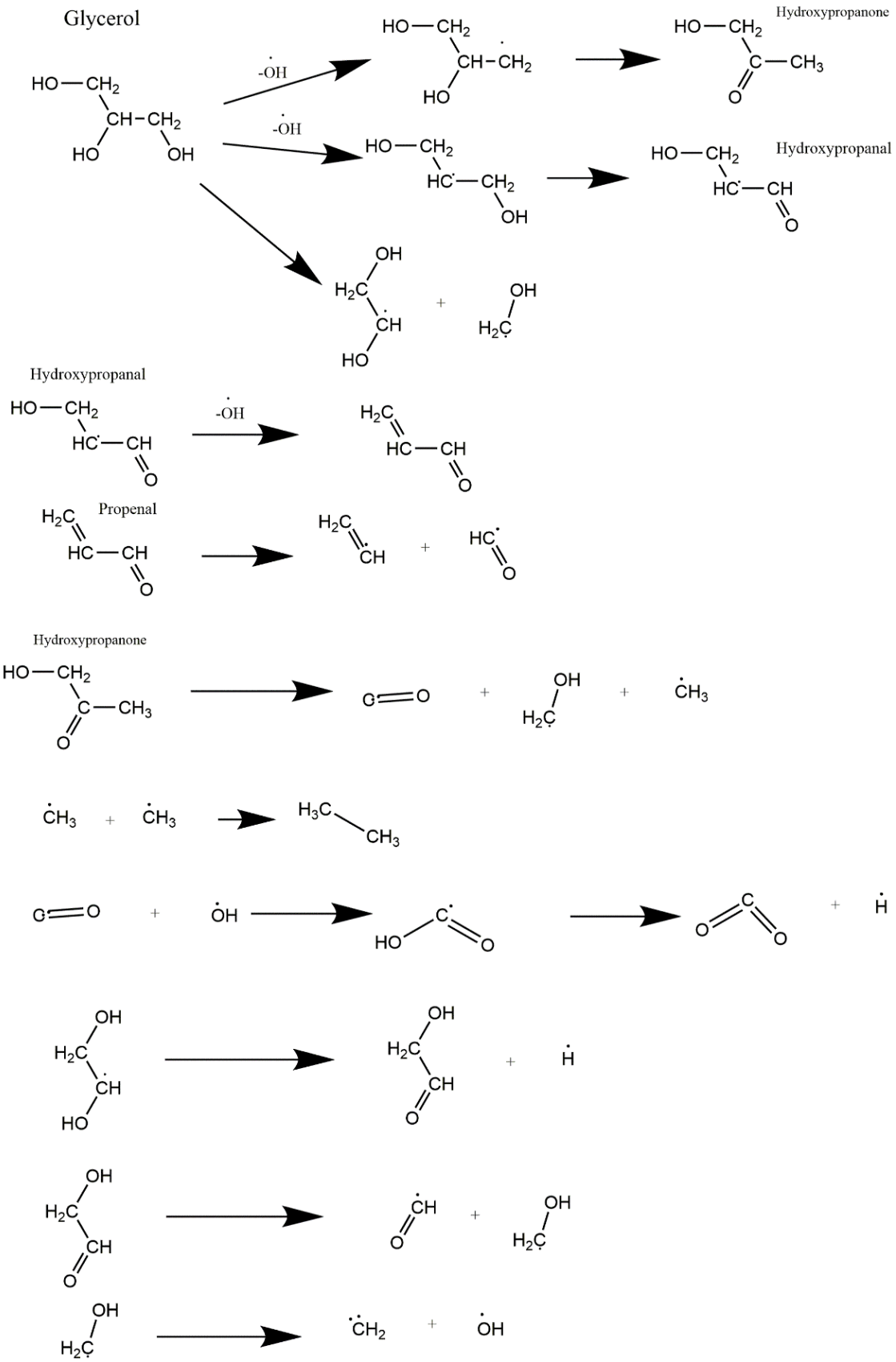
Glycerol
-OH
-OH
Hydroxypropanone
Hydroxypropanal
Hydroxypropanal
-OH
Propenal
Hydroxypropanone

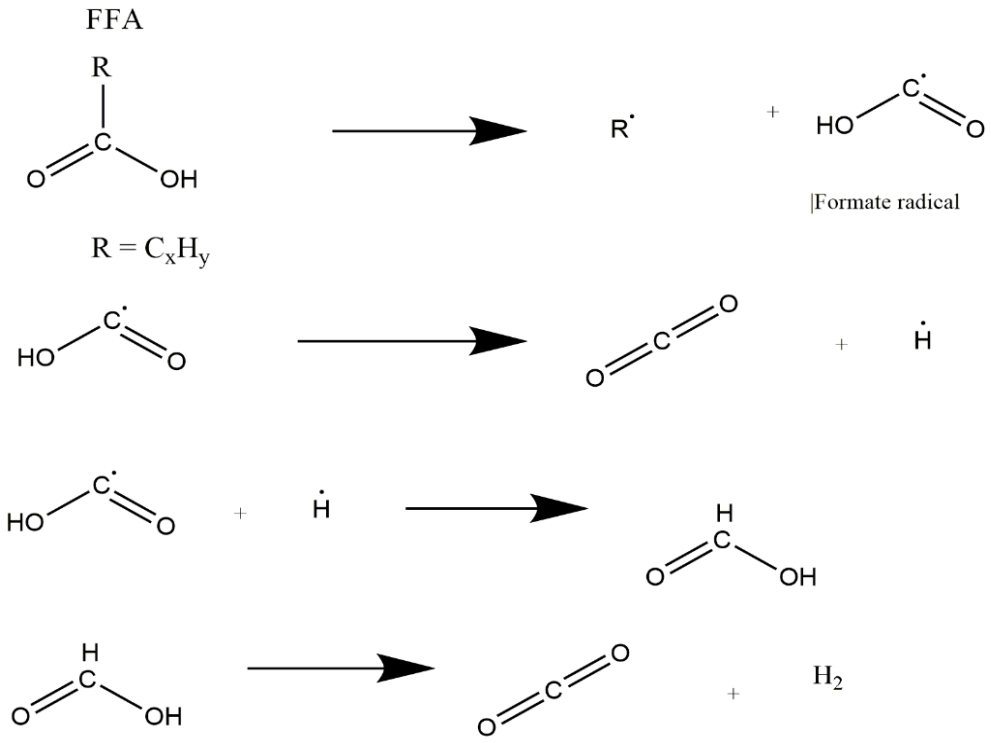

Figure 5.5: Proposed mechanism of cold plasma assisted waste glycerol decomposition

Formic acid and hydrocarbons were the products of FFA decomposition (Li *et al.*, 2011a). The formic acid is likely then dehydrogenated to CO_2, particularly in the absence of hydrogen radicals. However, from the experimental data, no correlation between FFA content and CO_2 formation was observed which suggests that CO_2 formation in N_2 is dominated by another reaction. The OH radicals formed would react with CO, and in turn dehydrogenate to CO_2 (Li *et al.*, 2007a; Feng *et al.*, 2009; Li *et al.*, 2011a). This only occurs in N_2, which suggests that the energy required for this pathway is closest to the energy of nitrogen radicals. Formic acid is generated under certain conditions at yields of up to 21wt.%. The proposed mechanism for cold plasma assisted glycerol decomposition is shown in Figure 5.5 above.

5.3.2 Effect of packing material and catalyst in the presence of cold plasma

Packing materials (e.g. $BaTiO_3$) had a slight effect on the conversion but enhanced the decomposition of acetol into gaseous products such as hydrocarbons and CO (Table 5.6). However, the degree of decomposition was lower for Al_2O_3 than $BaTiO_3$. This is because the packing materials and their properties alter the electric field, consequently electron energy by varying the discharge gap (*D)* and/or the gas density *n* (proportional to gas pressure) (Eliasson and Kogelschatz, 1991; Aerts *et al.*, 2015) . When introducing packing

beads, the discharge gap in the DBD reactor is the gap between the beads, which is much smaller than the gap without packing materials (1.5 mm), thereby enhancing local electric fields. This occurs due to refraction of the electric field as shown in Figure 5.6, making the local electric field non-uniform and stronger than the external sources. Furthermore, the strength of the electric field near the contact points between the beads can be significantly higher than that in the void by a factor of 10–250 depending on the shape, porosity, and permittivity of the beads (Fridman, 2008). An increase in dielectric constant/permittivity of materials can result in a further increase in electric field, particularly near the contacting points (Aerts *et al.*, 2015).

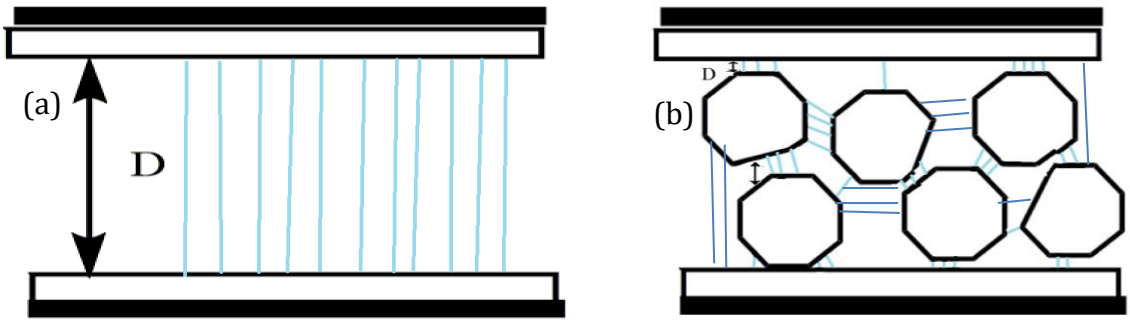

Figure 5.6: Schematic discharge gap (D) and discharge line (a) without packing and (b) with packing material

When the catalyst Ni/Al_2O_3 was embedded in the plasma zone, up to 99wt.% waste glycerol was converted into gaseous products. Ni/Al_2O_3 is a common hydrodeoxygenation catalyst (Bartholomew and Farrauto, 1976) and therefore was used to examine the ability of integrated H_2 production from plasma and deoxygenation of the liquid at near ambient conditions. When a catalyst is introduced, chemical reactions in the plasma occur as both gas phase reactions and as heterogeneous reactions on the catalyst surface (Zhang *et al.*, 2017). Therefore, a catalyst may significantly influence the plasma chemistry. The interactions between DBD plasma and catalysts are complex as the catalyst with its dielectric properties can modify the electric field and the electric field may affect catalyst effectiveness, i.e. altering the surface properties of the catalyst to allow operation at much lower temperatures and more effectively. These plasma-catalyst interactions have been studied for CO_2 decomposition (Kraus *et al.*, 2001); (Zhang *et al.*, 2017). The conversion was slightly reduced when increasing power to 50W due to the observed formation of plasma arcs.

Table 5.6: Effect of packing materials and catalysts on conversion and product distribution under a N_2 environment at 7 seconds residence time

Packing material	No packing	$BaTiO_3$			Ni/Al_2O_3			Al_2O_3		
Plasma power, W	50	10	30	50	10	30	50	10	30	50
Conversion, %	56.98 ±2.03	26.85 ± 4.7	45.29 ±5.9	60.97 ±6.2	44.82 ±4.3	99.13 ±0.5	83.96 ±4.1	7.99 ±2.8	21.43 ±4.5	40.86 ±4.7
Total gas yield, wt.%	27.6 ±0.97	18.92 ±1.82	44.79 ±4.71	60.71 ±5.50	38.55 ±2.03	99.13 ±0.42	83.94 ±4.05	4.26 ±0.82	14.91 ±1.72	34.12 ±2.16
CO_2	8.96	6.49	8.23	13.80	23.81	44.98	11.11	-	4.05	9.99
H_2	3.35	0.24	1.50	2.45	1.22	7.02	4.94	0.06	0.41	1.31
CH_4	3.66	-	0.44	0.87	0.38	3.46	2.77	0.99	1.18	2.27
CO	7.63	0.96	7.45	12.21	2.99	34.81	53.50	0.87	7.74	15.89
C_2	2.46	4.43	11.44	14.72	8.07	5.36	6.31	1.50	1.00	3.83
C_3	0.93	2.93	4.17	6.74	2.08	1.88	2.39	0.39	0.37	0.52
C_4	0.61	3.87	6.03	7.59	-	1.61	2.30	0.45	0.17	0.31
C_5	-	-	5.52	2.32	-	-	0.61	-	-	-
Liquid products, wt.%	29.29 ±1.67	7.55 ±2.88	0.50 ±1.19	0.26 ±0.70	7.08 ±2.28	0.20 ±0.08	0.02 ±0.05	3.73 ±1.96	6.52 ±2.81	6.74 ±2.53
Propenal	-	0.23	0.05	0.04	0.81	0.01	0.02	0.02	0.05	0.13
Acetol	29.29	7.32	0.45	0.22	6.27	0.19	-	3.71	6.47	6.61
Unreacted feedstock, wt.%										
Glycerol	34.52	64.06	47.60	35.19	52.81	0.81	15.24	58.26	46.22	31.47
Fatty acids	5.17	8.21	6.37	3.47	2.01	0.04	0.60	31.54	30.34	25.89
Glycerides	3.42	0.88	0.75	0.37	0.17	0.01	0.08	2.21	2.01	1.78

Figure 5.7 shows that the water content in the liquid phase was around 50 % lower than that in the feedstock and remained almost constant at 4wt.% or 6wt.% with increasing power in the case of $BaTiO_3$ and Al_2O_3. This is because the decomposition of H_2O into OH radicals and the generation of water via dehydration pathways were in equilibrium. With Ni/Al_2O_3, the water content remained similar to that in the raw material up to 25W and then sharply decreased to zero at 30W. This was due to the consumption of OH radicals by hydrocarbons and ketones, followed by decomposition to form carbon oxides. An increase in the water content at powers above 30 W was due to plasma arcing (heterogeneous environment).

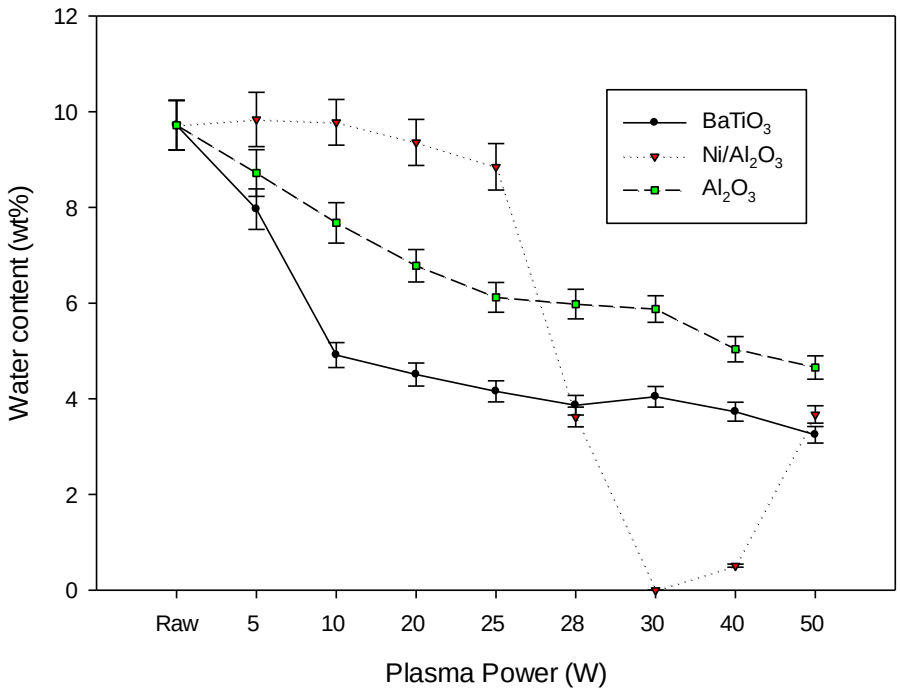

Figure 5.7: Water content at various plasma powers for packing materials and catalyst Ni/Al_2O_3 at 7 seconds residence time under N_2

After 1 hour operating time, the conversion of waste glycerol in the presence of Ni/Al_2O_3 significantly decreased, by approximately 35wt.%. This is due to fouling, which is in agreement with previous studies (Atong and Sricharoenchaikul, 2009). The same behaviour was observed for Al_2O_3 but not for $BaTiO_3$. The spent and fresh Ni/Al_2O_3 catalyst was then analysed using BET, SEM with EDS and XRD. For the fresh catalyst, SEM-EDS analysis (Figure 5.8a) showed large particles of diameter of 0.5-1 mm with mainly Ni, Al and O elements with a ratio of O/Al comparable to that reported in literature (Olefjord and Nylund, 1994; Chyrkin *et al.*, 2017). In contrast, SEM images of the spent Ni/Al_2O_3

catalyst show rounded surfaces with very few pores and bubble like nodes visible on the material's surface (Figure 5.8b). From XRD analysis (Figure 5.8d), the spent catalyst had an additional reflection at 21°, indicating a partial coverage of solid carbon on the surface (Li *et al.*, 2007b). The very high degree of fouling which occurred within the 1 hour running time was carbon based, but contained significant potassium content (up to 15.5%). The nodules formed at the areas where carbon accumulated. The resulting fouling on these points retained OH groups so more waste glycerol adhered to it, building up into a nodule. The pores were largely clogged with waste glycerol and some deposits could be formed internally. The sample was also regenerated successfully via pyrolysis at 450°C and analysed, which showed no significant differences from the initial catalyst (Figure 5.8c) as evidenced by the similar conversion and product distribution obtained over the regenerated catalyst. Additionally, when the spent catalyst was regenerated at 550^{o}C in N_2, the additional peak at 21^{o} disappeared. It was found (Mok *et al.*, 2013; Jia *et al.*, 2017) that spent catalysts can be regenerated by cold plasma at lower temperatures and with shorter residence times than by conventional regeneration methods. However, this is not in the scope of this study.

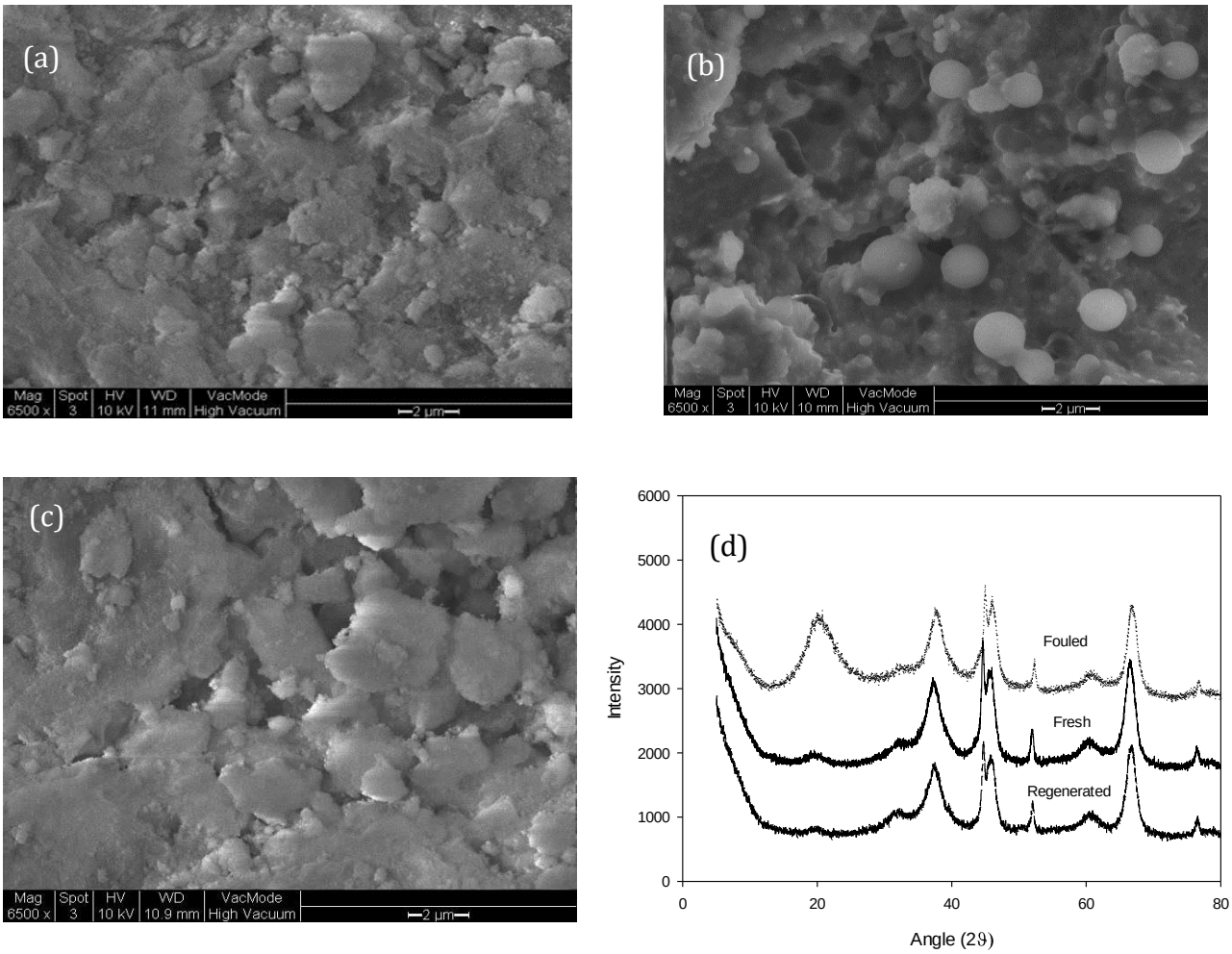

Figure 5.8: SEM image of at x6500 magnification of (a) fresh, (b) spent and (c) regenerated catalysts and (d) XRD of fresh, spent and regenerated Ni/Al_2O_3.

5.3.3 Modelling and validation

As the earlier model for cold plasma assisted glycerol decomposition was designed for pure glycerol feedstocks, it did not include decomposition reactions for FFA and therefore cannot accurately model these components. However, process yields can be approximated by regarding the other feedstock components as unreactive and predicting each product yield based on the initial glycerol content (58.96wt.% from Table 3.2). This allows the contribution of the other feedstock components to be determined by comparison separately from glycerol decomposition. The model parameters utilised in pure glycerol modelling were used directly without modification with the other components of waste glycerol included as unreactive additions. The results of this are shown in Table 5.7.

Table 5.7: Comparison between modelling and experimental data for cold plasma assisted waste glycerol decomposition under N_2 based on initial glycerol content

	Modelling data			Experimental data		
Plasma power, W	10W	30W	50W	10W	30W	50W
Glycerol conversion, %	4.09	8.38	15.34	76.26	60.67	96.61
Gas yields (wt.%)						
CO_2	-	-	0.14	-	3.46	10.79
H_2	0.62	1.11	2.49	0.91	1.01	2.72
CH_4	-	0.09	1.04	7.14	3.25	4.44
CO	-	0.10	3.29	2.14	8.56	9.90
C_2H_4	-	0.01	1.30	10.91	7.82	6.36
C_3H_8	-	-	0.01	-	0.88	2.40
C_4H_{10}	-	-	-	-	0.56	1.58
Liquid yields, wt.%						
Formic acid	-	0.01	0.30	-	5.67	-
Propenal	-	-	-	-	-	-
Acetol	3.47	7.06	6.77	44.91	34.92	52.20

Modelling underpredicted the conversion of glycerol in the waste glycerol feedstock by 80%. This indicates that introducing more volatile components into the feedstock and impurities (alkaline metals) has a very significant effect on glycerol conversion and product yields. This is as expected, as many of the dominant products of waste glycerol decomposition (Table 5.5) (e.g. CO_2 and hydrocarbons) are highly unlikely to derive from glycerol decomposition and over 40% of the reaction inputs are assumed as unreactive. This may also indicate that the alkaline metals can act as catalysts.

H_2 yields from modelling agreed well with experimental data. However, the yields of carbon oxides were significantly underpredicted, especially CO_2, which was underpredicted by >98%. This is an indicator that these components primarily arise from decomposition of another feedstock component, most likely FFA or FAME. CO_2 can be generated from FFA by splitting the hydrocarbon chain adjacent to the carboxylic acid group followed by reformation to CO_2. In contrast, formation from glycerol requires formation of methanol followed by hydroxyl radical attack. As can be seen in Figure 5.5, the pathway from FFA required far fewer reactions, which supports the theory that FFA is the source of the abundant CO_2 in the experimental data. The lower levels of CO_2 shown with pure glycerol provide more evidence to support this conclusion (0.25wt.% vs. 10.79wt.%). The hydrocarbon yields are similarly higher in the experimental data, as FFA

cracking generates hydrocarbons directly. The ratio between conversion and acetol yields shows that the model predicted a greater selectivity to acetol than observed experimentally. At 50W, the model predicted 44% selectivity, while the experimental data indicated 54% selectivity.

In summary, the model significantly underpredicted the conversion and yields from waste glycerol decomposition, which indicates that the decomposition products from other components such as FFA assist with inducing glycerol decomposition or that the alkaline metals in the waste glycerol have catalytic effects.

5.4 Summary

In this chapter, the decomposition of glycerol was studied with plasma power and carrier gas as independant variables. The use of N_2 increased conversion by more than 400% relative to equivalent H_2 experiments, thought to be due to the dominant pathways being initiated via dehydrogenation reactions. Compared to thermal processes, gas-liquid cold plasma assisted decomposition of glycerol produces a greater proportion of hydrocarbons and alcohols as opposed to aldehydes, which was linked to the rapid decomposition of aldehydes in cold plasma. The two phase cold plasma system permits many intermediates such as methanol, acetol and methyl methanoate to be isolated, as the liquid phase prevents excited electron induced reactions in the bulk, which has the effect of protecting liquid phase intermediates and permitting higher selectivities to these products.

The reaction mechanism of glycerol decomposition was proposed to be primarily through dehydration of glycerol to acetol and cracking of glycerol to methanol cation radicals and glycolaldehyde. A full model of the glycerol decomposition process was developed and used to determine the probable radical formation and interaction pathways that occur under cold plasma treatment of glycerol. However, the model underpredicted the yields of carbon oxides and liquid phase intermediates and overpredicted hydrocarbon yields, but the trends in the product yields were similar to those observed experimentally. Attempts to model the decomposition of glycerol in a H_2 environment revealed that the presence of H_2 appeared to lower the effective mean electron temperature. This is attributed to the relatively low maximum energy level of H_2 (13.6eV) preventing the

formation of higher energy radicals. This was not observed for methanol in Chapter 4 as methanol is volatile enough to be decomposed by electrons directly.

For waste glycerol, the carrier gas was found to be a significant factor in the conversion and product distribution. H_2 carrier gas favours the formation of hydrocarbon products and propenal, and preferentially decomposes FFA molecules. N_2 carrier gas produces the highest yield of acetol due to preferentially decomposing glycerol. He carrier gas favours CO and preferentially decomposes glycerides. The effect of reaction time was more pronounced than packing materials. Approximately 99% waste glycerol was converted into gaseous products at 30W, of which 7wt.% was H_2 when using Ni/Al_2O_3. The Ni/Al_2O_3 catalyst deactivated quickly within a 1 hour operating time due to the deposition of carbons and impurities from the waste glycerol feedstock i.e. potassium. This indicates that cold plasma is effective at extending the lifespan of catalysts under fouling conditions, but is not capable of regenerating fouled catalyst with the plasma powers utilised. Further study would be needed to establish if higher power cold plasma is capable of regenerating these catalysts. However, the catalyst could be regenerated easily in 550°C oxygen free N_2. This study reveals opportunities to convert waste into high added value products over a short period of time at near ambient conditions with the products easily tuned according to demand.

Extending the glycerol model to waste glycerol gave a generally poor fit in terms of product yields. This indicates that decomposition of other waste glycerol components such as FFA or water assist with the decomposition of glycerol, likely through generating radicals that initiate glycerol decomposition. The alkaline metals may also contribute by acting as homogenous catalysts.

Chapter 6. Cold plasma assisted triglyceride decomposition

Triglyceride containing sources are one of the key renewable sources for biofuel production. However, sources of pure triglycerides for biofuels are limited and often compete for land with food production. Therefore, the use of more sustainable and plentiful waste triglycerides is desirable. The most common method of converting triglycerides into biofuel is alkaline catalysed transesterification with methanol to form fatty acid methyl esters (FAME). However, the process generates around 10wt.% low value waste glycerol (40-75% purity) and is prone to fouling via saponification, particularly when the feedstock contains high levels of free fatty acids (FFAs) and water. Catalytic cracking of triglycerides at high temperatures (typically >360°C) and ambient pressures to produce liquid fuels has been studied. However, the catalyst is prone to fouling, requires a greater specific energy input and the selectivity to liquid hydrocarbons is low (typically < 48%).

In this chapter, cold plasma assisted triglyceride decomposition was studied in comparison with conventional thermal decomposition to understand the role of highly energetic electrons on the decomposition of triglycerides, thereby establishing reaction mechanisms. Pure triglycerides were considered first to study the process without the effects of impurities. This entailed determination of the effect of carrier gas, plasma power, external heating, residence time and the presence of packing material/catalysts in the plasma zone. The proposed mechanisms were then applied to waste cooking oil. The effects of these variables were analysed to determine a detailed mechanism for decomposition of pure triglycerides and compared with the results from treatment of impure triglycerides to determine the effects of the impurities on the cold plasma decomposition process.

6.1 Pure triglycerides

6.1.1 Effects of plasma power and carrier gas

Table 6.1 revealed that the conversion of triglycerides together with the yields of gaseous components increased with increasing plasma power for both N_2 and H_2 carrier gases, with and without additional heating. For example, the conversion increased from 17.06% to 50.94% in N_2 carrier gas and from 33.62% to 51.52% in H_2 carrier gas when increasing plasma power from 10W to 50W. This is due to the generation of an increased

concentration of excited species at higher plasma powers (Shrestha, 2012). These excited species trigger initiation reactions (Paulmier and Fulcheri, 2005), thereby increasing the rate of decomposition.

Table 6.1: Cold plasma assisted decomposition of pure triglycerides without catalysts at a residence time of 11 seconds and gas to liquid ratio of 40:1 (vol/vol) at atmospheric pressure (error:±5%)

Method	**Cold plasma**						**Thermal only**		**Cold plasma with external heating**	
Carrier gas	H_2			N_2			H_2		N_2	
Plasma power (W)	10	30	50	10	30	50	N/A	N/A	50	50
Temperature (°C)	N/A	N/A	N/A	N/A	N/A	N/A	250	300	250	300
Conversion (%)	33.62	39.40	51.52	17.06	33.91	50.94	12.50	18.05	52.37	68.83
Solids (wt.%)	-	-	-	-	0.02	0.20	-	-	0.23	-
Total gas yield	4.02	6.64	10.59	2.36	6.81	14.41	0.55	3.26	19.82	37.73
Gas yields (wt.%)										
CO_2	0.57	0.84	1.69	0.71	1.02	1.90	0.13	1.47	2.20	2.83
H_2	0.83	0.99	1.47	0.92	1.46	1.89	0.36	1.07	3.00	7.01
CO	0.53	1.71	1.82	0.23	2.76	6.99	0.04	0.44	10.01	17.57
CH_4	1.80	2.67	4.84	0.39	1.11	1.85	0.02	0.25	3.36	7.40
C_2	0.21	0.26	0.47	0.08	0.30	0.98	-	0.02	1.00	1.79
C_3	0.07	0.13	0.22	0.04	0.08	0.65	-	-	0.22	0.85
C_4	0.01	0.04	0.08	-	0.08	0.17	-	-	0.03	0.29
Liquid yields (wt.%)										
Water	1.86	0.15	0.15	0.16	0.09	0.20	0.16	0.18	0.53	2.50
Acetol	0.90	0.12	0.45	0.02	0.03	0.09	0.01	0.02	0.01	0.15
FFA	10.97	10.25	13.61	2.83	6.25	9.48	6.96	7.73	5.04	6.93
Glycerol	0.23	0.01	0.02	-	0.01	0.01	-	-	-	0.02
FAME	-	0.01	0.02	-	0.01	0.02	-	-	0.03	0.10
Other fatty acid esters	-	0.01	0.06	-	-	0.01	-	-	0.02	0.06
C14-18 Hydrocarbons	-	0.01	0.02	-	0.01	0.02	-	-	0.01	0.03
Monoglycerides	5.64	7.68	10.34	4.08	7.14	10.34	1.75	2.27	9.14	7.47
Diglycerides	10.00	14.52	16.26	7.61	13.54	16.16	3.07	4.60	17.75	13.84

Table 6.1 shows the carrier gas had a strong effect on product distribution/yields. The H_2 environment promoted condensation reactions to generate FFAs and water, as evidenced by an increase in the yield of FFA by >30% (e.g. 13.61wt.% vs 9.48wt.%). A higher yield of methane in H_2 than in N_2 (4.84% in H_2 vs. 1.85% in N_2) can be explained because abundant hydrogen radicals favour the stabilisation process ($CH_3\cdot + H\cdot = CH_4$) compared to propagation to form longer chain hydrocarbons ($CH_3\cdot + CH_3\cdot = C_2H_5\cdot + H\cdot$ or $CH_3\cdot + CH_3\cdot = C_2H_6$) (k= 2.68 $x10^{-10}$ vs 2.00$x10^{-11}$ cm^3/molecule s^{-1}). This suggests that H_2 carrier gas is more suitable for generating gaseous hydrocarbons from triglyceride decomposition. In contrast, N_2 favoured the formation of carbon oxides (CO and CO_2) and H_2, indicating that the N_2 carrier gas promotes dehydrogenation reactions. A small amount of CO was detected (0.44wt.%) at 300°C without plasma, as shown in Table 6.1, which supports this hypothesis. This was also reported in literature (Billaud *et al.*, 2003) for thermal decomposition process under a N_2 environment.

The liquid products were at relatively low yields at all tested powers for both carrier gases, with only FFA and glycerides exceeding 10wt.%. This is as expected as cold plasma only initiates reactions at the gas-liquid interface or via liquid phase radicals generated at the phase boundary (Di *et al.*, 2016), thus limiting the decomposition rate of non-volatile liquids. For example, at 10W in H_2 environment, 33.62% triglycerides converted into 10.97wt.% FFA, 5.64wt.% monoglycerides and 10wt.% diglycerides. However, when triglycerides were treated with cold plasma at close to thermal decomposition temperatures (i.e. external heating at 300°C), a 26% increase in conversion was observed (increasing from 50.93% to 68.89%). Additionally, increasing temperature increased the total gas yield (from 14.41wt.% without heating to 19.82wt.% at 250°C then to 37.73wt.% at 300°C).

A reduction in the water yield in H_2 from 1.86wt.% to 0.15wt.% when increasing plasma power from 10W to 30W could be because water decomposes to hydrogen and hydroxyl radicals at high plasma powers (Sein *et al.*, 2012), which are then consumed in the generation of CO_2. This also explains why the water content remained almost constant between 30 and 50W despite the increase in FFA (CO_2 increases from 0.84 to 1.69wt.%). The low water content of the products (0.16wt.% at 10W) at all powers in N_2 is due to this decomposition reaction occurring at all plasma powers, likely due to the higher energy states of N_2. This is in contrast to H_2, where this reaction only occurs at powers ≥30W. The

decomposition of water is evidenced by the increase in H_2 and CO_2 as a result of reactions between hydroxyl radicals and carbonaceous species (such as CO or FFA), followed by decomposition to CO_2 and hydrocarbons (Buszek *et al.*, 2011; Koeta *et al.*, 2012). Additionally, CO_2 and hydrocarbons can potentially react in the plasma environment to form H_2 and CO, which may account for the high CO yields under N_2 environment (6.99wt.% vs 1.82wt.% under H_2 at 50W) and smaller than expected increases in CO_2 (0.71wt.% at 10W vs 1.90wt.% at 50W under N_2).

Cracking of the FFA hydrocarbon chains was reported previously during catalytic decomposition of rapeseed oil to break FFA into hydrocarbons and CO_2 (Bielansky *et al.*, 2012). This work also highlighted that the fatty acid chains in triglyceride molecules are likely to also decompose, but could not confirm this. The yield of FFA was lower in N_2 than in H_2 for all tested plasma powers. This is because the abundant hydrogen radicals under H_2 react with other radicals to produce stable products (e.g. $CH_3\cdot + H\cdot \rightarrow CH_4$) ($k=2x10^{-10} cm^3 mole^{-1} s^{-1}$ vs $k=3.1x10^{-17} cm^3 mole^{-1} s^{-1}$ for an equivalent radial initiation reaction). In contrast, the N_2 environment supplies highly energetic excited species (>13eV), permitting more rapid cleavage of C-C/C=O bonds to hydrocarbons, H_2 and CO_2. A similar pathway was reported in conventional thermal decomposition of octadecanoic acid (Shin *et al.*, 2012).

Triglycerides are known to lose one, two or three fatty ester branches during decomposition to form diglycerides, monoglycerides and glycerol respectively, along with FFAs (Reaction 6.1) (Bokade and Yadav, 2009). This was previously established as the dominant reaction because the ester bond (C-O) has the lowest bond energy.

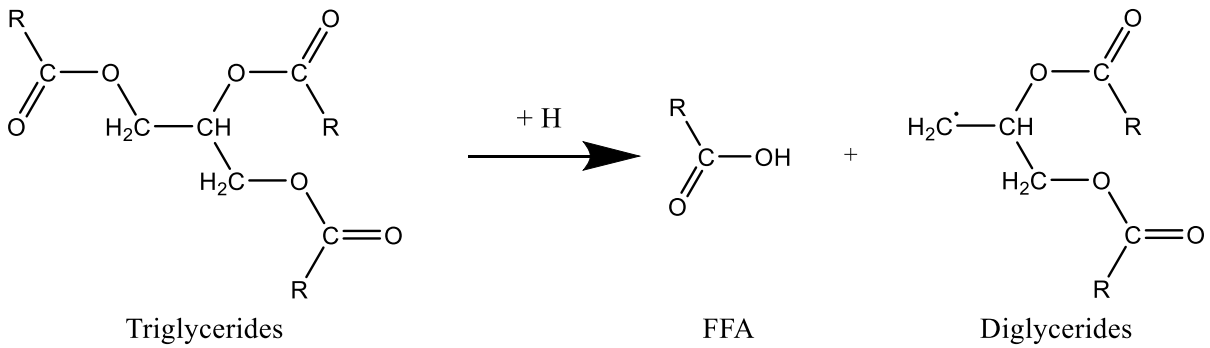

Reaction 6.1 De-esterification of glycerides

Although splitting of C-C bonds to produce FAME is also technically possible (Reaction 6.2), low yields of FAME are typical due to the higher dissociation energy of the C-C bond (351KJ/mol vs 296KJ/mol) and the lower rate constant ($2.5x10^2$ cm^3/molecule s^{-1} vs $7.8x10^{10}$ cm^3/molecule s^{-1}) (NIST).

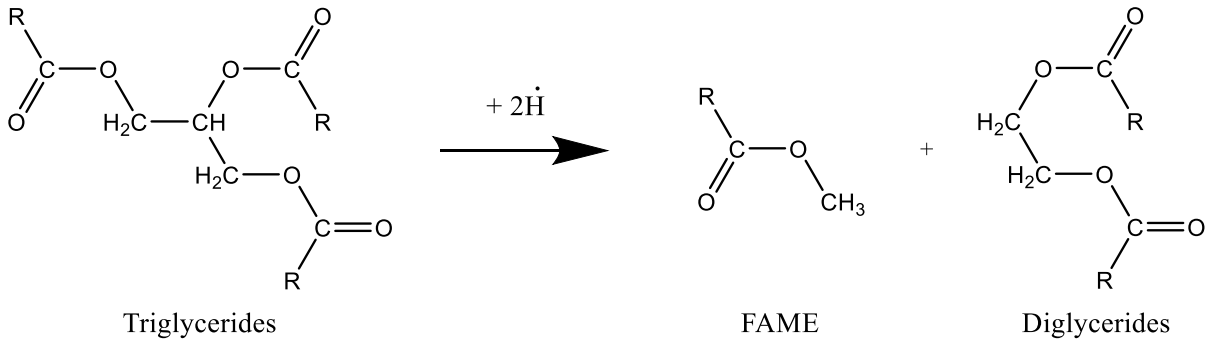

Reaction 6.2: Cracking glycerides to generate FAME

The yields of monoglycerides and diglycerides increased with increasing plasma powers, i.e. 5.64wt.% to 10.34wt.% for monoglycerides and 10.00wt.% to 16.26wt.% for diglycerides in H_2. Although the same behaviour was also observed in conventional thermal processes (10-40 seconds residence time) (Wiggers *et al.*, 2009), the de-esterification rate was much higher in cold plasma process at atmospheric temperature and combined cold plasma and heating than in conventional thermal process at the same temperature range of 250-300^{o}C (Table 6.1).

Diglyceride and monoglyceride yields were 3.07wt.% (diglyceride) and 1.75wt.% (monoglyceride) in thermal decomposition at 250°C compared to 17.75wt.% (diglyceride) and 9.14wt.% (monoglyceride) at 50W and 250°C or 7.61wt.% (diglyceride) and 4.08wt.% (monoglyceride) at 10W (Table 6.1). The electron temperature under cold plasma follows appropriate electron energy distribution curves, which have the greatest probability values near the effective electron temperature, which decreases as the electron temperature increases, as shown in Figure 4.1 (Michelmore *et al.*, 2013). This implies the majority of electrons are low energy but a small proportion have a very high energy level. The relative proportions depend on the plasma power and carrier gas. At any given power, electrons of sufficient energy to decompose triglycerides are present, but with increased plasma powers, the proportion of electrons with sufficient energy increases rapidly. The liquid phase feedstock prevents electrons from decomposing

triglycerides directly, but electrons can excite N_2 or gaseous decomposition products to give excited species. These species can be of higher energy than the activation energy for thermal decomposition of triglycerides to glycerides and FFA, (220KJ/mol, equivalent 2.23 eV) (Wako *et al.*, 2017) with the proportion with sufficient energy increasing with plasma power.

As shown in Table 6.1, although de-esterification of triglycerides occurred, the glycerol yield was very small (0.01-0.02wt.%) except for 10W in H_2 environment (0.23wt.%). This was due to the decomposition of glycerol to acetol, which was reported under the effect of temperature (Chiu *et al.*, 2006; Li *et al.*, 2009; Quispe *et al.*, 2013) and cold plasma (Harris *et al.*, 2018). With H_2 as the carrier gas, hydrogen radicals were more abundant, which would favour de-esterification reactions (Reaction 6.1) and induce radical termination reactions (e.g. $CH_3\cdot + H\cdot \rightarrow CH_4$).

A small amount of viscous paste (<0.1g) formed on the reactor surfaces at high powers (30-50W), both with and without external heating, but did not affect glyceride conversion over a 4 hour operation period. The paste was analysed by GC and solid FTIR analysis and resembled oxopolymerised glycerides, as detailed in relatively low temperature triglyceride pyrolysis studies (Paulose and Chang, 1978; Versteegh *et al.*, 2004; Brühl, 2014). Oxopolymerised glycerides would form when two triglyceride molecule chains interact with hydroxyl radicals, allowing the affected hydrocarbon chains to form cross linkages (Reaction 6.3) (Paulose and Chang, 1978; Brühl, 2014).

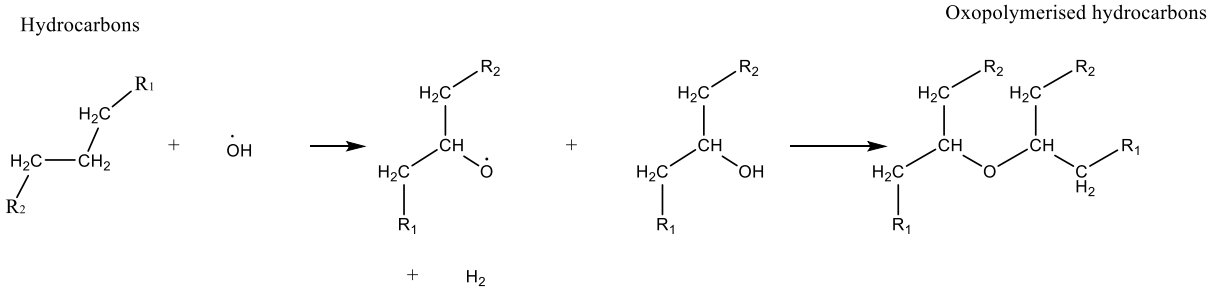

Reaction 6.3: Oxopolymerised solid formation mechanism (Versteegh et al., 2004)

This oxopolymerisation reaction (Reaction 6.3) repeats on different locations on the chains, slowly building up a polymer. This provides evidence that water is forming from de-esterification under N_2 to supply the required hydroxyl radicals via decomposition. The solid was not observed to form under H_2, as the formation of a C-O radical group

requires dehydrogenation, which is hindered by abundant hydrogen due to Le Chateliers principle.

The results shown in Table 6.1 confirm that cold plasma could decompose triglycerides to produce FFA, CO_2, CO, H_2 and hydrocarbons i.e. CH_4 (51.5% conversion) at atmospheric conditions. The similarity in the product distribution between conventional thermochemical process and cold plasma confirms that both processes occur via radical mechanisms, despite the differing product yields. However, thermochemical and cold plasma decomposition result in different product yields, which indicates differences in the reaction kinetic constants between the two methods.

Table 6.1 shows the conversion derived from conventional thermal decomposition varied from 12.50% to 18.05% with the gas yield of 0.55wt.%-3.26wt.%, which agreed well with literature (Xu *et al.*, 2010; Palanisamy and Gevert, 2016). Increasing temperatures above 250°C increased conversion (Tudorachi and Mustata, 2015; Li *et al.*, 2017), producing H_2, hydrocarbons, CO and FFA. Therefore thermal decomposition of vegetable oils is commonly performed at 350-500°C to obtain high conversion, therefore producing high yields of fatty acids (C_1-C_{18}), hydrocarbons (C_1-C_{18}) and H_2 (Maher and Bressler, 2007). Up to 77% conversion of soybean oil was achieved during distillation of the oil at 350°C to produce 28.3wt.% hydrocarbons up to C_{12}, 12.2wt.% free fatty acids and traces of aromatics with the formation of waxy semisolids, over an unspecified residence time (Schwab *et al.*, 1988).

In summary, although cold plasma can decompose triglycerides at atmospheric conditions without catalysts, the conversion was low (around 51% at 50W and 250°C or 69% at 50W and 300°C). Therefore, the use of packing materials and/or catalysts was tested, as they would be expected to enhance the electric field, improving the conversion and product yields. As the N_2 carrier gas promotes cracking and dehydrogenation, it was chosen as the carrier gas to study the effects of packing material on the decomposition of triglycerides.

6.1.2 Effect of packing materials and catalysts

The effect of packing $BaTiO_3$ and Ni/Al_2O_3 catalyst in the plasma zone on the performance of decomposition of rapeseed oil was investigated. $BaTiO_3$ is a widely available, strongly dielectric material that has been studied extensively, with internal bond energies close to those of organic bonds. It has a dielectric constant of around 700 Fm^{-1} at ambient temperatures, and hence provides a lower energy route across the discharge gap than through the gas phase, which reduces the effective discharge gap and targets the plasma onto the liquid and packing material as discussed in Chapter 5. $BaTiO_3$ also releases electromagnetic waves with energies close to those used to decompose organic chemical bonds, due to the presence of of Ti-O-Ti bonds which have excitation energies in this energy range (Yu *et al.*, 2012). Hence, $BaTiO_3$ has the potential to improve process efficiency both by favouring electron generation in an effective energy range (1-1.4eV) and by concentrating the resulting plasma into the desired region of the reactor via the dielectric effect, as shown in Figure 5.6.

Ni/Al_2O_3 has proven to be effective during prior studies for catalysing triglyceride cracking and dehydrogenation, notably obtaining 91% yields of hydrocarbons after 4 hours via cracking of fatty acid chains at 280-360°C (Yenumala *et al.*, 2017). As a result, Ni/Al_2O_3 was used in this work to investigate the effects of a catlytic cracking catalyst. Alumina was used as the catalyst support due to its ready availability as expanded structures compared to other catalyst supports (Liu *et al.*, 2005; Imran *et al.*, 2014), its low cost and its effects on acidic active site concentrations for cracking catalysts, such as nickel (Bartholomew and Farrauto, 1976; Krylova, 2008). Alumina has a low dielectric constant (7 Fm^{-1}) (Narayana Rao, 1950) compared to nickel (effectively infinite), which would, in theory, concentrate incoming plasma onto the surface of the nickel as shown in Figure 5.6. This plasma focussing should synergise well with cold plasma, either by increasing reaction rates or by permitting higher energy reactions to occur.

As introducing a packing material reduces the available volume in the plasma zone, maintaining constant gas and liquid flowrates with packing reduces the residence time. This can be corrected for by reducing the flowrates, but this increases the specific input energy as defined below. To ensure that these paired variables do not obfuscate catalytic effects, both constant specific input energy and constant residence time experiments were performed.

$$Specific\ input\ energy\ (\frac{Joules}{litre}) = \frac{Power\ (\frac{Joules}{second})}{Volumetric\ flow\ rate\ (\frac{Litres}{second})}$$

Equation 6.4: Definition of specific input energy

Packing with $BaTiO_3$ resulted in a 18-28% increase in conversion (Table 6.2), leading to a 18-23% increase in the gas yield (6.81wt.% to 8.86% at 30W and from 14.41wt.% to 17.49wt.% at 50W) even with a 40% shorter residence time (7 seconds compared to around 11 seconds without packing). This suggests the energy available per excited species is higher when packing $BaTiO_3$, which in turn greatly increases the proportion of collisions that induce a reaction. This is explained by the $BaTiO_3$ focussing the plasma due to its overall higher dielectric constant than the other potential packing materials, resulting in a greater proportion of high-energy excited species (electrons, radicals and ions). A significant increase in conversion indicates these high-energy excited species act to split triglycerides into monoglycerides and diglycerides. These monoglycerides and diglycerides and glycerol decompose further to produce smaller compounds such as FFA and glycerol in the liquid phase. Glycerol decomposes further into acetol then propenal, while FFA decomposes further to gaseous products such as hydrocarbons and CO. Propenal is typically unstable under cold plasma and decomposes to carbon monoxide, hydrogen and ethene.

Table 6.2: Effect of packing materials/catalysts on cold plasma assisted decomposition of rapeseed oil at atmospheric conditions with N_2 carrier gas and ratio of carrier gas to liquid of 40:1 (vol/vol) (error: ±2.4%)

	Packing material	**Ni/Al_2O_3**			**$BaTiO_3$**			**Ni/Al_2O_3**		**$BaTiO_3$**	
	Plasma power (W)	10	30	50	10	30	50	30	50	30	50
	Residence time (seconds)	7	7	7	7	7	7	11	11	11	11
	Conversion (%)	23.29	50.16	74.61	20.86	46.90	68.22	54.78	90.04	50.17	75.44
	Solids (wt.%)	-	0.38	0.97	-	-	0.17	0.53	1.26	-	0.26
	Total gas yield (wt.%)	2.97	7.36	14.86	2.22	8.86	17.49	9.92	19.4	11.71	23.26
Gaseous yields (wt.%)	CO_2	1.47	2.15	3.13	1.05	2.87	2.45	2.54	3.69	3.39	2.89
	H_2	0.50	1.39	1.89	0.49	1.46	2.42	1.53	2.08	1.60	2.66
	CO	0.54	2.74	6.67	0.12	2.90	9.08	3.01	7.46	3.48	10.16
	CH_4	0.47	0.95	2.03	0.42	1.29	2.88	1.64	3.4	1.73	3.57
	C_2	-	0.13	0.87	0.14	0.21	0.43	0.34	0.71	0.40	0.83
	C_3	-	-	0.29	-	0.10	0.18	0.63	1.56	0.81	2.36
	C_4	-	-	-	-	0.03	0.07	0.07	0.15	0.09	0.19
	C_5	-	-	-	-	-	-	0.13	0.32	0.19	0.55
	C_6	-	-	-	-	-	-	0.01	0.03	0.02	0.04
Liquid yields (wt.%)	Water	0.11	0.11	0.12	1.10	1.17	0.26	0.11	0.12	1.12	0.24
	Acetol	0.09	0.19	0.26	0.07	0.19	0.72	0.19	0.25	0.19	0.66
	FFA	3.35	7.86	10.88	2.51	9.00	13.67	7.78	10.45	8.64	12.44
	Glycerol	-	0.01	0.01	0.01	0.02	0.06	0.01	-	0.02	0.02
	FAME	0.22	3.99	8.81	0.05	0.10	0.09	4.15	11.02	0.10	0.11
	Other fatty acid esters	0.22	1.15	1.52	0.10	0.36	0.57	1.20	1.90	0.37	0.54
	$C_{14\text{-}18}$ Hydrocarbons	0.02	0.07	0.04	0.03	0.09	0.10	0.18	1.17	0.05	0.05
	Monoglycerides	5.30	9.47	13.81	3.12	9.45	12.86	9.89	16.12	9.74	13.81
	Diglycerides	11.01	19.95	24.30	6.88	17.68	22.40	20.82	28.35	18.23	24.05

At 50W plasma power in $BaTiO_3$ packing, 0.72wt.% acetol was produced compared to 0.09wt.% without packing (Table 6.1), which suggests that more glycerol was generated but was dehydrogenated to acetol and water (Li *et al.*, 2009; Hemings *et al.*, 2012). This conclusion also applied at other powers, with 30W at $BaTiO_3$ generating 0.19wt.% acetol instead of 0.03wt.% without catalyst. A small amount of paste formed on the $BaTiO_3$ (up to 0.26wt.%), with an identical composition to the paste identified in Table 6.1, suggesting the packing material does not affect solid formation.

At the same residence time (7 seconds), Ni/Al_2O_3 had a similar effect on triglyceride decomposition. The conversion increased with plasma powers and was slightly higher than that in the case of $BaTiO_3$. However, the yield of FAME was much higher with Ni/Al_2O_3, up to 8.81wt.% compared to 0.09wt.% for $BaTiO_3$ packing at 50W. This indicates that Ni/Al_2O_3 promotes the cracking of triglycerides into FAME as reported in literature (Zarchin *et al.*, 2015; Yenumala *et al.*, 2017). The increase in the FAME yield could be due to the catalyst acting to break the glycerol backbone of triglycerides, releasing FAME and an ethylene glycol based diester. This ethylene glycol diester can be broken into two FAME molecules. Esterification between FFA and methyl radicals is an alternative route for FAME formation regardless of catalyst, as shown in Table 6.1. Ni/Al_2O_3 is a cracking and dehydrogenation catalyst (Ortega García and Mar Juárez, 2017) and thus unselectively decomposes all C-C and C-H bonds, including decomposing the glycerol backbone to produce FAME at moderate yields (up to 11.02wt.%). The location where nickel cracks glycerides is likely to be random, which explains the relatively low yield of FAME compared to transesterification (90%) (Yang *et al.*, 2018).

Nickel acts as a catalyst for cracking and dehydrogenation by acting as a proton acceptor. When a hydrocarbon chain makes contact with nickel metal, a hydrogen atom is removed and binds to the nickel. The resulting charged region pulls in a hydrogen atom from an adjacent carbon, which causes the chain to split in two, with one side containing a double bond and the other with a radical group on the split carbon end. This also acts to remove hydrogen, but has no particular effect on other groups such as alcohol groups. The nickel is primarily bonded in the structure, as shown in Figure 6.1, to the surface of the Al_2O_3

and inside the pores, though this has no effect on the mechanism. These reactions are illustrated in Figure 6.1 below:

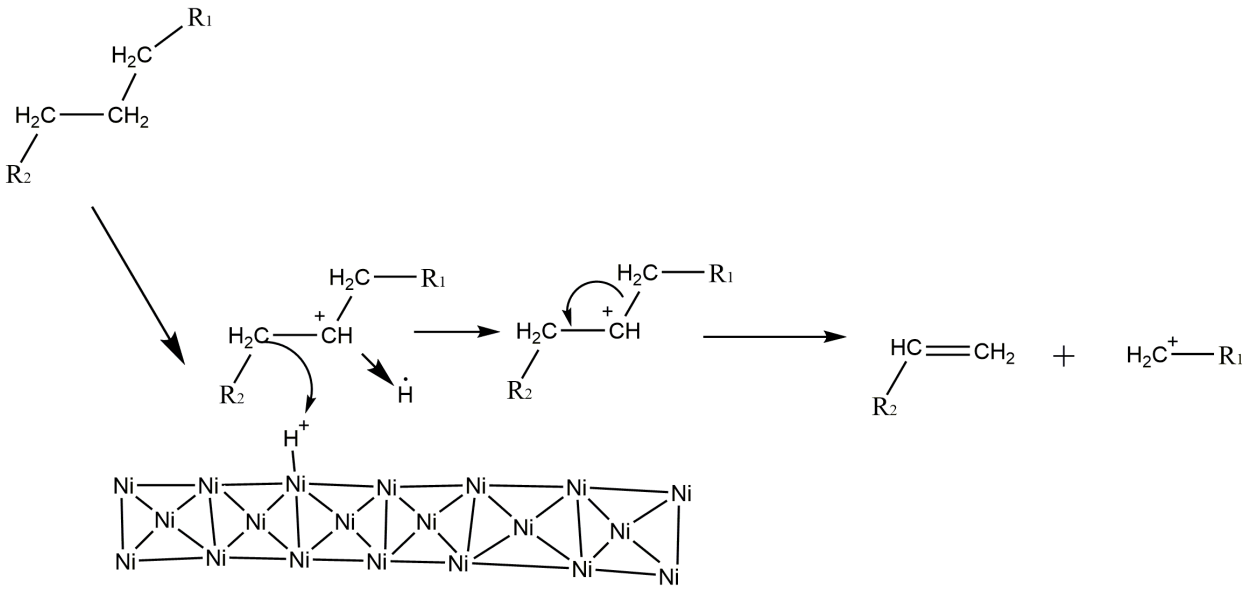

Figure 6.1: Catalytic cracking mechanism for hydrocarbon chains with a nickel catalyst (Bartholomew and Farrauto, 1976; Yenumala *et al.*, 2017)

With $BaTiO_3$ packing, increasing the residence time from 7 seconds to 11 seconds led to a small increase (6-10%) in the conversion and subsequently the product yields (Table 6.3), which exceeds the stated error ranges. This indicates that an equilibrium was reached between their formation and decomposition at a residence time of around 7seconds at atmospheric conditions (pressure and temperature) in N_2 environment. A mechanism was proposed with triglycerides as the initial reactants, FFA, other fatty acid esters and FAME as intermediates, and gaseous products as final products which was confirmed and discussed in detail in the reaction pathways below (Figure 6.5). However, for Ni/Al_2O_3, the increased residence time of 11 seconds resulted in very high conversion at 50W, up to 90% from 74.6%. The yields from Ni/Al_2O_3 catalysed runs for hydrocarbon, hydrogen and carbon oxide are much higher than with other packing materials, with significantly increased FAME yields. Traces of heptane, octane and nonane were also detected in the liquid phase but yields were below 0.01wt.%.

Interestingly, total solid yields decreased when the residence time increased, though catalyst activity at any given time is not affected by the change in residence time. The rate

of deactivation is approximately 10% loss of activity per 1 hour for all Ni/Al_2O_3-catalysed runs. This would reflect the longer residence time allowing decomposition of the soaps into hydrocarbons and smaller soaps, which does not affect catalyst lifespan.

Introducing a packing material or catalyst into heated cold plasma increased the conversion and hence greater gas yields were produced. Significantly higher yields of gaseous hydrocarbons (C_1-C_5) and FAME were observed for $BaTiO_3$ and Ni/Al_2O_3 compared to those without heating. For example, hydrocarbons (C_1-C_5) increased up to 803% (from 3.56 to 32.16wt.%) for $BaTiO_3$ and 1284% (from 3.19 to 44.16wt.%) for Ni/Al_2O_3 compared to unheated catalysts at 30W. FFA increased when heating the cold plasma zone (around 18wt.%) compared to without heating (9-13.67wt.%) for the case of $BaTiO_3$ but slightly decreased in the case of Ni/Al_2O_3. The higher hydrocarbon yield could be due to the increased volatility of compounds in the reactor. Introducing external heating to a cold plasma reactor significantly increased the gas yield e.g. from 17.49wt.% to 59.76wt.% at 50W in the case of $BaTiO_3$ packing whereas the overall liquid yields decreased, except for water increasing from 0.26wt.% to 2.41wt.%. For example, the mass fraction of residual glycerides was reduced from 67wt.% to 18wt.%. The reduction in the yields of FFA and FAME (Tables 6.2 and 6.3) are due to the decreasing rate of their formation from glycerides as a result of glyceride depletion and more rapid decomposition of FFA/FAME due to the increased temperature.

Table 6.3: Effect of external heating on cold plasma assisted decomposition of rapeseed oil at a gas: liquid ratio of 40:1 (vol/vol) in a N_2 environment and external heating at 300°C (errors:±1.5%)

Catalyst	**$BaTiO_3$**		**Ni/Al_2O_3**		**$BaTiO_3$**		**Ni/Al_2O_3**	
Plasma power (W)	30	50	30	50	30	50	30	50
Residence Time (seconds)	7	7	7	7	11	11	11	11
Conversion (%)	94.20	96.97	76.99	92.73	93.16	95.76	77.86	92.25
Solids (wt.%)	0.03	0.08	0.25	0.84	0.03	0.05	0.15	0.41
Total gas yield (wt.%)	42.01	59.76	42.06	67.39	51.85	67.40	56.43	80.49
Gas yield (wt.%)								
CO_2	8.73	5.16	6.54	6.60	9.78	5.32	6.02	6.37
H_2	2.75	3.42	2.63	2.67	3.78	4.71	3.62	3.67
CO	16.03	19.02	15.14	13.97	16.67	19.40	15.75	14.74
CH_4	11.48	25.11	14.13	35.16	16.07	26.41	22.61	39.01
C_2	1.86	4.34	2.85	7.09	3.32	6.51	5.30	10.59
C_3	0.90	1.90	0.61	1.53	1.38	3.13	2.04	5.23
C_4	0.22	0.65	0.13	0.34	0.58	1.30	0.78	2.01
C_5	0.05	0.16	0.03	0.04	0.24	0.54	0.30	0.77
Liquid yield (wt.%)								
Water	4.29	2.41	0.66	0.57	1.41	0.86	0.31	0.20
Acetol	0.33	0.57	0.17	0.30	0.07	0.13	0.05	0.07
FFA	18.19	18.17	11.71	6.32	6.03	5.98	5.22	1.83
Glycerol	-	0.03	0.02	0.03	-	0.01	0.01	0.01
FAME	0.17	0.12	6.42	11.03	0.03	0.02	1.90	2.59
Other fatty acid esters	0.56	0.65	1.60	1.68	0.09	0.11	0.55	0.45
C_{14-18} Hydrocarbons	0.10	0.07	0.37	0.27	0.02	0.02	0.03	0.01
Monoglycerides	16.15	8.57	4.40	1.39	19.05	11.99	4.23	1.67
Diglycerides	12.37	6.57	9.34	2.91	14.59	9.19	8.98	2.51

With external heating, the liquid phase primarily contains FFA and water (18.17 and 2.41wt.% respectively at 50W $BaTiO_3$) (Table 6.3). CO (19.02wt.% at 300°C vs 9.08wt.% at ambient temperature) and H_2 (3.42wt.% at 300°C vs 2.42wt.% at ambient temperature) were more abundant at higher temperatures (50W $BaTiO_3$), suggesting that increased temperature increases the rate of dehydrogenation. This fits with standard kinetic data from conventional thermal dehydrogenation modelling studies (Yenumala *et al.*, 2017), where the equilibrium shifts towards completion as the temperature is increased due to the endothermic nature of dehydrogenation. The results of their study (Yenumala *et al.*, 2017) indicated that increasing temperature increases conversion but reduces selectivity to the desired liquid products, which reflects prior data for conventional thermal methods (Palanisamy and Gevert, 2016). As the highest temperature used in this study (300°C) was insufficient to induce pyrolysis reactions (Dandik and Aksoy, 1998) over the 11 second residence time (triglyceride pyrolysis temperature: >400°C), the reaction rate was not affected by pyrolysis reactions. This allowed the interactions between temperature and plasma power to be isolated. DBD induced plasma primarily acts in the gas phase so only the surface of any liquid is likely to be affected (Burlica *et al.*, 2010) as established in earlier works on quenching radicals and surface modification of cellulose (Deslandes *et al.*, 1998). Therefore, introducing external heating overcomes mass transfer limitations between the gas and liquid phase, which in turn increases the conversion. With a higher temperature, shorter chain FFA and FAME partially evaporate, exposing them to the plasma directly, promoting full decomposition.

The feedstock and products were transesterified for a selection of runs to determine the effect of cold plasma on the FA chain length distribution for both FFA and glycerides (Figure 6.2). H_2 had a very limited effect on FA chain length compared to N_2, which reduced chain length by 2 carbons on average and produced C_{14} FA, which is not detected in the feedstock (Figure 6.2).

However, Ni/Al_2O_3 had a significant effect on chain length with no fatty acid chains longer than C_{16} remaining in the liquid phase as FFA or as part of glycerides, due to its induction of catalytic cracking. $BaTiO_3$ has little effect on chain length compared to no packing cases. These changes in chain length from cracking are shown in Figure 6.2, which includes FFA, FAME and the fatty acids comprising the glyceride feedstock simultaneously.

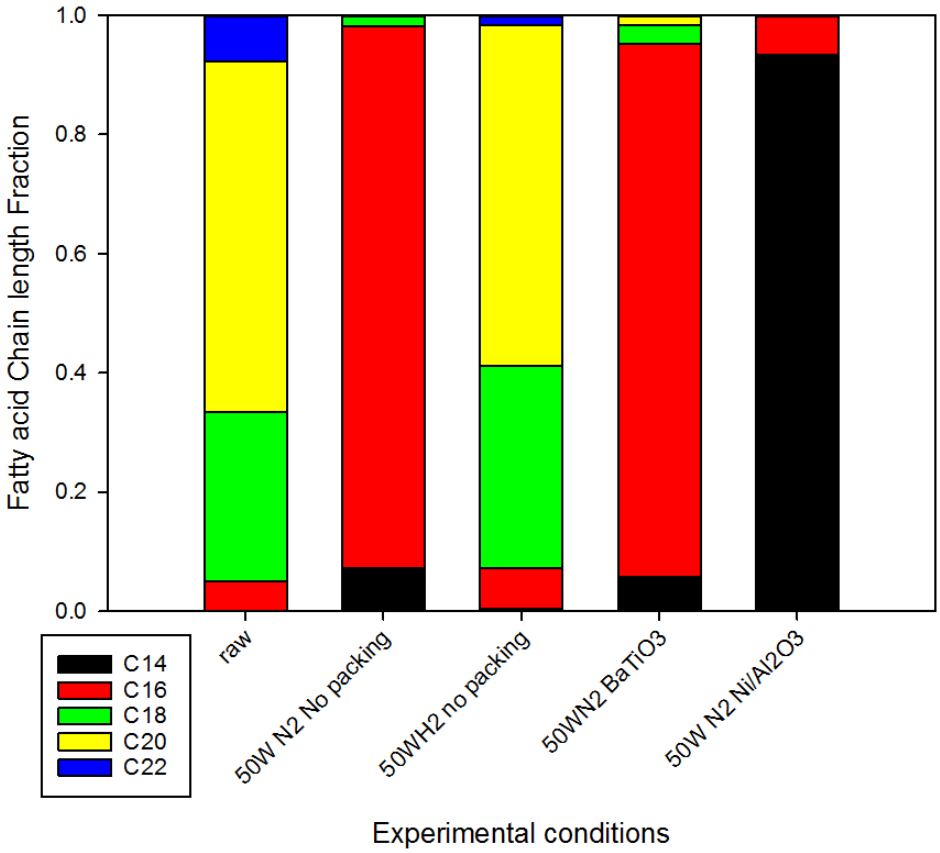

Figure 6.2: Fatty acid chain length distribution for raw rapeseed oil and products of its cold plasma decomposition for various operating conditions

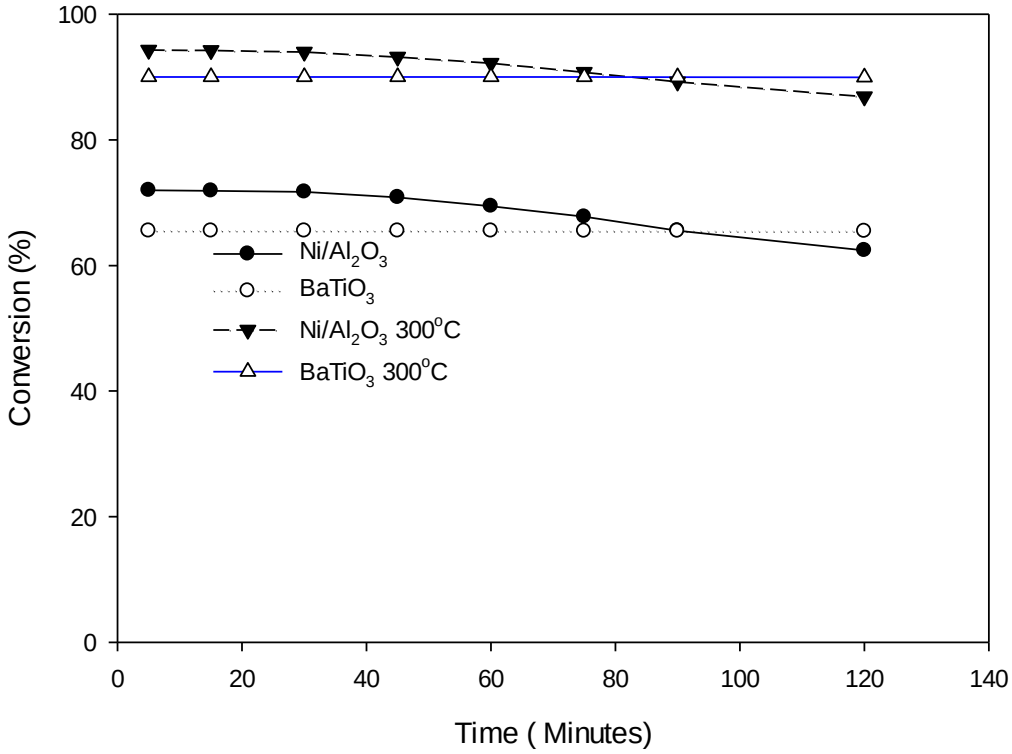

Figure 6.3: Activity profile of $BaTiO_3$ and Ni/Al_2O_3 with running time at ambient temperature and 300°C under N_2.

Ni/Al_2O_3 generated approximately 5 times more solids than $BaTiO_3$ when unheated, primarily fatty acid derived nickel soaps (0.35wt.% at 30W, 0.74wt.% at 50W) due to the reaction of FFA with nickel from the catalyst with traces of oxypolymerised glycerides (similar to that without packing: 0.03-0.23wt.%). These solids formed on the catalyst surface, which in turn decreased the conversion with time as illustrated by Figure 6.3. The catalyst released nickel soaps (from reactions between FFA and nickel in the catalyst), polymers of FFA (Figure 6.4 (b)) (Mello *et al.*, 2015) and traces of sodium and potassium soaps (approximately 2ppm sodium and potassium (Black, 1970).

Flexible rod like structures were observed over the surface of the catalyst (Figure 6.4(b)) which was mainly composed of nickel soaps. The fouling composition was confirmed by EDS of the fouled catalyst, which showed that nickel was lost during operation especially at increased temperatures and that carbon was deposited in the form of FFA (Table 6.4). With external heating to 300°C (Figure 6.4(c)), nodules form on the catalyst surface but the extent of solid fouling is greatly decreased. These nodules formed from glycerol and FFA deposition around the acidic active sites, which explains the decrease in FFA and

glycerol content between 30 and 50W in N_2 environment with Ni/Al_2O_3 as a catalyst (Table 6.3). Glycerides cannot form these nodules as they are much less polar than FFA/glycerol and hence have lower affinities for acidic areas (Bokade and Yadav, 2009; Jain *et al.*, 2011; Eze *et al.*, 2015).

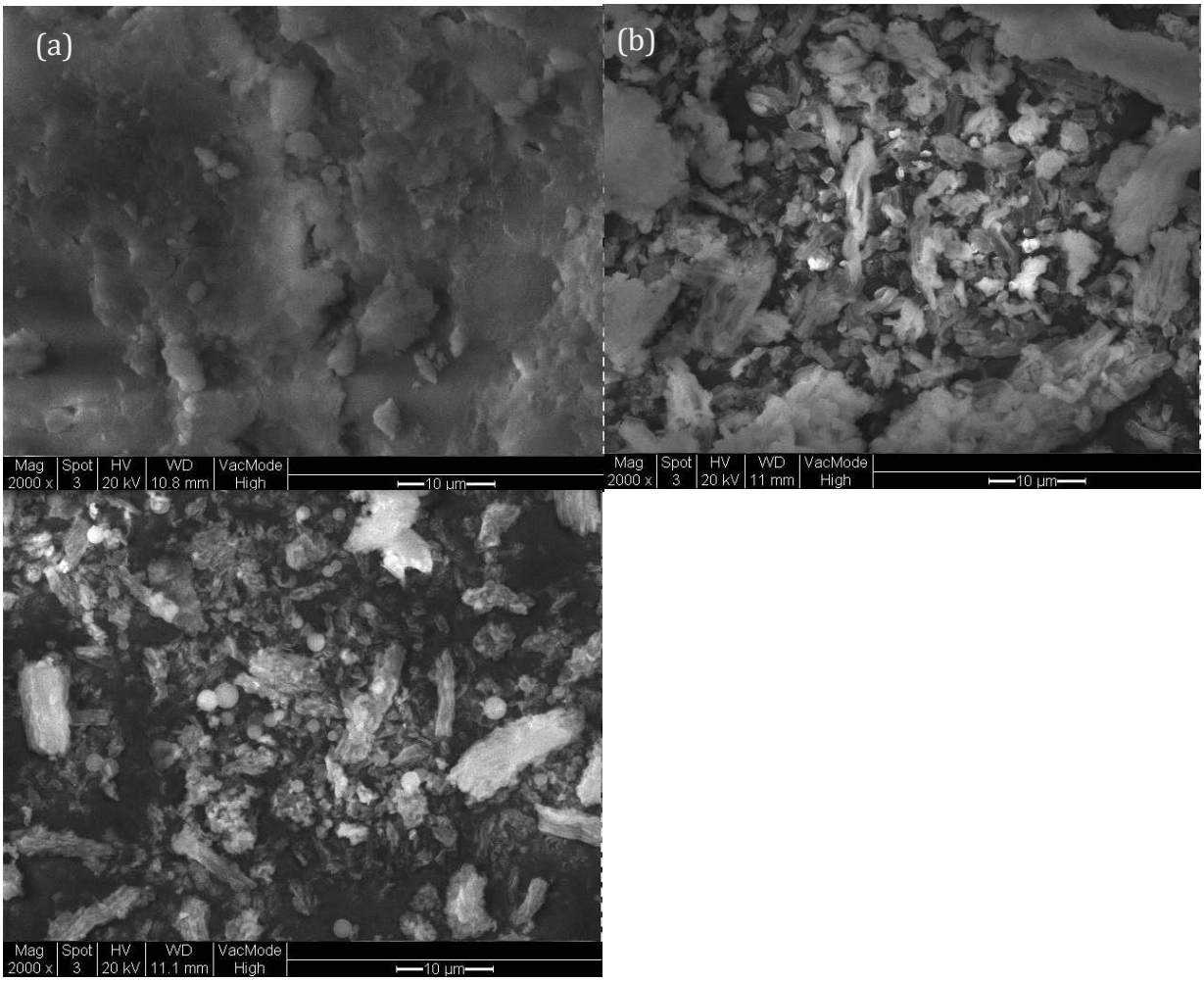

Figure 6.4: SEM images of (a) unused Ni/Al_2O_3 catalyst, (b) after triglyceride cold plasma decomposition at 50W and (c) 50W plasma with external heating of 300°C under N_2

Table 6.4: EDS analysis of fresh and spent Ni/Al_2O_3 catalyst operated at atmospheric temperature and 300°C at 50W plasma power (product distribution in Table 6.2 and 6.3)

	Aluminium (counts/sec)	**Nickel (counts/sec)**	**Carbon (counts/sec)**
Fresh	36.95	3.21	0.00
Ambient temperature Spent catalyst	31.89	2.25	6.12
300°C Spent catalyst	33.15	1.89	2.00

Nickel saponification is well known in the fat hydrogenation industry, where it is the primary source of Ni contamination in butter and other fats (Drozdowski and Zajac, 1977; Klimmek, 1984). The formation of these nickel soaps (Drozdowski and Zajac, 1977; Klimmek, 1984) is known to be catalysed by either a low pH (pH<5) environment or the presence of hydrogen radicals. Previous work has established that the nickel soaps coat the surface of the catalyst and reduce its surface area via agglomerating Ni particles (Drozdowski and Zajac, 1977). $BaTiO_3$ performance was not affected by solid formation over two hours of operation. In contrast, Ni/Al_2O_3 was significantly affected over two hours and soaps were built up both at ambient and higher temperatures (Table 6.4). Fouling affected the performance of Ni/Al_2O_3 catalyst after around 30 minutes of operation, and the catalyst was deactivated steadily as shown in Figure 6.3. The solid yields obtained at ambient temperature were 207% greater than those from the 300°C runs (1.26 vs 0.41wt.%).

6.1.3 Mechanisms

Decomposition of the feedstock is primarily via electrical excitation from the plasma field. This can produce excited species, release electrons or decompose bonds, depending on the species and power available. The probability of a bond breaking depends on the presence and abundance of radicals and the bond energy. The presence of a catalyst can improve the probability of breaking any given bond, both due to increasing effective energy density near the active sites and by actively catalysing cracking reactions at the Lewis acid sites on the nickel catalyst.

According to the kinetic theory for decomposition reactions, which is still applicable in the presence of cold plasma, low energy bonds are more readily decomposed and so the decomposition of these bonds dominates when the electron temperature (i.e. plasma power) is low. Higher energy bonds begin to decompose as electron temperature increases, and the proportion of radicals energetic enough to induce the reaction increases. In triglycerides, there are three main bond types: C-H, C-C and C-O of which the lowest energy bond is C-C (346KJ/kg), followed by C-O (358KJ/kg) and C-H (413KJ/kg). Therefore, the probability of C-C cracking is higher than C-O cracking based on the electron energy distribution shown in Chapter 4 (Figure 4.1). Triglycerides would theoretically crack along the hydrocarbon chains, as these are the weakest bonds, to form hydrocarbons and glycerides with shortened hydrocarbon chains (Figure 6.2). Previous studies (Corma Canos *et al.*, 2007) indicated the possibility of cracking FA chains but determination of the chain length distribution was not performed. Cracking of the fatty acid chains would occur at all times, generating hydrocarbons and shortening the chain length of all glycerides, FFA, FAME and other fatty acid esters (Billaud *et al.*, 2003), as observed in Figure 6.2.

It was also reported (Fridman, 2008) that the glycerol molecule could cleave to form FAME molecules and diesters, which was observed experimentally (up to 11.02wt.%) (Table 6.2). However, due to steric effects, glycerides are more likely to decompose to hydrocarbons than to FAME, as each fatty acid chain within the glyceride contains more than 15 C-C bonds (producing hydrocarbons on decomposition), whereas the glycerol backbone only contains two C-C bonds (generating FAME on decomposition). The bond energies of the backbone and hydrocarbon chains are marginally different (348KJ/mol for the backbone vs 367KJ/mol for the chains), but this does not offset the steric effects and the resulting rate constants are not significantly different ($k= 5.01x10^{-12}$ for the backbone vs $4.78x10^{-12}cm^3$/molecule s^{-1} for the FA chain) (NIST). This explains the low selectivity to FAME overall.

Hydrogen radicals derived from cleaved C-H bonds throughout the glyceride molecule can stabilise fragments that are released after cracking. They react with unstable radicals such as methyl radicals via a termination reaction, which inhibits further decomposition

reactions. This is evidenced by the lower yields of mid length hydrocarbons (C_4 to C_9) under hydrogen (0.17wt.% under N_2 vs 0.08wt.% under H_2) (Table 6.2).

From the experimental results obtained in this study (Tables 6.1, 6.2 and 6.3), hydrocarbons were among the most abundant products (from C-C bond cracking), while FFA (from de-esterification at a C-O bond) yields increased significantly as plasma power increased. The cracking and de-esterification based mechanism, detailed in Reactions 6.1 and 6.2, are very similar to how thermal cracking operates (320-500°C) (Wako *et al.*, 2017). However, there are some key differences that explain the relative lack of long chain hydrocarbons, such as mass transfer limitations between the gas and liquid phases. Cold plasma primarily affects the gas phase with some interactions with the liquid phase at the surface, in contrast to thermal decomposition where no stable liquid phase exists. This means that cold plasma is slower at decomposing non-volatiles than volatile components, while thermal decomposition results in more extensive decomposition. Glycerides and fatty acids are not volatile at the temperatures reached in the cold plasma reactor even with external heating to 300°C. However, hydrocarbons are more volatile, which exposes them to the more intense electric field in the gas phase, which induces further decomposition. This results in the formation of shorter chain hydrocarbons (C_1-C_6), which are abundantly produced at all powers (e.g. 44.16wt.% at 50W N_2 at 300°C with Ni/Al_2O_3). H_2 is also released from splitting of the C-H bonds.

Based on the presence of FFA at all conditions, it can be concluded that the decomposition of triglycerides to FFA and diglycerides is the dominant reaction under cold plasma, which agreed with previous studies for catalytic decomposition of triglycerides over Ni/Al_2O_3 (Yenumala *et al.*, 2017). However, the presence of other fatty acid esters, aldehydes and hydrocarbons suggests that some triglycerides decompose to other fatty acid esters and aldehydes by release of a fatty acid chain, similarly to thermal decomposition (Kulkarni and Dalai, 2006). Diglycerides would also form oxopropyl fatty acid esters due to the presence of an alcohol group in the place of an FFA chain. Monoglycerides would decompose similarly, either to glycerol and FFA or FAME and ethandiol due to the number of remaining fatty acid chains (Yenumala *et al.*, 2017).

A small amount of FAME was also generated at all powers in N_2 environment with yields increasing with plasma power (0.22 at 10W vs 3.99wt.% at 30W with Ni/Al_2O_3). The generation of a FAME molecule from a triglyceride molecule via hydrocracking of the glycerol backbone would also produce a radical ethandiol fatty acid di-ester. This would likely stabilise to ethendiol fatty acid di-ester, or to 2 FAME molecules depending on the concentration of hydrogen radicals, with hydrogen radicals favouring increased FAME yields. This would explain the higher FAME yields at higher plasma powers, as the more abundant hydrogen radicals allow the unstable radical ethandiol di-ester to reform to 2 FAME molecules, tripling the effective yield of FAME. This reaction pathway was also observed for thermal processes with a zirconium sulfate catalyst (Eterigho, 2012).

Formic acid and hydrocarbons were the dominant products of FFA decomposition (Li *et al.*, 2011a). The formic acid is likely then dehydrogenated to CO_2 via dehydrogenation reactions, particularly in the absence of hydrogen radicals (Santillan-Jimenez *et al.*, 2014). FAME and other fatty acid esters also decompose to produce formic acid and hydrocarbons and release methanol or acetol respectively.

Any glycerol formed during decomposition would most likely convert to acetol and then propenal (Hemings *et al.*, 2012; Harris *et al.*, 2018). Propenal can then decompose to hydrocarbons and CO, which were detected in the N_2 environment (Table 6.1). This fits with experimental data as acetol levels were lower than expected (0.09wt.% at 50W N_2) given the extent of glyceride decomposition (50.94% at 50W N_2), while hydrocarbons and CO were the dominant products.

Triglyceride decomposition

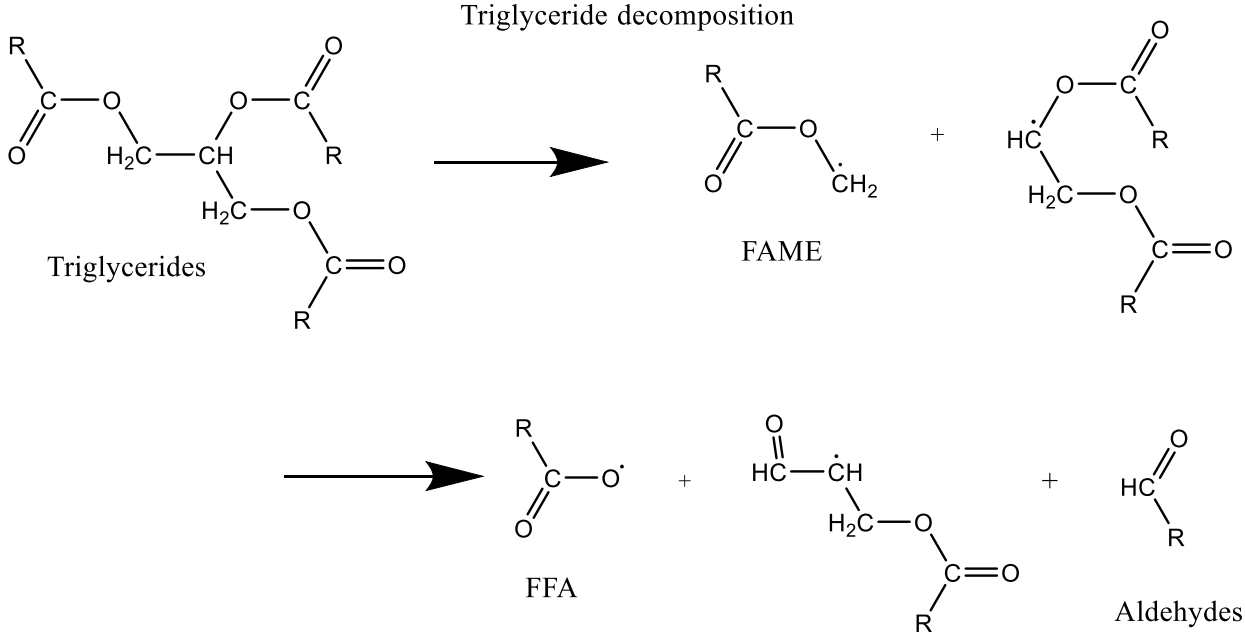

ethyl fatty acid diester decomposition

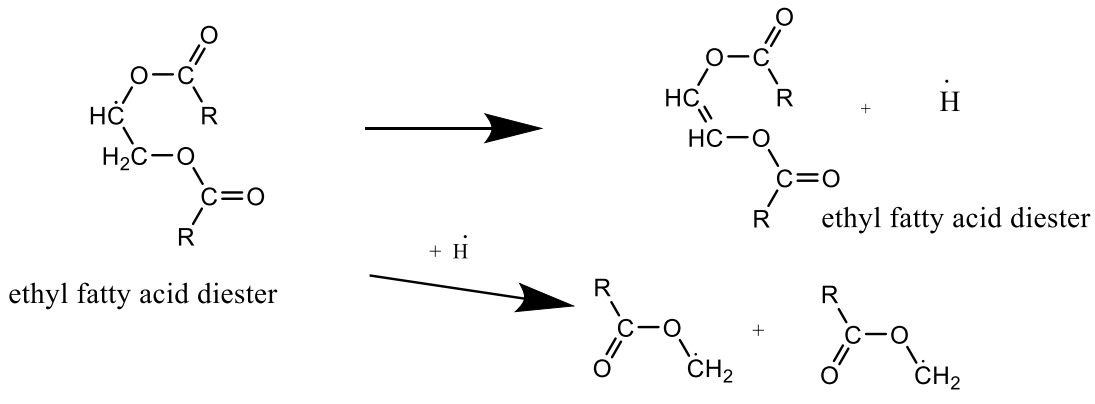

Diglyceride decomposition

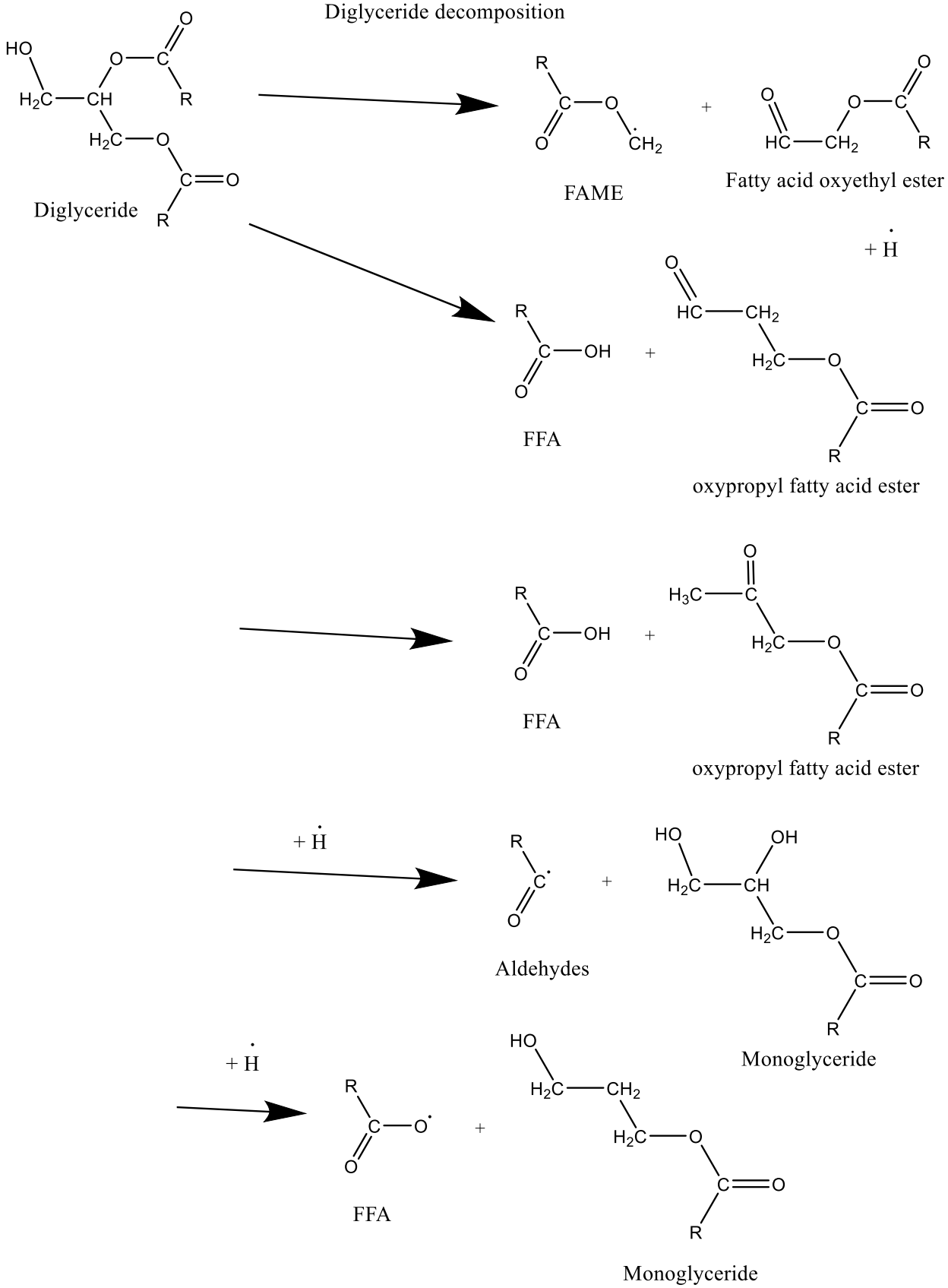

oxypropyl fatty acid ester decomposition

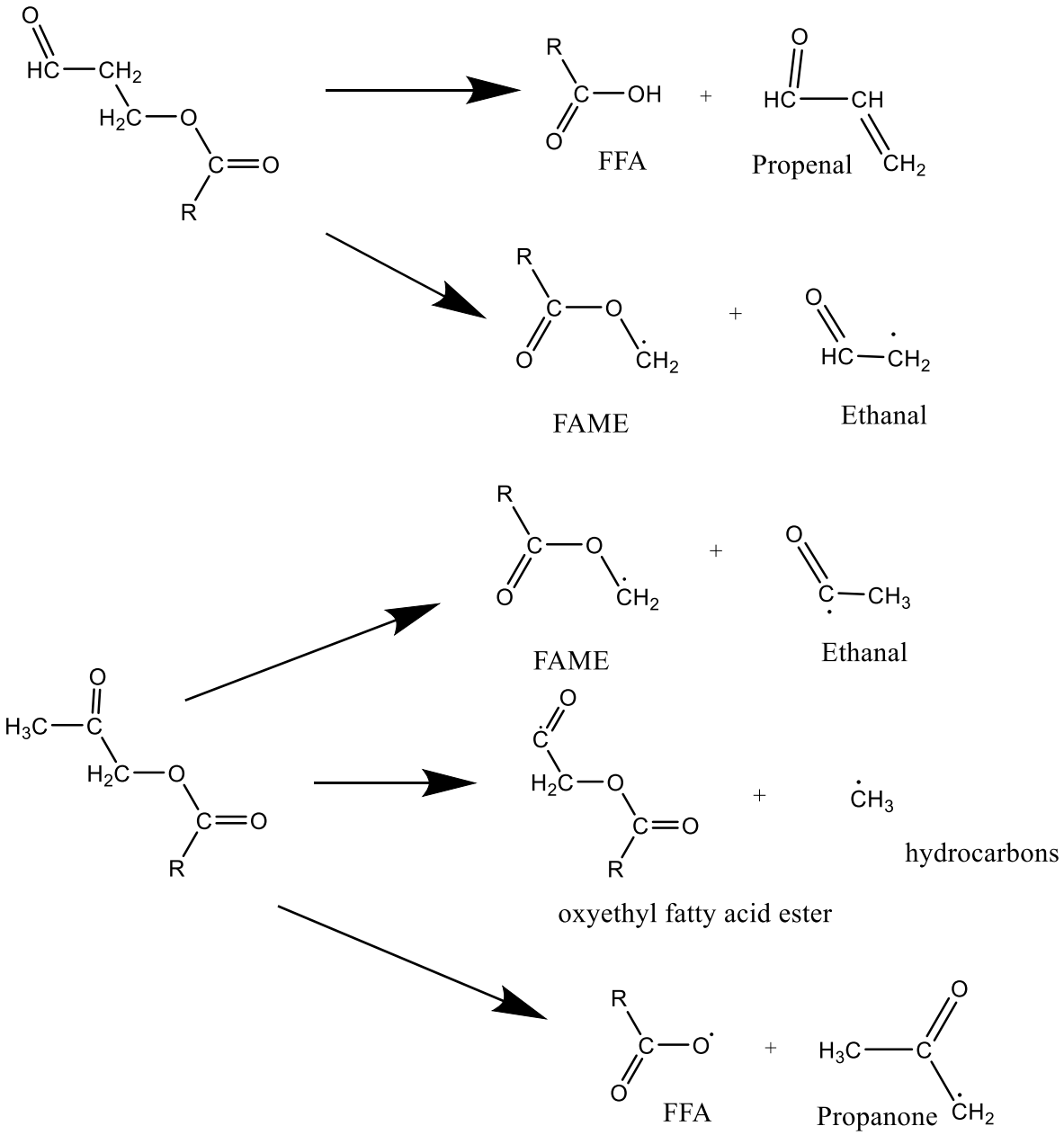

oxyethyl fatty acid ester decomposition

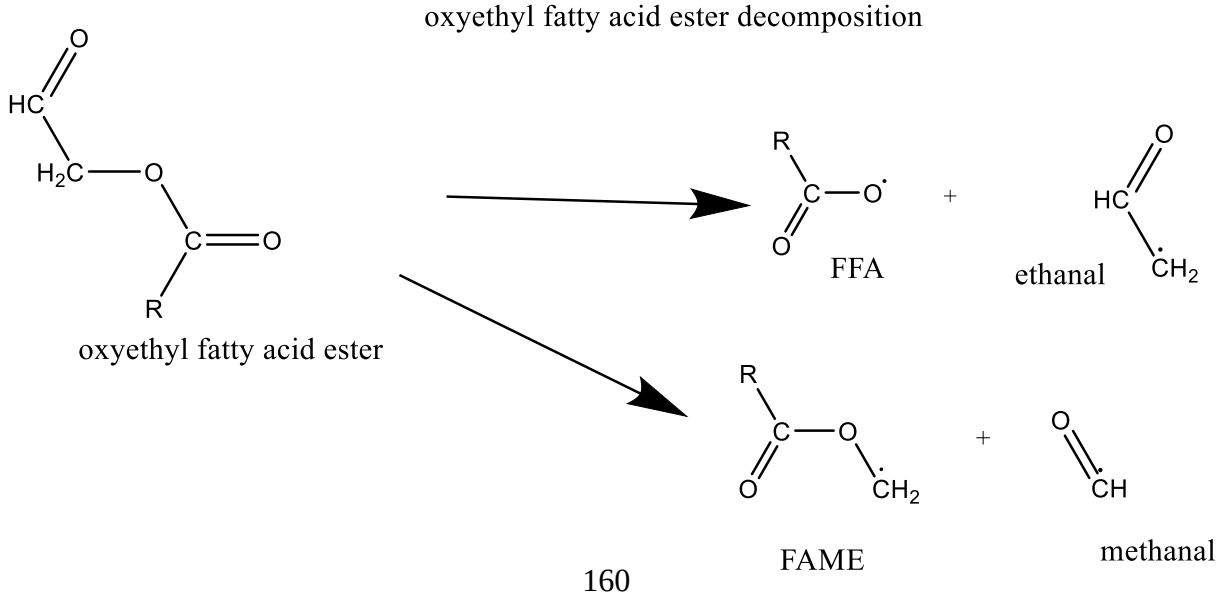

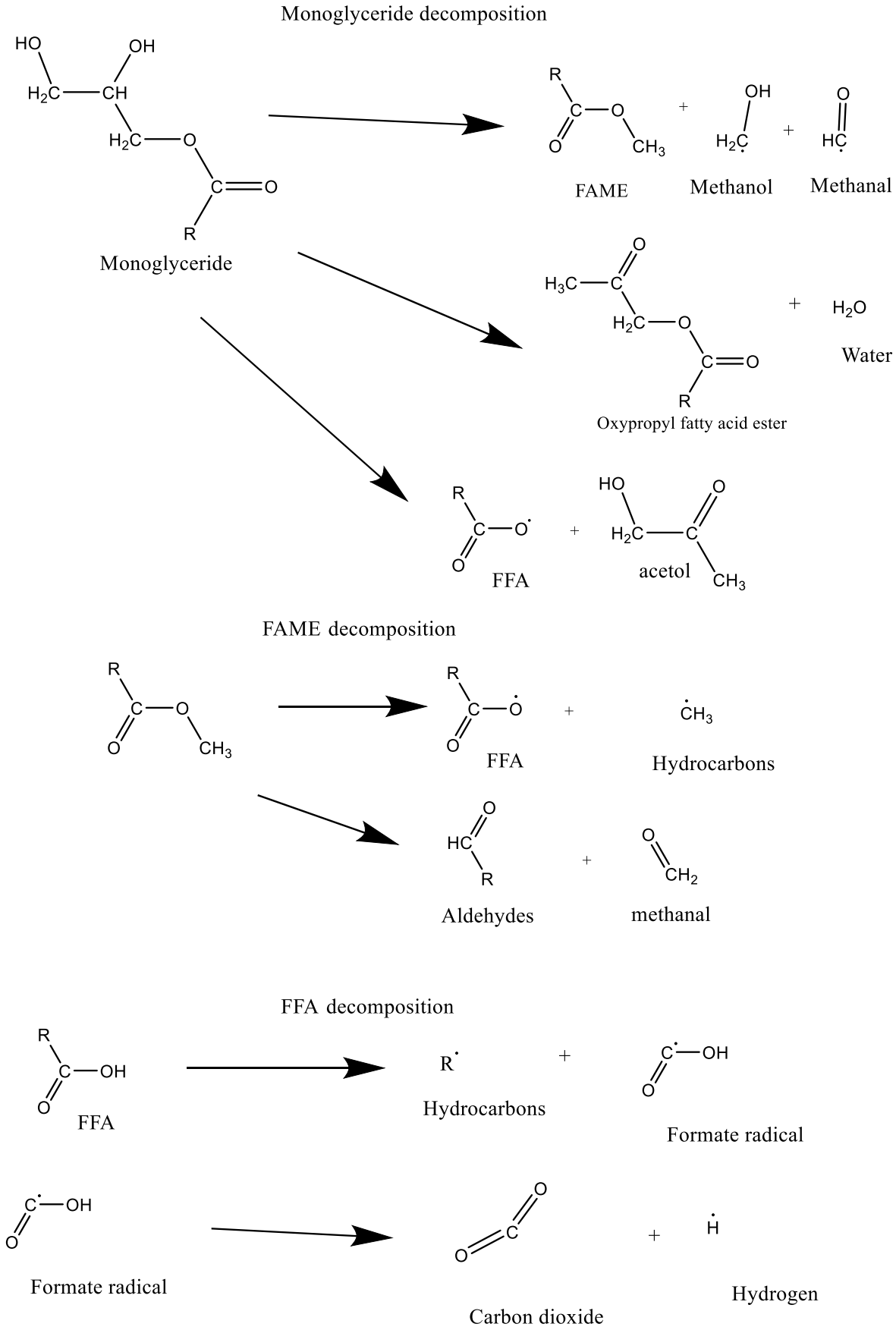

Figure 6.5: Proposed mechanism of cold plasma assisted triglyceride decomposition

6.2 Waste cooking oil (WCO)

In this section, the feasibility of processing untreated waste cooking oils to value added products using gas-liquid cold plasma was established. The effects of carrier gas, plasma power, reaction temperature, residence time and packing material/ catalysts in the plasma zone and their interactions on product distribution and conversion were investigated.

6.2.1 Initial studies

Table 6.5 shows that the conversion of WCO in a H_2 environment increased with plasma power. This is due to increasing concentrations of high energy excited species and electrons at higher powers, which collide with molecules to induce reactions. However, N_2 shows almost zero conversion at 10W (-1.46%) and 50W (-0.75%) likely due to esterification between mono/diglycerides and FFA cancelling out the forward reaction. Notably, at 30W, there was an apparent negative conversion (around -6%), providing evidence of an esterification reaction to generate glycerides from FFA and/or FAME. This was observed experimentally as the distribution of the glycerides was shifted from monoglycerides towards triglycerides/diglycerides (89.3wt.% at 10W vs 94.4wt.% at 30W diglycerides/triglycerides under N_2), while the FFA content dropped sharply (from 12.43wt.% for the feedstock (Table 3.3) to 5.80wt.% at 30W). Some of the FFA may have been converted to gaseous products/ liquid hydrocarbons and aldehydes, but the gas, hydrocarbon and aldehyde yields have not shown a significant increase (0.04wt.% at 30W) and cannot account for the large decrease in FFA yield (6.63wt.% at 30W). Esterification has been shown to occur under cold plasma (Chapters 4 and 5), but would require highly energetic radicals and high plasma power (Gorin and Taylor, 1934; Burlica *et al.*, 2010).

Under the N_2 environment, CO_2 marginally increased with plasma power, from 1.58 to 2.13wt.%. However, the total gas yield under N_2 was low overall (4.01-4.15wt.% for WCO vs 6.81-14.41wt.% for pure triglycerides) compared to the equivalent pure triglyceride results shown in Table 6.1 above. This is most likely due to a competing reaction, which would consume reaction initiators such as radicals and reduce the concentration available for triglyceride decomposition. A decrease in FFA from 12.43wt.% in the feedstock to

5.15wt.% at 10W and complete consumption of glycerol at low powers (10-30W) under N_2 indicates that esterification of glycerides with FFA is likely to have occurred, which is supported by the increasing yields of glycerides with increasing plasma power. At 50W, glycerol and FFA yields increase, which indicates the decomposition of glycerides begins to dominate over the esterification reaction at 50W. This is evidenced by the increase in conversion (-0.75% at 50W vs -6.04% at 30W) and the increased yields of FFA (10.18 at 50W vs 5.8wt.% at 30W), glycerol and hydrocarbons.

In the H_2 environment, CO and CO_2 were not formed, which could be due to the presence of abundant hydrogen radicals preventing cracking and dehydrogenation of carboxylic or alcohol groups. A similar finding was observed during hydrogenation of WCO at 120°C with supercritical propane (183bar) (Piqueras *et al.*, 2009). In contrast to the pronounced negative conversions under N_2 in this work, esterification of monoglycerides /diglycerides was not observed (68.42wt.% glycerides at 10W to 53.66wt.% at 50W) under H_2. This indicates the decomposition of glycerides dominates over glyceride reformation at all powers under H_2.

Table 6.5: Cold plasma assisted WCO decomposition without packing materials at a residence time of 11 seconds, atmospheric conditions and a ratio of gas to liquid of 40:1 (vol/vol) (errors: ±3wt.% for conversion, 4% for product yields)

Carrier gas	**H_2**			**N_2**		
Plasma power (W)	10	30	50	10	30	50
Glyceride Conversion (%)	2.73	7.67	30.01	-1.46	-6.04	-0.75
Solids (wt.%)	-	-	-	-	-	-
Total gas yield (wt.%)	4.55	5.55	17.52	3.21	4.15	4.01
CO_2	-	-	-	1.58	1.93	2.13
H_2	-	-	-	0.06	0.05	0.04
CO	-	-	-	0.99	1.59	1.28
CH_4	4.55	5.55	13.16	0.44	0.39	0.48
C_2	-	-	3.38	0.15	0.19	0.23
C_3	-	-	0.62	-	-	0.05
C_4	-	-	0.23	-	-	0.02
C_5	-	-	0.09	-	-	-
C_6	-	-	0.03	-	-	-
C_7	-	-	-	-	-	-
Liquid yield (wt.%)						
Water	4.25	1.83	0.36	2.70	1.63	1.97
Acetol	0.28	1.47	12.42	0.89	0.39	0.03
FFA	12.47	7.23	4.54	5.15	5.80	10.18
Glycerol	1.78	1.99	-	-	-	0.98
FAME	2.31	4.21	4.49	3.42	4.24	2.21
Other fatty acid esters	4.12	6.23	5.35	9.47	6.29	4.82
$C_{14\text{-}18}$ Hydrocarbons	0.93	0.98	0.84	1.69	1.23	1.88
$C_{14\text{-}18}$ Aldehydes/ketones	0.89	0.95	0.83	1.71	1.27	2.46
Monoglycerides	11.13	11.12	9.71	7.66	4.22	1.25
Diglycerides	11.68	23.13	15.79	25.93	33.76	24.74
Unreacted triglycerides	45.61	35.30	28.16	38.17	37.02	45.27

In the H_2 environment at 10W, high yields of fatty acid methyl esters (FAME) (2.31wt.%), other fatty acid esters (FAE) (4.12wt.%), FFA (12.47wt.%) and water (4.25wt.%) were observed. The presence of these and the abundant methane yield (4.55wt.%) provide evidence of cracking reactions. However, the glyceride content of the feedstock (Table 3.3) is almost unaffected by 10W plasma. This indicates that low power gas-liquid plasma

may be utilised for selective decomposition of FAE from glyceride samples or if high selectivity to gaseous hydrocarbons is required. As the plasma power increased to 30W, the FAME: other fatty acid esters ratio significantly decreased (from 1:1.8 to 1:1.5), accompanied by a reduction in FFA yields (12.47wt.% to 7.23wt.%). This suggests that increased plasma power favours the decomposition of the glycerol backbone over the removal of a fatty acid chain from glyceride molecules. This is supported by the significantly increased yields of methane (5.55wt.% compared to 4.55wt.%) in the gas phase.

As the power increased to 50W, the gas yield increased significantly, to 17.52wt.%. A slight decrease in long chain hydrocarbons (C_{14}-C_{18}) (0.98wt.% to 0.84wt.%) was observed between 30W and 50W under H_2, and the presence of hydrocarbons up to heptane was observed at 50W. Additionally, a plateau in FAME (4.21 vs 4.49wt.%) and decrease in FFA (7.23 vs 4.54wt.%) yields were apparent under the same conditions. These yields can be explained by decomposition of FAME, long chain hydrocarbons and FFA to short chain hydrocarbons and water. Evidence for this conclusion is the sharp increase in short chain hydrocarbon yields (C_1-C_8) (17.52wt.% from 5.55wt.%) and increased water/acetol yields (4.25wt.%) under H_2. This reaction pathway is reflected in literature accounts for thermal cracking of FFA (Sang, 2003), which can occur at relatively low temperatures (400°C), similar to that required for FAME generation (Billaud *et al.*, 2003; Bhatia *et al.*, 2007). Methane is the only hydrocarbon generated at 10-30W under H_2, which most likely indicates the hydrogen radical concentration is sufficiently high to prevent polymerisation of methyl radicals via termination reactions, as discussed in Chapter 5.1.2.

A large increase in acetol yield (from 1.47wt.% to 12.42wt.%) from 30W to 50W in the H_2 environment indicates that extensive de-esterification of glycerides generated glycerol, which further decomposed to acetol. The decrease in glyceride content (68.42wt.% at 10W to 53.66wt.% at 50W), supports this conclusion.

The high yields of FAE and FFA and reduced glyceride contents suggest that H_2 is effective for promoting glyceride decomposition. In contrast, N_2 preferentially deoxygenates

FFA/FAME, as evidenced by the increased carbon oxide and hydrocarbon content. To compare, hydrodeoxygenation of triglycerides requires 380-420°C, 10-20Bar H_2 and catalysts such as sulfated zirconia and HZSM-5, to produce deoxygenated liquid fuels (51.12wt.%) and carbon oxides (10.87wt.%) over a 45-90 minute reaction time (Charusiri *et al.*, 2006).

Conventional thermal decomposition of WCO was investigated using a range of different catalysts. For glyceride hydrogenation at 30bar and 280-360°C using Ni/Al_2O_3 catalyst**,** the dominant products were FFA and diglycerides (Yenumala *et al.*, 2017). FFA was found to decompose further to hydrocarbons, aldehydes and alcohols with little effect on the glycerol backbone (Billaud *et al.*, 2003). Similar results were reported in a N_2 environment, producing mostly FFA and glycerides (Maher and Bressler, 2007). It was found (Kulkarni and Dalai, 2006; Azahar *et al.*, 2016) that triglycerides can decompose to oxopropyl fatty acid esters when heated to 180°C for > 4 hours. This supports the conclusion that other fatty acid esters derive from dehydration of glycerides, as the feedstock (Table 3.3) contains both FAE (which includes oxopropyl fatty acid esters) and other dehydration products such as FFA, in contrast to the unused oils. The WCO used in this work contained some oxopropyl fatty acid esters initially (6.14wt.% of 9.18wt.% other fatty acid esters) (Table 3.3) due to its prior use, reflecting prior studies on Tricaproin decomposition at 250°C (Lien and Nawar, 1973).

Compared to studies on conventional thermal decomposition or hydrogenation at 400˚C, cold plasma produced a lower conversion but can tolerate fouling effectively over long operation times and operate without a catalyst. The process can be tuned to favour specific products, such as acetol. Direct production of acetol from triglycerides has not been achieved in thermal processes to date regardless of catalyst choice and the formation of hydrocarbons and removal of FFA are potentially beneficial. If the selectivity to acetol can be optimised and the conversion increased, it may be possible to generate acetol and liquid hydrocarbons from triglycerides directly using cold plasma.

As shown in Table 6.6, temperature is the dominant factor for thermal decomposition of FAME, FFA and FAE, with the yields of these components dropping significantly at

increased temperatures (10.81 to 8.58wt.% FFA at 250°C and 300°C respectively). FFA is generated at significant levels at all temperatures and plasma powers due to its continuous formation from glyceride dehydration. A very high water yield was observed at high temperatures (e.g. 22.43wt.% in H_2 and 25.82wt.% in N_2 at 300°C), which provides strong evidence of glyceride dehydration to FFA and glycerol.

Due to their structural similarities to FFA, FAME and FAE would also be decomposed at high temperatures to hydrocarbons, as shown experimentally (59.86wt.% at 300°C), and CO_2 (4.50wt.% at 300°C) (Table 6.6).

The gaseous yields appear to exceed the conversion values in Table 6.6, due to the decomposition of FFA, FAME and FAE to gaseous products. This is because the conversion is limited as it is calculated based on the total glyceride content of the feedstock and products, which does not take into account decomposition of other components into gaseous products. This limitation is necessitated by the complexity of the feedstock and products, but provides an effective measure of glyceride decomposition within the cold plasma.

Table 6.6: Comparison of thermal decomposition and combined heating/cold plasma of WCO at 11 second residence time and a 40:1 gas to liquid ratio (errors: 5%)

Catalyst	**Thermal**				**Thermal + 50W plasma**			
Carrier gas	H_2		N_2		H_2		N_2	
Temperature (°C)	250	300	250	300	250	300	250	300
Glycerides Conversion (%)	2.08	12.11	2.63	16.20	54.72	63.99	26.66	81.45
Total gas yield	1.40	1.34	5.63	3.45	28.95	69.23	23.88	50.33
Gas yield (wt.%)								
CO_2	-	0.42	-	1.70	1.32	4.50	2.96	3.92
H_2	-	0.01	-	-	-	-	2.58	1.18
CH_4	0.84	0.08	3.38	0.36	7.68	10.52	3.93	5.60
CO	-	0.32	-	0.31	2.44	5.84	8.82	5.85
C_2	0.56	0.06	2.25	0.59	4.89	18.34	1.73	13.28
C_3	-	0.26	-	0.38	9.32	21.71	3.26	14.96
C_4	-	0.13	-	0.10	2.05	5.28	0.46	3.46
C_5	-	0.03	-	0.01	1.13	2.74	0.12	1.95
C_6	-	0.03	-	-	0.10	0.21	0.03	0.12
C_7	-	0.01	-	-	0.01	0.10	-	0.01
Liquid yield (wt.%)								
Water	15.74	22.43	13.75	25.82	0.07	0.04	0.09	0.04
Acetol	0.54	1.36	0.77	1.88	0.46	0.17	5.72	1.94
FFA	10.81	8.58	10.38	9.42	9.57	9.74	24.60	12.33
Glycerol	1.86	4.04	0.47	0.13	0.33	0.01	0.19	0.03
FAME	0.09	0.02	0.03	-	7.15	9.63	3.68	0.47
Other fatty acid esters	0.25	0.05	0.10	0.02	10.17	6.95	1.80	0.28
C14-18 Hydrocarbons	0.02	0.01	0.01	-	0.50	0.96	0.51	0.10
C14-18 aldehydes/ketones	0.04	0.01	0.01	-	0.51	0.97	0.47	0.06
Monoglycerides	10.12	8.10	12.35	9.22	18.83	19.20	28.84	9.15
Diglycerides	11.64	17.42	19.88	19.72	10.40	4.79	14.85	3.03
Unreacted Triglycerides	47.50	36.64	36.64	30.33	2.80	1.48	8.18	0.91

As shown in Table 6.6, applying external heating to 50W cold plasma increased the total gas yield (i.e. increasing from ≤5.63wt.% to ≥23.88wt.% under N_2) and conversion of glycerides significantly (from 16.2wt.% to 81.45wt.% under N_2). In the H_2 environment, significant yields of FAME and FFA but little acetol were observed compared to those in N_2 environment. This is expected as acetol formation can be prevented by hydrogen radicals (Li *et al.*, 2009). The N_2 environment produced a high yield of hydrocarbons (39.38wt.% at 300°C) in the gas phase with predominantly FFA (12.33wt.%) and acetol (1.94wt.%) in the liquid phase.

In the H_2 environment at 50W, increasing the temperature increased FAME yields (to 9.63wt.%), indicating these conditions favour hydrocracking of the glycerol backbone to generate FAME. Increased rates of cracking would promote decomposition of the fatty acid chains to generate hydrocarbons, which was reflected in the gas phase results (58.9wt.% hydrocarbons at 50WH_2 and 300°C). Increasing the reactor temperature (300°C) meant that any FAME and short chain FFA (up to C_{12}) present in the reactor could evaporate. The high energy electrons in the gas phase could then decompose them rapidly and hence increase conversion (from 30.01% at ambient temperature to 63.99% at 300°C at 50W) and thus FFA/hydrocarbon yields. This would explain the higher selectivity to FAME and hydrocarbons observed experimentally under H_2 compared to N_2 in Table 6.6.

6.2.2 Effects of packing material

The use of $BaTiO_3$ increased gas phase product yields (4.01wt.% vs 6.28wt.%) for N_2 (Table 6.7) compared to those without packing (Table 6.5), but little effect was observed for H_2. In the liquid phase, a large decrease in triglycerides (18.19wt.% vs 45.61wt.%) coupled with an increase in FAME (6.31wt.% vs 4.49wt.%) and FAE (13.51wt.% vs 5.35wt.%) yields were observed. This suggests that $BaTiO_3$ enhances the decomposition of triglycerides to FAME or FAE

Table 6.7: Cold plasma assisted WCO decomposition at atmospheric temperature with packing material/catalyst at a residence time of 7 seconds and a 40:1 liquid to gas ratio (vol/vol) (errors:10%)

	Catalyst	$BaTiO_3$			$BaTiO_3$			Ni/Al_2O_3			Ni/Al_2O_3		
	Carrier gas	H_2			N_2			H_2			N_2		
	Plasma power (W)	10	30	50	10	30	50	10	30	50	10	30	50
	Glyceride Conversion (%)	0.34	14.68	33.17	2.53	52.88	43.77	-1.36	-0.66	1.41	2.35	31.05	12.33
	Total gas yield (wt.%)	11.82	13.78	16.69	3.01	4.91	6.28	1.83	3.41	4.59	4.41	5.99	9.15
Gaseous Yields (wt.%)	**CO_2**	-	-	-	1.96	4.09	4.70	1.75	1.64	2.20	1.24	4.24	4.40
	H_2	0.02	0.26	0.26	0.12	0.19	0.95	0.02	0.05	0.06	0.80	0.21	0.23
	CO	-	-	-	0.60	0.34	0.18	0.07	0.99	1.33	1.17	0.74	2.68
	CH_4	11.81	12.15	14.32	0.32	0.26	0.41	-	0.44	0.59	0.90	0.53	1.40
	C_2	-	1.07	1.62	0.02	0.03	0.03	-	0.22	0.29	0.22	0.17	0.28
	C_3	-	0.23	0.35	-	0.01	0.01	-	0.05	0.08	0.05	0.05	0.09
	C_4	-	0.05	0.12	-	-	-	-	0.03	0.04	0.03	0.04	0.05
	C_5	-	0.01	0.03	-	-	-	-	-	0.01	-	0.01	0.03
Liquid Yields (wt.%)	**Water**	0.15	0.15	0.10	0.24	0.15	0.13	2.19	1.17	0.13	0.16	0.13	0.14
	Acetol	0.90	0.05	0.08	-	-	0.14	0.61	-	-	0.91	0.42	0.76
	FFA	7.67	6.40	13.93	17.86	56.85	45.65	15.81	10.26	7.44	10.41	3.73	2.95
	Glycerol	0.05	0.16	0.18	0.12	1.12	0.24	0.16	0.83	0.03	0.71	0.05	-
	FAME	2.41	6.69	6.31	2.75	1.44	0.93	2.19	4.45	6.08	6.95	31.30	22.72
	Other fatty acid esters	4.77	10.58	13.51	5.46	5.30	5.79	5.42	7.57	9.98	6.83	9.05	2.19
	$C_{14\text{-}18}$ Hydrocarbons	0.88	0.93	0.97	0.80	0.63	0.53	0.05	0.67	0.78	0.31	0.29	0.03
	$C_{14\text{-}18}$ Aldehydes	0.86	0.91	0.96	0.82	0.64	0.51	0.05	0.44	0.53	0.24	0.28	0.02
	Monoglycerides	27.40	14.92	19.97	45.18	14.55	11.23	1.99	9.40	27.34	9.32	25.99	36.40
	Diglycerides	24.90	31.25	15.23	13.99	13.39	21.34	35.87	35.13	28.19	25.26	17.31	21.10
	Unreacted Triglycerides	18.19	14.18	12.07	9.77	5.39	7.20	33.83	26.67	14.91	36.57	5.47	4.51

As shown in Table 6.7, the glyceride conversion in the presence of Ni/Al_2O_3 was much lower than that in $BaTiO_3$ (31.05% vs 52.88% at 30W). This is because Ni/Al_2O_3 favours C-C bond cracking reactions (Bartholomew and Farrauto, 1976), which reduces fatty acid chain lengths and cracks glycerides to FAME and unstable diols. By comparison, $BaTiO_3$ can be observed to induce de-esterification, from increased FFA yields (57.85wt.% under $BaTiO_3$ vs 3.73wt.% Ni/Al_2O_3 at 30W) (Table 6.7), therefore increasing overall glyceride conversion. Supporting this conclusion, the presence of $BaTiO_3$ reduces the triglyceride content (5.39-18.19wt.%) significantly compared to no packing material (28.16-45.61wt.%).

Ni/Al_2O_3 was found to promote the formation of FAME (31.3wt.% with Ni/Al_2O_3 vs 1.44wt.% with $BaTiO_3$ at 30W N_2) as opposed to de-esterification products (e.g. acetol and glycerol). This was also concluded in Section 6.1 for pure triglcyerides**.** FAME is predominantly formed from cracking the glycerol backbone of triglycerides, which is catalysed by Ni/Al_2O_3 (Yenumala et al., 2017). Cracking of the fatty acid chains would also be catalysed by Ni/Al_2O_3, which explains the high yields of gaseous hydrocarbons.

When a catalyst is introduced to the plasma, plasma initiated chemical reactions predominantly occur both as gas phase reactions and as heterogeneous reactions on the catalyst surface (Zhang et al., 2017). Therefore, a catalyst may significantly influence the plasma chemistry both by providing Lewis acid active sites and by focussing the plasma onto its surface via the dielectric effect (Figure 5.6), increasing the temperature sufficiently to induce limited thermal decomposition. Plasma also imparts a charge to the catalyst, which helps attract feedstock molecules towards the active sites. The interaction between DBD plasma and the catalyst is complex, as the catalyst's dielectric properties can modify the electric field and the electric field may, in turn, affect catalyst effectiveness via altering the surface properties of the catalyst. One notable effect of the catalyst on the electric field is allowing operation at much lower temperatures and with greater efficiency (Kraus et al., 2001). These plasma-catalyst interactions have been previously studied for CO_2 decomposition (Kraus *et al.*, 2001; Zhang *et al.*, 2017).

Tables 6.7 and 6.8 show that increasing the residence time increases glyceride conversion (from 43.77% to 77.91% at 50W in N_2 for $BaTiO_3$). A slight increase in the gas yield was observed (18.70wt.% at 11 seconds vs 6.28wt.% at 7 seconds for 50W N_2 with $BaTiO_3$) with an increase in residence time, as shown in Table 6.7 and 6.8, particularly carbon oxides and gaseous hydrocarbons (C_1-C_6). This is due to more extensive cracking reactions at the longer residence time (Cho *et al.*, 2014). A similar behaviour was observed for Ni/Al_2O_3, as increasing residence time also increased conversion from 31.05% to 94.48% at 30W (Table 6.8).

Initial decomposition product yields were not affected by residence time, notably FFA (56.85wt.% vs 57.56wt.% at 30W in N_2) for $BaTiO_3$ and FAME/FAE (35.01wt.% vs 40.35wt.% at 30W in N_2) for Ni/Al_2O_3. Increasing the residence time from 7 to 11 seconds improved glyceride conversions (Table 6.8 vs Table 6.7), which is most likely due to the increase (around 70%) in specific input energy and allowing decomposition to progress further.

In the presence of $BaTiO_3$, applying external heating (300°C) to cold plasma slightly increased the conversion compared to experiments carried out at atmospheric temperature (87.63% vs. 77.91%) (Table 6.8 and 6.9). However, the yield of FFA decreased with heating (35.47wt.% compared to 57.56wt.%) which suggests that the increased hydrocarbon yield (18.27 vs 7.22wt.%) was from FFA decomposition. This implies a very high rate of decarbonylation to convert FAME, FAE and FFA into CO_2, CO and hydrocarbons (Wako *et al.*, 2017). This is due to the energy states of N_2 and H_2 molecules, which are close to the bond energy of the C-O bond (358KJ/mol) (3.69eV) (San Fabián and Pastor-Abia, 2007). At a sufficiently high temperature i.e. 300°C, FAME and FAE can evaporate, where the N_2 excited species can rapidly decompose them to FFA and methanal/propenal (Koeta *et al.*, 2012). FFA and glycerides would not evaporate under these conditions, remaining in the liquid phase (Neretti *et al.*, 2017), hence reducing the rate of glyceride decomposition compared to decomposition of more volatile components such as FAME. This effect also explains the high yields of propenal derived from glyceride decomposition (up to 15.46wt.% with a 11 second residence time) (Table 6.9).

Table 6.8: Cold plasma assisted WCO decomposition with packing materials at a residence time of 11 seconds, gas: liquid ratio of 40:1 (vol/vol) (errors:4%) in N_2 environment

Catalyst/packing material	$BaTiO_3$		Ni/Al_2O_3	
Plasma power (W)	30	50	30	50
Glyceride Conversion (%)	79.14	77.91	94.48	86.21
Total gas yield (wt.%)	12.95	18.70	21.84	36.95
Gas yields (wt.%)				
CO_2	5.06	5.49	6.03	5.71
H_2	0.38	0.78	0.46	0.50
CO	2.81	5.20	1.49	2.89
CH_4	1.05	1.80	4.74	7.68
C_2	1.37	1.82	3.82	6.85
C_3	1.21	1.60	2.61	5.92
C_4	0.60	1.09	1.50	4.07
C_5	0.25	0.52	0.69	1.91
C_6	0.16	0.25	0.33	0.92
C_7	0.08	0.14	0.18	0.51
Liquid yield (wt.%)				
Water	0.52	1.34	0.94	2.01
Acetol	0.16	0.16	3.71	1.96
FFA	57.56	51.63	18.38	9.41
Glycerol	1.30	0.52	0.11	-
FAME	1.95	1.42	37.87	29.86
Other fatty acid esters	7.17	7.25	10.95	5.15
$C_{14\text{-}18}$ hydrocarbons	0.53	0.33	1.08	2.19
$C_{14\text{-}18}$ aldehydes/ketones	0.51	0.30	0.53	0.99
Monoglycerides	8.51	12.31	2.93	7.02
Diglycerides	6.45	4.43	1.22	3.22
Triglycerides	2.39	1.63	0.44	1.23

The use of Ni/Al_2O_3 only resulted in a small increase in glyceride conversion when used at 300°C (94.31% with Ni/Al_2O_3 vs 87.63% with $BaTiO_3$ at 50W N_2), although the yields of FAME and hydrocarbons increased significantly (83.85wt.% from 24.66wt.%) (Table 6.9). FFA yields with Ni/Al_2O_3 at 300°C are marginally reduced with increased residence time (15.11wt.% to 12.56wt.%), which are highly similar to the initial feedstock FFA

content (12.43wt.%). This likely indicates an equilibrium between FFA decomposition and formation of FFA from thermal glyceride decomposition occurring at higher temperatures.

The extent of catalyst fouling was greater at 300^{o}C than at ambient temperatures, which is likely due to the temperature being sufficiently high to melt the nickel soaps, (melting point: approximately 100^{o}C) which condense in the base of the reactor. This rapidly exposes the remaining nickel, which then reacts with more FFA to form more fouling and depletes the catalyst further.

When heating was applied (Table 6.9), the gas yields increased significantly, indicating that thermal effects are responsible for the increased gas product formation (compared to Table 6.7) (Yenumala *et al.*, 2017). Aldehydes such as ethanal and propenal increased (e.g. propenal from 12.43wt.% to 15.46wt.%) with residence time at the expense of longer hydrocarbons (C8+) (0.42wt.% to 0wt.%) and FAME. This indicates the generation rate of aldehydes from glycerides is very high at 300°C as aldehydes are known to be unstable in plasma (Koeta *et al.*, 2012), which is reflected by the very high gas yields obtained under these conditions (up to 75.82wt.%)

Table 6.9: Cold plasma assisted WCO decomposition with packing materials at 300°C external heating in N_2 environment at both residence times at a 40:1 ratio (errors:±4%)

Catalyst	$BaTiO_3$		Ni/Al_2O_3		$BaTiO_3$		Ni/Al_2O_3	
Plasma power (W)	30	50	30	50	30	50	30	50
Residence time (seconds)	7	7	7	7	11	11	11	11
Glycerides Conversion (%)	61.48	87.63	64.89	94.31	66.10	89.30	72.74	96.45
Total gas yield (wt.%)	22.53	39.86	36.69	68.35	29.66	44.48	47.59	75.82
Gas yields (wt.%)								
CO_2	1.99	2.99	2.99	3.03	2.59	3.47	3.91	3.97
H_2	0.58	0.62	0.70	0.76	0.76	0.78	0.90	0.87
CO	10.89	20.61	5.23	8.88	0.34	2.47	0.78	2.87
CH_4	1.83	3.18	8.94	13.97	2.42	3.81	11.72	16.01
CH_2O	0.06	1.72	0.97	1.93	13.72	19.31	6.04	7.29
C_2	2.69	3.60	7.41	13.33	0.12	2.51	1.48	2.70
C_3	2.39	3.17	5.17	11.74	3.73	4.28	9.63	14.26
C_4	1.18	2.18	2.94	8.09	3.13	3.52	6.72	12.71
C_5	0.48	1.03	1.35	3.80	1.72	2.48	3.82	8.93
C_6	0.30	0.49	0.64	1.83	0.74	1.26	1.76	4.24
C_7	0.14	0.27	0.35	1.01	0.40	0.60	0.83	1.98
Liquid yields (wt.%)								
C_8	0.05	0.18	0.11	0.28	-	-	-	-
C_9	0.01	0.07	0.02	0.12	-	-	-	-
C_{10}	-	0.02	-	0.02	-	-	-	-
Water	0.70	2.23	0.84	1.40	0.89	2.73	1.02	1.69
Ethanal	0.06	4.16	1.07	1.91	0.08	5.08	1.31	2.29
Propenal	0.42	12.43	1.79	3.17	0.53	15.46	2.18	3.81
Acetol	0.27	0.07	3.38	0.77	0.34	0.11	4.11	0.93
FFA	35.47	25.41	15.11	4.37	32.22	18.11	12.56	3.38
Glycerol	0.07	0.04	0.12	0.05	0.09	0.05	0.15	0.06
FAME	8.44	5.26	11.68	14.84	1.44	0.61	6.43	7.71
Other fatty acid esters	1.70	0.74	8.94	12.61	5.31	3.79	1.86	1.33
$C_{14\text{-}18}$ hydrocarbons	5.73	4.08	2.23	1.92	0.66	0.38	0.11	0.03
$C_{14\text{-}18}$ aldehydes/ketones	0.56	0.39	0.51	0.29	0.61	0.30	0.01	-
Monoglycerides	14.51	4.62	15.89	2.13	13.53	4.27	10.88	1.42
Diglycerides	11.27	3.51	8.54	1.61	9.02	2.85	7.25	0.94

A similar range of products were observed for both pure and waste triglycerides. This would indicate that the reaction pathway for WCO is the same as the mechanism for pure triglycerides decomposition, as described in Figure 6.5.

High temperature (>500°C) thermal decomposition is known to be effective for preventing accumulation of organic fouling deposits, as established in literature (Maher and Bressler, 2007; Palanisamy and Gevert, 2016). To determine if this effect can sustain Ni/Al_2O_3 catalytic activity, the catalysts were examined before and after use for triglyceride decomposition at atmospheric temperature and 300°C. $BaTiO_3$ retained full activity but Ni/Al_2O_3 was partially deactivated regardless of temperature. The amount of fouling on the surface was reduced at 300°C but activity was lost more rapidly (Figure 6.3). Regenerating the catalyst at 550°C in N_2 restored the original appearance and most of the activity, which was observed during this work, but some activity was permanently lost. This was consistent with the formation of nickel soaps (Klimmek, 1984), which can melt and resolidify at the base of the reactor, as described above.

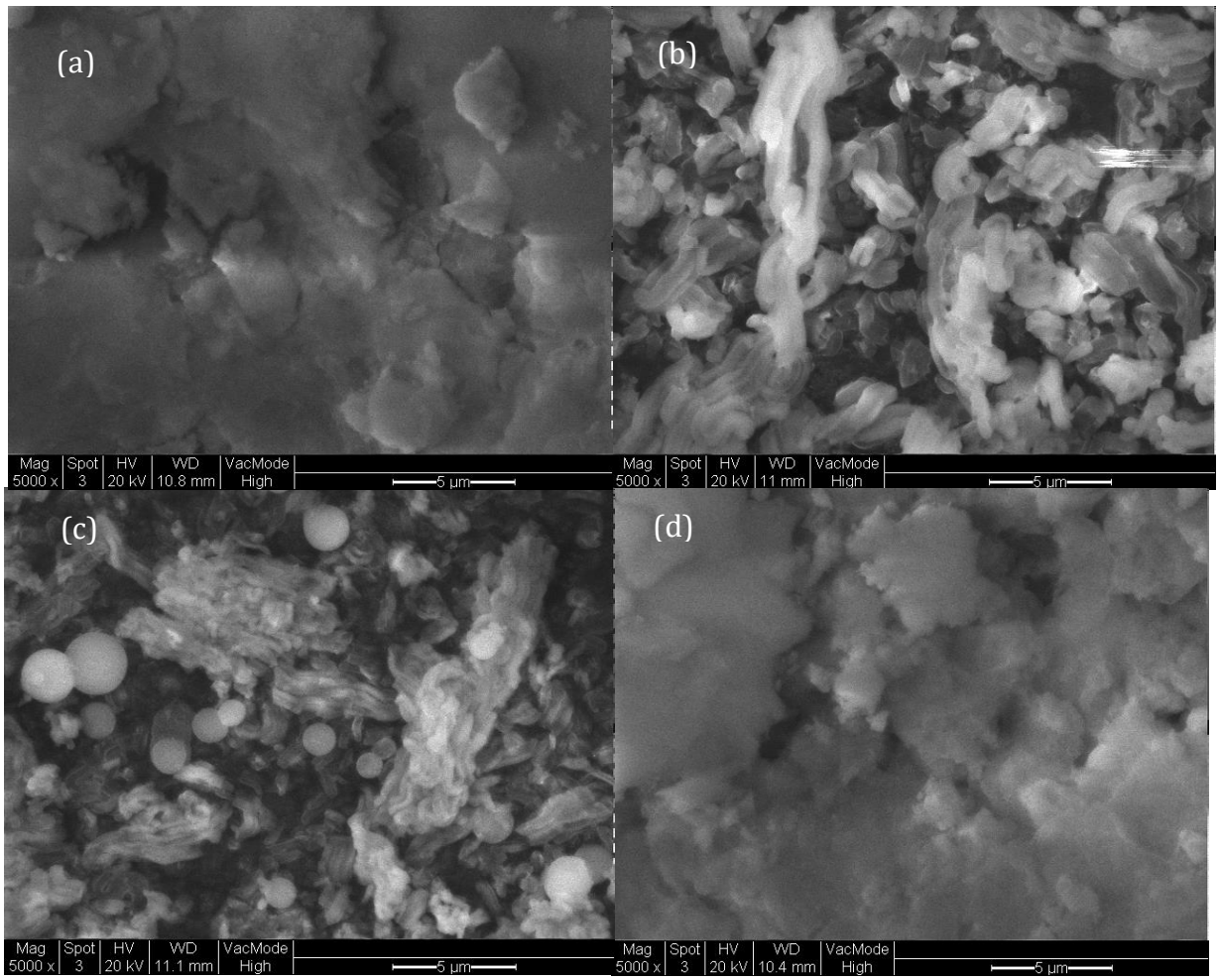

Figure 6.6: SEM images of (a) fresh catalyst, (b) 10W spent (c) 50W spent and (d) regenerated Ni/Al_2O_3 catalysts (x5000 magnification)

Table 6.10 reveals nickel loss from the packing material, with a 30% loss over 2 hour running time. This is supported by ICP-OES results (Table 6.11 below), which indicate a 40% nickel loss. The nickel remains attached to the catalyst surface as nickel soaps, as evidenced by the spent catalyst retaining most of the lost nickel when the fouling is not removed. Flexible rod like structures were observed over the surface of the spent catalyst, which is likely the FFA derived fouling (Figure 6.6(b) and (c)). At 50W (Figure 6.6(c)), nodules form on the surface, similarly to the results from waste glycerol plasma decomposition as discussed in Chapter 5 and the triglyceride SEM results in Section 6.1.2, with identical compositions.

Table 6.10: EDS data of spent and fresh Ni/Al_2O_3 catalysts

Plasma power: 50W	**Aluminium (counts/sec)**	**Nickel (counts/sec)**	**Carbon (counts/sec)**
Fresh catalyst	36.95	3.21	-
Ambient temperature spent catalyst	31.89	2.25	6.12
300°C Spent catalyst	33.15	1.89	2.00

Thermal regeneration removed the outer layer and revealed the original material (Figure 6.6(d)), which had no any significant difference in appearance from the fresh catalyst (Figure 6.6(a)). It has been reported (Mok *et al.*, 2013; Jia *et al.*, 2017) that spent catalysts from pyrolysis oil cracking can be regenerated using cold plasma decomposition, depending on the fouling composition. However, gas-liquid cold plasma was not observed to prevent the fouling formation during this study, due to the presence of liquids (which block energetic electrons from decomposing fouling deposits) and the chemical bonding between the FA/glycerol and the active sites.

Table 6.11: ICP-OES data for spent and fresh Ni/Al_2O_3 catalysts at ambient temperatures

Plasma power: 50W	**Nickel content (mg/g)**
Fresh catalyst	108.9
Spent catalyst with fouling deposit	105.6
Spent catalyst	68.7

6.2.3 Other catalysts

The abundance of FFA (12.43wt.%) in WCO increased the extent of Ni/Al_2O_3 fouling, and the fouling rate accelerated further with increased temperatures and residence times

(Table 6.10). To address this, other cracking catalysts such as zeolites and zirconia were tested in a N_2 environment. Zeolites (Charusiri *et al.*, 2006; Bhatia *et al.*, 2007), and zirconia (Charusiri and Vitidsant, 2005) have been used previously for catalytic cracking yet contain no metals to undergo saponification reactions and hence should be resistant to fouling. As shown in Table 6.12 below, Zirconia, HZSM-5 and Faujasite Y (Y-Zeolite) were examined for cold plasma assisted triglyceride decomposition.

Without heating, the gas yield was low for all catalysts (Table 6.12) (i.e. less than 25wt.%) and the chemical composition of the liquid phase was relatively unaffected, with reduced FFA/FAME yields as the only major change (15.74wt.% to 11.14wt.% for Zirconia). The rate of cracking was lower for zeolites ($7Fm^{-1}$) than for Ni/Al_2O_3 (effectively infinite dielectric constant) likely due to their relative dielectric properties (Liu *et al.*, 2010). As a result, zeolite catalysts do not focus the plasma as well as Ni/Al_2O_3 (Zhang *et al.*, 2017), therefore reducing catalyst activity. As both zeolites and nickel catalyse cracking reactions, differences in catalytic activity likely stem from a different surface area or active site concentration. However, both Ni/Al_2O_3 and zeolite catalysts induce cracking reactions via Lewis acid sites at similar area densities (Charusiri *et al.*, 2006).

The pore size of the zeolite catalysts could also be a major factor. From literature, zeolites are known to induce cracking reactions at acidic active sites inside the material, with less than 1% of the acid sites visible on the external surface (Zhang *et al.*, 2017). However, zeolites typically have very small pores, e.g. HZSM-5 has pores of 0.55-0.56nm and Faujasite HY (Y-Zeolite) has 0.76nm pores (Weitkamp, 2000; Milina *et al.*, 2014), compared to fatty acids which have a length of >1.97nm and the full triglyceride has three fatty acids bonded in parallel to a 0.29nm diameter glycerol molecule ('PubChem Compound Database,' 2018). Triglyceride molecules thus would not fit into the pores, limiting catalysed cracking reactions to external acid sites. Pore size is not a limiting factor for Ni/Al_2O_3, as the pores in the Al_2O_3 supports are 0.5-3μm (Pelissari *et al.*, 2017), which is significantly larger than the triglyceride molecule.

The results in Table 6.12 indicate that zirconia is a potentially useful catalyst for releasing H_2 gas and deoxygenating WCO through decarbonylation, as evidenced by the high yields

of CO_2 (2.67wt.%) and CO (5.32wt.%) at 50WN_2. The yield of glycerides was also marginally reduced without external heating (67.54wt.% vs 75.00wt.%). However, while zirconia has not been used for decarbonylation in literature, zirconium oxide is known to have synergistic effects with nickel for decarbonylation and decarboxylation of FFA, which may support the conclusion that zirconia catalyses decarbonylation reactions (Foraita *et al.*, 2015).

HZSM-5 was a very effective catalyst for the production of gaseous products, especially H_2 (2.51wt.%) and CO (10.30wt.%). However, the CO_2 yields were also very high (4.49wt.% at 50W) (Table 6.12), which suggests that HZSM-5 catalyses decarbonylation. This is supported by high hydrocarbon yields at 50W, both in the gaseous (6.08wt.%) and liquid phases (1.59wt.%).

Faujasite HY (Y-Zeolite) was also found to induce dehydrogenation and decarbonylation under all studied conditions (Table 6.12). The H_2 yield was low (0.93wt.%), as were the hydrocarbon and liquid phase yields. The glyceride content was not affected, which indicates this catalyst is largely ineffective at promoting decomposition of glycerides to smaller products. The lack of activity relative to other zeolites may be due to a relatively low active site concentration or dielectric effects.

To address the relatively low glyceride conversions with zeolites, external heating was introduced for zirconia and Y-Zeolite to determine the effect of increased temperature. When external heating was applied, the performance of the catalysts was comparable to that of $BaTiO_3$ under the same conditions (300°C with 50WN_2). Zirconia produced relatively high yields of FAME (12.41wt.%) and FAE (15.30wt.%) compared to other catalysts except Ni/Al_2O_3. CO_2 (12.80wt.%) and CO (13.50wt.%) yields were also increased with the external heating. The amount of hydrocarbons (17.35wt.%) generated at 50W was greatly increased by heating, though the chain length distribution was shifted towards shorter chain molecules (C_1 to C_6). Ni/Al_2O_3 produced higher yields of hydrocarbons (56.11wt.% vs 17.35wt.%) but the average chain length (2.6 for Ni/Al_2O_3 vs 1.7 for zeolite) was longer than that observed for zirconia, which implies zirconia is

more effective at inducing cracking reactions than Ni/Al_2O_3 under nitrogenous cold plasma, given equivalent conversion.

Additionally, the residual glyceride (67.54wt.%) and FFA (4.06wt.%) (30W N_2) contents after plasma treatment at 300°C were higher with zirconia than the equivalent Ni/Al_2O_3 catalysed experiments (5.91wt.% and 3.38wt.% respectively) (Table 6.9). This indicates that the catalytic activity of zirconia is lower than Ni/Al_2O_3 and would require improvements to be a useful alternative to Ni/Al_2O_3. However, if the activity can be improved, zirconia may be useful for modifying process selectivities without catalyst deactivation or requiring a longer residence time.

HZSM-5 and sulfated zirconia have been used to catalyse cracking of triglycerides in previous works. The highest conversion observed (68 %) with a 59wt.% yield of FAME was achieved with sulfated zirconia at 300°C over a 2 hour residence time (Eterigho, 2012). In comparison to prior studies, this work shows that cold plasma with a zirconia catalyst and external heating to 300°C produced 12.41wt.% FAME and 17.35wt.% hydrocarbons up to C_6, with a total conversion of 72.51 % (Table 6.12) with a much shorter reaction time (around 7 seconds). This work has achieved comparable conversion and significantly higher yields of hydrocarbons, which indicates additional deoxygenation reactions occur under cold plasma.

Table 6.12: Cold plasma assisted WCO decomposition in N_2 environment at a residence time of 7 seconds with selected catalysts and 30W plasma power at a gas:liquid ratio of 40:1(vol/vol) (errors: ±5%)

Catalyst	**Zirconia**		**Y-Zeolite**		**HZSM-5**
External heating (°C)	-	300	-	300	-
Glycerides Conversion (%)	18.78	72.51	11.93	68.36	28.74
Total gas yield (wt.%)	11.11	43.56	2.13	49.94	23.37
Gaseous yield (wt.%)					
CO_2	2.67	12.80	-	9.48	4.49
H_2	1.58	0.19	0.93	0.50	2.51
CO	5.32	13.50	-	8.96	10.30
CH_4	1.26	7.39	1.05	2.43	4.49
CH_2O	-	0.12	-	3.49	-
C_2	0.13	7.87	0.08	9.39	1.50
C_3	0.13	1.53	0.07	5.62	0.08
C_4	0.01	0.42	0.01	2.90	0.01
C_5	-	0.12	-	0.45	-
C_6	-	0.02	-	0.15	-
C_7	-	-	-	0.07	-
Liquid yield (wt.%)					
C_8	-	-	-	0.02	-
C_9	-	-	-	0.01	-
Water	0.22	0.05	0.25	0.87	0.33
Ethanal	-	0.43	-	1.27	-
Propenal	-	1.55	-	2.67	-
Acetol	0.08	0.12	-	0.05	0.06
FFA	4.06	2.13	7.80	5.48	1.30
Glycerol	0.53	0.03	1.55	0.54	0.01
FAME	7.08	12.41	5.56	4.72	10.19
Other fatty acid esters	8.44	15.30	8.80	7.00	3.89
C14-18 hydrocarbons	0.94	1.16	0.67	1.15	1.59
Monoglycerides	8.86	13.24	6.64	11.97	9.64
Diglycerides	20.01	6.52	22.25	8.03	18.04
Unreacted triglycerides	38.67	3.10	44.35	6.31	31.58

6.3 Summary

In this chapter, gas-liquid cold plasma was used to promote decomposition of pure triglycerides and WCO. By modifying the plasma power, residence time, carrier gas and packing material, it was possible to greatly increase the selectivity of the process to FFA, FAME, H_2, hydrocarbons or CO as desired. Solid catalysts were used to focus the plasma via the dielectric effect and induce selective decomposition via cracking at the catalyst's Lewis acid sites, which would reduce the need for downstream processing and potentially improve energy efficiency. Compared to catalytic cracking at 400^{o}C, cold plasma assisted WCO decomposition can increase the yields of desirable liquid products such as FAME and liquid hydrocarbons by up to 45% without heating or the presence of a catalyst. The significance of this approach is that the process can be easily tuned toward specific products with high yields with a very short residence time (around 10 seconds) at ambient conditions.

The carrier gas was found to have a significant effect on the process. H_2 favoured the decomposition of glycerides while N_2 deomposed fatty acids and FAME. Adding either catalysts/packing material enhanced the conversion, increasing from around 40wt.% to 60-90wt.% depending on plasma power. In the presence of Ni/Al_2O_3 catalyst and 50W plasma power, the formation of fatty acid esters and hydrocarbons was favoured, resulting in yields of up to 51wt.% fatty acid esters or 60.86wt.% yield of hydrocarbons (C_1-C_{18}), of which C_1-C_3 were the most abundant. The primary effect of $BaTiO_3$ was to increase the rate of hydrolysis reactions, resulting in up to 200% higher FFA yields. Ni/Al_2O_3 lost its activity rapidly under all conditions due to the formation of nickel soaps.

Increasing the reactor temperature to 300°C increased conversion significantly, but also increased the rate of decomposition of FFA/FAME to hydrocarbons and carbon oxides. Increasing the residence time increased not only conversion but also selectivity to FAME and other fatty acid esters. Zirconia and HZSM-5 were also effective catalysts for FAME production without extensive fouling but produced lower conversion and FAME yields than was achieved with Ni/Al_2O_3 .

Chapter 7. Decomposition of glucose and cellulose

Cellulose is an abundant natural polymer, which can be used as a feedstock for production of valuable furans and pyrans (i.e. furfural and levoglucosan) and other chemicals. Conversion of cellulose to furan/pyran products is generally performed via either thermal dehydration or a two step process involving hydrolysis to glucose followed by chemical or thermal degradation.

Direct pyrolysis of cellulose (without hydrolysis) is an alternative method of furan/pyran production, but has greatly reduced product selectivity and a wider range of products compared to glucose pyrolysis, while requiring a higher temperature of 600°C compared to 500°C for glucose.

In this chapter, the feasibility of using cold plasma for producing valuable liquid products from cellulose and glucose. As cellulose is a glucose polymer, analysis of the cold plasma decomposition of glucose decomposition was used to inform further study into the effect of cold plasma on cellulose decomposition. Glucose decomposition with cold plasma was performed under a range of carrier gases (H_2, N_2) and plasma powers (10-50W). The effects of operating conditions on the product distribution and surface morphology and composition of the solid residue were examined. Glucose was decomposed in its solid state to simplify separation of liquid phase products and prevent the solvent from interacting with the decomposition process. The mechanism for glucose decomposition under cold plasma in terms of the product distribution was proposed and considered in relation to pyrolysis. Cellulose decomposition under cold plasma was also studied and used to compare the product distribution and solid properties to the literature sources for cellulose pyrolysis. This was used as a basis for discussion on the mechanism of cold plasma induced cellulose decomposition, which can be applied to cold plasma assisted direct valorisation of oil rich biomass or upgrading of lignocellulosic biomass derived pyrolysis oils.

7.1 Cold plasma assisted glucose decomposition

7.1.1 Glucose decomposition products

Table 7.1 shows the results obtained from solid glucose decomposition over a 30 minute residence time at ambient temperature with a 40ml/min carrier gas flowrate. The solid fraction decreased (from 2wt.% to 28wt.%) with plasma power over the tested range in both H_2 and N_2 environments to form mainly gaseous products. The rapid mass loss from the solid feedstock is due to the increased rate of decomposition at high plasma powers (Shrestha, 2012) which promote initiation reactions (Paulmier and Fulcheri, 2005). Compared to conventional pyrolysis of glucose at 500°C (Vinu and Broadbelt, 2012), where the liquid yield was 71.9wt.%, the liquid yield was very low from cold plasma at 50W, at around 3.69wt.%. The solid yield was much higher at 50W (70.84wt.%) under cold plasma than from pyrolysis at 500°C (23.7wt.%) (Vinu and Broadbelt, 2012).

The gaseous product yields were significantly higher in cold plasma decomposition than in pyrolysis under N_2 (4.4wt.% at 500°C vs 25.5wt.% at 50W) (Fan *et al.*, 2015). The increased yields of gaseous products could be due to an increase in cracking reactions under cold plasma (Fan *et al.*, 2015). For conventional pyrolysis, glucose decomposes via dehydrogenation and dehydration reactions, which favour liquid products (Yu-Wu *et al.*, 2013). In addition to dehydrogenation and dehydration, cold plasma appears to induce cracking reactions, which increase the yields of gaseous products.

Table 7.1: Cold plasma initiated decomposition of solid glucose at ambient temperature without a catalyst with a residence time of 30 minutes and a gas flow rate of 40ml/min (errors: ±0.1%)

Carrier gas	N_2			H_2		
Plasma power (W)	10	30	50	10	30	50
Solid yield (wt.%)	97.79	87.13	72.20	97.82	85.77	70.84
Conversion (%)	2.21	13.71	28.89	2.18	13.39	28.07
Total Gas yield (wt.%)	2.21	11.14	25.20	2.18	11.66	25.47
CO_2	0.23	3.64	11.40	0.97	2.62	9.05
CO	1.81	6.06	10.82	0.19	5.48	11.14
CH_4	-	0.37	0.73	0.48	2.12	1.47
C_2	-	0.27	0.54	0.40	0.75	1.40
C_3	-	0.22	0.51	0.15	0.59	1.28
C_4	-	-	0.07	-	0.11	0.89
C_5	-	-	-	-	-	0.25
H_2	0.17	0.58	1.13	-	-	-
Liquid product yields (wt.%)	-	1.73	2.60	-	2.57	3.69
Water	-	1.58	2.18	-	2.24	2.92
Formic acid	-	0.12	0.33	-	0.27	0.55
Methanol	-	0.03	0.09	-	0.06	0.22

Table 7.1 shows that the gas products were predominantly carbon oxides (CO and CO_2), with small amounts of hydrocarbons, for both H_2 and N_2 carrier gases. H_2 was detected under N_2 carrier gas but the hydrogen flowrate remained constant before and after the reactor in the case of H_2 carrier gas. The yields of carbon oxides remained almost constant for all tested powers (10.82 vs 11.14wt.% CO), but the relative yields of hydrocarbons were shifted towards longer chain molecules under H_2 (0.89wt.% under 50W H_2 vs 0.07wt.% C_4H_{10} under 50W N_2).

CO formation was almost identical for both H_2 and N_2 carrier gases except at low power (10W), where the N_2 environment produced more CO than the H_2 environment (1.81wt.% vs 0.19wt.%). Based on the structure of glucose, CO formation can be explained by cracking and dehydrogenation reactions, especially from the sixth carbon as it is located outside the glucose ring structure (Reaction 7.1).

Unlike thermal decomposition of glucose at 500°C (Cui *et al.*, 2013), the product distribution obtained from cold plasma did not contain any aldehyde or ketone products. This could be due to their instability in cold plasma conditions, as discussed in Chapter 4, as they rapidly decompose to CO (Zhang *et al.*, 2015).

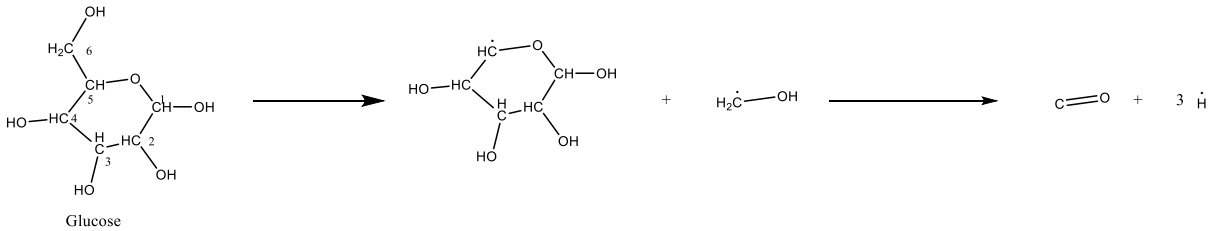

Reaction 7.1: Formation route for CO generation in the presence of cold plasma

A 17-39% higher yield of CO_2 under a N_2 environment than under a H_2 environment was observed at plasma powers above 10W. An increase in CO_2 yield with increasing plasma power suggests that the reformation of CO to CO_2 via hydroxyl radical attack (as discussed in Chapters 4 ,5 and 6) and dehydrogenation are the dominant routes, but are opposed by abundant hydrogen (Li *et al.*, 2011b). Previous chapters have demonstrated that this route for formation of CO_2 from CO and hydroxyl radicals occurs under cold plasma conditions, providing further evidence for this theory.

Conventional pyrolysis of glucose (Wang *et al.*, 2012b) found that CO_2 was an abundant product in the gas phase (5.08mol%) at >500°C, whereas CO was not observed. The increased water content from pyrolysis (15.8wt.%) compared to cold plasma (2.92wt.%), would provide a higher concentration of hydroxyl radicals to convert CO to CO_2. Under cold plasma, the lower water content resulted in both CO and CO_2 being present at detectable levels under all plasma powers and carrier gases.

Hu et al. (2018) reported that high energy reactions producing CO_2 from furans/ glucose were energetically favourable in highly excited nitrogen (Hu *et al.*, 2018). These reactions are based on splitting the furan rings that form from the initial decomposition of glucose to release carboxylic acids (Reaction 7.2). These carboxylic acids then decompose to CO_2 by dehydrogenation and cracking reactions such as dehydrogenation of formic acid (Gorin and Taylor, 1934).

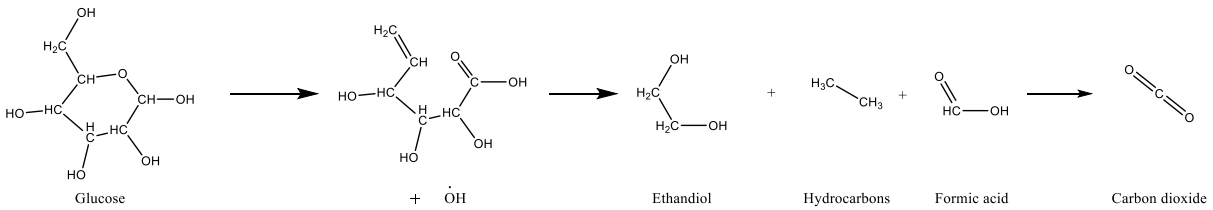

Reaction 7.2: Predicted cold plasma decomposition route for CO_2 formation from glucose.

As shown in Table 7.1, hydrocarbons were also produced under cold plasma (1.85wt.% in N_2 and 5.29wt.% in H_2), which was not reported in conventional thermal decomposition of glucose or mechanism studies on glucose or cellulose decomposition/dehydration (Cui *et al.*, 2013; Mayes *et al.*, 2014). The formation of hydrocarbons from cold plasma decomposition of glucose requires the removal of oxygen from the carbon backbone, which are only present as hydroxyl or ether groups. Therefore, the presence of hydrocarbons confirms that splitting of the C-O bond to release hydroxyl radicals occurs under cold plasma, as concluded in Chapter 4. The higher yield of hydrocarbons in the H_2 environment than in the N_2 is an indicator of hydrodeoxygenation reactions (Jérôme *et al.*, 2016). It was also confirmed by increased water yield (2.92wt.% under H_2 vs 2.18wt.% under N_2). The higher CH_4 yield (e.g. 2.12wt.% CH_4 vs 0.75wt.% C_2H_6) suggests that the dominant route is the splitting of the C-C bond between C5 and C6 to produce methanol (Greenhalf *et al.*, 2012), which then deoxygenates to methyl radicals as shown in Reaction 7.3, reflecting the methanol decomposition mechanism determined in Chapter 4.

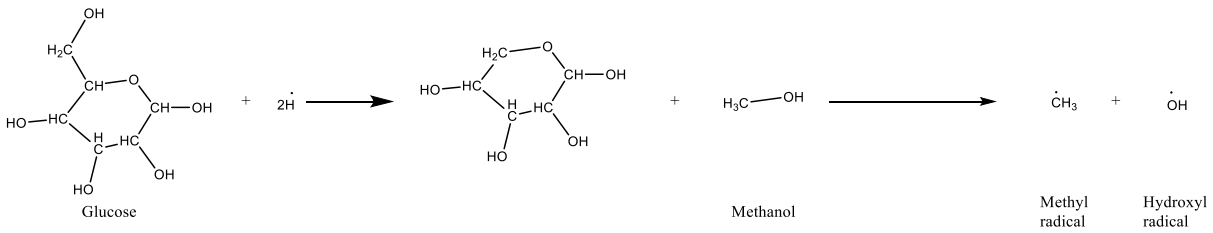

Reaction 7.3: Proposed cold plasma route for formation of gaseous hydrocarbons from glucose.

It was reported (Vinu and Broadbelt, 2012; Hu *et al.*, 2018) that conventional thermal decomposition of glucose (i.e. at 500°C) could produce up to 25wt.% liquid yield, of which 5-hydroxymethylfurfural and furfural were the main products with lesser yields of levoglucosan and other furan derivatives. Mayes et al. also found that furans and pyrans derived from glucose pyrolysis at 500°C were predominantly 5-HMF (6wt.%) and levoglucosan (9wt.%), as well as 12 other furans/pyrans at above 0.5wt.% yields (Mayes *et al.*, 2014). It was reported (Balat, 2008; Vasiliou *et al.*, 2009; Khani *et al.*, 2014) that both cold plasma and conventional thermal decomposition follow radical mechanisms. However, no pyrans or furans were detected experimentally in this work. This could indicate that furans were not extracted from the solid.

As furans and pyrans are semi-polar, they can form hydrogen bonds with glucose molecules or its polar derivatives (Montejo *et al.*, 2004) therefore preventiong their release from the glucose structure at atmospheric conditions. In contrast, the temperatures in thermal processes, i.e. 500-700°C (Cui *et al.*, 2013) are well above the boiling point of furans/pyrans (<385°C), and so evaporate the liquid products, which are condensed downstream.

FTIR analysis of solid residues under N_2 (Figure 7.1) showed significant increases in absorption at 1020 (C-O group), 1620 (C=C group) and 3600 cm^{-1} (OH group) compared to pure glucose at plasma powers of 30W and 50W. The FTIR spectra for solid samples at 10W in the N_2 environment and all tested plasma powers in the H_2 environment were indistinguishable from those obtained from raw glucose (Figures 7.1 and 7.2). Under N_2 at 10W, solid mass loss was only 2.2wt.%, which is unlikely to cause any significant changes to the product spectra. Under a H_2 environment, the surface was not affected even at high mass loss (29wt.% at 50W). Even decomposition of the surface would not affect

the FTIR spectra provided that the decomposition products were extracted from the solid. As pyrans and furans were likely to remain in the solid, these would have to be converted to components with similar groups to glucose. This could occur through hydrogenation of ketone and aldehyde groups to alcohol groups. The hydrogenation of C=O groups under H_2 was discussed in Chapter 4.

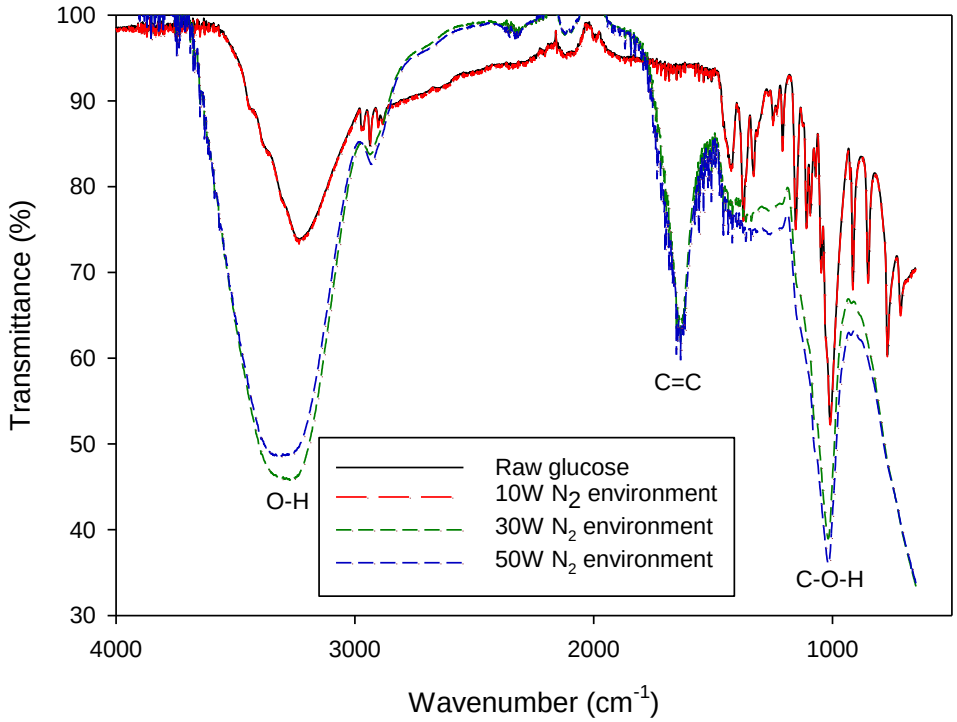

Figure 7.1:FTIR spectra of glucose derived solids from cold plasma assisted decomposition in a N_2 environment at different plasma powers

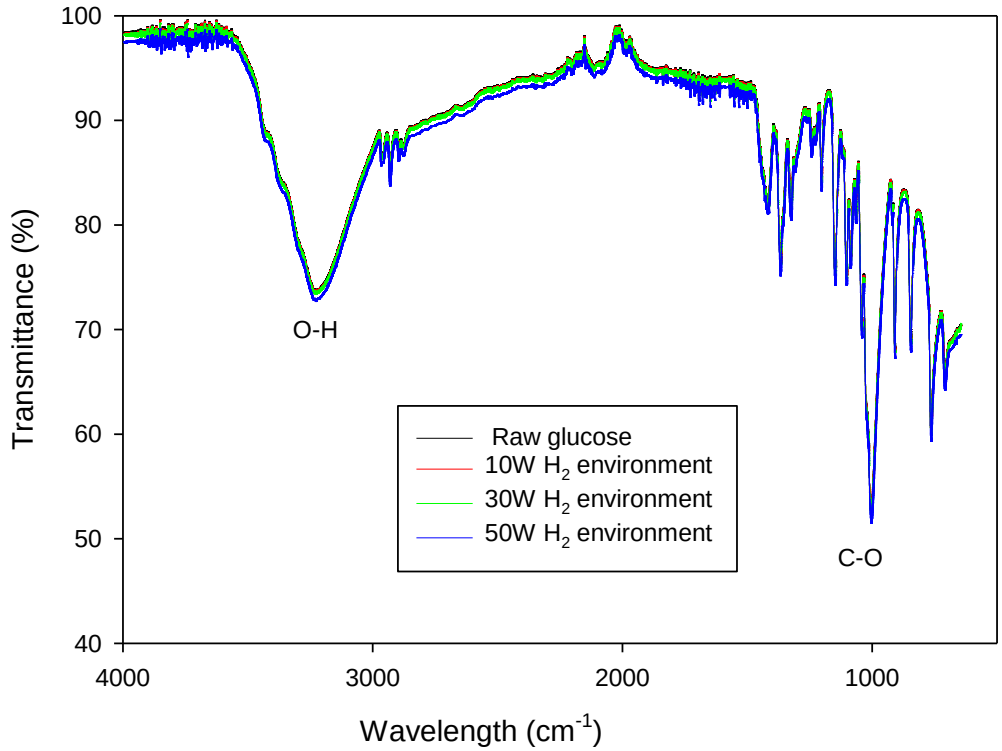

Figure 7.2: FTIR spectra of glucose derived solids from cold plasma assisted decomposition in a H_2 environment at different plasma powers

The C=C peak in Figure 7.1. indicates that glucose loses hydrogen under cold plasma at powers above 10 W, which reflects the H_2 yields shown in Table 7.1 (>0.58wt.%). The increase in the magnitude of the OH peak could be due to either the decomposition of glucose into smaller molecules (such as water) that adsorb to the remaining glucose or the open ring to form D-glucose followed by the conversion of the aldehyde group to an alcohol.

CHN analysis presented in Table 7.2 showed slight differences between the raw glucose sample and the solid residues. In the H_2 environment, carbon content decreased with increasing plasma power (36.20 to 34.41wt.%) whereas there was an increase in hydrogen content (7.07wt.% to 8.38wt.%), indicating extensive hydrogenation of the solid. A small increase in oxygen content (56.40 to 57.18wt.%) is likely to be due to the presence of water adsorbed to undecomposed glucose via hydrogen bonding as explained above. Water is primarily formed via the release of OH radicals under both carrier gases, which is a pre-requisite for generation of hydrocarbons from glucose (Table 7.1 and

Figure 7.1). Very little water was observed (<0.01wt.%) while hydrocarbons are detectable in the gas phase (1.03wt.%) at 10 W under a H_2 environment (Table 7.1) which can be explained by the water adsorption theory above.

Table 7.2: CHN analysis of raw glucose and solid residues obtained at various plasma powers after 30 minute residence time in N_2 and H_2 environment (40ml/min gas flow rate) (errors: ±0.05wt.%)

Plasma power (W)	**Raw glucose**	**H_2 environment**			**N_2 environment**		
		10	30	50	10	30	50
C (wt.%)	36.20	36.22	35.12	34.41	36.16	37.26	37.62
H (wt.%)	7.07	7.27	7.28	8.38	7.09	7.30	7.77
N (wt.%)	0.33	0.33	0.14	0.03	0.31	0.53	0.77
O (wt.%) *	56.40	56.18	57.46	57.18	56.44	54.91	53.84

*By difference

In the N_2 environment, carbon and hydrogen contents increased slightly with plasma power (37.26wt.% at 30W to 37.62wt.% at 50W for carbon; 7.30wt.% at 30W to 7.77wt.% for hydrogen at 50W) (Table 7.2). However, at 10W, there were no significant changes for both carrier gases. A decrease in oxygen content could be due to release of CO and CO_2 in the gas phase. The increased intensity of the FTIR O-H group and the increased water yield in N_2 environment suggest that condensation reactions of OH groups occur rapidly compared to other decomposition reactions. Removal of OH groups via C-O bond cracking, evidenced by the formation of hydrocarbons, would make the solid residue less polar. This decreased polarity would reduce the incidence of hydrogen bonding with water and other liquid products, which would increase liquid yields (<0.01wt.% to 2.60wt.%), as observed at higher powers (Table 7.1). A small decrease in the OH peak size from 30W to 50W in Figure 7.1 supports this, as higher plasma powers would increase the rate of the condensation reactions, reducing the polarity of the glucose further and hence reducing the water content of the solid.

Another important observation from Table 7.2 was that the nitrogen content of the solid residue increased from 0.33wt.% in the raw sample to 0.77wt.% at 50W in the N_2 environment. This suggests that nitrogen from the carrier gas can be substituted onto glucose molecules directly. XPS was performed on the 50W N_2 sample (Figure 7.3). This detected the presence of surface nitrogen at 1.87wt.%, exclusively at a binding energy of

399 eV, corresponding to amine groups, which may indicate cold plasma has potential for surface modification applications (Deslandes *et al.*, 1998). No peak was detected at 405eV however, indicating that amide groups were not present, in contrast to that observed during FTIR.

Cellulose modification with nitrogen cold plasma has been reported (Pertile *et al.*, 2010; Flynn *et al.*, 2013) but this did not include glucose modification. The findings from their work were similar to the results for glucose cold plasma treatment, with partial decomposition of the cellulose and limited amounts of nitrogen introduced (2.6wt.%) (Deslandes *et al.*, 1998; Pertile *et al.*, 2010). A difference is that the nitrogen content found experimentally on glucose was significantly lower (0.77wt.%) (Table 7.2), which may indicate that cellulose is more readily nitrogenated.

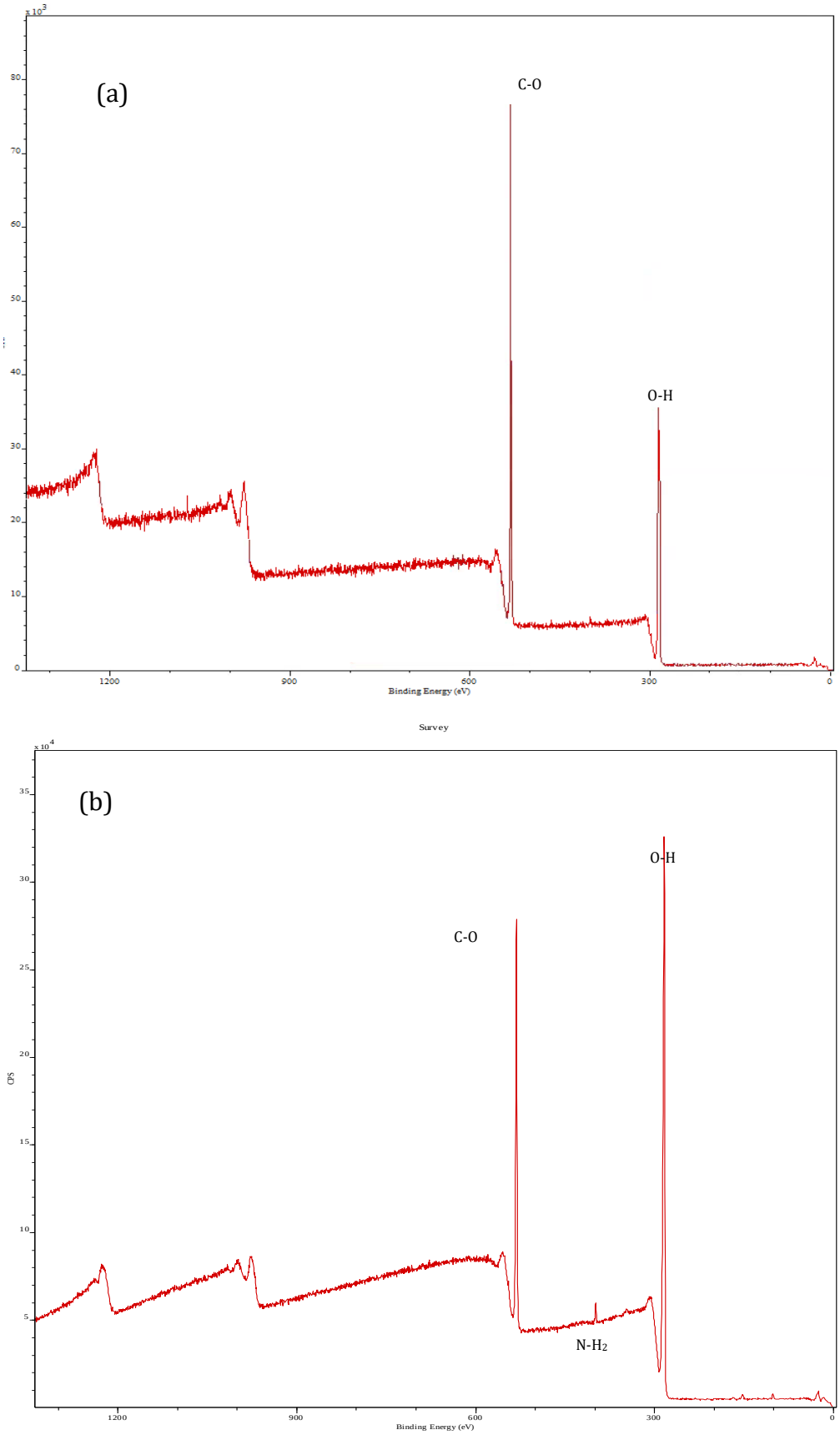

Figure 7.3: XPS spectra of (a) raw and (b) 50W N_2 cold plasma treated glucose

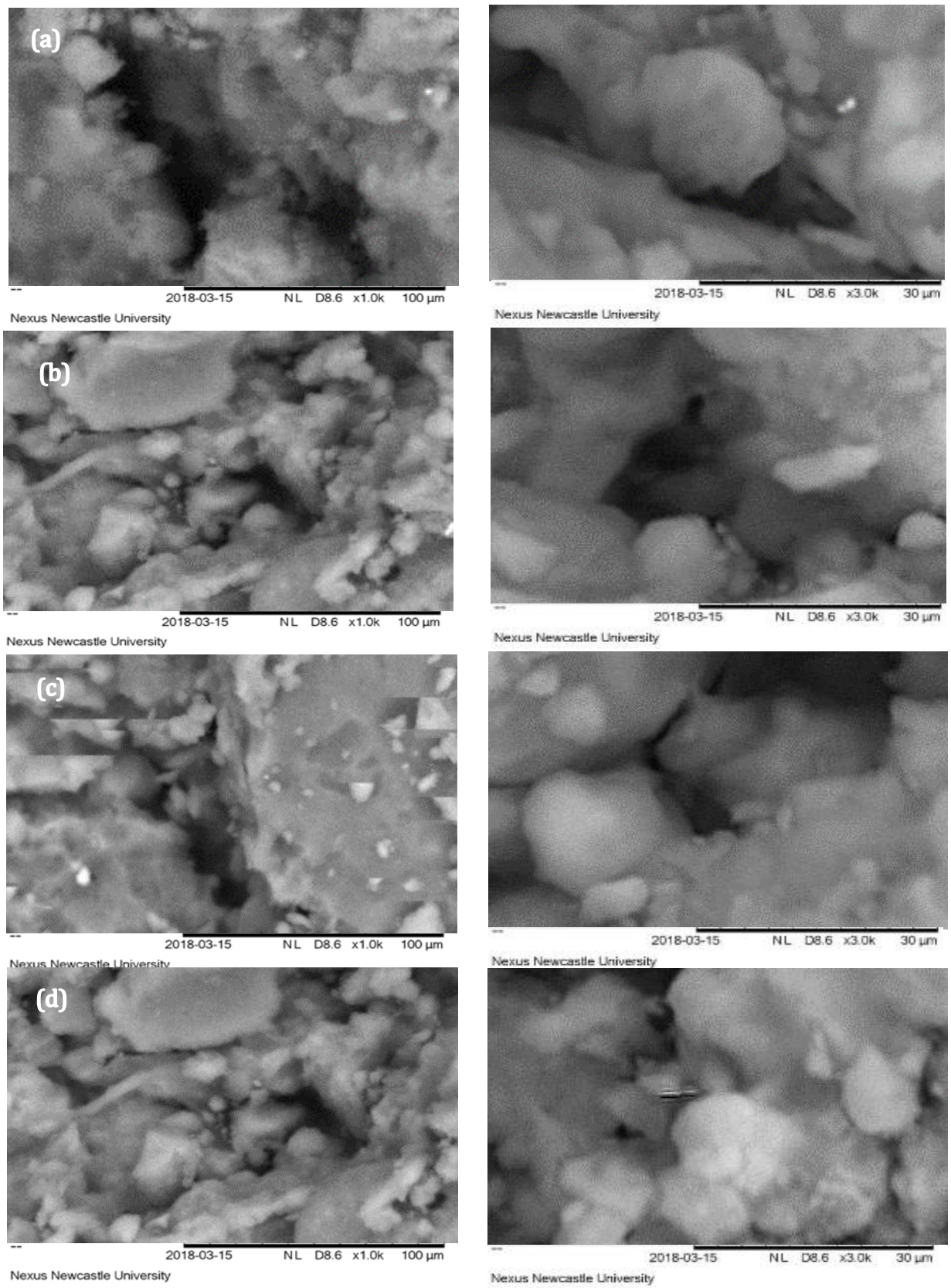

Figure 7.4: SEM images of cold plasma treated glucose samples at x1000 (left) and x3000 (right) magnifications (a) Raw glucose (b) 10W H_2 (c) 30W H_2 (d) 50W H_2 - continued overleaf

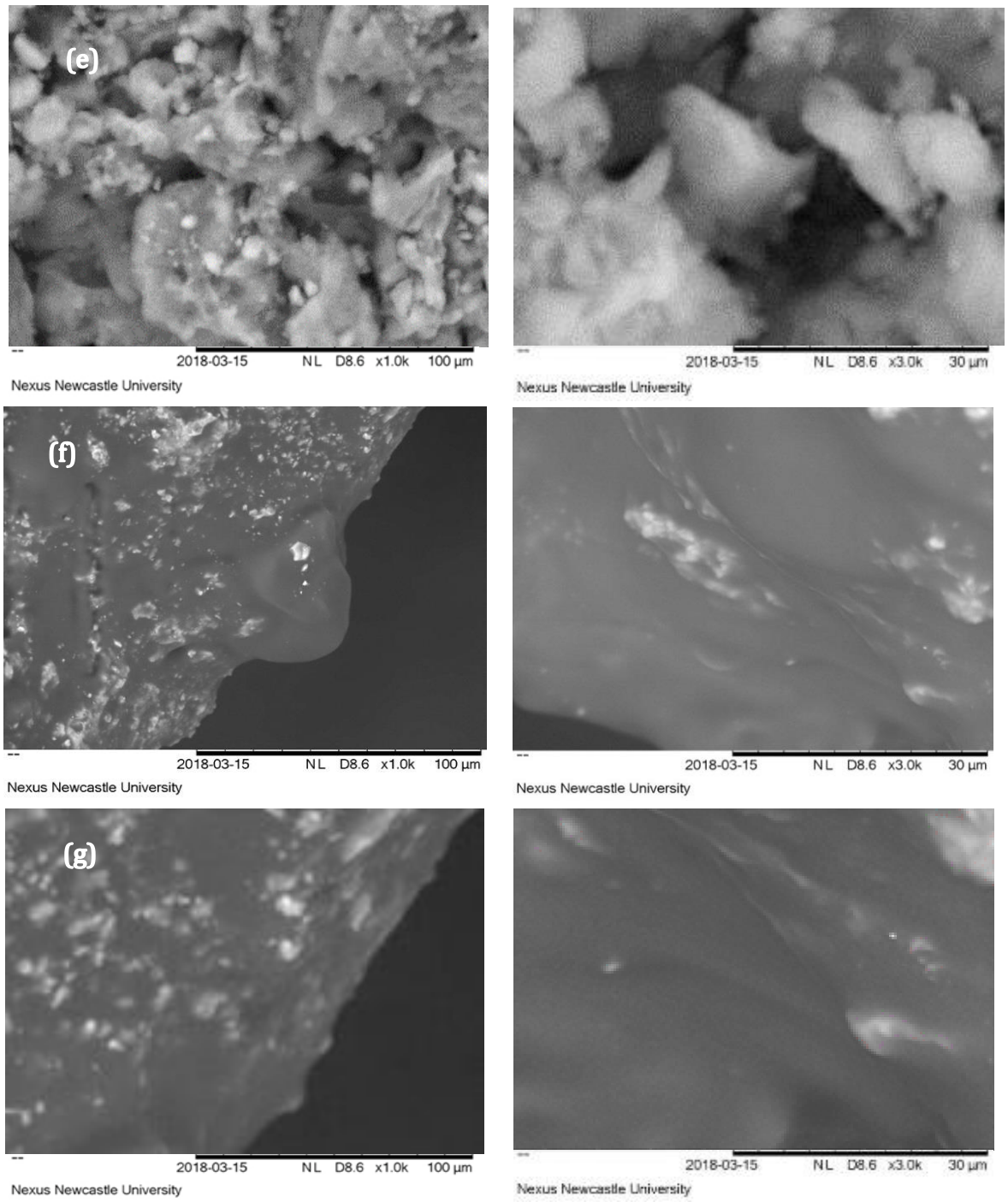

Figure 7.4: SEM images of cold plasma treated glucose samples at x1000 (left) and x3000 (right) magnifications (a) Raw glucose (b) 10W H_2 (c) 30W H_2 (d) 50W H_2 (e) 10W N_2 (f)30W N_2 (g) 50W N_2

SEM analysis was performed on the glucose derived samples (Figure 7.4), but only the samples obtained at 30W and 50 W in an N_2 environment (Figure 7.4 (f) and (g)) showed significant changes from the initial glucose. At x3000 magnifications, the structure was distorted which resembles bubbles, indicating that plasma decomposes material inside

the particles to gaseous products, similar to microwave decomposition (Zhai *et al.*, 2012). This has potential for producing expanded structures from glucose, and implies that subsurface decomposition of cellulose is possible, which will require further study.

Formation of furans under cold plasma can be explained due to interaction of a C-O^- group with an adjacent hydroxyl group or direct release of a hydroxyl group, initiating dehydration reactions to form an intermediate (Reaction 7.4). This intermediate then reforms the ring structure to a variety of furan products, which can typically undergo further cracking or condensation reactions (Hu *et al.*, 2018) as shown in Reaction 7.5. An example of glucose conversion to 5-HMF via condensation reactions is shown in Reaction 7.4, which was also observed in thermal processes (Mayes *et al.*, 2014).

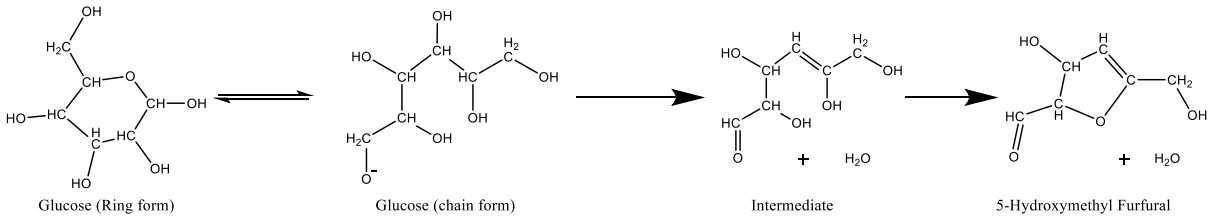

Reaction 7.4 Proposed cold plasma decomposition pathway from glucose to 5-HMF

Cold plasma initiated decomposition of the glucose ring form would generate levoglucosan, via a condensation reaction between hydroxyl groups to form one additional ester bond (Reaction 7.5). Levoglucosan can however dehydrate to levoglucosenone or to various aldehydes and ketones via C-C bond cracking. These aldehydes were not detected experimentally, due to their instability under cold plasma, as they decompose to CO and H_2. Both CO (10.82wt.%) and H_2 (1.13wt.%) were detected at high yields at 50W, which supports this potential pathway.

The furan/pyran formation and decomposition reactions detailed above have been shown to occur for thermal decomposition (Mayes *et al.*, 2014). As cold plasma and thermal decomposition both initiate reactions via radical and energetic species interactions (Du *et al.*, 2007; Troe, 2007; Brudnik *et al.*, 2009), this provides supporting evidence for the derived cold plasma decomposition mechanisms. Other than this, there is little evidence for these pathways as none of the initial products were detected except water and carbon oxides. However, FTIR analysis indicates an increase in the ester and aldehyde groups

(Figure 7.1) and CHN analysis shows a loss of oxygen under N_2 (Table 7.2) , which would reflect these proposed reactions.

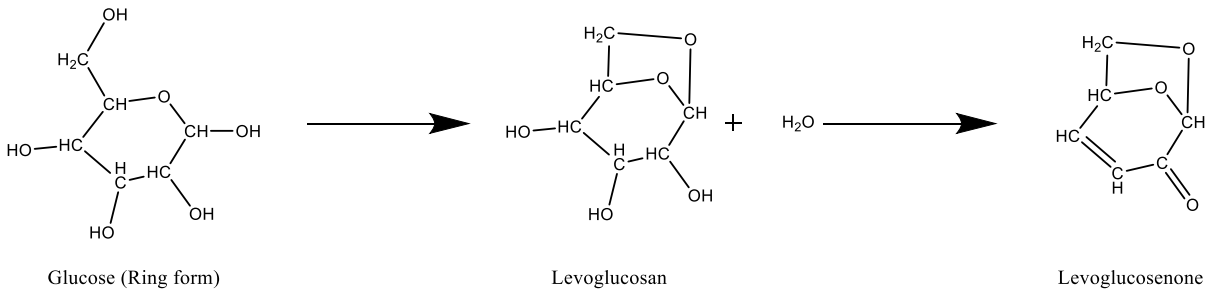

Reaction 7.5: Predicted cold plasma decomposition route from glucose to levoglucosan and levoglucosenone (Pyrans)

From the experimental data obtained in this chapter, these reactions (Reactions 7.4 and 7.5) are the likely initiation reactions for cold plasma assisted decomposition. However, the lack of detectable furans or pyrans prevents this from being confirmed. The generation of water (>2.92wt.%), carboxylic acids, alcohols and hydrocarbons, which would be expected from furan/ pyran formation, provides evidence for these pathways.

From experimental results, it can be concluded that the N_2 environment favours cracking and dehydrogenation reactions whereas the H_2 environment promotes dehydration and hydrogenation reactions. These agree with the conclusions for other feedstocks, as discussed in Chapters 4, 5 and 6. The conclusions fit well with kinetic theory (Baulch *et al.*, 1992; Raju *et al.*, 2013) and reflect the thermal decomposition pathways (Hu *et al.*, 2018), but with increased potential for improving selectivity and product distribution control.

7.2 Cold plasma assisted cellulose decomposition

7.2.1 Cellulose decomposition products

Table 7.3 shows an increase in cellulose conversion with increasing plasma power, leading to an increase in the product yields. This is due to the increased availability of high energy excited species at high plasma powers for initiating reactions. More hydrocarbons (C_1-C_5) were generated in the H_2 environment than in the N_2 environment, which can be explained due to the abundant hydrogen radicals promoting termination steps while nitrogen favoured further cracking reactions (Baulch *et al.*, 1992; Raju *et al.*, 2013). It was

found that cold plasma at 10W had a negligible effect on cellulose decomposition (mass loss: <0.1wt.%) because cellulose has a very stable structure. Therefore, to account for this, the range of plasma powers tested was increased to 30-70W in this section.

Table 7.3: Cold plasma initiated cellulose decomposition at atmospheric conditions at 30 minutes residence time, 40ml/min gas flow rate (errors: ±0.1%)

Carrier gas	**N_2**			**H_2**		
Plasma Power (W)	30	50	70	30	50	70
Solid (wt.%)	77.26	36.14	17.45	81.83	42.35	28.30
Liquid (wt.%)	10.46	48.66	37.61	9.96	41.76	32.82
Gas (wt.%)	12.28	15.20	44.94	8.21	15.89	38.88
Conversion (%)	52.74	63.86	82.55	22.17	57.65	71.70
Gas yield (wt.%)						
H_2	1.00	1.37	2.28	-	-	-
CO_2	4.02	4.57	8.58	-	2.15	7.01
CH_4	0.66	1.73	4.58	1.53	1.87	3.58
CO	5.85	5.91	25.15	1.77	8.90	21.43
C_2	0.51	0.89	2.69	3.78	2.10	5.12
C_3	0.23	0.67	1.22	0.77	0.55	1.10
C_4	-	0.06	0.44	0.29	0.27	0.55
C_5	-	-	-	0.06	0.04	0.08
Liquid product yields (wt.%)						
Water	10.46	13.91	10.81	9.60	13.87	13.14
Formic acid	-	-	0.13	0.36	0.26	0.28
Methanol	-	-	-	-	-	0.56
Acetic acid	-	-	-	-	-	0.28
Other compounds (see Table 7.4)	-	34.75	26.67	-	27.63	18.56
H_2 Consumption (ml/min)	-	-	-	7.36	9.75	12.83

In addition to hydrocarbons, both CO and CO_2 were the most abundant gaseous products at most powers (Table 7.3) (except 30W H_2, which produced no CO_2), which indicates extensive dehydrogenation and cracking reactions on alcohols/ketone and carboxylic acids respectively. Under an N_2 environment, H_2 was generated at significant yields (up

to 2.28wt.%), reflecting the dehydrogenation reactions indicated by the carbon oxide yields.

The N_2 environment produced a higher liquid yield than the H_2 environment at all powers (48.66 vs 41.71wt.% at 50W) (Table 7.3). This reflects the excitation levels of the carrier gas, with H_2 having an excited state at 3.7eV compared to 6.1eV for N_2. The high energy species allow decomposition of the stronger cellulose bonds in cellulose (i.e. C-C). This allows generation of CO_2 and CO at lower powers than is possible under H_2.

In a H_2 environment, hydrogen radicals promote dehydration and hydrogenation, stabilising compounds and intermediates. This is true especially at low plasma powers where excited electrons are not abundant enough to decompose solids rapidly. These reactions would consume hydrogen, which was observed to increase with plasma power, i.e. 7.36 ml/min H_2 consumed at 30W to 9.75 ml/min at 50W and 12.83 ml/min at 70W.

Overall, the high water yields (10-14wt.%) indicates extensive condensation reactions were occurring, which likely implies the formation of furan/pyrans and corroborates the results for glucose decomposition.

Table 7.4: GC-MS analysis of complex liquid products from cold plasma initiated cellulose decomposition (errors: ±0.5%)

Liquid composition	**50W H_2**	**70W H_2**	**50W N_2**	**70W N_2**
	Area%	Area%	Area%	Area%
Furan	-	-	13.89	6.84
Furfural	-	-	4.17	9.29
1-hydroxy 2-propanone	-	0.98	0.99	-
Furanone	-	0.92	1.68	1.88
2-cyclopentanone	15.02	3.13	8.80	17.44
Propanoic acid	-	2.21	1.95	-
5-methyl furfural	4.79	1.84	3.84	8.46
Furanmethanol	-	3.44	0.93	1.04
1,2-cyclopentanedione	-	5.58	1.22	8.52
2-Hydroxy-3-methyl-2-cyclopenten-1-one	-	2.76	0.46	3.61
Ethenediol	-	6.87	5.98	7.49
Dihydro-4-hydroxy-2(3H)-furanone	6.13	23.97	0.23	1.29
1,3 Propandiol	-	6.26	2.15	4.33
Maltol	-	2.76	3.41	3.81
Levoglucosenone (LGO)	16.67	7.06	40.39	5.29
1,4;3,6-Dianhydro-α-D-Glucopyranose (DGP)	7.32	5.28	3.44	6.97
2-Furanol	-	10.80	0.68	-
5-Hydroxymethyl furfural	50.07	15.40	1.96	12.13
Furfuryl alcohol	-	-	2.78	-
1,2 Cyclopentandiol	-	-	0.69	-
Levoglucosan	-	0.74	0.34	1.61

As shown in Table 7.4, the liquid phase products were strongly affected by the carrier gas. The data in Table 7.4 show relative % of individual components for all plama powers and carrier gases. Due to high energy excited species, N_2 was less selective, with 22 compounds at 50W compared to 6 under a H_2 environment. H_2 favoured the formation of furfural and its derivatives (the products of repeated hydrogenation of the hydroxyl groups on the glucose monomers) at 50W and above. Levoglucosenone, Dihydro-4-hydroxy-2(3H)-furanone and 2-Cyclopentanone were also present in the liquid phase. These products are all known products from thermal dehydration of glucose or cellulose (Zhang *et al.*, 2015; Hu *et al.*, 2018).

Levoglucosenone can be formed from levoglucosan molecules via removal of an additional hydroxyl radical, followed by a condensation reaction to leave a single ketone group. This reaction was shown to occur for cold plasma treatment of glucose, which supports this pathway (Figure 7.5)

Similarly, Dihydro-4-hydroxy-2(3H)-furanone is a furan decomposition product, which can potentially be derived through cracking of glucose between carbons 4 and 5 followed by further condensation reactions (Reaction 7.6).

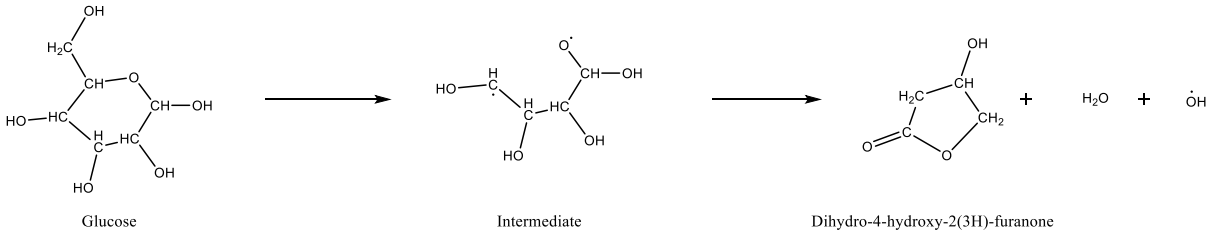

Reaction 7.6: Predicted formation pathway for formation of Dihydro-4-hydroxy-2(3H)-furanone.

2-Cyclopentanone is another observed decomposition product, which could form via a wide variety of pathways. The simplest would be hydrogenation of furfural, another common furan molecule. This would occur via hydrogenating the C=O bond and splitting the C-O ether bond, which results in the molecule reforming to cyclopentanone oligomers (Reaction 7.7).

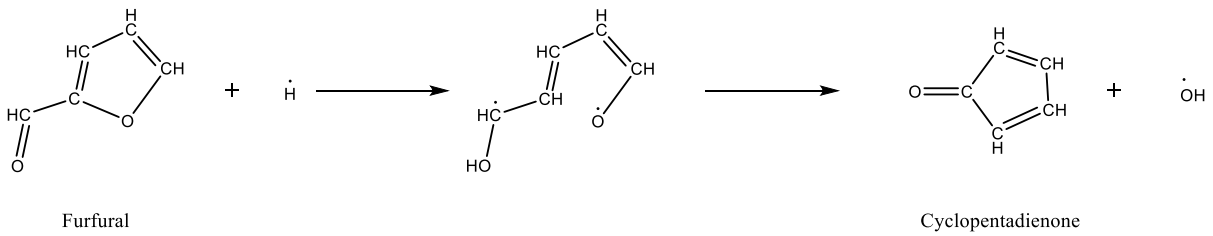

Reaction 7.7: Predicted route for formation of cyclopentanone and other cyclic ketones from furans.

Thermal decomposition of cellulose (at 500°C) produces a range of furans and pyrans, similar to glucose decomposition processes (Holgate *et al.*, 1995; Vinu and Broadbelt, 2012; Cui *et al.*, 2013). Thermal decomposition primarily produced water and CO_2 at yields of 4.2 and 7.5wt.% respectively. In addition to CO_2, the gas phase predominantly contains H_2 (0.9wt.%) and aldehydes such as formaldehyde and acetaldehyde (1.38wt.% combined). In terms of non-water liquid products, levoglucosan (9wt.%) is the most

abundant product in the liquid phase, followed by formic acid (6.2wt.%) and glycolaldehyde (5.8wt.%). In addition, a variety of furanic products with a total yield of 5.8wt.% were collected, with 5-HMF being the most abundant of these (2.9wt.%).

These results reflect the cold plasma induced decomposition data well, especially in the N_2 environment. The presence of CO was observed under cold plasma, in contrast to the thermal process. This likely indicates dehydrogenation of ketones or lower hydroxyl radical concentrations. Both of these are evident in the experimental data (Table 7.3), with significantly greater H_2 yields under cold plasma (2.28wt.%) which are derived from dehydrogenation and would convert hydroxyl radicals to water. Aldehydes were not observed, due to their instability under cold plasma (Koeta *et al.*, 2012), which explains the absence of CO in thermal decomposition studies. The water and carboxylic acid yields from cold plasma agree well with those from thermal decomposition.

The range of pyrans/furans obtained thermally was more limited than under cold plasma in an N_2 environment, whereas the inverse was true for cold plasma under H_2. Both types of cold plasma primarily generate furan based products. However, both carrier gases primarily generate furans, i.e. 5-HMF, at high selectivities (50.07%) with levoglucosenone (16.67%) and cycloketones (15.02%). These indicate that cold plasma favours furanic over pyran derived products, as opposed to thermal processes. This may be due to the different process kinetics,due to the different initation mechanism (high energy excited species compared to high temperature (i.e. 500°C).

7.2.2 Cellulose decomposition mechanism

Most current studies utilise acid catalysed hydrolysis of cellulose to glucose, before pyrolysis to liquid products to improve conversion (VandeVyver *et al.*, 2011). Some studies on direct thermal decomposition of cellulose have been performed, with 600°C found to be optimal for producing liquid products and 800°C inducing complete gasification (Henrique *et al.*, 2015). Mechanism studies on cellulose decomposition have established that four decomposition pathways occur in parallel, as illustrated in Table 7.5 (Wang *et al.*, 2012b).

Table 7.5: Initial cellulose thermal degradation products (Wang *et al.*, 2012b).

Product	Reaction
Levoglucosan	Dehydrogenation reaction between C1 and C6 hydroxyl groups, depolymerisation
3,4 anhydroaltose	Dehydrogenation of C1 and C3
5-HMF	Dehydrogenation of open ring cellulose segments, formation of furan ring via dehydrogenation between C2 and C5
Hydrocarbon chains	Ring opening reactions/cracking of cellulose backbone

The range of compounds derived through the 4 pathways are similar to those obtained via glucose decomposition in literature and in Section 7.1, except with a greater proportion of furans and hydrocarbons from dehydration reactions. The reaction rate for cellulose decomposition was higher than for glucose decomposition under the same conditions(Wang *et al.*, 2012b; Zhang *et al.*, 2015). The increase in solid mass loss was also observed in this study at all tested powers. Most of the products detected in the liquid phase from nitrogen cold plasma assisted cellulose decomposition correspond to those predicted by the aforementioned pathways, with the remainder being cracking products such as propanoic acid and ethendiol. This supports the proposal that cellulose cold plasma decomposition under nitrogen has the same mechanism as thermal decomposition at 600°C.

Based on the results obtained in the H_2 environment (Tables 7.3 and 7.4), the thermal and cold plasma reaction pathways are similar. This is because hydrogen only generates a small number of decomposition products, which are all obtainable from repeated dehydrogenation of the thermally predicted initial products, particularly at low plasma powers (50 W).

7.2.3 Cellulose solid characterisation and properties

Solid XPS analysis, shown in Table 7.6, shows that raw cellulose had an approximate 2:3 carbon to oxygen ratio on the surface of the material, compared to 2:2.25 in the bulk material via CHN analysis as shown in Table 7.7. Nitrogen was also detected at increasing levels under H_2 (of much lower magnitude than under N_2) as the cold plasma power increases which is most likely due to mass loss of the other elements due the scale of the increase compared to the solid mass loss (19-82wt.%). CHNO analysis, shown in Table

7.7, reflects this, as the nitrogen content within the bulk increases from 0.67wt.% to 0.81wt.% at 70W H_2, which is outside the experimental error range.

In the N_2 environment, the oxygen content was markedly reduced when 30 W plasma is applied, with higher powers having little further effect on reducing oxygen content as shown in Table 7.7. This suggests that oxygen remains in the solid in stable furnctional groups, such as C=O.

Table 7.6: XPS results of cold plasma treated cellulose solid products (errors:±0.05%)

Composition (wt.%)		**H_2 environment**			**N_2 environment**		
Plasma power (W)	**Raw cellulose**	30W	50W	70W	30W	50W	70W
C	40.50	51.77	59.22	65.76	46.60	60.53	51.87
N	1.14	1.32	1.97	2.39	14.87	8.92	9.94
O	58.19	46.74	38.59	31.50	38.53	30.55	38.19

Table 7.7: CHN results for raw cellulose and cold plasma treated cellulose products under H_2 and N_2 carrier gases (errors:±0.05%)

Composition (wt.%)		**H_2 environment**			**N_2 environment**		
Plasma power (W)	**Raw Cellulose**	30W	50W	70W	30W	50W	70W
C (wt.%)	42.99	50.34	57.60	63.88	49.89	56.41	54.37
H (wt.%)	7.11	7.06	7.03	7.01	6.87	6.71	6.52
N (wt.%)	0.67	0.71	0.76	0.81	2.97	3.11	3.45
O (wt.%) *	49.23	41.89	34.61	28.3	40.27	33.77	35.66
*** By difference**							

The pronounced difference in nitrogen content on the material surface (Table 7.6) produced with both carrier gases is a strong indicator of surface modification of the cellulose with nitrogenous groups. For the bulk solid, the largest nitrogen content is at 70W, indicating that higher cold plasma powers allow more rapid substitution of nitrogenous groups. This is supported by the decrease in overall mass of the solid (Table 7.3) with increasing cold plasma power.

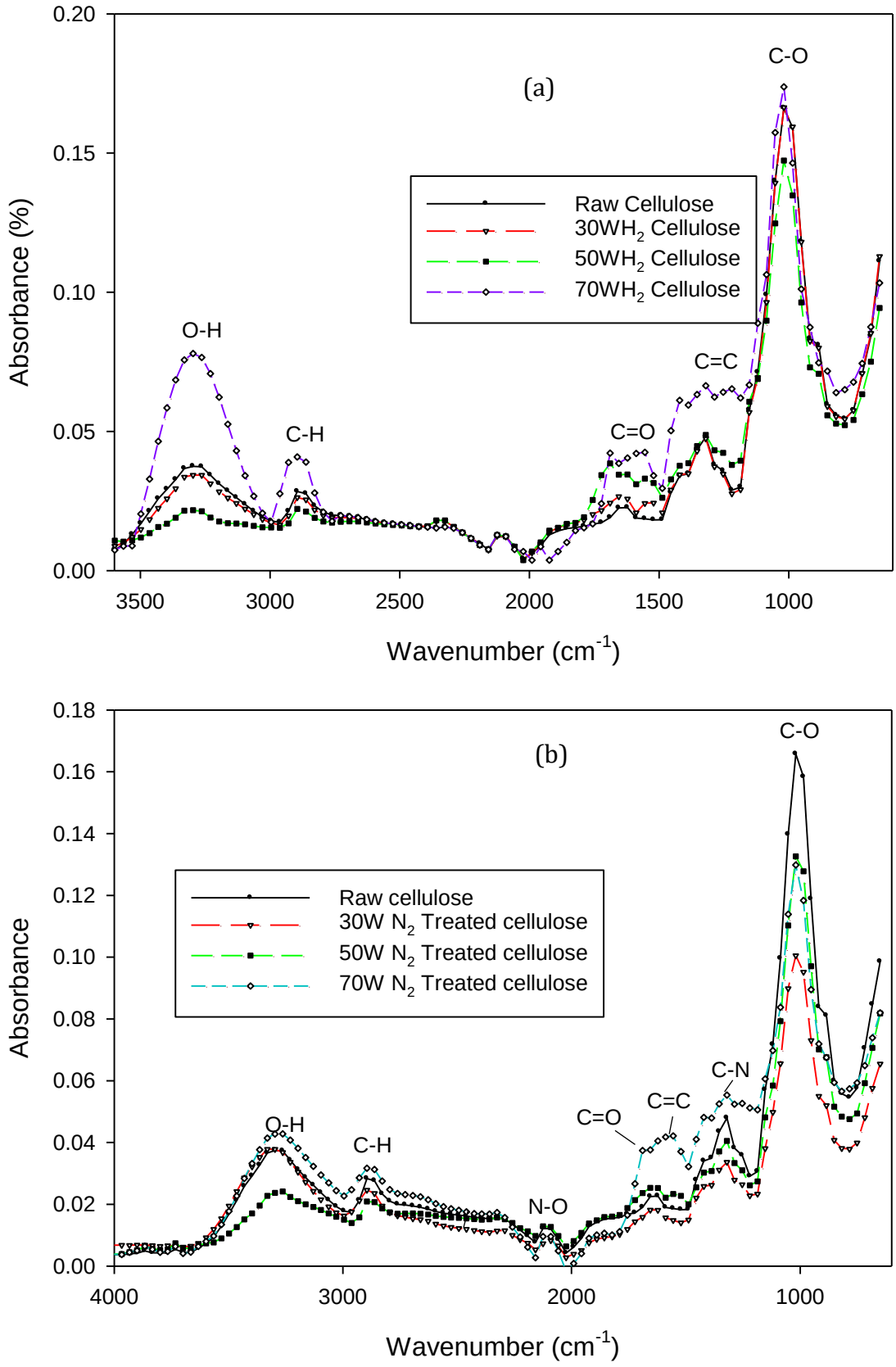

Figure 7.5: Solid phase FTIR of raw cellulose and (a) H_2 cold plasma treated cellulose (b) N_2 cold plasma treated cellulose at plasma power range of 30-70W

In the H_2 environment (Figure 7.5(a)), cold plasma derived solid residues revealed significant levels of ketone/aldehyde group formation, as indicated by peaks of increasing area at 1650cm^{-1} with increased plasma power. C=C bonds were visible at 1700 cm^{-1} at 50W and 70W, but were absent in the raw cellulose and in the 30W H_2 cold plasma treated cellulose, which indicates dehydrogenation or condensation reactions which reduce the solid's hydrogen content. The FTIR absorption signal at 1200cm^{-1} (corresponding to C-O-C bonds) is present at all powers but was greatly increased at 70W (>200%). This implies the formation of the ether cross-linkages observed in the formation of levoglucosan and levoglucosenone (Reaction 7.5). These ether bonds would also form in glucose bonded into cellulose chains, which indicates that the FTIR signal increase was due to these bonds forming in the cellulose chains at high powers (50-70W).

Interestingly, the peak height of the C-O (alcohol) (1130cm^{-1}) and O-H (3600cm^{-1}) groups were minimised at low powers (30-50W) under both carrier gases. The reduction in these peaks relative to the C=O peak indicates more rapid decomposition of alcohol groups than ketone groups, as would be expected from their relative bond energies (358KJ/mol vs 799KJ/mol).

Peaks were observed close to 1306cm^{-1} for both carrier gases, corresponding to C-H bonds bending. This bending peak consistently decreased with plasma power, indicating dehydrogenation reactions. The gaseous and liquid product distributions shown in Tables 7.3 and 7.4 reflect this, as the products were typically dehydrogenated relative to cellulose and hydrogen was generated at significant yields (up to 2.28wt.%). This was also observed (Figure 7.5(a)) in the increased C=C bond peak at 1650cm^{-1}, which indicates the solid material was less saturated than the raw cellulose and hence was less hydrogen rich.

In the N_2 environment, the C-O alcohol peak decreased when cold plasma was applied (Figure 7.5(b)). This implies that alcohol groups were more easily removed compared to other chemical groups at low powers (30W) due to their lower bond energy (Fridman, 2008).

The peaks shown at 3600 cm^{-1} were maximised under N_2 at 30W and decreased marginally for 50W and 70W (Figure 7.5(b)). As very few additional alcohol groups can be substituted onto cellulose (Flynn *et al.*, 2013), this indicates the formation of amine

groups, which produce a larger hydrogen bonding peak than alcohol groups due to the additional hydrogen atom (Deslandes *et al.*, 1998). An amine group peak at 1600 cm^{-1} is visible for plasma powers ≥50W and an N-O group peak at 2400 cm^{-1} only appears at 50W. Comparison with XPS results indicates that both amine and amide groups are present at these powers, as evidenced by peaks at 3.99eV and 4.05eV respectively (Figure 7.6).

Several small peaks are visible under N_2 at all powers from 1230-1500cm^{-1} (Figure 7.5(b)), which may indicate various locations of amine groups. Nitrogenous peaks are difficult to resolve due to traces often overlapping with the raw cellulose, except in the case of 50W in an N_2 environment, which clearly displays both amine and nitrile groups. The FTIR and XPS analysis indicates that the solid residue from cold plasma decomposition retains a similar structure to raw cellulose, but additional groups are substituted in place of alcohol groups, most notably amine groups but also amide groups at higher plasma powers (>50W).

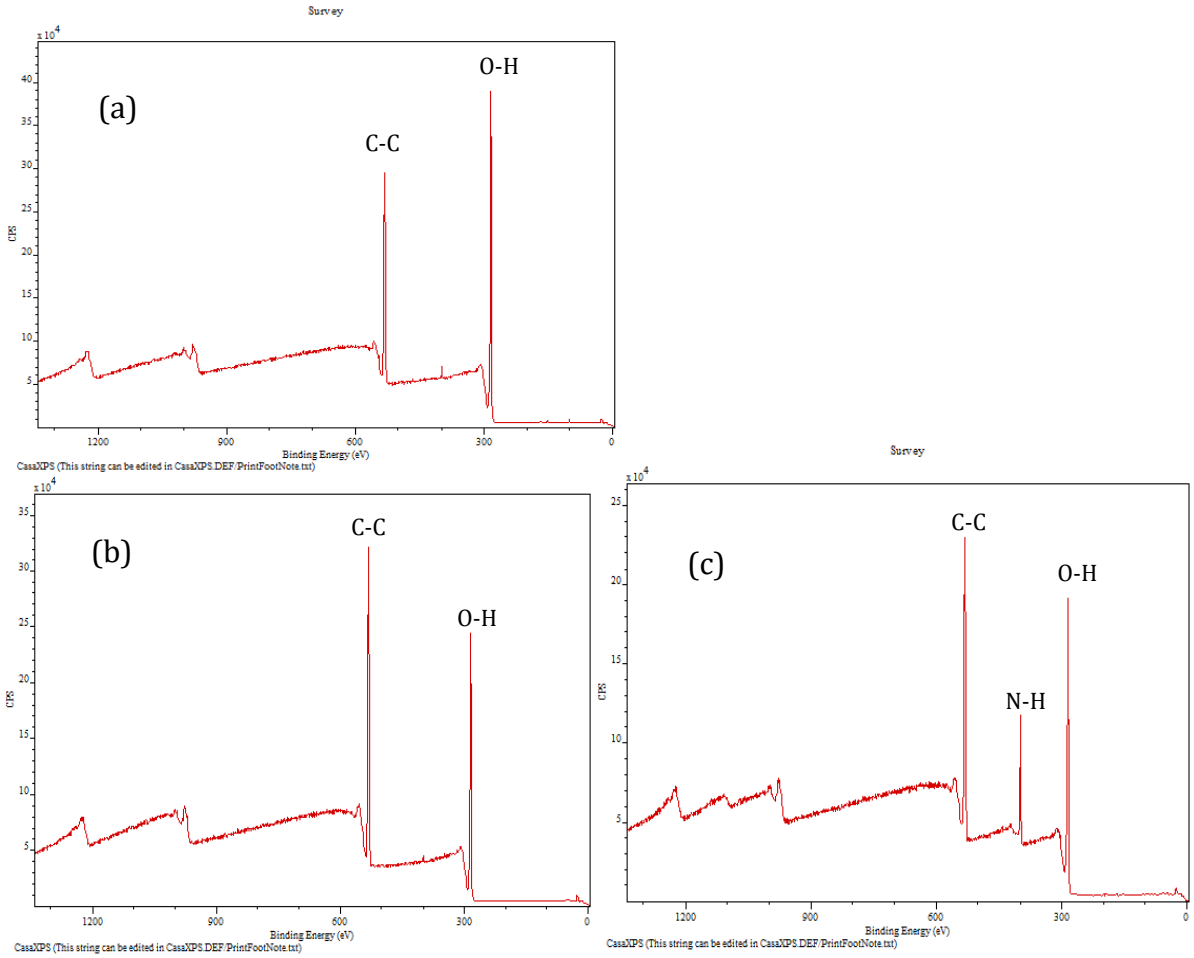

Figure 7.6: Complete XPS spectra of (a) raw cellulose (b) 70W H_2 and (c) 70W N_2 cold plasma treated cellulose

SEM analysis of the raw cellulose sample (Figure 7.7(a-b)) shows that the unprocessed cellulose was fibrous with a diameter of 10-50µm and a length of 50-500µm. In 7.6(a), it can be seen that the clusters were irregular but contain some linkage between fibres. At higher magnifications (b), the individual fibres were shown to be of consistant diameter with some unusual extrusions present near the clusters from loose cellulose strands and mechanical damage.

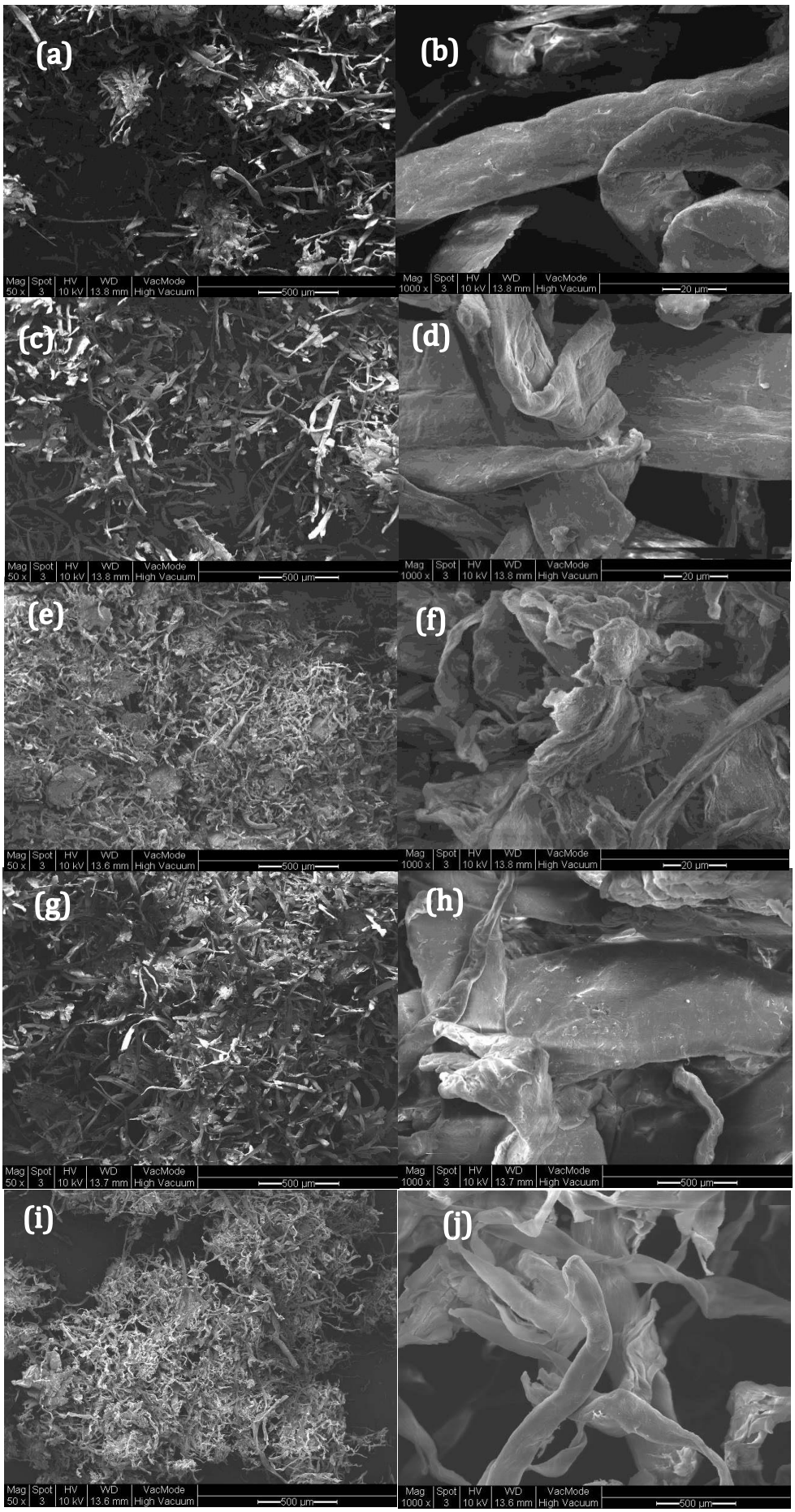
(a)
Mag 50 x | Spot 3 | HV 10 kV | WD 13.8 mm | VacMode High Vacuum | 500 µm
(b)
Mag 1000 x | Spot 3 | HV 10 kV | WD 13.8 mm | VacMode High Vacuum | 20 µm
(c)
Mag 50 x | Spot 3 | HV 10 kV | WD 13.8 mm | VacMode High Vacuum | 500 µm
(d)
Mag 1000 x | Spot 3 | HV 10 kV | WD 13.8 mm | VacMode High Vacuum | 20 µm
(e)
Mag 50 x | Spot 3 | HV 10 kV | WD 13.6 mm | VacMode High Vacuum | 500 µm
(f)
Mag 1000 x | Spot 3 | HV 10 kV | WD 13.8 mm | VacMode High Vacuum | 20 µm
(g)
Mag 50 x | Spot 3 | HV 10 kV | WD 13.7 mm | VacMode High Vacuum | 500 µm
(h)
Mag 1000 x | Spot 3 | HV 10 kV | WD 13.7 mm | VacMode High Vacuum | 500 µm
(i)
Mag 50 x | Spot 3 | HV 10 kV | WD 13.6 mm | VacMode High Vacuum | 500 µm
(j)
Mag 1000 x | Spot 3 | HV 10 kV | WD 13.6 mm | VacMode High Vacuum | 500 µm

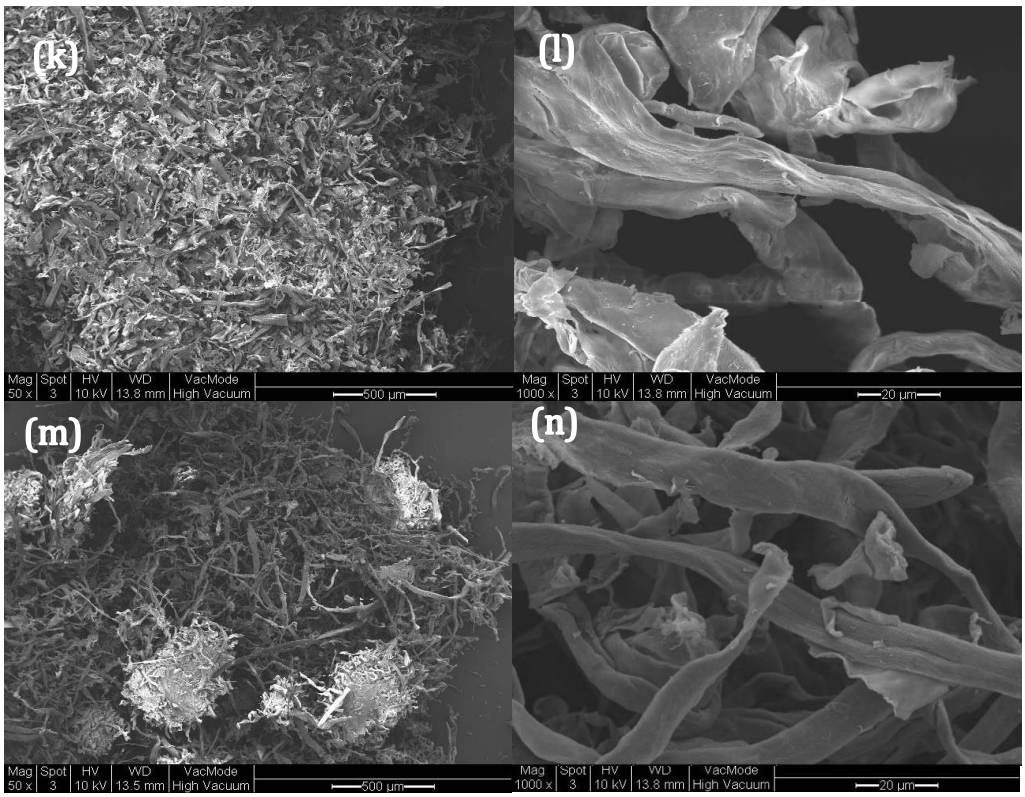

Figure 7.7: SEM images of raw and cold plasma treated cellulose at x50 (left) and x1000 (right) magnifications: (a-b) Raw cellulose (c-d) 30W H_2 (e-f) 30W N_2 (g-h) 50W H_2 (i-j) 50W N_2 (k-l) 70W H_2 (m-n) 70W N_2

Cold plasma treatment under H_2 at 30W had little effect on the individual fibre strands (Figure 7.7(c)) but appeared to break down some of the clumps visible in the untreated cellulose. This could indicate that the clumps were only weakly connected and low power cold plasma was able to separate the strands. At higher magnifications (Figure 7.7(d)) , the strands are relatively unchanged from the untreated cellulose though more distorted sections are visible.

N_2 treatment at 30W (Figure 7.7(e)) , by contrast, appears to expand the clumps to form a network of strands similar to an expanded surface. Plate like structures are also visible (Figure 7.7(f)). This is related to the reduction in strand thickness from decomposition during treatment and the resulting species may act as an adhesive to bond the thinner strands together. The plates may therefore be clumps that have been degraded with the strands bonded thoroughly via polymerised decomposition products until the boundaries are no longer visible.

50W H_2 cold plasma treatment (Figure 7.7 (g-h)) appears to show few changes from 30W treatment in terms of strand length and diameter, but the proportion of clumping visible is increased. At higher magnifications, the structure appears largely unaffected except that more surface defects are visible from release of decomposition products.

Under 50W N_2 plasma (Figure 7.7 (i)), the cellulose strands can be seen to aggregate into large clusters. Strands that are in close proximity are often linked by what appears to be polymerised decomposition products, and the plate like structures visible at 30W can be seen to have strands running through them (Figure 7.7 (j)). This would support the polymerisation of liquid decomposition products resulting in aggregation of fibrous particles into clusters and ribbon/plate structures.

Under 70W plasma (Figure 7.7 (k-l)), the clumping typical of N_2 also occurs under H_2, with the strands visibly bonded together into clumps and small plate like regions. However, the solid structure is much more uniform in terms of the aggregation pattern, with fewer plates visible. This difference in structure would suggest that the nitrogen carrier gas produced localised decomposition while 70W H_2 produced a similar level of decomposition evenly across the entire surface. The trend of increasing surface defects as power increased is apparent, and significant mass loss from the strands can be seen with the strands approximately halving in diameter.

70W N_2 (Figure 7.7 (m-n)) appears to produce extremely localised aggregation with a relatively loose structure elsewhere. Higher magnifications show the strands are approximately 60% thinner than in the untreated cellulose, and often appear to be flattened into ribbon structures. The reduced degree of inter-strand bonding visible in (Figure 7.7 (n)) may be caused by the strong plasma field rapidly gasifying any liquid decomposition products before they can polymerise and form cross linkages. The small dense clumps may be where the cellulose was densely packed, trapping liquid decomposition products, which form cross-linkages.

The magnitude of the cold plasma power has a marginal effect on the solid residue in terms of elemental and chemical bond composition. The primary difference is the introduction of nitrogenous groups such as amine and amide groups at higher powers.

The highest bulk nitrogen content recorded was 3.45wt.% on the 70W N_2 plasma, compared to 0.81wt.% at 70W H_2.

For all plasma powers and carrier gases, the structure of the solid residue was strongly affected by the cold plasma. Large reductions in the diameter of the cellulose fibres for both carrier gases at high powers and aggregation of cellulose fibres occured at all powers. Additionally, tiny fibres less than 10nm in diameter were formed at higher powers, which are likely to be a mixture of decomposed cellulose chain fragments or polymerised decomposition products. The plasma treated materials exhibited expanded surface structures such as plate and ribbon structures at the micro scale, which may make the solid residue an effective catalyst support for future study.

7.3 Summary

The carrier gas had a significant effect on selectivity, with the N_2 environment promoting condensation and decarboxylation reactions and the H_2 environment promoting cracking and hydrogenation.

For glucose, increasing plasma power increased the conversion up to 29% at 50W to form mainly gaseous products (89-90%), predominantly carbon oxides and hydrogen with traces of hydrocarbons (C_1-C_4). The liquid yield was very low compared to conventional thermal decomposition, theorised to be due to the low temperature being insufficient to remove furans and pyrans from the solid material. Hydrogenation occurred but there was little effect on the solid structure under a H_2 environment. Nitrogen content increased from 0.67wt.% (raw material) to 0.81%wt.% at 50W cold plasma under H_2 due to mass loss of other elements (carbon, hydrogen and oxygen).

Cold plasma power can be used to introduce nitrogenous groups onto cellulose. The highest yield of nitrogen was 14.87 wt.% for the 30W N_2 cold plasma. This opens up opportunities for surface modification/treatment using cold plasma at atmospheric conditions.

The structure of the solid residue is strongly affected by cold plasma. Large reductions in the diameter of the cellulose fibres were observed for both carrier gases at high plasma powers (≥50W) and aggregation of cellulose fibres occurred at all tested powers (30W-

70W). Additionally, nanofibres (≤10nm diameter) were formed at all powers which are likely to be a mixture of decomposed cellulose chain fragments or polymerised decomposition products. The plasma treated materials exhibit expanded surface structures such as plate and ribbon structures at the micro scale which may make the solid residue an effective catalyst support. The gaseous products from cellulose decomposition were similar to those obtained from glucose decomposition but had a lower ratio of CO_2 to CO (3.21:1 vs 0.89:1) and a greater overall gas yield (44.94 vs 25.2wt.%). However, a high liquid yield was obtained from cold plasma assisted cellulose decomposition (up to 48.66wt.%).

This work demonstrates the ability of cold plasma to decompose glucose and cellulose to gaseous products and carbonaceous expanded materials and has determined the full range of liquid products obtainable from cellulose decomposition with cold plasma. Use of H_2 as the carrier gas permited the production of several ketones and furans at selectivities up to approximately 20%, while N_2 carrier gas produced a similar range of products to thermal processing methods.

Chapter 8. Applications

The results of this work have revealed many applications where cold plasma in both single phase and gas-liquid phase would be highly advantageous. Much higher throughputs of a given feedstock and hence reaction rates can be obtained with a liquid feedstock due to the higher density of liquids compared to vapours. This effect could be used for producing hydrogen peroxide from liquid water, requiring a smaller reactor and a lower energy input than production of hydrogen peroxide in the gaseous phase.

Chapter 4 revealed that the presence of the liquid phase can prevent the decomposition of less volatile products, allowing significant yields to be isolated. The yields of unexpected products observed in this work were low (1-5wt.%) but could potentially be improved by appropriate catalysts or optiming reaction conditions. This can permit the use of novel synthesis pathways not possible in other reactors to create value added products, which could potentially include production of propanol from methanol and ethane or formic acid from carbon dioxide. This effect applies mostly with relatively short chain liquids, as they are likely to produce more volatile liquids, which can then accumulate.

Cold plasmas are highly fouling resistant due to the capability of cold plasma to protect the catalyst by decomposing any organic fouling that forms. Cold plasma can also operate without a catalyst, so that any fouling that does form has almost no effect. Additionally, catalysts that have dielectric properties, such as metallic catalysts, titanium dioxide and barium titanate, synergise extremely well with the plasma. The plasma is focussed by the catalyst to the active sites on the catalyst surface, which both increases the energy available, hence reaction rate, and inhibits fouling. The combination of these makes dual phase cold plasma highly appropriate for waste glycerol valorisation or pyrolysis oil upgrading, as the cold plasma acts to protect the catalyst and the plasma is focused near the catalyst surface which increases catalyst activity. The ability to operate with liquid inputs allows larger throughputs and allows operation below the boiling point of larger feedstock compounds, which favours liquid phase products.

Cold plasma synergises well with catalysts with dielectric properties, so it may be possible to employ a catalyst that promotes only cracking and hydrocracking reactions. For

example, with glycerol, it would favour the formation of methanol, which is highly desired for use in the biodiesel production industry.

Findings from Chapter 6 revealed that gas-liquid cold plasma can permit high selectivity de-esterification reactions when operated at low powers. If this could be intensified, e.g. by using a catalyst, it may be possible to perform de-esterification of any liquid phase ester with gas-liquid cold plasma. This work details its use for triglycerides, to produce FFA which could then be esterified to FAME or other fatty acid esters. This would require an additional reaction step, but the overall residence time would be greatly reduced as the esterification reaction between methanol and FFA reaches full conversion within 90 minutes and the plasma residence time is less than 15 seconds, compared to >3 hours with acid catalyst transesterification.

Glucose decomposition (Chapter 7) shows dehydrogenation at higher powers. However, glucose has an OH group on every carbon atom so dehydrogenation forms ketone groups which produce high yields of various furans and levoglucosan, up to 57% and 16% respectively. Methanol is also released at relatively large yields of up to 10%. Similar results occur in glucose pyrolysis at 500°C, except the selectivity to furans is increased and levoglucosan is generally a trace product (Hu et al., 2018). However, 500°C thermal decomposition is capable of breaking down furans into smaller chemicals such as dialdehydes and diols, reducing selectivity to furans (Seshadri and Westmoreland, 2012). Cold plasma therefore could be useful for high selectivity formation of furans and levoglucosan from glucose and, by extension, for other carbohydrate feedstocks.

Additionally, solid-gas cold plasma has been demonstrated to be capable of substituting nitrogen onto cellulose molecules at 30W-70W plasma powers (Chapter 7), though dehydrogenation also occurs which limits its value. The resulting solid is extremely carbon rich and has a high internal surface area and surface acidity. This indicates cold plasma may be an effective method for producing high surface area activated carbon. If non-nitrogenous activated carbon is required, the use of a non-reactive carrier gas such as helium is likely to have the same effect in dehydrogenation without introducing nitrogen to the structure. As with gas-liquid cold plasma, selectivities can be tuned towards any desired products in the gas, liquid or solid phases. The plasma also induces decomposition of cellulose to furans, pyrans and other useful chemicals, which means

plasma can either introduce nitrogen to cellulose or depolymerise cellulose to produce glucose pyrolysis products without the need for hydrolysis. In the presence of hydrogen, the liquid phase contains only 6 cyclic species at relatively high selectivities (10-20wt.%), while nitrogen produces a wide range of furans, pyrans and cyclic hydrcarbons at lower selectivities (up to 10wt.%). As valorisation of both cellulose and triglycerides can be performed under the same cold plasma conditions, decomposition of oil rich biomass to generate both fuels and value added chemicals is potentially feasible.

Chapter 9. Conclusions and Future work

9.1 Conclusion

This thesis explored the feasibility and effectiveness of utilising two phase cold plasma for valorisation of waste triglycerides and waste products from commercialised transesterification processes. A range of feedstocks from the biodiesel production process were subjected to two phase cold plasma initiated decomposition within a dielectric barrier discharge reactor. The effects of reaction conditions such as carrier gas, plasma power, temperature and packing materials (including catalysts) were studied to enable optimisation and tuning of the product distribution.

A methanol feedstock was used initially to test the concept of gas-liquid cold plasma promoted decomposition. Without a catalyst or increased temperatures, cold plasma promoted the decomposition of methanol to hydrogen, carbon oxides and hydrocarbons. Initial conversions of up to 25% were achieved within an 11 second residence time at 50W plasma power, which could potentially be improved using catalysts. A kinetic model was developed which simulated the process effectively within the range of conditions studied. Further work would be required to extend the model to other process conditions.

Glycerol decomposition was studied to test the concept of valorising the waste glycerol produced by transesterification processes and the effectiveness of a cold plasma reactor with a non-volatile liquid feedstock. Conversions up to 92% were obtained and moderate yields of acetol were recorded (17wt.%) without catalysts, establishing the feasibility of the concept. Unlike thermal processes which favour aldehyde and ketone products, gas-liquid cold plasma decomposition of glycerol favours hydrocarbons and alcohols, as a result of the rapid decomposition of aldehydes in cold plasma. From the data, a full reaction mechanism was proposed and a kinetic model developed that simulated the process effectively for nitrogen carrier gas. Extending the model to simulate the hydrogen environment significantly overpredicted the conversion at higher plasma powers, but a correlation was observed between experimental results and the model results for a reduced plasma power. This difference was attributed to the reduced range of hydrogen excited states (all lower than 14eV) compared to nitrogen (>25eV), which distorts the energy distribution of radicals under hydrogen. This effect could be utilised to improve process selectivities to low energy reactions, and has potential for further extending the

ability to tune the process dynamics. Further research into other carrier gases with different energy distributions could permit fine control of the reaction pathways during decomposition.

Analysis of waste glycerol decomposition showed that the reactor design is tolerant of impurities within the feedstock and is resilient to fouling both with and without catalysts. Typically, no fouling was observed under most conditions and very high conversions could be obtained. For example, conversions of up to 91% were obtained without a catalyst. The exception was the use of Ni/Al_2O_3 as the catalyst, which is initially effective at improving conversion but loses activity with time due to nickel saponification reactions. Cold plasma decomposition of waste glycerol typically produces predominantly hydrocarbons and hydrogen, but acetol (52wt.%) and formic acid (20wt.%) can also be produced at high selectivities through process tuning.

Experimental work on triglyceride decomposition using gas-liquid cold plasma found that triglycerides can be converted to either FFA or FAME selectively depending on the choice of carrier gas. Packing materials were shown to maximise overall conversion (up to 90%.) Lower temperature operation favoured the production of FFA or FAME, while increased temperature operation generated predominantly gaseous products. Liquid hydrocarbons were also generated at relatively low yields (<5wt.%) at all temperatures, which suggests that direct conversion of triglycerides to liquid hydrocarbons is possible. This would compare favourably with current alternatives to transesterification due to the lower power requirements if all the FAE generated could be converted to liquid hydrocarbons, which is a potential area for future work.

Impure glycerides in the form of waste cooking oil were successfully decomposed to FAME and/or FFA, with the product distributions following the same trends observed for pure glycerides. However, under hydrogen at low powers, esterification of FFA with glycerides was observed with a 6% net increase in glyceride content, likely due to the presence of hydrogen limiting de-esterification reaction rates. Waste cooking oil decomposition was successfully tuned to produce yields of FAE/liquid hydrocarbons over 50wt.% without requiring methanol, heating or high pressures and with a residence time of under 11 seconds.

Glucose and cellulose decomposition were studied to investigate the possibility of one step valorisation of oil rich biomass for producing liquid fuels (hydrocarbons and/or FAE) and value added products. Cold plasma was demonstrated to be effective for decomposing cellulose to gaseous (20-60wt.%) and liquid products (30-40wt.%), with relatively little solid residue (10-45wt.%). The hydrogen carrier gas generated a limited range of valuable products (e.g. levoglucosenone, cyclopentanone and 5-HMF) at high selectivities (up to 20wt.%) while nitrogen generated a wider range of valuable products (>20) at lower selectivities (up to 10wt.%). The observed two phase effects and the tunablity of cold plasma present significant research opportunities to utilise novel synthesis pathways to create value added products.

All the main components of oil rich biomass have been shown to be decomposed or destabilised at relatively low plasma powers (10-70W) with common carrier gases (hydrogen, nitrogen). This suggests that direct decomposition of oil-rich biomass by cold plasma is likely to be a useful area for further research.

This thesis has demonstrated the feasibility and effectiveness of utilising gas-liquid cold plasma for valorisation of waste triglycerides and waste products from commercialised transesterification processes, indicating its potential as a method of sustainable liquid fuel generation.

9.2 Future work

Esterification of methanol

Further experimental investigations are recommended for the formation of methyl methanoate from pure methanol and glycerol to determine if cold plasma has the potential to induce esterification reactions without catalysts and to quantify the extent of reaction. This could possibly work for a reaction between carbon dioxide and methanol at more modest conversions. Investigation of this topic was not possible in this work due to time constraints. The aim should be to develop kinetics for the conversion of a methanol/ formic acid mixture to methyl methanoate under cold plasma, with further study of methanol conversion under a carbon dioxide carrier gas. The findings could indicate a catalyst free method of inducing esterification and potentially a method for valorising waste carbon dioxide streams.

Detailed gas-liquid plasma model

An area of potential added value for this work would be the development of an improved kinetics model for gas-liquid cold plasma. The model utilised within this work makes a series of assumptions and while the results fit the process, the applicability is limited to one carrier gas and a single reactor design and energy efficiency.

To reduce the number of assumptions and increase the accuracy of the model, the following modifications are suggested:

- Use of a fluid flow model with meshing to allow the distribution of the two phases to be simulated, which would also allow the effect of the flow distribution to be studied as a variable.
- In addition to electron temperature, electron density should also be included. Electron density would effectively act as a reactant in initiation reactions. Tests with this may reveal if electron or ion temperature and concentrations are the dominant factor in plasma-initiated reactions.
- The effects of plasma heating should also be included, which necessitates a non-isothermal simulation. DBD reactors have a high degree of plasma heating, so the heating effects are likely to be significant. The significance of plasma heating is supported by the internal temperature of the reactor in operation increasing to 45-75°C within 1 minute from 20°C as measured in this work.

On the experimental side, additional tests with a mounted optical probe to allow the line intensity method to be used would be highly desirable. This could not be done in this work due to both time constraints and the reactor design being incompatible with the available optical probes. Tests with two phase plasma in the presence of an optical probe could be used to help determine the two phase effect on electron temperature and inform future work on the topic

Catalysts

Results obtained for waste glycerol and waste cooking oil with cracking catalysts are highly promising, but the nickel used in the early tests was highly susceptible to fouling with both feedstocks. Other catalytic cracking catalysts, primarily zeolites, were tested for waste cooking oil and were found to be more fouling resistant but were of lower activity than nickel.

This work theorises that the higher activity of nickel than zeolites is due to the dielectric effect focussing plasma onto the nickel surface, while the zeolite catalysts have low dielectric constants.

Additional tests with a dielectric cracking catalyst which is not vulnerable to saponification would be desirable and may have the potential to generate high conversion of both waste glycerol and waste cooking oil without extensive fouling.

Oil rich biomass cold plasma testing

In this work, cold plasma was shown to be capable of both decomposing triglycerides to hydrocarbons/FAME and decomposing cellulose to valuable furans/pyrans. These results could be tested together by exposing oil rich biomass to cold plasma, which could potentially simultaneously produce both fuel compounds and valuable cyclic products such as levoglucosenone. The work done on the separate species would aid interpretation of the results.

This would also likely generate a carbon rich solid material similar to the products from cellulose decomposition, and would offer insights into the decomposition of protein, lignin and other biological materials under gas-liquid cold plasma conditions.

Pyrolysis oil upgrading

Chapter 7 indicated that decomposition of carbohydrate derivatives to hydrocarbons, carbon oxides and hydrogen is feasible under gas-liquid cold plasma conditions. Gas-liquid cold plasma is more resistant to fouling than many other processes. This indicates that cold plasma may be suitable for upgraing pyrolysis oil from liginocellulosic biomass into usable fuels. Tests with a fresh pyrolysis oil feedstock would be able to explore this possibility and may present the possibility of a low cost and sustainable alternative to hydrodeoxygenation for second and third generation biofuels.

References

1. Abbot, J. and Dunstan, P.R. (1997) 'Catalytic Cracking of Linear Paraffins: Effects of Chain Length', *Industrial & Engineering Chemistry Research*, 36(1), pp. 76-82.
2. Adjaye, J.D. and Bakhshi, N.N. (1995) 'Catalytic conversion of a biomass-derived oil to fuels and chemicals I: Model compound studies and reaction pathways', *Biomass and Bioenergy*, 8(3), pp. 131-149.
3. Aerts, R., Somers, W. and Bogaerts, A. (2015) 'Carbon Dioxide Splitting in a Dielectric Barrier Discharge Plasma: A Combined Experimental and Computational Study', *ChemSusChem*, 8(4), pp. 702-716.
4. Agblevor, F.A., Mante, O., Abdoulmoumine, N. and McClung, R. (2010) 'Production of Stable Biomass Pyrolysis Oils Using Fractional Catalytic Pyrolysis', *Energy & Fuels*, 24, pp. 4087-4089.
5. Altshuler, S. (1953) 'Excitation cross section for helium atoms. II', *Physical Review*, 89(5), pp. 1093-1095.
6. An, G., Sun, Y., Zhu, T. and Yan, X. (2011) 'Degradation of phenol in mists by a non-thermal plasma reactor', *Chemosphere*, 84(9), pp. 1296-1300.
7. An, K., Yu, S.W., Li, X.J., Shen, Y.Y., Zhou, B., Zhang, G.J. and Liu, X.P. (2015) 'Microwave plasma reactor with conical-reflector for diamond deposition', *Vacuum*, 117, pp. 112-120.
8. Apparao, U., Vijayalakshmi, S. and Ranjitha, J. (2016) 'A review on current research activities: Biological conversion of crude glycerol from biodiesel industry into value-added products', *International Journal of ChemTech Research*, 9(4), pp. 576-586.
9. Aresta, M., Dibenedetto, A., Nocito, F. and Pastore, C. (2007) 'A study on the carboxylation of glycerol to glycerol carbonate with carbon dioxide: The role of the catalyst, solvent and reaction conditions', *Atmospheric Environment*, 41(2), pp. 407-416.
10. Atabani, A.E., Silitonga, A.S., Badruddin, I.A., Mahlia, T.M.I., Masjuki, H.H. and Mekhilef, S. (2012) 'A comprehensive review on biodiesel as an alternative energy resource and its characteristics', *Renewable and Sustainable Energy Reviews*, 16(4), pp. 2070-2093.
11. Atadashi, I.M., Aroua, M.K., Abdul Aziz, A.R. and Sulaiman, N.M.N. (2013) 'The effects of catalysts in biodiesel production: A review', *Journal of Industrial and Engineering Chemistry*, 19(1), pp. 14-26.
12. Atong, D. and Sricharoenchaikul, V. (2009) *Proceedings of the ASME 3rd International Conference on Energy Sustainability 2009, ES2009*. Available at: https://www.scopus.com/inward/record.uri?eid=2-s2.0-77953766349&partnerID=40&md5=0a9f84e1feb3b4c7d95b11e258598ce2.
13. Auprêtre, F., Descorme, C. and Duprez, D. (2002) 'Bio-ethanol catalytic steam reforming over supported metal catalysts', *Catalysis Communications*, 3(6), pp. 263-267.
14. Ayoub, M., Sufian, S., Hailegiorgis, S.M., Ullah, S. and Uemura, Y. (2017) *IOP Conference Series: Materials Science and Engineering*. Available at: https://www.scopus.com/inward/record.uri?eid=2-s2.0-85028644857&doi=10.1088%2f1757-899X%2f226%2f1%2f012073&partnerID=40&md5=68e9080c4b343ad0870617efa8754587.
15. Aysu, T. (2015) 'Catalytic pyrolysis of Alcea pallida stems in a fixed-bed reactor for production of liquid bio-fuels', *Bioresource Technology*, 191(0), pp. 253-262.
16. Azahar, W.N.A.W., Bujang, M., Jaya, R.P., Hainin, M.R., Mohamed, A., Ngadi, N. and Jayanti, D.S. (2016) 'The potential of waste cooking oil as bio-asphalt for alternative binder – An overview', *Jurnal Teknologi*, 78(4), pp. 111-116.
17. Babaeva, N.Y. and Naidis, G.V. (2018) 'Modeling of Plasmas for Biomedicine',

Trends in Biotechnology, 36(6), pp. 603-614.
18. Bahri, M., Haghighat, F., Rohani, S. and Kazemian, H. (2016) 'Impact of design parameters on the performance of non-thermal plasma air purification system', *Chemical Engineering Journal*, 302, pp. 204-212.
19. Balat, M. (2008) 'Mechanisms of thermochemical biomass conversion processes. Part 1: Reactions of pyrolysis', *Energy Sources, Part A: Recovery, Utilization and Environmental Effects*, 30(7), pp. 620-635.
20. Bartholomew, C.H. and Farrauto, R.J. (1976) 'Chemistry of nickel-alumina catalysts', *Journal of Catalysis*, 45(1), pp. 41-53.
21. Baulch, D.L., Pilling, M.J., Cobos, C.J., Cox, R.A., Esser, C., Frank, P., Just, T., Kerr, J.A., Troe, J., Walker, R.W. and Warnatz, J. (1992) 'Evaluated Kinetic Data for Combustion Modelling', *Journal of Physical and Chemical Reference Data*, 21(3), pp. 411-734.
22. Beebe, S.J. (2013) 'Bioelectrics in basic science and medicine: Impact of electric fields on cellular structures and functions', *Journal of Nanomedicine and Nanotechnology*, 4(2), p. 5.
23. Bender, M.L. (1960) 'Mechanisms of Catalysis of Nucleophilic Reactions of Carboxylic Acid Derivatives', *Chemical Reviews*, 60(1), pp. 53-113.
24. Bhatia, S., Leng, C.T. and Tamunaidu, P. (2007) 'Modeling and Simulation of Transport Riser Reactor for Catalytic Cracking of Palm Oil for the Production of Biofuels', *Energy & Fuels*, 21(6), pp. 3076-3083.
25. Bi, Y.T., Wang, G., Shi, Q., Xu, C.M. and Gao, J.S. (2014) 'Compositional Changes during Hydrodeoxygenation of Biomass Pyrolysis Oil', *Energy & Fuels*, 28(4), pp. 2571-2580.
26. Bi, Z. and He, B.B. (2016) 'Phospholipid transesterification in sub-/super-critical methanol with the presence of free fatty acids', *Fuel*, 166, pp. 461-466.
27. Bichon, P., Asheim, M., Sperle, A.J.T., Fathi, M., Holmen, A. and Blekkan, E.A. (2007) 'Hydrogen from methanol steam-reforming over Cu-based catalysts with and without Pd promotion', *International Journal of Hydrogen Energy*, 32(12), pp. 1799-1805.
28. Bielansky, P., Weinert, A., Schönberger, C. and Reichhold, A. (2012) 'Gasoline and gaseous hydrocarbons from fatty acids via catalytic cracking', *Biomass Conversion and Biorefinery*, 2(1), pp. 53-61.
29. Billaud, F., Guitard, Y., Tran Minh, A.K., Zahraa, O., Lozano, P. and Pioch, D. (2003) 'Kinetic studies of catalytic cracking of octanoic acid', *Journal of Molecular Catalysis A: Chemical*, 192(1), pp. 281-288.
30. Black, L.T. (1970) 'Direct determination of sodium in soybean oil by flame photometry', *Journal of the American Oil Chemists Society*, 47(9), pp. 313-315.
31. Boey, P.-L., Ganesan, S., Maniam, G.P., Khairuddean, M. and Lim, S.-L. (2012) 'A new catalyst system in transesterification of palm olein: Tolerance of water and free fatty acids', *Energy Conversion and Management*, 56, pp. 46-52.
32. Bokade, V.V. and Yadav, G.D. (2009) 'Transesterification of Edible and Nonedible Vegetable Oils with Alcohols over Heteropolyacids Supported on Acid-Treated Clay', *Industrial & Engineering Chemistry Research*, 48(21), pp. 9408-9415.
33. Boocock, D.G.B., Konar, S.K. and Glaser, G. (2008) 'The Formation of Petrodiesel by the Pyrolysis of Fatty Acid Methyl Esters Over Activated Alumina', in *Progress in Thermochemical Biomass Conversion*. pp. 1517-1524.
34. BP (2017) *BP Statistical Review*

35. *of World Energy* (6.2017). Available at: https://www.bp.com/en/global/corporate/energy-economics/statistical-review-of-world-energy/renewable-energy/biofuels-production.html.

36. Bridgwater, A.V. (2012) 'Review of fast pyrolysis of biomass and product upgrading', *Biomass and Bioenergy*, 38, pp. 68-94.
37. Brudnik, K., Gola, A.A. and Jodkowski, J.T. (2009) 'Theoretical kinetic study of the formation reactions of methanol and methyl hypohalites in the gas phase', *Journal of Molecular Modeling*, 15(9), pp. 1061-1066.
38. Brühl, L. (2014) 'Fatty acid alterations in oils and fats during heating and frying', *European Journal of Lipid Science and Technology*, 116(6), pp. 707-715.
39. Burlica, R., Shih, K.Y. and Locke, B.R. (2010) 'Formation of H2and H2O2in a water-spray gliding arc nonthermal plasma reactor', *Industrial and Engineering Chemistry Research*, 49(14), pp. 6342-6349.
40. Buszek, R.J., Sinha, A. and Francisco, J.S. (2011) 'The isomerization of methoxy radical: Intramolecular hydrogen atom transfer mediated through acid catalysis', *Journal of the American Chemical Society*, 133(7), pp. 2013-2015.
41. Caetano, N.S., Caldeira, D., Martins, A.A. and Mata, T.M. (2017) 'Valorisation of Spent Coffee Grounds: Production of Biodiesel via Enzymatic Catalysis with Ethanol and a Co-solvent', *Waste and Biomass Valorization*, 8(6), pp. 1981-1994.
42. Chan, F.L. and Tanksale, A. (2014) 'Catalytic steam gasification of cellulose using reactive flash volatilization', *ChemCatChem*, 6(9), pp. 2727-2739.
43. Chang, J.-S. (2001) 'Recent development of plasma pollution control technology: a critical review', *Science and Technology of Advanced Materials*, 2(3-4), pp. 571-576.
44. Charusiri, W. and Vitidsant, T. (2005) 'Kinetic Study of Used Vegetable Oil to Liquid Fuels over Sulfated Zirconia', *Energy & Fuels*, 19(5), pp. 1783-1789.
45. Charusiri, W., Yongchareon, W. and Vitidsant, T. (2006) 'Conversion of used vegetable oils to liquid fuels and chemicals over HZSM-5, sulfated zirconia and hybrid catalysts', *Korean Journal of Chemical Engineering*, 23(3), pp. 349-355.
46. Chen, L., Fu, J., Yang, L., Chen, Z., Yuan, Z. and Lv, P. (2014a) 'Catalytic hydrotreatment of fatty acid methyl esters to diesel-like alkanes over hβ zeolite-supported nickel catalysts', *ChemCatChem*, 6(12), pp. 3482-3492.
47. Chen, W., Luo, Z.Y., Yu, C.J., Li, G.X., Yang, Y., Zhang, J.X. and Lu, K.Y. (2014b) 'Catalytic transformations of acids, aldehydes, and phenols in bio-oil to alcohols and esters', *Fuel*, 135, pp. 55-62.
48. Chiaramonti, D., Buffi, M., Rizzo, A.M., Lotti, G. and Prussi, M. (2016) 'Bio-hydrocarbons through catalytic pyrolysis of used cooking oils and fatty acids for sustainable jet and road fuel production', *Biomass and Bioenergy*, 95, pp. 424-435.
49. Chiu, C.W., Dasari, M.A., Suppes, G.J. and Sutterlin, W.R. (2006) 'Dehydration of glycerol to acetol via catalytic Reactive distillation', *American Institute of Chemical Engineers Journal*, 52(10), pp. 3543-3548.
50. Cho, M.H., Mun, T.Y., Choi, Y.K. and Kim, J.S. (2014) 'Two-stage air gasification of mixed plastic waste: Olivine as the bed material and effects of various additives and a nickel-plated distributor on the tar removal', *Energy*, 70, pp. 128-134.
51. Choudhury, N.D., Chutia, R.S., Bhaskar, T. and Kataki, R. (2014) 'Pyrolysis of jute dust: effect of reaction parameters and analysis of products', *Journal of Material Cycles and Waste Management*, 16(3), pp. 449-459.
52. Chouhan, A.P.S. and Sarma, A.K. (2011) 'Modern heterogeneous catalysts for biodiesel production: A comprehensive review', *Renewable and Sustainable Energy Reviews*, 15(9), pp. 4378-4399.
53. Chyrkin, A., Pillai, R., Galiullin, T., Wessel, E., Grüner, D. and Quadakkers, W.J. (2017) 'External A-Al2O3 scale on Ni-base alloy 602 CA. – Part I: Formation and long-term stability', *Corrosion Science*, 124, pp. 138-149.
54. Corma, A., Huber, G.W., Sauvanaud, L. and O'Connor, P. (2007) 'Processing biomass-derived oxygenates in the oil refinery: Catalytic cracking (FCC) reaction

pathways and role of catalyst', *Journal of Catalysis*, 247(2), pp. 307-327.
55. Corma Canos, A., Iborra, S. and Velty, A. (2007) 'Chemical routes for the transformation of biomass into chemicals', *Chemical Reviews*, 107(6), pp. 2411-2502.
56. Crance, M. (1988) 'Multiphoton ionisation of hydrogen. A non-perturbative calculation of strong-field effects', *Journal of Physics B: Atomic, Molecular and Optical Physics*, 21(15), pp. 2697-2708.
57. Cui, F.M., Zhang, X.Y. and Shang, L.M. 805-806 (2013) 'Thermogravimetric analysis of glucose-based and fructose-based carbohydrates' *Advanced Materials Research* [Conference Paper]. pp. 265-268. Available at: https://www.scopus.com/inward/record.uri?eid=2-s2.0-84886315054&doi=10.4028%2fwww.scientific.net%2fAMR.805-806.265&partnerID=40&md5=0be30f908c7b9b3c1f8b1118db1fe7b7.
58. Cui, G. and Fang, W. (2011) 'Mechanistic photodissociation of glycolaldehyde: Insights from ab initio and RRKM calculations', *ChemPhysChem*, 12(7), pp. 1351-1357.
59. Czylkowski, D., Hrycak, B., Jasiński, M., Dors, M. and Mizeraczyk, J. (2016) 'Microwave plasma-based method of hydrogen production via combined steam reforming of methane', *Energy*, 113, pp. 653-661.
60. Dandik, L. and Aksoy, H.A. (1998) 'Pyrolysis of used sunflower oil in the presence of sodium carbonate by using fractionating pyrolysis reactor', *Fuel Processing Technology*, 57(2), pp. 81-92.
61. Danuthai, T., Jongpatiwut, S., Rirksomboon, T., Osuwan, S. and Resasco, D.E. (2009) 'Conversion of methylesters to hydrocarbons over an H-ZSM5 zeolite catalyst', *Applied Catalysis A: General*, 361(1-2), pp. 99-105.
62. Das, J.N. and Bhattacharyya, P.K. (1992) 'Electron-Hydrogen-Atom Ionization Calculation in Two Modified Forms of the Born Approximation', *Journal of Physics B: Atomic, Molecular and Optical Physics*, 25(1), pp. 249-258.
63. Demirbas, A. (2008) 'Effect of Alkali on Liquid Yields from the Pyrolysis of Olive Oil', *Energy Sources, Part A: Recovery, Utilization, and Environmental Effects*, 30(11), pp. 1060-1064.
64. Demirbas, A., Bafail, A., Ahmad, W. and Sheikh, M. (2016) 'Biodiesel production from non-edible plant oils', *Energy Exploration and Exploitation*, 34(2), pp. 290-318.
65. Deng, Q., Wang, Q., Wang, Q., Huang, Q. and Yin, P. (2009) *3rd International Conference on Bioinformatics and Biomedical Engineering, iCBBE 2009*. Available at: https://www.scopus.com/inward/record.uri?eid=2-s2.0-72749111676&doi=10.1109%2fICBBE.2009.5163501&partnerID=40&md5=6c0bf903bb9bd1758c04dd1ba8113399.
66. Derakhshesh, M., Abedi, J. and Hassanzadeh, H. (2010) 'Mechanism of methanol decomposition by non-thermal plasma', *Journal of Electrostatics*, 68(5), pp. 424-428.
67. Derakhshesh, M., Abedi, J. and Omidyeganeh, M. (2009) 'Modeling of hazardous air pollutant removal in the pulsed corona discharge', *Physics Letters, Section A: General, Atomic and Solid State Physics*, 373(11), pp. 1051-1057.
68. Deslandes, Y., Pleizier, G., Poiré, E., Sapieha, S., Wertheimer, M.R. and Sacher, E. (1998) 'The surface modification of pure cellulose paper induced by low-pressure nitrogen plasma treatment', *Plasmas and Polymers*, 3(2), pp. 61-76.
69. Di, L., Li, Z., Lee, B. and Park, D.W. (2017) 'An alternative atmospheric-pressure cold plasma method for synthesizing Pd/P25 catalysts with the assistance of ethanol', *International Journal of Hydrogen Energy*, 42(16), pp. 11372-11378.
70. Di, L.B., Duan, D.Z., Zhan, Z.B. and Zhang, X.L. (2016) 'Gas-Liquid Cold Plasma for Synthesizing Copper Hydroxide Nitrate Nanosheets with High Adsorption Capacity', *Advanced Materials Interfaces*, 3(24), p. 5.
71. Dianningrum, L.W., Choi, H., Kim, Y., Jung, K.D., Susanti, R.F., Kim, J. and Sang, B.I.

(2014) 'Hydrothermal gasification of pure and crude glycerol in supercritical water: A comparative study', *International Journal of Hydrogen Energy*, 39(3), pp. 1262-1273.
72. Dieke, G.H. (1958) 'The molecular spectrum of hydrogen and its isotopes', *Journal of Molecular Spectroscopy*, 2(1-6), pp. 494-517.
73. Dijkmans, T., Pyl, S.P., Reyniers, M.F., Abhari, R., Van Geem, K.M. and Marin, G.B. (2013) 'Production of bio-ethene and propene: Alternatives for bulk chemicals and polymers', *Green Chemistry*, 15(11), pp. 3064-3076.
74. Ding, Z. and Chen, G. (2011) 'Analysis and algorithms for the computation of the excited states of helium', *Journal of Computational and Applied Mathematics*, 235(8), pp. 2041-2062.
75. Do, P.T., Chiappero, M., Lobban, L.L. and Resasco, D.E. (2009) 'Catalytic deoxygenation of methyl-octanoate and methyl-stearate on Pt/Al2O3', *Catalysis Letters*, 130(1-2), pp. 9-18.
76. Drozdowski, B. and Zajac, M. (1977) 'Effect of concentration of some nickel catalyst poisons in oils on the course of hydrogenation', *Journal of the American Oil Chemists' Society*, 54(12), pp. 595-599.
77. Du, C.M., Yan, J.H. and Cheron, B. (2007) 'Decomposition of toluene in a gliding arc discharge plasma reactor', *Plasma Sources Science and Technology*, 16(4), pp. 791-797.
78. Dundich, V.O., Khromova, S.A., Ermakov, D.Y., Lebedev, M.Y., Novopashina, V.M., Sister, V.G., Yakimchuk, A.I. and Yakovlev, V.A. (2010) 'Nickel catalysts for the hydrodeoxygenation of biodiesel', *Kinetics and Catalysis*, 51(5), pp. 704-709.
79. Eide, I. and Neverdal, G. (2014) 'Fingerprinting Bio-Oils from Lignocellulose and Comparison with Fossil Fuels', *Energy & Fuels*, 28(4), pp. 2617-2623.
80. Eliasson, B. and Kogelschatz, U. (1991) 'Modeling and Applications of Silent Discharge Plasmas', *Institute of Electrical and Electronics Engineers Transactions on Plasma Science*, 19(2), pp. 309-323.
81. Eterigho, E.J. (2012) *Development and application of heterogeneous catalysts for direct cracking of triglycerides for biodiesel production*. Newcastle University.
82. Eze, V.C., Harvey, A.P. and Phan, A.N. (2015) 'Determination of the kinetics of biodiesel saponification in alcoholic hydroxide solutions', *Fuel*, 140, pp. 724-730.
83. Fan, Y., Cai, Y., Li, X., Yin, H., Chen, L. and Liu, S. (2015) 'Regeneration of the HZSM-5 zeolite deactivated in the upgrading of bio-oil via non-thermal plasma injection (NTPI) technology', *Journal of Analytical and Applied Pyrolysis*, 111, pp. 209-215.
84. Feng, J., Sun, Y., Zhao, D., Zheng, Z., Xu, Y., Yang, H., Zhu, H. and Zhou, X. (2009) 'Modeling of carbon monoxide removal by corona plasma', *Plasma Science and Technology*, 11(5), pp. 598-603.
85. Fernández, Y., Arenillas, A., Díez, M.A., Pis, J.J. and Menéndez, J.A. (2009) 'Pyrolysis of glycerol over activated carbons for syngas production', *Journal of Analytical and Applied Pyrolysis*, 84(2), pp. 145-150.
86. Festel, G., Würmseher, M., Rammer, C., Boles, E. and Bellof, M. (2014) 'Modelling production cost scenarios for biofuels and fossil fuels in Europe', *Journal of Cleaner Production*, 66, pp. 242-253.
87. Floyd, T.L., Weeks, D.A. and Ullrich, R. (2007) *A and WM, Annual International Conference on Incineration and Thermal Treatment Technologies, IT3*. Available at: https://www.scopus.com/inward/record.uri?eid=2-s2.0-77956797654&partnerID=40&md5=d3b4d8381c03d5c6b73b19d18b24f8d1.
88. Flynn, C.N., Byrne, C.P. and Meenan, B.J. (2013) 'Surface modification of cellulose via atmospheric pressure plasma processing in air and ammonia-nitrogen gas', *Surface and Coatings Technology*, 233, pp. 108-118.
89. Foraita, S., Fulton, J.L., Chase, Z.A., Vjunov, A., Xu, P., Baráth, E., Camaioni, D.M., Zhao, C. and Lercher, J.A. (2015) 'Impact of the oxygen defects and the hydrogen

concentration on the surface of tetragonal and monoclinic ZrO2 on the reduction rates of stearic acid on Ni/ZrO2', *Chemistry - A European Journal*, 21(6), pp. 2423-2434.
90. Fortes, I.C.P. and Baugh, P.J. (1999) 'Study of analytical on-line pyrolysis of oils from Macauba fruit (Acrocomia sclerocarpa M) via GC/MS', *Journal of the Brazilian Chemical Society*, 10, pp. 469-477.
91. French, R. and Czernik, S. (2010) 'Catalytic pyrolysis of biomass for biofuels production', *Fuel Processing Technology*, 91(1), pp. 25-32.
92. Fridman, A. (2008) *Plasma chemistry*.
93. Gangwar, R.K., Levasseur, O., Naudé, N., Gherardi, N., Massines, F., Margot, J. and Stafford, L. (2015) 'Determination of the electron temperature in plane-to-plane He dielectric barrier discharges at atmospheric pressure', *Plasma Sources Science and Technology*, 25(1).
94. Garcia, L., French, R., Czernik, S. and Chornet, E. (2000) 'Catalytic steam reforming of bio-oils for the production of hydrogen: effects of catalyst composition', *Applied Catalysis a-General*, 201(2), pp. 225-239.
95. Ge, W.J., Duan, X.F., Li, Y.P. and Wang, B.W. (2015) 'Plasma-Catalyst Synergy During Methanol Steam Reforming in Dielectric Barrier Discharge Micro-plasma Reactors for Hydrogen Production', *Plasma Chemistry and Plasma Processing*, 35(1), pp. 187-199.
96. Go, A.W., Sutanto, S., Ong, L.K., Tran-Nguyen, P.L., Ismadji, S. and Ju, Y.H. (2016) 'Developments in in-situ (trans) esterification for biodiesel production: A critical review', *Renewable and Sustainable Energy Reviews*, 60, pp. 284-305.
97. Goldstein, J.I., Newbury, D.E., Michael, J.R., Ritchie, N.W.M., Scott, J.H.J. and Joy, D.C. (2017) *Scanning electron microscopy and x-ray microanalysis*.
98. Gomes, J.F.P., Puna, J.F.B., Gonçalves, L.M. and Bordado, J.C.M. (2011) 'Study on the use of MgAl hydrotalcites as solid heterogeneous catalysts for biodiesel production', *Energy*, 36(12), pp. 6770-6778.
99. Gorin, E. and Taylor, H.S. (1934) 'The Photo-decomposition of Formic Acid Vapor', *Journal of the American Chemical Society*, 56(10), pp. 2042-2047.
100. Greenhalf, C.E., Nowakowski, D.J., Harms, A.B., Titiloye, J.O. and Bridgwater, A.V. (2012) 'Sequential pyrolysis of willow SRC at low and high heating rates - Implications for selective pyrolysis', *Fuel*, 93, pp. 692-702.
101. Gutierrez, A., Kaila, R.K., Honkela, M.L., Slioor, R. and Krause, A.O.I. (2009) 'Hydrodeoxygenation of guaiacol on noble metal catalysts', *Catalysis Today*, 147(3-4), pp. 239-246.
102. Haas, M.J., Scott, K.M., Marmer, W.N. and Foglia, T.A. (2004) 'In situ Alkaline Transesterification: An Effective Method for the Production of Fatty Acid Esters from Vegetable Oils', *JAOCS, Journal of the American Oil Chemists' Society*, 81(1), pp. 83-89.
103. Hanif, M.A., Nisar, S. and Rashid, U. (2017) 'Supported solid and heteropoly acid catalysts for production of biodiesel', *Catalysis Reviews - Science and Engineering*, 59(2), pp. 165-188.
104. Harling, A.M., Whitehead, J.C. and Zhang, K. (2005) 'NOx formation in the plasma treatment of halomethanes', *Journal of Physical Chemistry A*, 109(49), pp. 11255-11260.
105. Harrington, K.J. and D'Arcy-Evans, C. (1985) 'Transesterification in Situ of Sunflower Seed Oil', *Industrial and Engineering Chemistry Product Research and Development*, 24(2), pp. 314-318.
106. Harris, J., Phan, A.N. and Zhang, K. (2018) 'Cold plasma catalysis as a novel approach for valorisation of untreated waste glycerol', *Green Chemistry*, 20(11), pp. 2578-2587.
107. Hartmann, W., Hammer, T., Kishimoto, T., Römheld, M. and Safitri, A. (2007) *Digest of Technical Papers-IEEE International Pulsed Power Conference*. Available at:

https://www.scopus.com/inward/record.uri?eid=2-s2.0-45149119489&doi=10.1109%2fPPC.2005.300427&partnerID=40&md5=443a96170ca300404709ea423b004be5.
108. Haruyama, T., Namise, T., Shimoshimizu, N., Uemura, S., Takatsuji, Y., Hino, M., Yamasaki, R., Kamachi, T. and Kohno, M. (2016) 'Non-catalyzed one-step synthesis of ammonia from atmospheric air and water', *Green Chemistry*, 18(16), pp. 4536-4541.
109. Hemings, E.B., Cavallotti, C., Cuoci, A., Faravelli, T. and Ranzi, E. (2012) 'A detailed kinetic study of pyrolysis and oxidation of glycerol (propane-1,2,3-triol)', *Combustion Science and Technology*, 184(7-8), pp. 1164-1178.
110. Henrique, M.A., Flauzino Neto, W.P., Silvério, H.A., Martins, D.F., Gurgel, L.V.A., Barud, H.D.S., Morais, L.C.D. and Pasquini, D. (2015) 'Kinetic study of the thermal decomposition of cellulose nanocrystals with different polymorphs, cellulose I and II, extracted from different sources and using different types of acids', *Industrial Crops and Products*, 76, pp. 128-140.
111. Hlina, M., Hrabovsky, M., Kavka, T. and Konrad, M. (2014) 'Production of high quality syngas from argon/water plasma gasification of biomass and waste', *Waste Management*, 34(1), pp. 63-66.
112. Hoang, T., Zhu, X., Mallinson, R. and Lobban, L. (2008) *Conference Proceedings - 2009 AIChE Spring National Meeting and 5th Global Congress on Process Safety*. Available at: https://www.scopus.com/inward/record.uri?eid=2-s2.0-78049283429&partnerID=40&md5=ef7df703ca91c32f428f5d3eb6b5afac.
113. Holgate, H.R., Meyer, J.C. and Tester, J.W. (1995) 'Glucose hydrolysis and oxidation in supercritical water', *AIChE Journal*, 41(3), pp. 637-648.
114. Hoydonckx, H.E., De Vos, D.E., Chavan, S.A. and Jacobs, P.A. (2004) 'Esterification and transesterification of renewable chemicals', *Topics in Catalysis*, 27(1-4), pp. 83-96.
115. Hsiao, M.C., Merritt, B.T., Penetrante, B.M., Vogtlin, G.E. and Wallman, P.H. (1995) 'Plasma-assisted decomposition of methanol and trichloroethylene in atmospheric pressure air streams by electrical discharge processing', *Journal of Applied Physics*, 78(5), pp. 3451-3456.
116. Hu, B., Lu, Q., Jiang, X., Dong, X., Cui, M., Dong, C. and Yang, Y. (2018) 'Pyrolysis mechanism of glucose and mannose: The formation of 5-hydroxymethyl furfural and furfural', *Journal of Energy Chemistry*, 27(2), pp. 486-501.
117. Hu, S., Luo, X., Wan, C. and Li, Y. (2012) 'Characterization of crude glycerol from biodiesel plants', *Journal of Agricultural and Food Chemistry*, 60(23), pp. 5915-5921.
118. Hu, X., Nicholas, J., Zhang, J.J., Linjewile, T.M., Filippis, P. and Agarwal, P.K. (2002) 'The destruction of N2O in a pulsed corona discharge reactor', *Fuel*, 81(10), pp. 1259-1268.
119. Huber, G.W., Iborra, S. and Corma, A. (2006) 'Synthesis of transportation fuels from biomass: Chemistry, catalysts, and engineering', *Chemical Reviews*, 106(9), pp. 4044-4098.
120. Immer, J.G., Kelly, M.J. and Lamb, H.H. (2010) 'Catalytic reaction pathways in liquid-phase deoxygenation of C18 free fatty acids', *Applied Catalysis A: General*, 375(1), pp. 134-139.
121. Imran, A., Bramer, E.A., Seshan, K. and Brem, G. (2014) 'High quality bio-oil from catalytic flash pyrolysis of lignocellulosic biomass over alumina-supported sodium carbonate', *Fuel Processing Technology*, 127, pp. 72-79.
122. Ing, W.C., Sheng, C.Y. and Bozzelli, J.W. (2003) 'Development of a detailed high-pressure reaction model for methane/methanol mixtures under pyrolytic and oxidative conditions and comparison with experimental data', *Fuel Processing Technology*, 83(1-3 SPEC.), pp. 111-145.
123. Isoardi, L., Bufferand, H., Chiavassa, G., Ciraolo, G., Schwander, F., Serre, E., Viazzo,

S., Fedorczak, N., Ghendrih, P., Gunn, J., Sarazin, Y. and Tamain, P. (2011) '2D modelling of electron and ion temperature in the plasma edge and SOL', *Journal of Nuclear Materials*, 415(1, Supplement), pp. S574-S578.
124. Iwasa, N., Mayanagi, T., Masuda, S. and Takezawa, N. (2000) 'Steam reforming of methanol over Pd-Zn catalysts', *Reaction Kinetics and Catalysis Letters*, 69(2), pp. 355-360.
125. Jain, S., Sharma, M.P. and Rajvanshi, S. (2011) 'Acid base catalyzed transesterification kinetics of waste cooking oil', *Fuel Processing Technology*, 92(1), pp. 32-38.
126. Janampelli, S. and Darbha, S. (2018) 'Selective and reusable Pt-WOx/Al2O3 catalyst for deoxygenation of fatty acids and their esters to diesel-range hydrocarbons', *Catalysis Today*, 309, pp. 219-226.
127. Jeczmionek, L. and Porzycka-Semczuk, K. (2014a) 'Hydrodeoxygenation, decarboxylation and decarbonylation reactions while co-processing vegetable oils over a NiMo hydrotreatment catalyst. Part I: Thermal effects - Theoretical considerations', *Fuel*, 131, pp. 1-5.
128. Jeczmionek, L. and Porzycka-Semczuk, K. (2014b) 'Hydrodeoxygenation, decarboxylation and decarbonylation reactions while co-processing vegetable oils over NiMo hydrotreatment catalyst. Part II: Thermal effects - Experimental results', *Fuel*, 128, pp. 296-301.
129. Jérôme, F., Chatel, G. and De Oliveira Vigier, K. (2016) 'Depolymerization of cellulose to processable glucans by non-thermal technologies', *Green Chemistry*, 18(14), pp. 3903-3913.
130. Jia, L.Y., Farouha, A., Pinard, L., Hedan, S., Comparot, J.D., Dufour, A., Ben Tayeb, K., Vezin, H. and Batiot-Dupeyrat, C. (2017) 'New routes for complete regeneration of coked zeolite', *Applied Catalysis B: Environmental*, 219, pp. 82-91.
131. Jiang, Y., Li, D., Li, Y., Gao, J., Zhou, L. and He, Y. (2013) 'In situ self-catalyzed reactive extraction of germinated oilseed with short-chained dialkyl carbonates for biodiesel production', *Bioresource Technology*, 150, pp. 50-54.
132. Joshi, N. and Lawal, A. (2012) 'Hydrodeoxygenation of pyrolysis oil in a microreactor', *Chemical Engineering Science*, 74, pp. 1-8.
133. Joshi, S., Gogate, P.R., Moreira, P.F., Jr. and Giudici, R. (2017) 'Intensification of biodiesel production from soybean oil and waste cooking oil in the presence of heterogeneous catalyst using high speed homogenizer', *Ultrasonics Sonochemistry*, 39, pp. 645-653.
134. Karuppiah, J., Linga Reddy, E., Manoj Kumar Reddy, P., Ramaraju, B., Karvembu, R. and Subrahmanyam, C. (2012) 'Abatement of mixture of volatile organic compounds (VOCs) in a catalytic non-thermal plasma reactor', *Journal of Hazardous Materials*, 237-238, pp. 283-289.
135. Kasim, F.H., Harvey, A.P. and Zakaria, R. (2010) 'Biodiesel production by in situ transesterification', *Biofuels*, 1(2), pp. 355-365.
136. Khani, M.R., Dejban Guy, E., Gharibi, M., Shahabi, S.S., Khosravi, A., Norouzi, A.A. and Shokri, B. (2014) 'The effects of microwave plasma torch on the cracking of Pyrolysis Fuel Oil feedstock', *Chemical Engineering Journal*, 237, pp. 169-175.
137. Khani, M.R., Khosravi, A., Gharibi, M., Shahabi, S.S., Guy, E.D. and Shokri, B. (2015) 'Conversion of Pyrolysis Fuel Oils by a Dielectric Barrier Discharge Reactor in the Presence of Methane and Ethane', *Chemical Engineering and Technology*, 38(8), pp. 1452-1459.
138. Kikhtyanin, O., Kelbichová, V., Vitvarová, D., Kubů, M. and Kubička, D. (2014) 'Aldol condensation of furfural and acetone on zeolites', *Catalysis Today*, 227, pp. 154-162.

139. Kildiran, G., Yücel, S.Ö. and Türkay, S. (1996) 'In-situ alcoholysis of soybean oil', *Journal of the American Oil Chemists' Society*, 73(2), pp. 225-228.
140. Klemm, D., Heublein, B., Fink, H.P. and Bohn, A. (2005) 'Cellulose: Fascinating biopolymer and sustainable raw material', *Angewandte Chemie-International Edition*, 44(22), pp. 3358-3393.
141. Klimmek, H. (1984) 'Influence of various catalyst poisons and other impurities on fatty acid hydrogenation', *Journal of the American Oil Chemists' Society*, 61(2), pp. 200-204.
142. Koeta, O., Blin-Simiand, N., Faider, W., Pasquiers, S., Bary, A. and Jorand, F. (2012) 'Decomposition of acetaldehyde in atmospheric pressure filamentary nitrogen plasma', *Plasma Chemistry and Plasma Processing*, 32(5), pp. 991-1023.
143. Kogelschatz, U., Eliasson, B. and Egli, W. (1997) 'Dielectric-barrier discharges. Principle and applications', *Journal De Physique. IV : JP*, 7(4), pp. 47-66.
144. Kongpatpanich, K., Nanok, T., Boekfa, B., Probst, M. and Limtrakul, J. (2011) 'Structures and reaction mechanisms of glycerol dehydration over H-ZSM-5 zeolite: A density functional theory study', *Physical Chemistry Chemical Physics*, 13(14), pp. 6462-6470.
145. Kouzu, M., Yamanaka, S., Kasuno, T., Tajika, M., Aihara, Y., Sugimoto, Y. and Hidaka, J. (2007) 'Development of biodiesel production technology from waste cooking oil with calcium oxide as solid base catalyst', *Journal of the Japan Petroleum Institute*, 50(2), pp. 79-86.
146. Kraus, M., Eliasson, B., Kogelschatz, U. and Wokaun, A. (2001) 'CO2 reforming of methane by the combination of dielectric-barrier discharges and catalysis', *Physical Chemistry Chemical Physics*, 3(3), pp. 294-300.
147. Krutof, A. and Hawboldt, K. (2016) 'Blends of pyrolysis oil, petroleum, and other bio-based fuels: A review', *Renewable and Sustainable Energy Reviews*, 59, pp. 406-419.
148. Krylova, I.V. (2008) 'The formation of alumina surface active in methanol decomposition and exoemission in thermocycling experiments', *Russian Journal of Physical Chemistry A*, 82(11), pp. 1925-1931.
149. Kulkarni, M.G. and Dalai, A.K. (2006) 'Waste cooking oil - An economical source for biodiesel: A review', *Industrial and Engineering Chemistry Research*, 45(9), pp. 2901-2913.
150. Kun-Asa, K., Attanatho, L. and Reubroycharoen, P. 757 KEM (2017) 'Pyrolysis of palm oil in a continuous flow microchannel reactor' *Key Engineering Materials* [Conference Paper]. pp. 166-170. Available at: https://www.scopus.com/inward/record.uri?eid=2-s2.0-85034058953&doi=10.4028%2fwww.scientific.net%2fKEM.757.166&partnerID=40&md5=01b47d6b4d5ddcd9bb2480504502f5e3.
151. Kuznetsova, E.G., Ryzhikova, V.A., Salomatina, L.A. and Sevastianov, V.I. (2016) 'Transdermal drug delivery and methods to enhance it', *Vestnik Transplantologii i Iskusstvennykh Organov*, 18(2), pp. 152-162.
152. Leoneti, A.B., Aragão-Leoneti, V. and de Oliveira, S.V.W.B. (2012) 'Glycerol as a by-product of biodiesel production in Brazil: Alternatives for the use of unrefined glycerol', *Renewable Energy*, 45, pp. 138-145.
153. Li, F., Wang, Y., Wang, D. and Wei, F. (2004) 'Characterization of single-wall carbon nanotubes by N2 adsorption', *Carbon*, 42(12-13), pp. 2375-2383.
154. Li, H., Niu, S. and Lu, C. (2017) 'Thermal Characteristics and Kinetic Calculation of Castor Oil Pyrolysis', *Procedia Engineering*, 205, pp. 3711-3716.
155. Li, J., Zhao, Z., Kazakov, A., Chaos, M., Dryer, F.L. and Scire Jr, J.I. (2007a) 'A comprehensive kinetic mechanism for CO, CH2O, and CH 3OH combustion', *International Journal of Chemical Kinetics*, 39(3), pp. 109-136.

156. Li, J.C., Yu, H., Yang, G.X., Peng, F., Xie, D.L., Wang, H.J. and Yang, J. (2011a) 'Steam Reforming of Oxygenate Fuels for Hydrogen Production: A Thermodynamic Study', *Energy & Fuels*, 25(6), pp. 2643-2650.
157. Li, M.S., Zhao, Z.P. and Wang, M.X. (2015) 'Controllable modification of polymer membranes by LDDLT plasma flow: membrane module scale-up and hydrophilic stability', *Chemical Engineering Science*, 122, pp. 53-63.
158. Li, Q., Wan, L., Zhang, S., Xu, Q. and Yan, Y. (2011b) 'Hydrodeoxygenation of bio-oil under mild conditions', *Shiyou Huagong/Petrochemical Technology*, 40(9), pp. 954-958.
159. Li, X., Zhou, Z., Xie, D. and Chen, G. (2009) 'Preparation of acetol from crude glycerol of biomass-based via catalytic reactive distillation', *Taiyangneng Xuebao/Acta Energiae Solaris Sinica*, 30(9), pp. 1159-1162.
160. Li, Y., Lian, S., Tong, D., Song, R., Yang, W., Fan, Y., Qing, R. and Hu, C. (2011c) 'One-step production of biodiesel from Nannochloropsis sp. on solid base Mg–Zr catalyst', *Applied Energy*, 88(10), pp. 3313-3317.
161. Li, Z., Teng, H. and Xiu, Z. (2011d) 'Extraction of 1,3-propanediol from glycerol-based fermentation broths with methanol/phosphate aqueous two-phase system', *Process Biochemistry*, 46(2), pp. 586-591.
162. Li, Z.Q., Lu, C.J., Xia, Z.P., Zhou, Y. and Luo, Z. (2007b) 'X-ray diffraction patterns of graphite and turbostratic carbon', *Carbon*, 45(8), pp. 1686-1695.
163. Lien, Y.C. and Nawar, W.W. (1973) 'Thermal decomposition of tricaproin', *Journal of the American Oil Chemists' Society*, 50(3), pp. 76-78.
164. Liu, C.-y., Yang, H., Jing, Z.-y., Xi, K.-z. and Qiao, C.-z. (2016) 'Hydrodeoxygenation of fatty acid methyl esters and isomerization of products over NiP/SAPO-11 catalysts', *Journal of Fuel Chemistry and Technology*, 44(10), pp. 1211-1216.
165. Liu, R.J., Crozier, P.A., Smith, C.M., Hucul, D.A., Blackson, J. and Salaita, G. (2005) 'Metal sintering mechanisms and regeneration of palladium/alumina hydrogenation catalysts', *Applied Catalysis A: General*, 282(1-2), pp. 111-121.
166. Liu, Y., Pan, Y.X., Kuai, P. and Liu, C.J. (2010) 'Template removal from ZSM-5 zeolite using dielectric-barrier discharge plasma', *Catalysis Letters*, 135(3-4), pp. 241-245.
167. Locke, B.R., Sato, M., Sunka, P., Hoffmann, M.R. and Chang, J.S. (2006) 'Electrohydraulic discharge and nonthermal plasma for water treatment', *Industrial and Engineering Chemistry Research*, 45(3), pp. 882-905.
168. Lupa, C.J., Wylie, S.R., Shaw, A., Al-Shamma'a, A., Sweetman, A.J. and Herbert, B.M.J. (2012) 'Experimental analysis of biomass pyrolysis using microwave-induced plasma', *Fuel Processing Technology*, 97, pp. 79-84.
169. Maher, K.D. and Bressler, D.C. (2007) 'Pyrolysis of triglyceride materials for the production of renewable fuels and chemicals', *Bioresource Technology*, 98(12), pp. 2351-2368.
170. Majewski, A., Morris, D.J., Kendall, K. and Wills, M. (2010) 'A continuous-flow method for the generation of hydrogen from formic acid', *ChemSusChem*, 3(4), pp. 431-434.
171. Mäki-Arvela, P., Kubickova, I., Snåre, M., Eränen, K. and Murzin, D.Y. (2007) 'Catalytic Deoxygenation of Fatty Acids and Their Derivatives', *Energy & Fuels*, 21(1), pp. 30-41.
172. Maleki, H., Kazemeini, M., Larimi, A.S. and Khorasheh, F. (2017) 'Transesterification of canola oil and methanol by lithium impregnated CaO–La2O3 mixed oxide for biodiesel synthesis', *Journal of Industrial and Engineering Chemistry*, 47(Supplement C), pp. 399-404.
173. Malik, M.A. (2010) 'Water Purification by Plasmas: Which Reactors are Most Energy Efficient?', *Plasma Chemistry and Plasma Processing*, 30(1), pp. 21-31.

174. Manara, P. and Zabaniotou, A. (2016) 'Co-valorization of Crude Glycerol Waste Streams with Conventional and/or Renewable Fuels for Power Generation and Industrial Symbiosis Perspectives', *Waste and Biomass Valorization*, 7(1), pp. 135-150.
175. Mayes, H.B., Nolte, M.W., Beckham, G.T., Shanks, B.H. and Broadbelt, L.J. (2014) 'The alpha-bet(a) of glucose pyrolysis: Computational and experimental investigations of 5-hydroxymethylfurfural and levoglucosan formation reveal implications for cellulose pyrolysis', *ACS Sustainable Chemistry and Engineering*, 2(6), pp. 1461-1473.
176. McDonald, A.M., D.

177. Han,Y. and Kengne, B. (2014) *PYROLYSIS BIO-OIL UPGRADING TO RENEWABLE FUELS*.
178. Mello, V.M., Martins, G.B.C., Montenegro, M.A. and Suarez, P.A.Z. (2015) 'Thermal processing of soybean oil to obtain bio-based polymers and bio-oil', *Industrial Crops and Products*, 66, pp. 255-261.
179. Mendow, G., Veizaga, N.S. and Querini, C.A. (2011) 'Ethyl ester production by homogeneous alkaline transesterification: Influence of the catalyst', *Bioresource Technology*, 102(11), pp. 6385-6391.
180. Menser, J., Daun, K., Dreier, T. and Schulz, C. (2016) *Imaging and Applied Optics 2016*. Heidelberg, 2016/07/25. Optical Society of America. Available at: http://www.osapublishing.org/abstract.cfm?URI=LACSEA-2016-LTh2I.3.
181. Michelmore, A., Steele, D.A., Whittle, J.D., Bradley, J.W. and Short, R.D. (2013) 'Nanoscale deposition of chemically functionalised films via plasma polymerisation', *RSC Advances*, 3(33), pp. 13540-13557.
182. Mikmeková, Š., Matsuda, K., Watanabe, K., Ikeno, S., Müllerová, I. and Frank, L. (2011) 'FIB induced damage examined with the low energy SEM', *Materials Transactions*, 52(3), pp. 292-296.
183. Milina, M., Mitchell, S. and Perez-Ramirez, J. (2014) 'Prospectives for bio-oil upgrading via esterification over zeolite catalysts', *Catalysis Today*, 235, pp. 176-183.
184. Missoum, K., Belgacem, M.N. and Bras, J. (2013) 'Nanofibrillated cellulose surface modification: A review', *Materials*, 6(5), pp. 1745-1766.
185. Mohamad, M.H., Awang, R. and Yunus, W.M.Z.W. (2011) 'A review of acetol: Application and production', *American Journal of Applied Sciences*, 8(11), pp. 1135-1139.
186. Mok, Y.S., Jwa, E. and Hyun, Y.J. (2013) 'Regeneration of C4H10 dry reforming catalyst by nonthermal plasma', *Journal of Energy Chemistry*, 22(3), pp. 394-402.
187. Montejo, M., Navarro, A., Kearley, G.J., Vázquez, J. and López-González, J.J. (2004) 'Intermolecular charge transfer and hydrogen bonding in solid furan', *Journal of the American Chemical Society*, 126(46), pp. 15087-15095.
188. Mortensen, P.M., Grunwaldt, J.D., Jensen, P.A., Knudsen, K.G. and Jensen, A.D. (2011) 'A review of catalytic upgrading of bio-oil to engine fuels', *Applied Catalysis a-General*, 407(1-2), pp. 1-19.
189. Mostaghimi, J. and Boulos, M.I. (2015) 'Thermal Plasma Sources: How Well are They Adopted to Process Needs?', *Plasma Chemistry and Plasma Processing*, 35(3), pp. 421-436.
190. Munshi, M.K., Lomate, S.T., Deshpande, R.M., Rane, V.H. and Kelkar, A.A. (2010) 'Synthesis of acrolein by gas-phase dehydration of glycerol over silica supported Bronsted acidic ionic liquid catalysts', *Journal of Chemical Technology and Biotechnology*, 85(10), pp. 1319-1324.
191. Narayana Rao, D. (1950) 'Dielectric constants of alumina', *Current science*, 19(4), p. 119.
192. Naz, M.Y., Ghaffar, A., Rehman, N.U., Shukrullah, S. and Ali, M.A. (2012) 'Optical characterization of 50Hz atmospheric pressure single dielectric barrier discharge

plasma', *Progress In Electromagnetics Research M*, 24, pp. 193-207.
193. Neretti, G., Taglioli, M., Colonna, G. and Borghi, C.A. (2017) 'Characterization of a dielectric barrier discharge in contact with liquid and producing a plasma activated water', *Plasma Sources Science and Technology*, 26(1).
194. Ngo, T.A., Kim, J. and Kim, S.S. (2014) 'Characteristics of palm bark pyrolysis experiment oriented by central composite rotatable design', *Energy*, 66, pp. 7-12.
195. Norjannah, B., Ong, H.C., Masjuki, H.H., Juan, J.C. and Chong, W.T. (2016) 'Enzymatic transesterification for biodiesel production: a comprehensive review', *RSC Advances*, 6(65), pp. 60034-60055.
196. Oasmaa, A., Kuoppala, E., Gust, S. and Solantausta, Y. (2003) 'Fast pyrolysis of forestry residue. 1. Effect of extractives on phase separation of pyrolysis liquids', *Energy & Fuels*, 17(1), pp. 1-12.
197. Olcese, R.N., Bettahar, M., Petitjean, D., Malaman, B., Giovanella, F. and Dufour, A. (2012) 'Gas-phase hydrodeoxygenation of guaiacol over Fe/SiO 2 catalyst', *Applied Catalysis B: Environmental*, 115-116, pp. 63-73.
198. Olefjord, I. and Nylund, A. (1994) 'Surface analysis of oxidized aluminium. 2. Oxidation of aluminium in dry and humid atmosphere studied by ESCA, SEM, SAM and EDX', *Surface and Interface Analysis*, 21(5), pp. 290-297.
199. Ortega García, F.J. and Mar Juárez, E. (2017) 'Heavy Oil Hydrocracking on a Liquid Catalyst', *Energy and Fuels*, 31(8), pp. 7995-8000.
200. Ouni, F., Khacef, A. and Cormier, J.M. (2009) 'Syngas Production from Propane Using Atmospheric Non-thermal Plasma', *Plasma Chemistry and Plasma Processing*, 29(2), pp. 119-130.
201. Palanisamy, S. and Gevert, B.S. (2016) 'Study of non-catalytic thermal decomposition of triglyceride at hydroprocessing condition', *Applied Thermal Engineering*, 107, pp. 301-310.
202. Pan, Y.X., Han, Y. and Liu, C.J. (2007) 'Pathways for steam reforming of dimethyl ether under cold plasma conditions: A DFT study', *Fuel*, 86(15), pp. 2300-2307.
203. Parapati, D.R., Guda, V.K., Penmetsa, V.K., Steele, P.H. and Tanneru, S.K. (2014) 'Single Stage Hydroprocessing of Pyrolysis Oil in a Continuous Packed-Bed Reactor', *Environmental Progress & Sustainable Energy*, 33(3), pp. 726-731.
204. Park, C., Graber, L. and Pamidi, S. (2017) 'The dielectric properties of gaseous cryogen mixtures of He, H2, Ne, and N2 in a temperature range of 50-80 K at pressures up to 2.0 MPa', *Journal of Applied Physics*, 121(8).
205. Park, Y.M., Chung, S.H., Eom, H.J., Lee, J.S. and Lee, K.Y. (2010) 'Tungsten oxide zirconia as solid superacid catalyst for esterification of waste acid oil (dark oil)', *Bioresource Technology*, 101(17), pp. 6589-6593.
206. Paulmier, T. and Fulcheri, L. (2005) 'Use of non-thermal plasma for hydrocarbon reforming', *Chemical Engineering Journal*, 106(1), pp. 59-71.
207. Paulose, M.M. and Chang, S.S. (1978) 'Chemical reactions involved in the deep-fat frying of foods: VIII. Characterization of nonvolatile decomposition products of triolein', *Journal of the American Oil Chemists' Society*, 55(4), pp. 375-380.
208. Pelissari, P.I.B.G.B., Angélico, R.A., Salvini, V.R., Vivaldini, D.O. and Pandolfelli, V.C. (2017) 'Analysis and modeling of the pore size effect on the thermal conductivity of alumina foams for high temperature applications', *Ceramics International*, 43(16), pp. 13356-13363.
209. Pertile, R.A.N., Andrade, F.K., Alves Jr, C. and Gama, M. (2010) 'Surface modification of bacterial cellulose by nitrogen-containing plasma for improved interaction with cells', *Carbohydrate Polymers*, 82(3), pp. 692-698.
210. Piqueras, C.M., Damiani, D.E. and Bottini, S.B. (2009) 'Effect of phase behavior in the hydrogenation of triglycerides under supercritical and near-critical propane', *The*

Journal of Supercritical Fluids, 50(2), pp. 128-137.
211. Poudel, J., Karki, S., Sanjel, N., Shah, M. and Oh, S.C. (2017) 'Comparison of biodiesel obtained from virgin cooking oil and waste cooking oil using supercritical and catalytic transesterification', *Energies*, 10(4).
212. 'PubChem Compound Database' (2018). June 25, 2018. National Center for Biotechnology Information. Available at: https://pubchem.ncbi.nlm.nih.gov/compound/753.
213. Quispe, C.A.G., Coronado, C.J.R. and Carvalho Jr, J.A. (2013) 'Glycerol: Production, consumption, prices, characterization and new trends in combustion', *Renewable and Sustainable Energy Reviews*, 27, pp. 475-493.
214. Ráhel, J. and Sherman, D.M. (2005) 'The transition from a filamentary dielectric barrier discharge to a diffuse barrier discharge in air at atmospheric pressure', *Journal of Physics D: Applied Physics*, 38(4), pp. 547-554.
215. Raju, B.R., Reddy, E.L., Karuppiah, J., Reddy, P.M.K. and Subrahmanyam, C. (2013) 'Catalytic non-thermal plasma reactor for the decomposition of a mixture of volatile organic compounds', *Journal of Chemical Sciences*, 125(3), pp. 673-678.
216. Rathnasingh, C., Raj, S.M., Jo, J.E. and Park, S. (2009) 'Development and evaluation of efficient recombinant Escherichia coli strains for the production of 3-hydroxypropionic acid from glycerol', *Biotechnology and Bioengineering*, 104(4), pp. 729-739.
217. Rodina, V.O., Ermakov, D.Y., Saraev, A.A., Reshetnikov, S.I. and Yakovlev, V.A. (2017) 'Influence of reaction conditions and kinetic analysis of the selective hydrogenation of oleic acid toward fatty alcohols on Ru-Sn-B/Al2O3 in the flow reactor', *Applied Catalysis B: Environmental*, 209, pp. 611-620.
218. Sadrameli, S.M., Green, A.E.S. and Seames, W. (2009) 'Modeling representations of canola oil catalytic cracking for the production of renewable aromatic hydrocarbons', *Journal of Analytical and Applied Pyrolysis*, 86(1), pp. 1-7.
219. Saka, S. and Kusdiana, D. (2001) 'Biodiesel fuel from rapeseed oil as prepared in supercritical methanol', *Fuel*, 80(2), pp. 225-231.
220. Salam, K.A., Velasquez-Orta, S.B. and Harvey, A.P. (2016) 'A sustainable integrated in situ transesterification of microalgae for biodiesel production and associated co-product-a review', *Renewable and Sustainable Energy Reviews*, 65, pp. 1179-1198.
221. Salciccioli, M. and Vlachos, D.G. (2012) 'Kinetic modeling of pt-catalyzed glycolaldehyde decomposition to syngas', *Journal of Physical Chemistry A*, 116(18), pp. 4621-4628.
222. San Fabián, E. and Pastor-Abia, L. (2007) 'Theoretical investigation of excited states of molecules. An application on the nitrogen molecule', *Theoretical Chemistry Accounts*, 118(3), pp. 637-642.
223. Sang, O.Y. (2003) 'Biofuel Production from Catalytic Cracking of Palm Oil', *Energy Sources*, 25(9), pp. 859-869.
224. Santillan-Jimenez, E. and Crocker, M. (2012) 'Catalytic deoxygenation of fatty acids and their derivatives to hydrocarbon fuels via decarboxylation/decarbonylation', *Journal of Chemical Technology and Biotechnology*, 87(8), pp. 1041-1050.
225. Santillan-Jimenez, E., Morgan, T., Shoup, J., Harman-Ware, A.E. and Crocker, M. (2014) 'Catalytic deoxygenation of triglycerides and fatty acids to hydrocarbons over Ni-Al layered double hydroxide', *Catalysis Today*, 237, pp. 136-144.
226. Sarma, S.J., Brar, S.K., Le Bihan, Y., Buelna, G. and Soccol, C.R. (2013) 'Hydrogen production from meat processing and restaurant waste derived crude glycerol by anaerobic fermentation and utilization of the spent broth', *Journal of Chemical Technology and Biotechnology*, 88(12), pp. 2264-2271.
227. Sato, R., Yasumatsu, D., Kumagai, S., Takeda, K., Hori, M. and Sasaki, M. (2014) 'An

atmospheric pressure inductively coupled microplasma source of vacuum ultraviolet light', *Sensors and Actuators a-Physical*, 215, pp. 144-149.
228. Schwab, A.W., Dykstra, G.J., Selke, E., Sorenson, S.C. and Pryde, E.H. (1988) 'Diesel fuel from thermal decomposition of soybean oil', *Journal of the American Oil Chemists' Society*, 65(11), pp. 1781-1786.
229. Sein, M.M., Bin Nasir, Z., Telgheder, U. and Schmidt, T.C. (2012) 'Studies on a non-thermal pulsed corona plasma between two parallel-plate electrodes in water', *Journal of Physics D: Applied Physics*, 45(22).
230. Seshadri, V. and Westmoreland, P.R. (2012) 'Concerted reactions and mechanism of glucose pyrolysis and implications for cellulose kinetics', *Journal of Physical Chemistry A*, 116(49), pp. 11997-12013.
231. Shafaghat, H., Rezaei, P.S. and Ashri Wan Daud, W.M. (2015) 'Effective parameters on selective catalytic hydrodeoxygenation of phenolic compounds of pyrolysis bio-oil to high-value hydrocarbons', *RSC Advances*, 5(126), pp. 103999-104042.
232. Shin, H.Y., Ryu, J.H., Park, S.Y. and Bae, S.Y. (2012) 'Thermal stability of fatty acids in subcritical water', *Journal of Analytical and Applied Pyrolysis*, 98, pp. 250-253.
233. Shrestha, R.T., R. B.; Subedi, D. P. (2012) 'ESTIMATION OF ELECTRON TEMPERATURE IN ATMOSPHERIC PRESSURE DIELECTRIC BARRIER DISCHARGE USING LINE INTENSITY RATIO METHOD', *KATHMANDU UNIVERSITY JOURNAL OF SCIENCE, ENGINEERING AND TECHNOLOGY*, 8(2), pp. 37-42.
234. Sing, K. (2001) 'The use of nitrogen adsorption for the characterisation of porous materials', *Colloids and Surfaces A: Physicochemical and Engineering Aspects*, 187-188, pp. 3-9.
235. Sobkowicz, M.J., Braun, B. and Dorgan, J.R. (2009) 'Decorating in green: surface esterification of carbon and cellulosic nanoparticles', *Green Chemistry*, 11(5), pp. 680-682.
236. Sowers, A.E. (2012) 'Mechanisms of Electroporation and Electrofusion', in *Guide to Electroporation and Electrofusion*. pp. 119-138.
237. Tamošiūnas, A., Valatkevičius, P., Gimžauskaitė, D., Jeguirim, M., Mėčius, V. and Aikas, M. (2016) 'Energy recovery from waste glycerol by utilizing thermal water vapor plasma', *Environmental Science and Pollution Research*, pp. 1-11.
238. Tan, Z.C., Xu, X.M., Liu, Y.G., Zhang, C.S., Zhai, Y.P., Liu, P., Li, Y. and Zhang, R.Q. (2014) 'Upgrading Bio-Oil Model Compounds Phenol and Furfural with In Situ Generated Hydrogen', *Environmental Progress & Sustainable Energy*, 33(3), pp. 751-755.
239. Tanneru, S.K., Parapati, D.R. and Steele, P.H. (2014) 'Pretreatment of bio-oil followed by upgrading via esterification to boiler fuel', *Energy*, 73, pp. 214-220.
240. Thomas, G.B. and Jen-Shih, C. (1997) 'Chemical Kinetic Modelling of Non-Equilibrium Ar-CO 2 Thermal Plasmas', *Japanese Journal of Applied Physics*, 36(7S), p. 4997.
241. Tian, G., Wang, G., Xu, C.M. and Gao, J.S. (2013) 'Coproduction of Syngas during Regeneration of Coked Catalyst for Upgrading Heavy Petroleum Feeds', *Industrial & Engineering Chemistry Research*, 52(47), pp. 16737-16744.
242. Tian, W., Lietz, A.M. and Kushner, M.J. (2016) 'The consequences of air flow on the distribution of aqueous species during dielectric barrier discharge treatment of thin water layers', *Plasma Sources Science and Technology*, 25(5).
243. Tran, D.-T., Le, B.-H., Lee, D.-J., Chen, C.-L., Wang, H.-Y. and Chang, J.-S. (2013) 'Microalgae harvesting and subsequent biodiesel conversion', *Bioresource Technology*, 140, pp. 179-186.
244. Tran, D.-T., Yeh, K.-L., Chen, C.-L. and Chang, J.-S. (2012) 'Enzymatic transesterification of microalgal oil from Chlorella vulgaris ESP-31 for biodiesel synthesis using immobilized Burkholderia lipase', *Bioresource Technology*, 108, pp. 119-

127.
245. Troe, J. (2007) 'Refined analysis of the thermal dissociation of formaldehyde', *Journal of Physical Chemistry A*, 111(19), pp. 3862-3867.
246. Tsang, W. (1987) 'Chemical Kinetic Data Base for Combustion Chemistry. Part 2. Methanol', *Journal of Physical and Chemical Reference Data*, 16(3), pp. 471-508.
247. Tsang, W. and Hampson, R.F. (1986) 'Chemical Kinetic Data Base for Combustion Chemistry. Part I. Methane and Related Compounds', *Journal of Physical and Chemical Reference Data*, 15(3), pp. 1087-1279.
248. Tudorachi, N. and Mustata, F. (2015) 'Thermal degradation and evolved gas analysis of some vegetable oils using TG/FT-IR/MS technique', *Journal of Thermal Analysis and Calorimetry*, 119(3), pp. 1703-1711.
249. Twaiq, F.A.A., Mohamad, A.R. and Bhatia, S. (2004) 'Performance of composite catalysts in palm oil cracking for the production of liquid fuels and chemicals', *Fuel Processing Technology*, 85(11), pp. 1283-1300.
250. U.S-National-Biodiesel-Board (2017) *Biodiesel production*. Available at: (http://biodiesel.org/what-is-biodiesel/biodiesel-basics) (Accessed: 10.5.2017).
251. Uhm, H.S., Kang, J.G., Choi, E.H. and Cho, G.S. (2012) 'Sterilization of medical equipment and contaminated articles by making use of a resistive barrier discharge', *Journal of the Korean Physical Society*, 61(4), pp. 551-556.
252. Utlu, Z. (2007) 'Evaluation of biodiesel fuel obtained from waste cooking oil', *Energy Sources, Part A: Recovery, Utilization and Environmental Effects*, 29(14), pp. 1295-1304.
253. Valliyappan, T., Bakhshi, N.N. and Dalai, A.K. (2008a) 'Pyrolysis of glycerol for the production of hydrogen or syn gas', *Bioresource Technology*, 99(10), pp. 4476-4483.
254. Valliyappan, T., Ferdous, D., Bakhshi, N.N. and Dalai, A.K. (2008b) 'Production of hydrogen and syngas via steam gasification of glycerol in a fixed-bed reactor', *Topics in Catalysis*, 49(1-2), pp. 59-67.
255. Van Bennekom, J.G., Venderbosch, R.H., Assink, D. and Heeres, H.J. (2011) 'Reforming of methanol and glycerol in supercritical water', *Journal of Supercritical Fluids*, 58(1), pp. 99-113.
256. VandeVyver, S., Geboers, J., Jacobs, P.A. and Sels, B.F. (2011) 'Recent Advances in the Catalytic Conversion of Cellulose', *ChemCatChem*, 3(1), pp. 82-94.
257. Vasiliou, A., Nimlos, M.R., Daily, J.W. and Ellison, G.B. (2009) 'Thermal decomposition of furan generates propargyl radicals', *Journal of Physical Chemistry A*, 113(30), pp. 8540-8547.
258. Velasquez-Orta, S.B., Lee, J.G.M. and Harvey, A. (2012) 'Alkaline in situ transesterification of Chlorella vulgaris', *Fuel*, 94, pp. 544-550.
259. Venderbosch, R.H., Ardiyanti, A.R., Wildschut, J., Oasmaa, A. and Heeresb, H.J. (2010) 'Stabilization of biomass-derived pyrolysis oils', *Journal of Chemical Technology and Biotechnology*, 85(5), pp. 674-686.
260. Versteegh, G.J.M., Blokker, P., Wood, G.D., Collinson, M.E., Sinninghe Damsté, J.S. and de Leeuw, J.W. (2004) 'An example of oxidative polymerization of unsaturated fatty acids as a preservation pathway for dinoflagellate organic matter', *Organic Geochemistry*, 35(10), pp. 1129-1139.
261. Vinu, R. and Broadbelt, L.J. (2012) 'A mechanistic model of fast pyrolysis of glucose-based carbohydrates to predict bio-oil composition', *Energy & Environmental Science*, 5(12), pp. 9808-9826.
262. Vlysidis, A., Binns, M., Webb, C. and Theodoropoulos, C. (2011) 'Glycerol utilisation for the production of chemicals: Conversion to succinic acid, a combined experimental and computational study', *Biochemical Engineering Journal*, 58-59(1), pp. 1-11.

263. Wako, F.M., Reshad, A.S. and Goud, V.V. (2017) 'Thermal degradation kinetics study and thermal cracking of waste cooking oil for biofuel production', *Journal of Thermal Analysis and Calorimetry*, pp. 1-9.
264. Wang, C., Jiang, H., Chen, C., Chen, R. and Xing, W. (2015) 'A submerged catalysis/membrane filtration system for hydrogenolysis of glycerol to 1,2-propanediol over Cu–ZnO catalyst', *Journal of Membrane Science*, 489, pp. 135-143.
265. Wang, C., Tian, Z., Wang, L., Xu, R., Liu, Q., Qu, W., Ma, H. and Wang, B. (2012a) 'One-step hydrotreatment of vegetable oil to produce high quality diesel-range alkanes', *ChemSusChem*, 5(10), pp. 1974-1983.
266. Wang, D., Van Gerpen, J. and He, B.B. (2013a) *American Society of Agricultural and Biological Engineers Annual International Meeting 2013, ASABE 2013*. Available at: https://www.scopus.com/inward/record.uri?eid=2-s2.0-84881631828&partnerID=40&md5=d64dc940d284be88484faddfee152567.
267. Wang, L., Zhang, M.M., Zhang, M., Sha, G.Y. and Liang, C.H. (2013b) 'Hydrodeoxygenation of Dibenzofuran over Mesoporous Silica COK-12 Supported Palladium Catalysts', *Energy & Fuels*, 27(4), pp. 2209-2217.
268. Wang, P.S., Tat, M.E. and Van Gerpen, J. (2005) 'The production of fatty acid isopropyl esters and their use as a diesel engine fuel', *JAOCS, Journal of the American Oil Chemists' Society*, 82(11), pp. 845-849.
269. Wang, Q., Cheng, Y. and Jin, Y. (2009) 'Dry reforming of methane in an atmospheric pressure plasma fluidized bed with Ni/γ-Al2O3 catalyst', *Catalysis Today*, 148(3-4), pp. 275-282.
270. Wang, Q., Shi, H., Yan, B., Jin, Y. and Cheng, Y. (2011) 'Steam enhanced carbon dioxide reforming of methane in DBD plasma reactor', *International Journal of Hydrogen Energy*, 36(14), pp. 8301-8306.
271. Wang, S.R., Guo, X.J., Liang, T., Zhou, Y. and Luo, Z.Y. (2012b) 'Mechanism research on cellulose pyrolysis by Py-GC/MS and subsequent density functional theory studies', *Bioresource Technology*, 104, pp. 722-728.
272. 'Waste glycerol gasified to make hydrogen', (2016) *TCE The Chemical Engineer*, 904, p. 20.
273. Weitkamp, J. (2000) 'Zeolites and catalysis', *Solid State Ionics*, 131(1), pp. 175-188.
274. Wiest, O. (1996) 'Density functional theory studies of the methanol radical cation hypersurface', *Journal of Molecular Structure: THEOCHEM*, 368(1-3 SPEC. ISS.), pp. 39-48.
275. Wiggers, V.R., Meier, H.F., Wisniewski Jr, A., Chivanga Barros, A.A. and Wolf Maciel, M.R. (2009) 'Biofuels from continuous fast pyrolysis of soybean oil: A pilot plant study', *Bioresource Technology*, 100(24), pp. 6570-6577.
276. Wiggers, V.R., Zonta, G.R., França, A.P., Scharf, D.R., Simionatto, E.L., Ender, L. and Meier, H.F. (2013) 'Challenges associated with choosing operational conditions for triglyceride thermal cracking aiming to improve biofuel quality', *Fuel*, 107, pp. 601-608.
277. Wildschut, J., Mahfud, F.H., Venderbosch, R.H. and Heeres, H.J. (2009) 'Hydrotreatment of Fast Pyrolysis Oil Using Heterogeneous Noble-Metal Catalysts', *Industrial & Engineering Chemistry Research*, 48(23), pp. 10324-10334.
278. Wolf, R.A., Primm, T., Florio, L. and Sparavigna, A. (2007) *International Nonwovens Technical Conference, INTC 2007: Joint INDA-TAPPI Conference*. Available at: https://www.scopus.com/inward/record.uri?eid=2-s2.0-52649101556&partnerID=40&md5=63078f507fadd713d25e94a738201d5a.
279. Wu, C., Wang, Z., Williams, P.T. and Huang, J. (2013a) 'Renewable hydrogen and carbon nanotubes from biodiesel waste glycerol', *Scientific Reports*, 3.
280. Wu, H., Liu, Y., Zhang, J. and Li, G. (2014) 'In situ reactive extraction of

cottonseeds with methyl acetate for biodiesel production using magnetic solid acid catalysts', *Bioresource Technology*, 174, pp. 182-189.
281. Wu, S., Shen, D., Hu, J., Xiao, R. and Zhang, H. (2013b) 'TG-FTIR and Py-GC-MS analysis of a model compound of cellulose- glyceraldehyde', *Journal of Analytical and Applied Pyrolysis*, 101, pp. 79-85.
282. Wyatt, V.T. and Haas, M.J. (2009) 'Production of fatty acid methyl esters via the in situ transesterification of soybean oil in carbon Dioxide-expanded methanol', *JAOCS, Journal of the American Oil Chemists' Society*, 86(10), pp. 1009-1016.
283. Xi-Ming, Z. and Yi-Kang, P. (2008) 'Using OES to determine electron temperature and density in low-pressure nitrogen and argon plasmas', *Plasma Sources Science and Technology*, 17(2), p. 024002.
284. Xu, J., Jiang, J., Sun, Y. and Chen, J. (2010) 'Production of hydrocarbon fuels from pyrolysis of soybean oils using a basic catalyst', *Bioresource Technology*, 101(24), pp. 9803-9806.
285. Yamaguchi, A., Hiyoshi, N., Sato, O., Rode, C.V. and Shirai, M. (2008) 'Enhancement of glycerol conversion to acetol in high-temperature liquid water by high-pressure carbon dioxide', *Chemistry Letters*, 37(9), pp. 926-927.
286. Yamaguchi, A., Hiyoshi, N., Sato, O. and Shirai, M. (2010) 'Dehydration of Triol Compounds in High-Temperature Liquid Water Under High-Pressure Carbon Dioxide', *Topics in Catalysis*, 53(7), pp. 487-491.
287. Yang, X.-X., Wang, Y.-T., Yang, Y.-T., Feng, E.-Z., Luo, J., Zhang, F., Yang, W.-J. and Bao, G.-R. (2018) 'Catalytic transesterification to biodiesel at room temperature over several solid bases', *Energy Conversion and Management*, 164, pp. 112-121.
288. Yang, Y. (2003) 'Direct Non-oxidative Methane Conversion by Non-thermal Plasma: Modeling Study', *Plasma Chemistry and Plasma Processing*, 23(2), pp. 327-346.
289. Yao, G., Wu, G., Dai, W., Guan, N. and Li, L. (2015) 'Hydrodeoxygenation of lignin-derived phenolic compounds over bi-functional Ru/H-Beta under mild conditions', *Fuel*, 150, pp. 175-183.
290. Ye, L., Zhang, F., Zhang, L. and Qi, F. (2012) 'Theoretical studies on the unimolecular decomposition of propanediols and glycerol', *Journal of Physical Chemistry A*, 116(18), pp. 4457-4465.
291. Yenumala, S.R., Maity, S.K. and Shee, D. (2017) 'Reaction mechanism and kinetic modeling for the hydrodeoxygenation of triglycerides over alumina supported nickel catalyst', *Reaction Kinetics, Mechanisms and Catalysis*, 120(1), pp. 109-128.
292. Yetter, R.A., Rabitz, H., Dryer, F.L., Maki, R.G. and Bruce Klemm, R. (1989) 'Evaluation of the rate constant for the reaction OH+H2CO: Application of modeling and sensitivity analysis techniques for determination of the product branching ratio', *The Journal of Chemical Physics*, 91(7), pp. 4088-4097.
293. Yu-Wu, Q.M., Weiss-Hortala, E. and Barna, R. (2013) 'Hydrothermal conversion of glucose in multiscale batch processes. Analysis of the gas, liquid and solid residues', *The Journal of Supercritical Fluids*, 79, pp. 76-83.
294. Yu, Q., Kong, M., Liu, T., Fei, J. and Zheng, X. (2012) 'Characteristics of the Decomposition of CO2 in a Dielectric Packed-Bed Plasma Reactor', *Plasma Chemistry and Plasma Processing*, 32(1), pp. 153-163.
295. Zaima, K. and Sasaki, K. (2014) 'Responses of OH (X2Π) and OH (A2Σ+) to high-energy electrons of dielectric barrier discharge in plasma-assisted burner flame', *Japanese Journal of Applied Physics*, 53(11).
296. Zarchin, R., Rabaev, M., Vidruk-Nehemya, R., Landau, M.V. and Herskowitz, M. (2015) 'Hydroprocessing of soybean oil on nickel-phosphide supported catalysts', *Fuel*, 139, pp. 684-691.
297. Zeng, J., Wang, X., Zhao, B., Sun, J. and Wang, Y. (2009) 'Rapid In Situ

Transesterification of Sunflower Oil', *Industrial & Engineering Chemistry Research*, 48(2), pp. 850-856.
298. Zhai, X., Zhang, P., Liu, C., Bai, T., Li, W., Dai, L. and Liu, W. (2012) 'Highly luminescent carbon nanodots by microwave-assisted pyrolysis', *Chemical Communications*, 48(64), pp. 7955-7957.
299. Zhang, B., Leng, E., Wang, P., Gong, X., Zhang, J., Zhang, Y. and Xu, M. (2015) 'Effect of reducing ends on the pyrolysis characteristics and product distribution of cellulose', *Journal of Analytical and Applied Pyrolysis*, 114, pp. 119-126.
300. Zhang, H., Zhu, F., Li, X., Cen, K., Du, C. and Tu, X. (2016) 'Enhanced hydrogen production by methanol decomposition using a novel rotating gliding arc discharge plasma', *RSC Advances*, 6(16), pp. 12770-12781.
301. Zhang, K., Zhang, G., Liu, X., Phan, A.N. and Luo, K. (2017) 'A Study on CO2 Decomposition to CO and O2 by the Combination of Catalysis and Dielectric-Barrier Discharges at Low Temperatures and Ambient Pressure', *Industrial and Engineering Chemistry Research*, 56(12), pp. 3204-3216.
302. Zhang, Y., Dubé, M.A., McLean, D.D. and Kates, M. (2003) 'Biodiesel production from waste cooking oil: 1. Process design and technological assessment', *Bioresource Technology*, 89(1), pp. 1-16.
303. Zhang, Y.M., Yao, M.Q., Sun, G.G., Gao, S.Q. and Xu, G.W. (2014) 'Characteristics and Kinetics of Coked Catalyst Regeneration via Steam Gasification in a Micro Fluidized Bed', *Industrial & Engineering Chemistry Research*, 53(15), pp. 6316-6324.
304. Zhao, P., Shen, Y., Ge, S., Chen, Z. and Yoshikawa, K. (2014) 'Clean solid biofuel production from high moisture content waste biomass employing hydrothermal treatment', *Applied Energy*, 131, pp. 345-367.
305. Zhu, X., Hoang, T., Lobban, L.L. and Mallinson, R.G. (2009) 'Plasma reforming of glycerol for synthesis gas production', *Chemical Communications*, (20), pp. 2908-2910.
306. Zhu, X.M. and Pu, Y.K. (2010) 'Optical emission spectroscopy in low-temperature plasmas containing argon and nitrogen: Determination of the electron temperature and density by the line-ratio method', *Journal of Physics D: Applied Physics*, 43(40).
307. Zuhaimi, N.A.S., Indran, V.P., Deraman, M.A., Mudrikah, N.F., Maniam, G.P., Taufiq-Yap, Y.H. and Ab Rahim, M.H. (2015) 'Reusable gypsum based catalyst for synthesis of glycerol carbonate from glycerol and urea', *Applied Catalysis A: General*, 502, pp. 312-319.

Appendices

Appendix A. Model scripts:

A.1: Methanol model

A.1.1: Methanol model main script

```
%{
Model of plasma degradation of methanol
By Jonathan Harris

%%
The Model

The model is a batch process, with the rate constants varying with
temperature. There are no temperature discontinuties, but heat is evolved
so
heat balances are required

This model assumes that the product remains in the vessel until the
simulation ends, this will be changed in later versions.

The reactions:
1:H2                 2H.
2:H. + Methanol      CH3. + H2O
3:H. + Methanol      CH2OH. + H2
4:H. + Methanol      CH3O. + H2
5: Methanol          CH2. + H2O
6: Methanol          CH2OH + H.
7: Methanol          CH3. + OH.
8: Methanol          CH3O. + H.
9: Methanol          CHOH + H2
10:CH3. + Methanol   Methane + CH2OH.
11:CH3. + CH2OH.     Ethanol
12:2CH3.             Ethane
13:CH2. + H2         CH3. + H.
14:Ethane            C2H5. + H.
15: CH3. + C2H5.     Propane
16: Propane          C3H7. + H.
17: CH3. + H.        Methane
18:C3H7. + CH3.      Butane
19: 2C2H5.           Butane
20: Butane           C4H9. + H.
21: C2H5. + C3H7.    Pentane
22: C4H9. + CH3.     Pentane
23: CH3O.            CH2O + H.
24: CH2O             CO + H2
25: CH3O. + H.       CH3. + OH.
26: CH3O. + H.       CH2O + H2
27: CH3O. + H.       CH3OH
28: H. + OH.         H2O
29: CHOH             CH2O
30: C2H5. + H.       Ethane
31: C3H7. + H.       Propane
32: C4H9. + H.       Butane
33: CH3. + H.        Methane
34: H2O              OH.+ H.
```

```
35. CO + OH.          CO2 + H.
36. C2H5. +OH         Ethanol
37. Ch2OH.            Ch3O.


The components
H2
H.
Methanol
Ethanol
H2O
CH3.
CH2..
OH.
CH2OH.
CH3O.
CHOH..
methane
ethane
propane
butane
pentane
C2H5.
C3H7.
C4H9.
%%
Units
Time            minutes
Temperature     degreees K
Heat capacity   Kj/kgK
mass            kg
Volume          dm3
Concentration   moles/dm3
flowrate        dm3/minute
%}
%{
PREPARATION

clear any persistent items from the MatLab workspace
%}

clear variables

% clear MatLab Command Window

clc

% close any open graph windows

delete(findall(0,'Type','figure'))

global NumberReactions;

NumberReactions = 36;
% revert first set to E as 10
global ArrheniusConstants
ArrheniusConstants = zeros(36,2);

ArrheniusConstants(1,1) = 3.64E-8;                % per s
ArrheniusConstants(2,1) = 4.23E-7;
ArrheniusConstants(3,1) = 1.02E-7;
```

```
ArrheniusConstants(4,1) = 3.62E-8;
ArrheniusConstants(5,1) = 3.67E-7;
ArrheniusConstants(6,1) = 3.34E-7;
ArrheniusConstants(7,1) = 2.7E-6;
ArrheniusConstants(8,1) = 1.29E-5;
ArrheniusConstants(9,1) = 2.12E-3;
ArrheniusConstants(10,1) = 4.38E-15;
ArrheniusConstants(11,1) = 3.44E-1;
ArrheniusConstants(12,1) = 9.56E-1;
ArrheniusConstants(13,1) = 1.46E-4;
ArrheniusConstants(14,1) = 1.26E-10;
ArrheniusConstants(15,1) = 8.17E-1;
ArrheniusConstants(16,1) = 1.58E-10;
ArrheniusConstants(17,1) = 8.92E-13;
ArrheniusConstants(18,1) = 3.58E-1;
ArrheniusConstants(19,1) = 1.26E-1;
ArrheniusConstants(20,1) = 1.58E-10;
ArrheniusConstants(21,1) = 1.80E-2;
ArrheniusConstants(22,1) = 1.62E-2;
ArrheniusConstants(23,1) = 1.55E-1;
ArrheniusConstants(24,1) = 1.51E-11;
ArrheniusConstants(25,1) = 6.9E-8;
ArrheniusConstants(26,1) = 3.31E-11;
ArrheniusConstants(27,1) = 4.79E-10;
ArrheniusConstants(28,1) = 1.7E-3;
ArrheniusConstants(29,1) = 0;
ArrheniusConstants(30,1) = 2.72E-10;
ArrheniusConstants(31,1) = 3.05E-11;
ArrheniusConstants(32,1) = 6.6E-11;
ArrheniusConstants(33,1) = 8.92E-13;
ArrheniusConstants(34,1) = 1.51E-9;
ArrheniusConstants(35,1) = 8.14E-1;
ArrheniusConstants(36,1) = 5.56;


ArrheniusConstants(1,2) = 431;                % kJ / kmol
ArrheniusConstants(2,2) = 133;
ArrheniusConstants(3,2) = 29.51;
ArrheniusConstants(4,2) = 3.725;
ArrheniusConstants(5,2) = 1000;
ArrheniusConstants(6,2) = 385;
ArrheniusConstants(7,2) = 378;
ArrheniusConstants(8,2) = 441;
ArrheniusConstants(9,2) = 362;
ArrheniusConstants(10,2) = 30.02;
ArrheniusConstants(11,2) = 39.9;
ArrheniusConstants(12,2) = 1.156;
ArrheniusConstants(13,2) = 3.2;
ArrheniusConstants(14,2) = 0.41;
ArrheniusConstants(15,2) = 0.67;
ArrheniusConstants(16,2) = 408;
ArrheniusConstants(17,2) = 43.48;
ArrheniusConstants(18,2) = 0.81;
ArrheniusConstants(19,2) = 0.8;
ArrheniusConstants(20,2) = 0.8;%*410
ArrheniusConstants(21,2) = 1.34;
ArrheniusConstants(22,2) = 0.48;
ArrheniusConstants(23,2) = 0.87;
ArrheniusConstants(24,2) = 114;
ArrheniusConstants(25,2) = 0;
ArrheniusConstants(26,2) = 0.1;
ArrheniusConstants(27,2) = 0.8;
ArrheniusConstants(28,2) = 1.09;
```

```
ArrheniusConstants(29,2) = 0;
ArrheniusConstants(30,2) = 0.5;
ArrheniusConstants(31,2) = 0.1;
ArrheniusConstants(32,2) = 1;
ArrheniusConstants(33,2) = 1;
ArrheniusConstants(34,2) = 409;
ArrheniusConstants(35,2) = 1.3;
ArrheniusConstants(36,2) = 399;

% now define constants

global Prop
Prop = zeros(11,2);
Prop(1,1) = 5.4E-6;
Prop(2,1) = 3.44E-5;
Prop(3,1) = 5.67E-4;
Prop(4,1) = 7.44E-3;
Prop(5,1) = 9.62E-4;
Prop(6,1) = 1.67E-6;
Prop(7,1) = 1.53E-4;
Prop(8,1) = 2.3E-7;
Prop(9,1) = 2.8E-7;
Prop(10,1) = 1.67E-0;
Prop(11,1) = 5.16E-6;

Prop(1,2) = 0;
Prop(2,2) = -0.612;
Prop(3,2) = -0.681;
Prop(4,2) = -0.612;
Prop(5,2) = -0.781;
Prop(6,2) = -0.681;
Prop(7,2) = -0.06;
Prop(8,2) = 0;
Prop(9,2) = 0;
Prop(10,2) = -0.681;
Prop(11,2) = -0.642;

Prop(1,3) = 119940;
Prop(2,3) = 163881.23;
Prop(3,3) = 9230.93;
Prop(4,3) = 24881.3;
Prop(5,3) = 23298.2;
Prop(6,3) = 18309.3;
Prop(7,3) = 1213.778;
Prop(8,3) = 12137.78;
Prop(9,3) = 0;
Prop(10,3) = 1830.93;
Prop(11,3) = 169882.6;

global R;
R = (8.314);  % KJ/kgK

global NumberComponents
NumberComponents = 22;

% define components
global Component2
Component2(1).name = 'H2';
Component2(1).Mwt = 2;
Component2(1).cp = 14.32;

Component2(2).name = 'H.';
```

```
Component2(2).Mwt = 1;
Component2(2).cp = 14.32;

Component2(3).name = 'Methanol';
Component2(3).Mwt = 32;
Component2(3).cp = 2.51;

Component2(4).name = 'Ethanol';
Component2(4).Mwt = 46;
Component2(4).cp = 2.470;

Component2(5).name = 'H2O';
Component2(5).Mwt = 18;
Component2(5).cp = 4.171;

Component2(6).name = 'CH3.';
Component2(6).Mwt = 15;
Component2(6).cp = 2.22;

Component2(7).name = 'CH2d';
Component2(7).Mwt = 14;
Component2(7).cp = 2.22;

Component2(8).name = 'OH.';
Component2(8).Mwt = 17;
Component2(8).cp = 4.18;

Component2(9).name = 'CH2OH.';
Component2(9).Mwt = 31;
Component2(9).cp = 2.51;

Component2(10).name = 'CH3O.';
Component2(10).Mwt = 31;
Component2(10).cp = 0.6767;

Component2(11).name = 'CHOHd';
Component2(11).Mwt = 30;
Component2(11).cp = 2.545;

Component2(12).name = 'Methane';
Component2(12).Mwt = 16;
Component2(12).cp = 2.22;

Component2(13).name = 'Ethane';
Component2(13).Mwt = 30;
Component2(13).cp = 1.75;

Component2(14).name = 'Propane';
Component2(14).Mwt = 44;
Component2(14).cp = 1.67;

Component2(15).name = 'Butane';
Component2(15).Mwt = 58;
Component2(15).cp = 1.67;

Component2(16).name = 'Pentane';
Component2(16).Mwt = 72;
Component2(16).cp = 1.67;

Component2(17).name = 'C2H5.';
```

```
Component2(17).Mwt = 29;
Component2(17).cp = 1.75;

Component2(18).name = 'C3H7.';
Component2(18).Mwt = 43;
Component2(18).cp = 1.67;

Component2(19).name = 'C4H9.';
Component2(19).Mwt = 57;
Component2(19).cp = 1.67;

Component2(20).name = 'CH2O';
Component2(20).Mwt = 30;
Component2(20).cp = 0.6767;

Component2(21).name = 'CO.';
Component2(21).Mwt = 28;
Component2(21).cp = 1.67;

Component2(22).name = 'CO2';
Component2(22).Mwt = 44;
Component2(22).cp = 0.871;

global DeltaHRxn;
DeltaHRxn = zeros(22,1);% kJ/kmol energy from reaction

global ReactorDimensions
ReactorDimensions(1) =0.1;    % wall thickness (cm)
ReactorDimensions(2) =1.2;    % Inner radius (cm)
ReactorDimensions(3) =10;    % Length (cm)


%{
SPECIFY Operating Conditions

determine initial charge in moles
%}

global ReactorCharge
ReactorCharge = [0.000001,     ...     kg H2
                 0.000001,    ...            H.
                 0.79,      ...           Methanol
                 0.000001,      ...            Ethanol
                 0.000001,      ...            water
                 0.000001,0.000001,0.000001,0.000001,...
                 0.000001,0.000001,0.000001,0.000001,...
                 0.000001,0.000001,0.000001,0.000001,...
                 0.000001,0.000001,0.000001,0.000001,0.000001];
% Determine initial volume
global ComponentVolume
global InitialVolume
ComponentVolume = zeros(22,1);

for i=1:22
    ComponentVolume(i) =ReactorCharge(i)/1;
end

InitialVolume = sum(ComponentVolume);

global HeatingRate
```

```
HeatingRate = 0;      %Kelvin/sec

global InitialTemperature
InitialTemperature = 300;    %K

global Power
Power = 60; %W

%%                          INITIALISE SIMULATION

%{
_____________________________________________________________________________

SET Time Interval

Set the simulation time interval (times are in SECONDS)
In this case, the simulation will run for 15 seconds

ispan includes the times from TemperatureProfile and MolarAdditionProfile

%}

EndTime = 15;          % seconds

ispan = [ 0 EndTime ];

ispan = sort (ispan);

ispan = unique (ispan);


%{

INITIALISE the Dependent Variables

In this example, the dependent variables in the differential equations are
    the reagents and products in kmol
    the reaction volume im m3
    the reaction temperature in K

InitialReactionVolume and InitialReactorTemperature are added to the vector
of initial values of dependent variables y0 passed to the integrator.

%}

y0 = [ReactorCharge InitialTemperature];

options = odeset ( 'NonNegative', 1:length(y0) );
%%

%{

SET Integrator Options

% The MatLab function length counts the elements in the vector y0

%}
```

```
%%                                  SIMULATION LOOP

%{
_____________________________________________________________________________

RUN THE SIMULATION
%}

for j = 2:length(ispan)

    [tSection, ySection] = ode15s(@NTPdecompmethanolratesv0, ...
                                  [ispan(j-1) ispan(j)], ...
                                  y0, ...
                                  options);

    nt = length(tSection);

    if j == 2
        t = tSection;
        y = ySection;
    else
        t = [t; tSection(2:nt)];
        y = [y; ySection(2:nt,:)];
    end

    y0 = ySection(nt,:);

end




%%                                  SHOW RESULTS


%_____________________________________________________________________________
%PLOT THE RESULTS

%Plot the reactor composition profile



figure ('name', 'Reactor composition');

grid off

plot (t, y(:,1:NumberComponents-1))

title ( 'Reactor composition')

ylabel ('Moles')
xlabel ('time  (seconds)')

legend (Component2(1:NumberComponents-1).name)

%{
```

```
Plot the temperature profile

%}

figure ('name', 'Reaction temperature');

plot (t, y(:,NumberComponents+1))            % plots columns 7 in matrix y

title ( 'Reactor temperature')

ylabel ('Temperature (K)')
xlabel ('time  (seconds)')




%Plot the reactor composition profile

figure ('name', 'Reactor Output');

grid off

plot (t, Product(3:5,:))

title ( 'Reactor Output')

ylabel ('Moles')
xlabel ('time  (seconds)')

legend (Component(3:NumberComponents-1).name)
```

A.1.2: Rate constant calculation script

```
%{
 This code was produced by Jonathan Harris as part of a PhD modelling
project at newcastle university in the year 2016. Use of this code for
other purposes is not permitted without permission of the author.

% working version
RateConstants.m

Produced to generate K values from Temperature or plasma power
The function RateConstants is called by the function Rates.

%}

function[k] = NTPdecompmethanolreactionv0(Temperature)
%{

This function calculates reaction rate constants for all reactions.

The gas constant R and the Arrhenius constants are global variables.

Temperature is an input parameter because some models will require rate
constants to be calculated at different Temperatures.
```

```
                    k = A exp ( - E / RT)

Calculation of K from power uses three constants of proportionality, from
literature. full equation:

k = Prop1 * Te^ Prop2 *e^(-Prop3/Te)

This is used for reactions where electrons participate, which are
reactions:
1, 5-9,14,16,20,24,33

INPUT

Temperature     reaction Temperature in Kelvin

OUTPUT

k               a vector of rate constants

GLOBAL

ArrheniusConstants      array of Arrhenius constants
                 ArrheniusConstants(ReactionNumber, 1) is FREQUENCY FACTOR
                 ArrheniusConstants(ReactionNumber, 2) is ACTIVATION ENERGY

R               gas constant

This MatLab function uses the global variables R and ArrheniusConstants.
The variables must be declared in this function to make them available.
Global variables which are not declared within this function cannot be used
inside this function.
%}

global R;
global ArrheniusConstants
global Power
global Prop

Te = Power * 421.71;
if Te == 0;
    Prop(:,:)= 0;
    Te = 1;
end
%{
The Prop values are set outside this function, are constants for plasma
decomposition

Calculate k values now, but set as a zeros matrix first
%}
% replace Temperature with Temperature
k(1:36)= 0;

k(1) = (ArrheniusConstants(1,1)* exp (- ArrheniusConstants(1,2) /(R *
Temperature))) ...
    +Prop(1,1) * Te^ Prop(1,2)*1000 *2.718^(-Prop(1,3)/Te);
k(2) = ArrheniusConstants(2,1)* exp (- ArrheniusConstants(2,2) /(R *
Temperature));
k(3) = ArrheniusConstants(3,1)* exp (- ArrheniusConstants(3,2) /(R *
Temperature));
```

```
k(4) = ArrheniusConstants(4,1)* exp (- ArrheniusConstants(4,2) /(R *
Temperature));
k(5) = (ArrheniusConstants(5,1)* exp (- ArrheniusConstants(5,2) /(R *
Temperature)))...
    +Prop(2,1) * Te^ Prop(2,2)*1000 *2.718^(-Prop(2,3)/Te);
k(6) = (ArrheniusConstants(6,1)* exp (- ArrheniusConstants(6,2) /(R *
Temperature)))...
    +Prop(3,1) * Te^ Prop(3,2)*1000 *2.718^(-Prop(3,3)/Te);
k(7) = (ArrheniusConstants(7,1)* exp (- ArrheniusConstants(7,2) /(R *
Temperature)))...
    +Prop(4,1) * Te^ Prop(4,2)*1000 *2.718^(-Prop(4,3)/Te);
k(8) = (ArrheniusConstants(8,1)* exp (- ArrheniusConstants(8,2) /(R *
Temperature)))...
    +Prop(5,1) * Te^ Prop(5,2)*1000 *2.718^(-Prop(5,3)/Te);
k(9) = (ArrheniusConstants(9,1)* exp (- ArrheniusConstants(9,2) /(R *
Temperature)))...
    +Prop(6,1) * Te^ Prop(6,2)*1000 *2.718^(-Prop(6,3)/Te);
k(10) = ArrheniusConstants(10,1)* exp (- ArrheniusConstants(10,2) /(R *
Temperature));
k(11) = ArrheniusConstants(11,1)* exp (- ArrheniusConstants(11,2) /(R *
Temperature));
k(12) = ArrheniusConstants(12,1)* exp (- ArrheniusConstants(12,2) /(R *
Temperature));
k(13) = ArrheniusConstants(13,1)* exp (- ArrheniusConstants(13,2) /(R *
Temperature));
k(14) = (ArrheniusConstants(14,1)* exp (- ArrheniusConstants(14,2) /(R *
Temperature)))...
    +Prop(7,1) * Te^ Prop(7,2)*1000 *2.718^(-Prop(7,3)/Te);
k(15) = ArrheniusConstants(15,1)* exp (- ArrheniusConstants(15,2) /(R *
Temperature));
k(16) = (ArrheniusConstants(16,1)* exp (- ArrheniusConstants(16,2) /(R *
Temperature)))...
    +Prop(8,1) * Te^ Prop(8,2)*1000 *2.718^(-Prop(8,3)/Te);
k(17) = ArrheniusConstants(17,1)* exp (- ArrheniusConstants(17,2) /(R *
Temperature));
k(18) = ArrheniusConstants(18,1)* exp (- ArrheniusConstants(18,2) /(R *
Temperature));
k(19) = ArrheniusConstants(19,1)* exp (- ArrheniusConstants(19,2) /(R *
Temperature));
k(20) = (ArrheniusConstants(20,1)* exp (- ArrheniusConstants(20,2) /(R *
Temperature)))...
    +Prop(9,1) * Te^ Prop(9,2)*1000 *2.718^(-Prop(9,3)/Te);
k(21) = ArrheniusConstants(21,1)* exp (- ArrheniusConstants(21,2) /(R *
Temperature));
k(22) = ArrheniusConstants(22,1)* exp (- ArrheniusConstants(22,2) /(R *
Temperature));
k(23) = ArrheniusConstants(23,1)* exp (- ArrheniusConstants(23,2) /(R *
Temperature));
k(24) = (ArrheniusConstants(24,1)* exp (- ArrheniusConstants(24,2) /(R *
Temperature)))...
    +Prop(10,1) * Te^ Prop(10,2)*1000 *2.718^(-Prop(10,3)/Te);
k(25) = ArrheniusConstants(25,1)* exp (- ArrheniusConstants(25,2) /(R *
Temperature));
k(26) = ArrheniusConstants(26,1)* exp (- ArrheniusConstants(26,2) /(R *
Temperature));
k(27) = ArrheniusConstants(27,1)* exp (- ArrheniusConstants(27,2) /(R *
Temperature));
k(28) = ArrheniusConstants(28,1)* exp (- ArrheniusConstants(28,2) /(R *
Temperature));
k(29) = ArrheniusConstants(29,1)* exp (- ArrheniusConstants(29,2) /(R *
Temperature));
k(30) = ArrheniusConstants(30,1)* exp (- ArrheniusConstants(30,2) /(R *
Temperature));
```

```
k(31) = ArrheniusConstants(31,1)* exp (- ArrheniusConstants(31,2) /(R *
Temperature));
k(32) = ArrheniusConstants(32,1)* exp (- ArrheniusConstants(32,2) /(R *
Temperature));
k(33) = (ArrheniusConstants(33,1)* exp (- ArrheniusConstants(33,2) /(R *
Temperature)))...
    +Prop(11,1) * Te^ Prop(11,2)*1000 *2.718^(-Prop(11,3)/Te);
k(34) = ArrheniusConstants(34,1)* exp (- ArrheniusConstants(34,2) /(R *
Temperature));
k(35) = ArrheniusConstants(35,1)* exp (- ArrheniusConstants(35,2) /(R *
Temperature));
k(36) = ArrheniusConstants(36,1)* exp (- ArrheniusConstants(36,2) /(R *
Temperature));
end
```

A.1.3: Reaction differential equation script

```
%{
This function is designed to calculate the rate of formation and removal of
each of the Components present

%}
function  [ dy_dt ] = NTPdecompmethanolratesv0( t, y )
%Working version
global Component2
global NumberComponents

% assumes no heat lost to jacket ( adibatic)

Moles = y(1:NumberComponents);

Temperature = y(NumberComponents+1);

%{

CALCULATE the reaction rate constants

%}

k = NTPdecompmethanolreactionv0(Temperature);


ReactionVolume =0;

for j = 1:21
    ReactionVolume = ReactionVolume + (Component2(j).Mwt * Moles(j));
end

%{
 Calculate rates of formation/removal of each Component.

%}
dMoles_dt(1) = (-k(1)* Moles(1)) -...
    (k(13)* Moles(7)*Moles(1))+ ...
    (k(3)+k(4))*Moles(2)*Moles(3)+...
    k(9)*Moles(3)+...
    k(24)*Moles(20)+...
    k(26)*Moles(10)*Moles(2);
```

```
dMoles_dt(2) = (2*k(1)*Moles(1)-(k(2)+k(3)+k(4))*Moles(2)*Moles(3)...
    +(k(6)+k(8))*Moles(3)+k(13)*Moles(1)*Moles(7)...
    +k(14)*Moles(13) +k(16)*Moles(14)...
    -k(17)*Moles(2)*Moles(6)+k(20)*Moles(15)...
    +k(23)*Moles(10)-(k(25)+k(26)+k(27))*Moles(2)*Moles(10)...
    -k(28)*Moles(2)*Moles(8)-k(30)*Moles(2)*Moles(17)...
    -k(31)*Moles(2)*Moles(18)-k(32)*Moles(2)*Moles(19))...
    +k(34)*Moles(5);

dMoles_dt(3) = (-(k(2)+ k(3) +k(4))*Moles(2)*Moles(3))...
    -((k(5)+k(6)+k(7)+k(8)+k(9))* Moles(3))-(k(10)*Moles(3)*Moles(6))...
    +(k(27)* Moles(10));

dMoles_dt(4) = k(11)*Moles(6)*Moles(9)+k(36)*Moles(17)*Moles(8);

dMoles_dt(5) = k(2)*Moles(2)*Moles(3) + k(5)*Moles(3)...
    +k(28)*Moles(2)*Moles(8)-k(34)*Moles(5);

dMoles_dt(6)= k(2)*Moles(2)*Moles(3)+k(7)*Moles(3)...
    -k(10)* Moles(3)- k(11)*Moles(6)*Moles(9)...
    -2*k(12)*Moles(6)*Moles(6) +k(13)*Moles(7)*Moles(1)...
    -k(15)*Moles(6)*Moles(17)-k(17)*Moles(6)*Moles(2)...
    -k(18)*Moles(6)* Moles(18)-k(22)*Moles(6)*Moles(19);

dMoles_dt(7)=k(5)*Moles(3)-k(13)*Moles(7)*Moles(1);

dMoles_dt(8)=k(25)*Moles(2)*Moles(10)+ k(7)*Moles(3)...
    +k(34)*Moles(5)-k(28)*Moles(2)*Moles(8)-k(35)*Moles(21)*Moles(8)...
    -k(36)*Moles(17)*Moles(8);

dMoles_dt(9)=k(3)*Moles(3)+k(6)*Moles(3)+ k(10)* Moles(3)...
    -k(11)*Moles(6)*Moles(9);

dMoles_dt(10)=(k(4)+k(8))*Moles(3)-
(k(26)+k(25)+k(27))*Moles(10)*Moles(2)...
   -k(23)*Moles(10);

dMoles_dt(11)=k(9)*Moles(3)-k(29)*Moles(11);

dMoles_dt(12)= k(10)*Moles(3)*Moles(6)+k(17)*Moles(6)*Moles(2)...
    -k(33)*Moles(12);

dMoles_dt(13)=k(12)*Moles(6)*Moles(6)-k(14)*Moles(13)...
    +k(30)*Moles(17)*Moles(2);

dMoles_dt(14)=k(15)*Moles(6)*Moles(17)-k(16)*Moles(14)...
    +k(31)*Moles(18)*Moles(2);

dMoles_dt(15)=k(18)*Moles(6)* Moles(18)+ k(19)*Moles(17)*Moles(17)...
    -k(20)*Moles(16) +k(32)*Moles(2)*Moles(18);

dMoles_dt(16)= k(21)*Moles(17)* Moles(18)+ k(22)*Moles(6)*Moles(19);

dMoles_dt(17)=k(14)*Moles(13)-k(15)*Moles(6)*Moles(17)...
    -(2*k(19)*Moles(17)*Moles(17))-k(21)*Moles(17)* Moles(18)...
    -k(30)*Moles(2)*Moles(17)-k(36)*Moles(17)*Moles(8);

dMoles_dt(18)=k(16)*Moles(14)-k(18)*Moles(6)* Moles(18)...
    -k(21)*Moles(17)* Moles(18)-k(31)*Moles(18)*Moles(2);
```

```
dMoles_dt(19)=k(20)*Moles(16)-k(22)*Moles(6)*Moles(19)...
    -k(32)*Moles(2)*Moles(19);

dMoles_dt(20)= k(23)*Moles(10)-k(24)*Moles(20)*...
    +k(26)*Moles(10)*Moles(2)+k(29)*Moles(11);

dMoles_dt(21)=k(24)*Moles(20)-k(35)*Moles(21)*Moles(8);

dMoles_dt(22)=k(35)*Moles(21)*Moles(8);

dT_dt=0;

% Copy all the derivatives into the output vector in the right order

dy_dt = [dMoles_dt dT_dt]' ;

end
```

A.2: Glycerol model

A.2.1:Glycerol model main script

```
%{
Model of plasma degradation of glycerol
By Jonathan Harris

%%
The Model

The model is a batch process, with the rate constants varying with
temperature. There are no temperature discontinuties, but heat is evolved
so
heat balances are required

This model assumes that the product remains in the vessel until the
simulation ends, this will be changed in later versions.

The reactions:
1. H2                  2 H.
2. H20                 H. + OH.
3. glycerol            acetol + H. + OH
4. acetol              CH2OH. + ethanal
5. acetol              ethenal + CH2O
6. ethanal             CO + CH3.
7. CO +OH.             COOH.
8. COOH.               CO2 + H.
9. CH2O                CO + H2
10. OH. + CH3.         Methanol
11. 2 CH3.             Ethene
12. acetol + H.        1,3 Propandiol
13. 1,3propandiol + H.   Propanol + H2O
14. 1,3propandiol      Propanal +H2O
15. glycerol           CH2OH. + ethendiol
16. ethendiol          glycerolaldehyde + H.
17. glycerolaldehyde     CHO. + CH2OH.
18. 2 H.               H2
19. H. + OH.           H20
20. acetol + water     glycerol
```

```
21. ethenol + CHO.      acetol
22. CH2OH. + ethanal    acetol
23. CO + CH3.        ethanal
24. COOH.            CO +OH.
25. CO2 + H.         COOH.
26. CO + H2          CH2O
27. Methanol         OH. + CH3.
28. Ethane           2 CH3.
29. 1,3 Propandiol   acetol + H.
30. Propanol + H2O   1,3propandiol + H.
31. Propanal +HO    1,3propandiol
32. CH2OH. + ethendiol      glycerol
33. glycerolaldehyde + H.   ethendiol
34. CHO. + CH2OH.    glyceraldehyde
35. CH3. + C2H5.     Propane
36. CH3. + H.        Methane
37: C3H7. + CH3.     Butane
38: 2C2H5.           Butane
39. C3H7. + H.       Propane
40. C2H5. + H.       Ethane
41. CHO.             CO + H.
42. CH2OH.           H. + CH2O
43. CH2OH.+ H.       OH. + CH3.
44. 2*CH2OH.         ethendiol
45. CH2OH. + H.      Methanol (rev 52)
46. ethendiol        2*CH2OH.
47. ch3. + Ch2OH     ethenol +2H.
48. ethanol          methanol + CH3
49. ethane           C2H5. + H.
50. propane          C3H7. + H.
51. methane          CH3. + H.
53. glycerol         Ethendiol + CH2OH.

The components
H2
H.
glycerol
acetol
glycerolaldehyde
water
OH.
CH2OH.
Ethanol
CHO.
Ethenal
CO
CH3.
COOH.
CO2
CH2O
Methanol
1,3-propandiol
propanol
propanal
ethendiol
C2H5.
C3H7.
Methane
Ethene
Propane
Butane
%%
```

```
Units
Time            minutes
Temperature     degreees K
Heat capacity   Kj/kgK
mass            kg
Volume          dm3
Concentration   moles/dm3
flowrate        dm3/minute
%}
%{
PREPARATION

clear any persistent items from the MatLab workspace
%}

clear variables

% clear MatLab Command Window

clc

% close any open graph windows

delete(findall(0,'Type','figure'))

global NumberReactions;

NumberReactions = 54;

global ArrheniusConstants
ArrheniusConstants = zeros(54,2);

ArrheniusConstants(1,1) = 2.61E-8;                % per s
ArrheniusConstants(2,1) = 1.49E-9;
ArrheniusConstants(3,1) = 5.36E-11;
ArrheniusConstants(4,1) = 2.12E-10;
ArrheniusConstants(5,1) = 4.47E-10;
ArrheniusConstants(6,1) = 4.88E-13;
ArrheniusConstants(7,1) = 3.14E+4;
ArrheniusConstants(8,1) = 1E-1;
ArrheniusConstants(9,1) = 3.49E-1;               % per s
ArrheniusConstants(10,1) = 9.93E-2;
ArrheniusConstants(11,1) = 1.42E1;
ArrheniusConstants(12,1) = 4.47E-10;
ArrheniusConstants(13,1) = 1.82E1;
ArrheniusConstants(14,1) = 5.36E-2;
ArrheniusConstants(15,1) = 1.11E-8;
ArrheniusConstants(16,1) = 1.89E-2;
ArrheniusConstants(17,1) = 4.47E-2;
ArrheniusConstants(18,1) = 6.62E-34;
ArrheniusConstants(19,1) = 1.58E-13;
ArrheniusConstants(20,1) = 3.69E-29;
ArrheniusConstants(21,1) = 1.45E-9;
ArrheniusConstants(22,1) = 1.79E-12;
ArrheniusConstants(23,1) = 9.75E-13;
ArrheniusConstants(24,1) = 6.58E4;
ArrheniusConstants(25,1) = 1.35E-10;
ArrheniusConstants(26,1) = 1.76E-34;
ArrheniusConstants(27,1) = 2.7E-7;
ArrheniusConstants(28,1) = 9.38E-3;
ArrheniusConstants(29,1) = 2.84E-11;
```

```
ArrheniusConstants(30,1) = 3.47E-11;
ArrheniusConstants(31,1) = 7.14E-12;
ArrheniusConstants(32,1) = 1.52E-11;
ArrheniusConstants(33,1) = 4.47E-5;
ArrheniusConstants(34,1) = 1.79E-12;
ArrheniusConstants(35,1) = 7.82E-2;
ArrheniusConstants(36,1) = 5.33E-2;
ArrheniusConstants(37,1) = 1.54E-3;
ArrheniusConstants(38,1) = 1.37E-3;
ArrheniusConstants(39,1) = 5.44E-11;
ArrheniusConstants(40,1) = 2.72E-10;
ArrheniusConstants(40,1) = 2.72E-10;
ArrheniusConstants(41,1) = 1.92E-10;
ArrheniusConstants(42,1) = 1.99E-5;
ArrheniusConstants(43,1) = 1.6E-3;
ArrheniusConstants(44,1) = 1.52E-11;
ArrheniusConstants(45,1) = 3.11E-10;
ArrheniusConstants(46,1) = 1.6E-10;
ArrheniusConstants(47,1) = 2.66E-11;
ArrheniusConstants(48,1) = 1.41E-11;
ArrheniusConstants(49,1) = 9.16E-11;
ArrheniusConstants(50,1) = 1.58E-11;
ArrheniusConstants(51,1) = 6.4E-11;
ArrheniusConstants(52,1) = 2.7E-11;
ArrheniusConstants(53,1) = 4.47E-10;
ArrheniusConstants(54,1) = 4.47E-10;

ArrheniusConstants(1,2) = 437;                % kJ / kmol
ArrheniusConstants(2,2) = 250;
ArrheniusConstants(3,2) = 800;
ArrheniusConstants(4,2) = 250;
ArrheniusConstants(5,2) = 48.58;
ArrheniusConstants(6,2) = 40.4;
ArrheniusConstants(7,2) = 0.738;
ArrheniusConstants(8,2) = 138;
ArrheniusConstants(9,2) = 146;
ArrheniusConstants(10,2) = -10.64;
ArrheniusConstants(11,2) = 0.73;
ArrheniusConstants(12,2) = 48.58;
ArrheniusConstants(13,2) = 277;
ArrheniusConstants(14,2) = 300;
ArrheniusConstants(15,2) = 337;
ArrheniusConstants(16,2) = 326;
ArrheniusConstants(17,2) = 48.56;
ArrheniusConstants(18,2) = -1.51;
ArrheniusConstants(19,2) = -0.48;
ArrheniusConstants(20,2) = -10.64;
ArrheniusConstants(21,2) = 13.35;
ArrheniusConstants(22,2) = 42.23;
ArrheniusConstants(23,2) = 28.25;
ArrheniusConstants(24,2) = 146;
ArrheniusConstants(25,2) = 94.58;
ArrheniusConstants(26,2) = 1.1;
ArrheniusConstants(27,2) = 302;
ArrheniusConstants(28,2) = 349;
ArrheniusConstants(29,2) = 39.8;
ArrheniusConstants(30,2) = -2.6;
ArrheniusConstants(31,2) = 7.38;
ArrheniusConstants(32,2) = -0.3;
ArrheniusConstants(33,2) = 48.58;
ArrheniusConstants(34,2) = 42.23;
ArrheniusConstants(35,2) = -1.8;
ArrheniusConstants(36,2) = -6.4;
```

```
ArrheniusConstants(37,2) = -2.8;
ArrheniusConstants(38,2) = -0.9;
ArrheniusConstants(39,2) = -0.8;
ArrheniusConstants(40,2) = 0.5;
ArrheniusConstants(41,2) = 67.15;
ArrheniusConstants(42,2) = -0.4;
ArrheniusConstants(43,2) = 0;
ArrheniusConstants(44,2) = -0.3;
ArrheniusConstants(45,2) = 0.2;
ArrheniusConstants(46,2) = 0;
ArrheniusConstants(47,2) = -2;
ArrheniusConstants(48,2) = 365;
ArrheniusConstants(49,2) = 421;
ArrheniusConstants(50,2) = 408;
ArrheniusConstants(51,2) = 436;
ArrheniusConstants(52,2) = 278;
ArrheniusConstants(53,2) = 48.58;
ArrheniusConstants(54,2) = 48.58;  %correct later
% now define constants

global Prop
Prop = zeros(21,3);

Prop(1,1) = 1.7E-4;   %H2
Prop(2,1) = 4.62E-1;   %h2o -2
Prop(3,1) = 6.87E-2;   %glycerol 4.67 -2
Prop(4,1) = 2.53E-2;   % acetol to alc + ketone 1.13
Prop(5,1) = 4.43E-5;   %acetol to 2 ketone
Prop(6,1) = 1.53E-1;   %ethenal to co and CH3
Prop(7,1) = 6.67E3;   %methanal decomp
Prop(8,1) = 5.94E-3;   %propandiol to propanol
Prop(9,1) = 1.94E-5;  % glycerol to methanol + ethendiol
Prop(10,1) = 1.62E-2;  %ethendiol to glyceraldehyde + H
Prop(11,1) = 1.67E-1;  %glyceraldehyde to cho and ch2oh
Prop(12,1) = 1.53E-9; %acetol + water to glycerol ( unlikely to happen)
Prop(13,1) = 1.7E-9;   %co + H2 to ch2o ( slow but can occur)( use
properties of H2 to H but reduce)
Prop(14,1) = 7.94E-2;  % methanol to Oh +ch3  5.94-3
Prop(15,1) = 1.53E-1;  %ethane to 2ch3
Prop(16,1) = 7.53E-8;  %Propanol to propandiol (unlikely)
Prop(17,1) = 8.53E-1;  %ethane to c2h5 + H
Prop(18,1) = 7.52E-2;  %propane to c3h7 + H
Prop(19,1) = 5.16E-1;  %methane to ch3 + H
Prop(20,1) = 4.94E-2; % methanol to CH2OH + H
Prop(21,1) = 5.53E-4; % glycerol to ethendiol + methanol
Prop(22,1) = 1.53E-1; %ethendiol to 2 Ch2OH

Prop(1,2) = 0;
Prop(2,2) = -0.781;
Prop(3,2) = -0.681;
Prop(4,2) = -0.08;
Prop(5,2) = -0.12;
Prop(6,2) = -0.06;
Prop(7,2) = -0.081;
Prop(8,2) = -0.612;
Prop(9,2) = -0.612;
Prop(10,2) = -0.781;
Prop(11,2) = -0.062;
Prop(12,2) = -0.06;
Prop(13,2) = 0;
Prop(14,2) = -0.612;
Prop(15,2) = -0.06;
Prop(16,2) = 0;
```

```
Prop(17,2) = -0.06;
Prop(18,2) = -0.03;
Prop(19,2) = -0.642;
Prop(20,2)= -0.612;
Prop(21,2) = -0.08;
Prop(22,2) = -0.12;


Prop(1,3) = 119940;
Prop(2,3) = 18298.2;
Prop(3,3) = 34309;
Prop(4,3) = 121377.8;
Prop(5,3) = 111277.8;
Prop(6,3) = 12137.78;
Prop(7,3) = 1830.93;
Prop(8,3) = 1788.13;
Prop(9,3) = 3788.13;
Prop(10,3) = 1829.82;
Prop(11,3) = 1230.93;
Prop(12,3) = 12137.78;
Prop(13,3) = 11994;
Prop(14,3) = 1788.13;
Prop(15,3) = 12137.78;
Prop(16,3) = 16994;
Prop(17,3) = 12137.78;
Prop(18,3) = 16994.12;
Prop(19,3) = 16988.26;
Prop(20,3) = 1788.13;
Prop(21,3) = 121377.8;
Prop(22,3) = 111277.8;

global R;
R = (8.314);  % KJ/kgK

global NumberComponents
NumberComponents = 27;

% define components
global Component3
Component3(1).name = 'H2';
Component3(1).Mwt = 2;
Component3(1).cp = 14.32;

Component3(2).name = 'H.';
Component3(2).Mwt = 1;
Component3(2).cp = 14.32;

Component3(3).name = 'glycerol';
Component3(3).Mwt = 92;
Component3(3).cp = 2.379;

Component3(4).name = 'acetol';
Component3(4).Mwt = 74;
Component3(4).cp = 2.210;

Component3(5).name = 'glycolaldehyde';
Component3(5).Mwt = 60;
Component3(5).cp = 2.201;

Component3(6).name = 'H2O';
Component3(6).Mwt = 18;
```

```
Component3(6).cp = 4.171;

Component3(7).name = 'OH.';
Component3(7).Mwt = 17;
Component3(7).cp = 4.18;

Component3(8).name = 'CH2OH.';
Component3(8).Mwt = 31;
Component3(8).cp = 2.51;

Component3(9).name = 'Ethanol';
Component3(9).Mwt = 46;
Component3(9).cp = 2.470;

Component3(10).name = 'CHO.';
Component3(10).Mwt = 29;
Component3(10).cp = 0.6767;

Component3(11).name = 'ethenal';
Component3(11).Mwt = 44;
Component3(11).cp = 2.012;

Component3(12).name = 'CO.';
Component3(12).Mwt = 28;
Component3(12).cp = 1.67;

Component3(13).name = 'CH3.';
Component3(13).Mwt = 15;
Component3(13).cp = 2.22;

Component3(14).name = 'COOH.';
Component3(14).Mwt = 45;
Component3(14).cp = 2.202;

Component3(15).name = 'CO2.';
Component3(15).Mwt = 44;
Component3(15).cp = 0.825;

Component3(16).name = 'CH2O';
Component3(16).Mwt = 30;
Component3(16).cp = 0.7704;

Component3(17).name = 'Methanol';
Component3(17).Mwt = 32;
Component3(17).cp = 2.51;

Component3(18).name = '1-3 propandiol';
Component3(18).Mwt = 76;
Component3(18).cp = 2.402;

Component3(19).name = 'propanol';
Component3(19).Mwt = 60;
Component3(19).cp = 2.589;

Component3(20).name = 'propanal';
Component3(20).Mwt = 58;
Component3(20).cp = 2.32;

Component3(21).name = 'ethenediol';
Component3(21).Mwt = 62;
```

```
Component3(21).cp = 2.424;

Component3(22).name = 'C2H5.';
Component3(22).Mwt = 29;
Component3(22).cp = 1.75;

Component3(23).name = 'C3H7.';
Component3(23).Mwt = 43;
Component3(23).cp = 1.67;

Component3(24).name = 'Methane';
Component3(24).Mwt = 16;
Component3(24).cp = 2.22;

Component3(25).name = 'Ethane';
Component3(25).Mwt = 30;
Component3(25).cp = 1.75;

Component3(26).name = 'Propane';
Component3(26).Mwt = 44;
Component3(26).cp = 1.67;

Component3(27).name = 'Butane';
Component3(27).Mwt = 58;
Component3(27).cp = 1.67;

%{
SPECIFY Operating Conditions

determine initial charge in moles
%}

global ReactorCharge
ReactorCharge = [2.00000,    ...    moles H2
                 0.00000,    ...           H.
                 0.79,      ...          glycerol
                 0.00000,      ...          acetol
                 0.00000,      ...          glyceraldehyde
                 0.00000,0.00000,0.00000,0.00000,...
                 0.00000,0.00000,0.00000,0.00000,...
                 0.00000,0.00000,0.00000,0.00000,...
                 0.00000,0.00000,0.00000,0.00000,...
                 0.00000,0.00000,0.00000,0.00000,...
                 0.00000,0.00000];
%{
Determine initial volume
global ComponentVolume
global InitialVolume
ComponentVolume = zeros(27,1);
%density in place of 1
for i=1:27
    ComponentVolume(i) =ReactorCharge(i)/1;
end

InitialVolume = sum(ComponentVolume);
%}

global InitialTemperature
InitialTemperature =298;    %K

global Power
```

```
Power = 50; %W

%%                          INITIALISE SIMULATION

%{
_____________________________________________________________________________

SET Time Interval

Set the simulation time interval (times are in SECONDS)
In this case, the simulation will run for 10 seconds


%}

EndTime = 12.74;          % seconds

ispan = [ 0 EndTime ];

ispan = sort (ispan);

ispan = unique (ispan);


%{

INITIALISE the Dependent Variables

In this example, the dependent variables in the differential equations are
    the reagents and products in kmol
    the reaction volume im m3
    the reaction temperature in K

InitialReactionVolume and InitialReactorTemperature are added to the vector
of initial values of dependent variables y0 passed to the integrator.

%}

y0 = [ReactorCharge InitialTemperature];

options = odeset ( 'NonNegative', 1:length(y0) );
%%

%{

SET Integrator Options

% The MatLab function length counts the elements in the vector y0

%}


%%                                SIMULATION LOOP

%{
_____________________________________________________________________________

RUN THE SIMULATION
```

```
%}

for j = 2:length(ispan)

    [tSection, ySection] = ode15s(@NTPglycerolratesv03, ...
                                  [ispan(j-1) ispan(j)], ...
                                  y0, ...
                                  options);

    nt = length(tSection);

    if j == 2
        t = tSection;
        y = ySection;
    else
        t = [t; tSection(2:nt)];
        y = [y; ySection(2:nt,:)];
    end

    y0 = ySection(nt,:);

end


%%                                SHOW RESULTS


%_____________________________________________________________________________
%PLOT THE RESULTS

%Plot the reactor composition profile



figure ('name', 'Reactor composition');

grid off

plot (t, y(:,1:NumberComponents-1))

title ( 'Reactor composition')

ylabel ('Moles')
xlabel ('time  (seconds)')

legend (Component3(1:NumberComponents-1).name)


%_____________________________________________________________________________
_

%Plot the temperature profile


figure ('name', 'Reaction temperature');

plot (t, y(:,NumberComponents+1))            % plots columns 7 in matrix y
```

```
title ( 'Reactor temperature')

ylabel ('Temperature (K)')
xlabel ('time  (seconds)')
```

A.2.2: Reaction constant calculation script

```
 %{
This function is designed to calculate the rate of formation and removal of
each of the Components present

%}
function  [ dy_dt ] = NTPglycerolratesv03( t, y )
%Working version
global NumberComponents



% assumes no heat lost to jacket ( adibatic)

Moles = y(1:NumberComponents);

Temperature = y(NumberComponents+1);

%{

CALCULATE the reaction rate constants

%}


k = Ntpglycerolreactionv03(Temperature);

%{
 Calculate rates of formation/removal of each Component2. The reactions
that
 can occur are:
Ignore this



Volume (1) = ((ReactorDimensions(2)^2)*3.141592)* ReactorDimensions(3);
global ResidenceTime
ResidenceTime = (Volume/N2Flow )*60;   % minutes
PartPliq = 10^(4.246 -(1510/( -98.989 + Temperature(1))));

if PartPliq > 1
    Evap =((0.003*((PartPliq -
101300))/PartPliq)*Moles(4))*Component2(4).Mwt;
else
    Evap = 0;
end

%}
dM_dt(1) = -(k(1)* Moles(1))+k(9)*Moles(16) +(k(18)*2*Moles(2)*
Moles(2))...
```

```
    -k(26)*Moles(1)*Moles(12)+k(42)*Moles(8)-
(k(43)+k(45))*Moles(1)*Moles(8)+k(3)*Moles(3)+2*k(47)*Moles(13)*Moles(8);

dM_dt(2) = +(2*k(1)*Moles(1))+k(2)*Moles(6)-k(12)*Moles(2)*Moles(4)...
    +k(13)*Moles(18)-(k(18)*Moles(2)*Moles(2))-k(19)*Moles(2)*Moles(7)...
    -k(25)*Moles(15)*Moles(2)-k(33)*Moles(2)*Moles(5) -
k(36)*Moles(2)*Moles(13)...
    -k(39)*Moles(2)*Moles(23)-k(40)*Moles(2)*Moles(22)+k(41)*Moles(10)...
    +k(49)*Moles(25)+k(50)*Moles(26)+k(51)*Moles(24)+k(52)*Moles(17);

dM_dt(3) = -k(3)*Moles(3)-k(15)*Moles(3)+k(20)*Moles(4)*Moles(6)...
    +k(32)*Moles(8)*Moles(21)-k(53)*Moles(3);

dM_dt(4) = +k(3)*Moles(3) -(k(4)+k(5))*Moles(4)-k(12)*Moles(4)*Moles(2)...
    -k(20)*Moles(4)*Moles(6) +k(21)*Moles(9)*Moles(10)
+k(22)*Moles(8)*Moles(11)...
    +k(29)*Moles(18);

dM_dt(5) = k(16)*Moles(21)-k(17)*Moles(5)-k(33)*Moles(5)*Moles(2)...
    +k(34)*Moles(10)*Moles(8);

dM_dt(6)=-k(20)*Moles(4)*Moles(6)+k(19)*Moles(2)*Moles(7)...
    -k(2)*Moles(6)+k(13)*Moles(18);

dM_dt(7)=k(2)*Moles(6)-k(7)*Moles(7)*Moles(12)-k(10)*Moles(7)*Moles(13)...
    -
k(19)*Moles(2)*Moles(7)+k(24)*Moles(14)+k(27)*Moles(17)+k(43)*Moles(8)*Mole
s(1)+k(3)*Moles(3);

dM_dt(8)=k(4)*Moles(4)+k(15)*Moles(3)+k(17)*Moles(5)-
k(22)*Moles(8)*Moles(11)...
    -k(32)*Moles(8)*Moles(21)-k(34)*Moles(10)*Moles(8)-k(42)*Moles(8)...
    -(k(43)+k(45))*Moles(1)*Moles(8)-(2*k(44))*Moles(8)*Moles(8)...
    +2*k(46)*Moles(21)-k(47)*Moles(13)*Moles(8)+k(52)*Moles(17)...
    +k(53)*Moles(3)+2*k(54)*Moles(21);

dM_dt(9)=-k(21)*Moles(9)*Moles(10)+k(47)*Moles(13)*Moles(8)...
    -k(48)*Moles(9);

dM_dt(10)=  k(17)*Moles(5)-k(21)*Moles(9)*Moles(10)...
    -k(34)*Moles(10)*Moles(8)-k(41)*Moles(10);

dM_dt(11)= k(4)*Moles(4)+ k(5)*Moles(4)-k(6)*Moles(11)-
k(22)*Moles(11)*Moles(8)...
    +k(23)*Moles(12)*Moles(13);

dM_dt(12)= k(6)*Moles(11)-k(7)*Moles(7)*Moles(12)+k(9)*Moles(16)...
    -k(23)*Moles(12)*Moles(13) +k(24)*Moles(14)-k(26)*Moles(12)*Moles(1)...
    +k(41)*Moles(10);

dM_dt(13)=k(6)*Moles(11)-k(10)*Moles(13)*Moles(7)-
(2*k(11)*Moles(13)*Moles(13))...
    -k(23)*Moles(13)*Moles(12)+k(27)*Moles(17)+(2*k(28)*Moles(24))...
    -k(35)*Moles(13)*Moles(22)-k(36)*Moles(13)*Moles(2)-
k(37)*Moles(13)*Moles(23)...
    +k(43)*Moles(8)*Moles(1)-
k(47)*Moles(13)*Moles(8)+k(48)*Moles(9)+k(51)*Moles(24);

dM_dt(14)=k(7)*Moles(7)*Moles(12)-(k(8)+k(24))*Moles(14)...
    +k(25)*Moles(15)*Moles(2);
```

```
dM_dt(15)=k(8)*Moles(14)-k(25)*Moles(15)*Moles(2);

dM_dt(16)=k(5)*Moles(4)-
k(9)*Moles(16)+k(26)*Moles(12)*Moles(1)+k(42)*Moles(8);

dM_dt(17)=k(10)*Moles(13)*Moles(7)-
k(27)*Moles(17)+k(45)*Moles(8)*Moles(1)...
    +k(48)*Moles(9)-k(52)*Moles(17);

dM_dt(18)=k(12)*Moles(4)*Moles(2)-k(13)*Moles(18)*Moles(2)-
(k(14)+k(29)*Moles(18))...
    +k(30)*Moles(19)*Moles(6)+k(31)*Moles(20)*Moles(6);

dM_dt(19)=k(13)*Moles(18)*Moles(2)-k(30)*Moles(19)*Moles(6);

dM_dt(20)= k(14)*Moles(18)-k(31)*Moles(20)*Moles(6);

dM_dt(21)=k(15)*Moles(3)-k(16)*Moles(21)-k(32)*Moles(8)*Moles(21)...
    +k(33)*Moles(5)*Moles(2)+k(44)*Moles(8)*Moles(8)-k(46)*Moles(21)...
    +k(53)*Moles(3)-k(54)*Moles(21);

dM_dt(22)=k(49)*Moles(25)-k(35)*Moles(22)*Moles(13) -
(2*k(38)*Moles(22)*Moles(22))-k(40)*Moles(22)*Moles(2);

dM_dt(23)=k(50)*Moles(26)-k(37)*Moles(23)*Moles(13)-
k(39)*Moles(23)*Moles(2);

dM_dt(24)=k(36)*Moles(13)*Moles(2)-k(51)*Moles(24);

dM_dt(25)=k(11)*Moles(13)*Moles(13)-k(28)*Moles(24)...
   +k(40)*Moles(22)*Moles(2)-k(49)*Moles(25);

dM_dt(26)=k(35)*Moles(22)*Moles(13)...
     +k(39)*Moles(23)*Moles(2)-k(50)*Moles(26);

dM_dt(27)=k(37)*Moles(23)*Moles(13)+(k(38)*Moles(22)*Moles(22));

dT_dt=0;

dy_dt = [dM_dt dT_dt]' ;

end
```

A.2.3: Component differential equation solver script

```
%{
 This code was produced by Jonathan Harris as part of a PhD modelling
project at newcastle university in the year 2016. Use of this code for
other purposes is not permitted without permission of the author.

Produced to generate K values from Temperature
This function is called by the function Rates.

%}

function[k] = Ntpglycerolreactionv03(Temperature)
```

```
%{

This function calculates reaction rate constants for all reactions.

The gas constant R and the Arrhenius constants are global variables.

Temperature is an input parameter because some models will require rate
constants to be calculated at different Temperatures.

                    k = A exp ( - E / RT)
Calculation of K from power uses three constants of proportionality, from
literature.
Full equation:

k = Prop1 * Te^ Prop2 *e^(-Prop3/Te)

This is used for reactions where electrons participate, which are
reactions:
1-6,9,14-17, 20,26-28,30,49-54

INPUT

Temperature     reaction Temperature in Kelvin

OUTPUT

k               a vector of rate constants

GLOBAL

ArrheniusConstants      array of Arrhenius constants
                 ArrheniusConstants(ReactionNumber, 1) is FREQUENCY FACTOR
                 ArrheniusConstants(ReactionNumber, 2) is ACTIVATION ENERGY

R               gas constant

This MatLab function uses the global variables R and ArrheniusConstants.
The variables must be declared in this function to make them available.
Global variables which are not declared within this function cannot be used
inside this function.
%}

global R;
global ArrheniusConstants
global Power
global Prop
global InitialTemperature

Te = InitialTemperature + Power * 421.71;
%{
These values are set outside this function

Calculate k values now, but set as a zeros matrix first
%}
% replace Temperature with Temperature

%*1000 to correct Cm-3 to L-1
k(1:54)= 0;
for i=1:54
```

```
    k(i) = ArrheniusConstants(i,1)* exp (- ArrheniusConstants(i,2) /(R *
Temperature));
end
for j=1:6
    k(j)=k(j)+Prop(j,1) * Te^ Prop(j,2)*1000 *2.718^(-Prop(j,3)/Te);
end

k(9)=k(9) +Prop(7,1) * Te^ Prop(7,2)*1000 *2.718^(-Prop(7,3)/Te);

for l=1:4
    k(l+13)=k(l+13)+Prop(l+7,1) * Te^ Prop(l+7,2)*1000 *2.718^(-
Prop(l+7,3)/Te);
end

k(20)= k(20)+ +Prop(12,1) * Te^ Prop(12,2)*1000 *2.718^(-Prop(12,3)/Te);

for m=1:3
    k(m+25)=k(m+25)+Prop(12+m,1) * Te^ Prop(12+m,2)*1000 *2.718^(-
Prop(12+m,3)/Te);
end
k(30)= k(30)+Prop(16,1) * Te^ Prop(16,2)*1000 *2.718^(-Prop(16,3)/Te);
k(49)= k(49)+Prop(17,1) * Te^ Prop(17,2)*1000 *2.718^(-Prop(17,3)/Te);
k(50)= k(50)+Prop(18,1) * Te^ Prop(18,2)*1000 *2.718^(-Prop(18,3)/Te);
k(51)= k(51)+Prop(19,1) * Te^ Prop(19,2)*1000 *2.718^(-Prop(19,3)/Te);
k(52)= k(52)+Prop(20,1) * Te^ Prop(20,2)*1000 *2.718^(-Prop(20,3)/Te);
k(53)= k(53)+Prop(21,1) * Te^ Prop(21,2)*1000 *2.718^(-Prop(21,3)/Te);
k(54)= k(54)+Prop(22,1) * Te^ Prop(22,2)*1000 *2.718^(-Prop(22,3)/Te);
end
```

Appendix B. Data handling

B.1: Gas analysis

B.1.1: Methanol

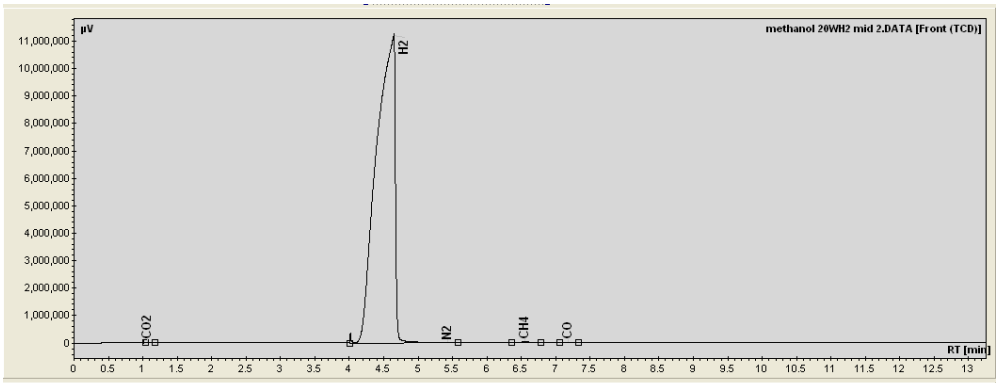

#	Name	Time [Min]	Quantity [%mol]	Height [µV]	Area [µV.Min]	Area % [%]
1	CO2	1.06	0.23	19523.9	777.0	0.022
3	H2	4.65	66.61	11252715.4	3526138.1	99.537
0	O2	5.00	N.D.	N.D.	N.D.	N.D.
4	N2	5.43	0.48	18333.2	2229.5	0.063
5	CH4	6.55	0.47	40056.1	6454.1	0.182
6	CO	7.18	0.33	10891.6	1551.6	0.044
Total			68.11	11688420.1	3542538.9	100.000

Figure B.1: Permanent gas GC results from methanol decomposition (10W H_2)

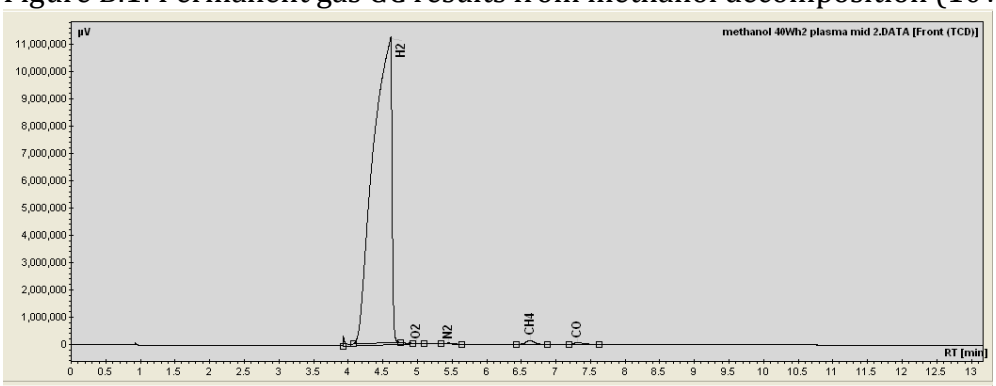

#	Name	Time [Min]	Quantity [%mol]	Height [µV]	Area [µV.Min]	Area % [%]
0	CO2	1.37	N.D.	N.D.	N.D.	N.D.
9	H2	4.62	67.48	11181915.8	3461556.7	98.643
8	O2	4.99	0.06	3806.4	412.3	0.012
2	N2	5.45	0.73	34403.2	3393.2	0.097
3	CH4	6.63	1.40	132480.6	19297.4	0.550
4	CO	7.31	2.42	61376.6	11122.7	0.317
Total			72.09	11905391.4	3509159.5	100.000

Figure B.2: Permanent gas GC results from methanol decomposition (30W H_2)

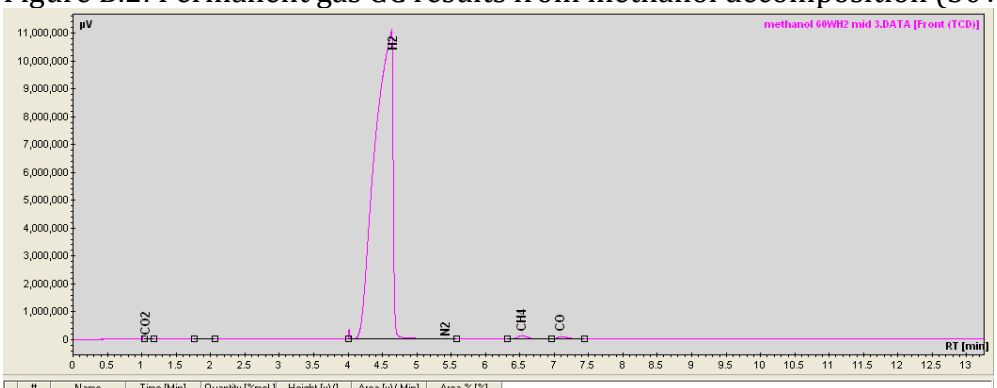

#	Name	Time [Min]	Quantity [%mol]	Height [µV]	Area [µV.Min]	Area % [%]
1	CO2	1.06	0.22	20430.3	769.8	0.023
4	H2	4.64	63.34	11128284.4	3353210.3	98.619
0	O2	5.00	N.D.	N.D.	N.D.	N.D.
5	N2	5.42	0.39	15188.6	1845.2	0.054
6	CH4	6.53	1.51	127293.7	20886.2	0.614
7	CO	7.10	3.54	89104.2	16400.2	0.482
Total			69.01	11742276.0	3400178.3	100.000

Figure B.3: Permanent gas GC results from methanol decomposition (50W H_2)

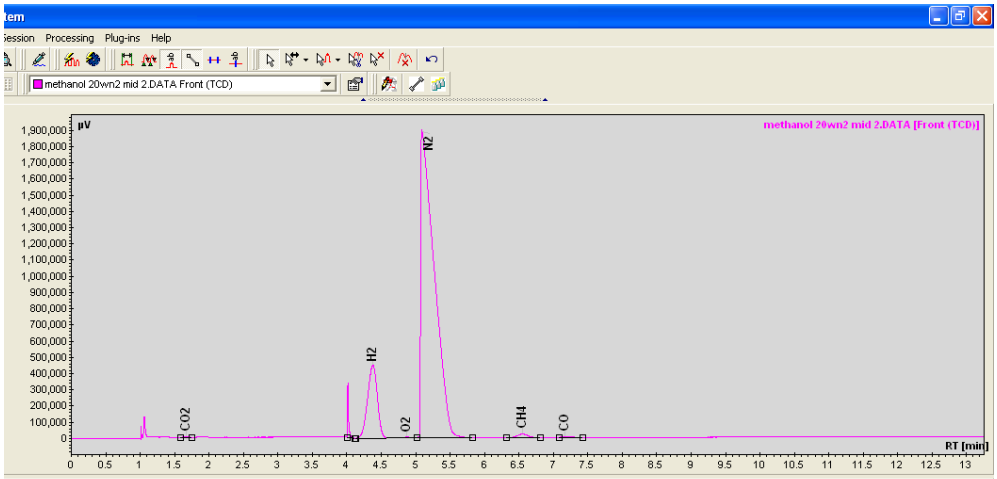

#	Name	Time [Min]	Quantity [%mol]	Height [μV]	Area [μV.Min]	Area % [%]
7	CO2	1.66	0.03	1096.8	98.7	0.019
2	H2	4.38	1.89	449725.5	73897.1	14.456
3	O2	4.87	0.11	9007.0	543.4	0.106
4	N2	5.09	124.49	1898065.2	427000.3	83.533
5	CH4	6.55	0.00	21885.2	3673.9	0.719
6	CO	7.16	0.26	5474.7	875.6	0.171
Total			126.78	2722839.0	511178.2	100.000

Figure B.4: Permanent gas GC results from methanol decomposition (10W N_2)

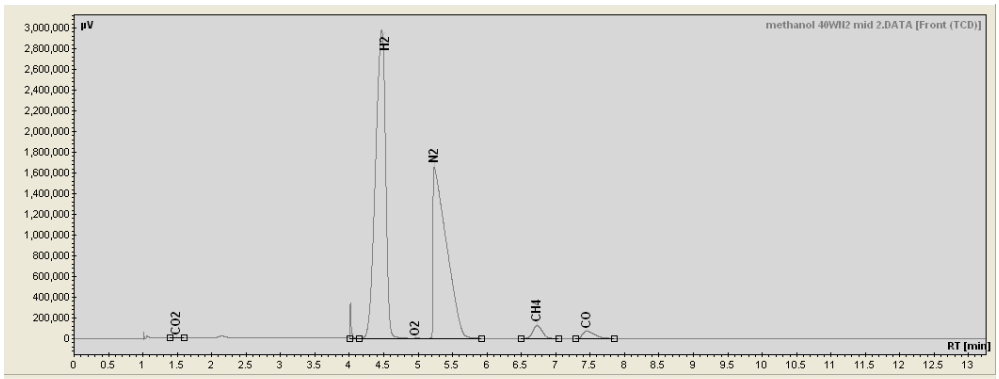

#	Name	Time [Min]	Quantity [%mol]	Height [μV]	Area [μV.Min]	Area % [%]
1	CO2	1.48	0.77	5078.9	408.3	0.044
3	H2	4.47	11.64	2974838.4	505602.9	55.007
4	O2	4.96	0.17	7379.5	538.6	0.059
5	N2	5.23	147.84	1653756.9	373815.9	40.670
6	CH4	6.73	2.83	124476.5	19571.8	2.129
7	CO	7.45	5.91	68622.4	13612.4	1.481
Total			169.16	5174987.2	919153.6	100.000

Figure B.5: Permanent gas GC results from methanol decomposition (30W N_2)

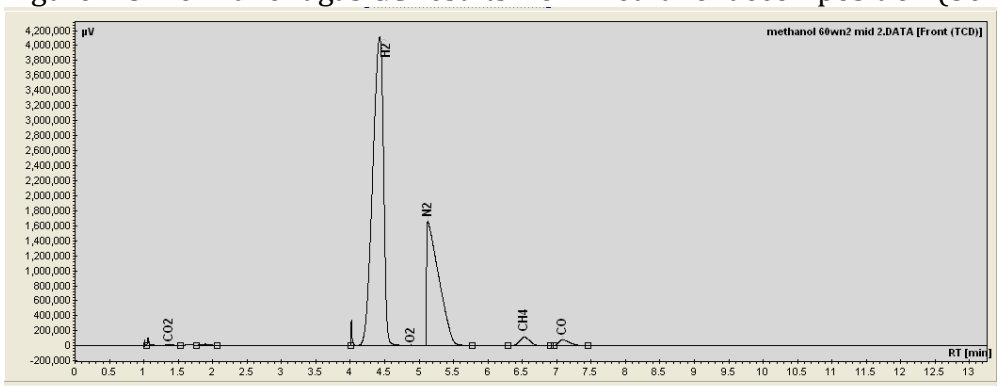

#	Name	Time [Min]	Quantity [%mol]	Height [μV]	Area [μV.Min]	Area % [%]
2	CO2	1.37	0.25	6830.5	866.0	0.077
5	H2	4.43	14.08	4113593.5	745438.3	65.962
6	O2	4.88	0.12	8659.5	820.0	0.073
7	N2	5.13	72.49	1654877.9	338875.2	29.986
8	CH4	6.53	1.41	115038.0	19424.5	1.719
9	CO	7.09	3.11	76109.1	14426.6	1.277
Total			91.46	6423309.6	1130095.7	100.000

Figure B.6: Permanent gas GC results from methanol decomposition (50W N_2)

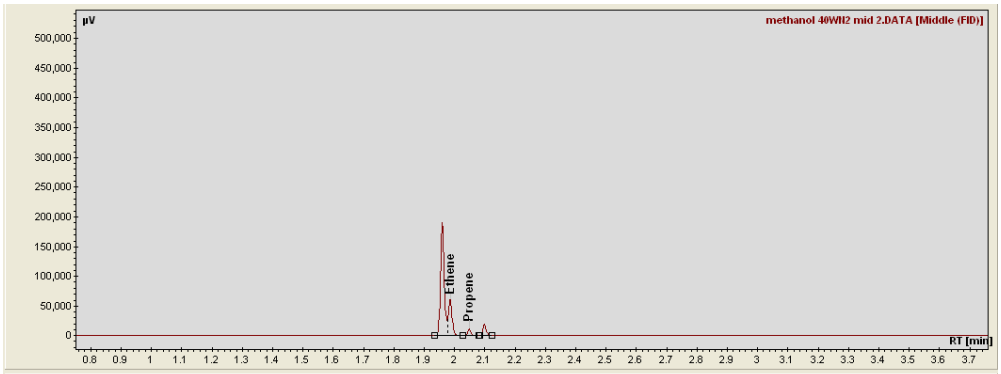

#	Name	Time [Min]	Quantity [wt %]	Height [µV]	Area [µV.Min]	Area % [%]
2	Ethene	1.99	6.53	61108.1	847.4	68.833
0	Ethane	1.99	N.D.	N.D.	N.D.	N.D.
0	Propane	2.05	N.D.	N.D.	N.D.	N.D.
1	Propene	2.05	0.00	10926.2	142.3	11.555
0	Butene	2.18	N.D.	N.D.	N.D.	N.D.
0	Butane	2.20	N.D.	N.D.	N.D.	N.D.
0	Pentene	2.50	N.D.	N.D.	N.D.	N.D.
0	Pentane	2.63	N.D.	N.D.	N.D.	N.D.
0	Hexene	3.55	N.D.	N.D.	N.D.	N.D.
0	Hexane	3.60	N.D.	N.D.	N.D.	N.D.
0	Heptene	5.40	N.D.	N.D.	N.D.	N.D.
0	Heptane	5.55	N.D.	N.D.	N.D.	N.D.
0	Octene	8.24	N.D.	N.D.	N.D.	N.D.
0	Octane	8.54	N.D.	N.D.	N.D.	N.D.
0	Decene	12.98	N.D.	N.D.	N.D.	N.D.
0	Decane	13.29	N.D.	N.D.	N.D.	N.D.
0	Dodecene	16.55	N.D.	N.D.	N.D.	N.D.
0	Dodecane	16.84	N.D.	N.D.	N.D.	N.D.
0	Tetradecene	19.43	N.D.	N.D.	N.D.	N.D.
0	Tetradecane	19.71	N.D.	N.D.	N.D.	N.D.
0	Hexadecene	21.92	N.D.	N.D.	N.D.	N.D.
0	Hexadecane	22.20	N.D.	N.D.	N.D.	N.D.
0	Octadecene	24.14	N.D.	N.D.	N.D.	N.D.
0	Octadecane	24.24	N.D.	N.D.	N.D.	N.D.
0	Eicosene	26.15	N.D.	N.D.	N.D.	N.D.
0	Eicosane	26.24	N.D.	N.D.	N.D.	N.D.
Total			6.53	91085.5	1231.1	100.000

Figure B.7: Hydrocarbon GC results from methanol decomposition (30W N_2)

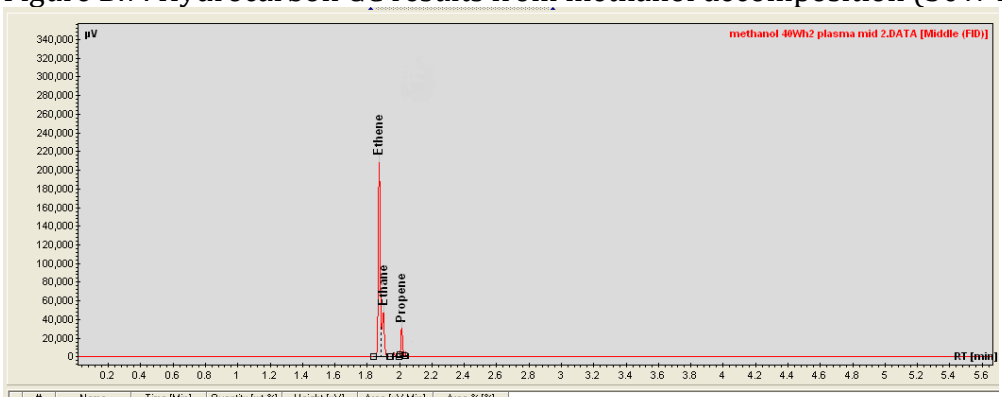

#	Name	Time [Min]	Quantity [wt %]	Height [µV]	Area [µV.Min]	Area % [%]
1	Ethene	1.87	22.54	208307.6	2924.8	31.657
7	Ethane	1.90	0.00	47181.2	779.4	8.436
8	Propene	2.01	0.00	28891.4	352.0	3.810
0	Propane	2.04	N.D.	N.D.	N.D.	N.D.
0	Butene	2.05	N.D.	N.D.	N.D.	N.D.
0	Butane	2.20	N.D.	N.D.	N.D.	N.D.
0	Pentene	2.50	N.D.	N.D.	N.D.	N.D.
0	Pentane	2.63	N.D.	N.D.	N.D.	N.D.
0	Hexene	3.55	N.D.	N.D.	N.D.	N.D.
0	Hexane	3.60	N.D.	N.D.	N.D.	N.D.
0	Heptene	5.40	N.D.	N.D.	N.D.	N.D.
0	Heptane	5.55	N.D.	N.D.	N.D.	N.D.
0	Octene	8.24	N.D.	N.D.	N.D.	N.D.
0	Octane	8.54	N.D.	N.D.	N.D.	N.D.
0	Decene	12.98	N.D.	N.D.	N.D.	N.D.
0	Decane	13.29	N.D.	N.D.	N.D.	N.D.
0	Dodecene	16.55	N.D.	N.D.	N.D.	N.D.
0	Dodecane	16.84	N.D.	N.D.	N.D.	N.D.
0	Tetradecene	19.43	N.D.	N.D.	N.D.	N.D.
0	Tetradecane	19.71	N.D.	N.D.	N.D.	N.D.
0	Hexadecene	21.92	N.D.	N.D.	N.D.	N.D.
0	Hexadecane	22.20	N.D.	N.D.	N.D.	N.D.
0	Octadecene	24.14	N.D.	N.D.	N.D.	N.D.
0	Octadecane	24.24	N.D.	N.D.	N.D.	N.D.
0	Eicosene	26.15	N.D.	N.D.	N.D.	N.D.
0	Eicosane	26.24	N.D.	N.D.	N.D.	N.D.
Total			22.54	638374.3	9239.0	100.000

Figure B.8: Hydrocarbon GC results from methanol decomposition (30W H_2)

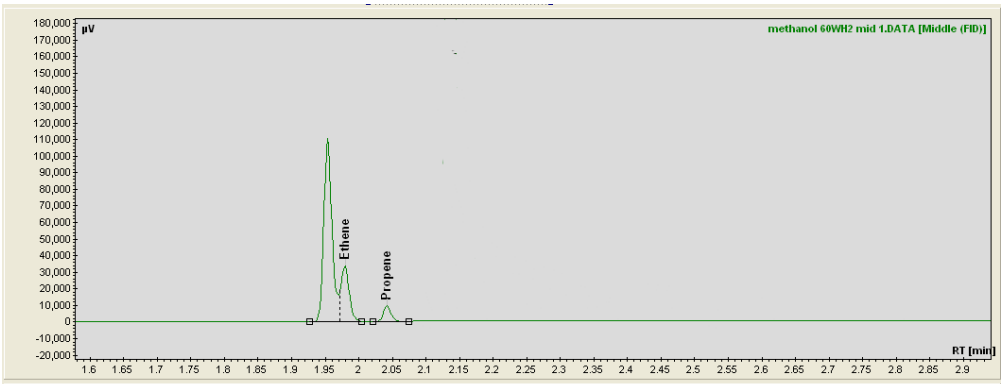

#	Name	Time [Min]	Quantity [wt %]	Height [µV]	Area [µV.Min]	Area % [%]
6	Ethene	1.98	3.47	33756.4	449.9	3.614
0	Ethane	1.99	N.D.	N.D.	N.D.	N.D.
0	Propane	2.04	N.D.	N.D.	N.D.	N.D.
1	Propene	2.04	0.00	9940.0	133.2	1.070
0	Butene	2.18	N.D.	N.D.	N.D.	N.D.
0	Butane	2.20	N.D.	N.D.	N.D.	N.D.
0	Pentene	2.50	N.D.	N.D.	N.D.	N.D.
0	Pentane	2.63	N.D.	N.D.	N.D.	N.D.
0	Hexene	3.55	N.D.	N.D.	N.D.	N.D.
0	Hexane	3.60	N.D.	N.D.	N.D.	N.D.
0	Heptene	5.40	N.D.	N.D.	N.D.	N.D.
0	Heptane	5.55	N.D.	N.D.	N.D.	N.D.
0	Octene	8.24	N.D.	N.D.	N.D.	N.D.
0	Octane	8.54	N.D.	N.D.	N.D.	N.D.
0	Decene	12.98	N.D.	N.D.	N.D.	N.D.
0	Decane	13.29	N.D.	N.D.	N.D.	N.D.
0	Dodecene	16.55	N.D.	N.D.	N.D.	N.D.
0	Dodecane	16.84	N.D.	N.D.	N.D.	N.D.
0	Tetradecene	19.43	N.D.	N.D.	N.D.	N.D.
0	Tetradecane	19.71	N.D.	N.D.	N.D.	N.D.
0	Hexadecene	21.92	N.D.	N.D.	N.D.	N.D.
0	Hexadecane	22.20	N.D.	N.D.	N.D.	N.D.
0	Octadecene	24.14	N.D.	N.D.	N.D.	N.D.
0	Octadecane	24.24	N.D.	N.D.	N.D.	N.D.
0	Eicosene	26.15	N.D.	N.D.	N.D.	N.D.
0	Eicosane	26.24	N.D.	N.D.	N.D.	N.D.
Total			3.47	467307.9	12449.5	100.000

Figure B.9: Hydrocarbon GC results from methanol decomposition (50W H_2)

B.1.2: Glycerol

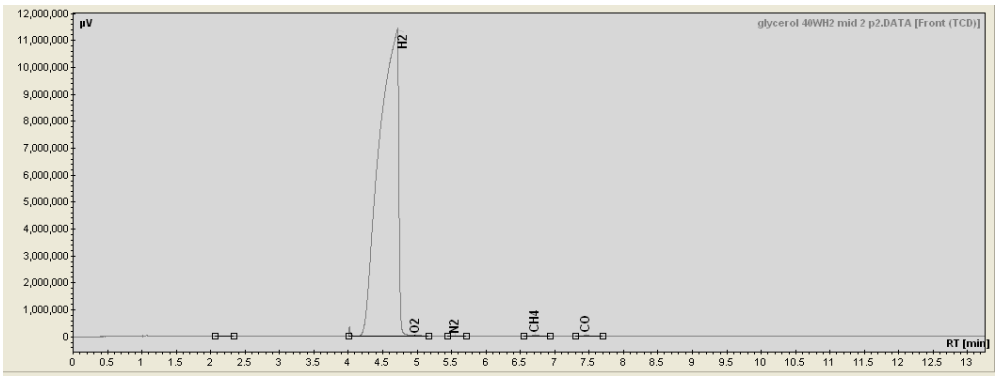

#	Name	Time [Min]	Quantity [%mol]	Height [µV]	Area [µV.Min]	Area % [%]
0	CO2	1.37	N.D.	N.D.	N.D.	N.D.
3	H2	4.72	70.26	11431003.3	3673834.1	99.386
4	O2	4.98	0.36	26535.9	2513.7	0.068
5	N2	5.55	0.34	15952.9	1571.5	0.043
6	CH4	6.72	0.20	35645.3	5065.8	0.137
7	CO	7.46	1.12	29198.2	5124.5	0.139
Total			72.27	11906668.6	3696520.1	100.000

Figure B.10: Permanent gas GC results from glycerol decomposition (10W H_2)

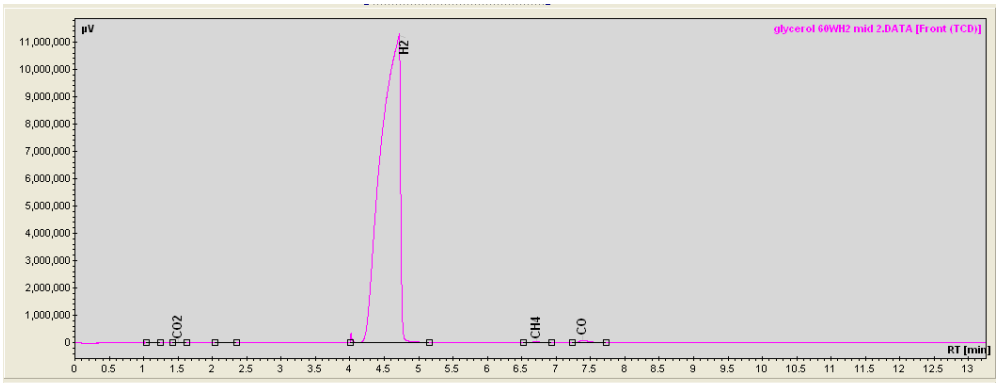

#	Name	Time [Min]	Quantity [%mol]	Height [µV]	Area [µV.Min]	Area % [%]
2	CO2	1.51	0.33	8481.4	706.7	0.019
5	H2	4.72	70.03	11295419.9	3661835.1	99.014
0	O2	5.00	N.D.	N.D.	N.D.	N.D.
0	N2	5.50	N.D.	N.D.	N.D.	N.D.
6	CH4	6.71	0.28	48734.7	6982.6	0.189
7	CO	7.38	3.67	87489.7	16858.0	0.456
Total			74.31	11836823.7	3698300.6	100.000

Figure B.11: Permanent gas GC results from glycerol decomposition (50W H_2)

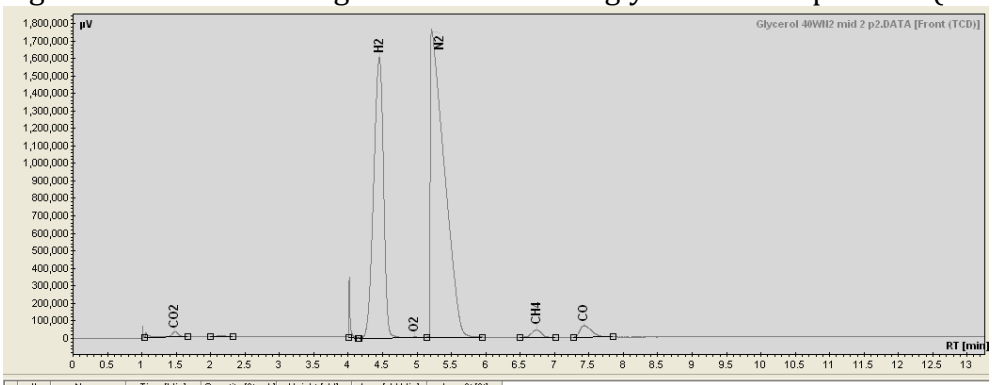

#	Name	Time [Min]	Quantity [%mol]	Height [µV]	Area [µV.Min]	Area % [%]
2	CO2	1.48	2.22	29293.6	2773.4	0.391
5	H2	4.45	5.19	1604204.4	265989.5	37.547
6	O2	4.97	0.06	5530.1	385.8	0.054
7	N2	5.21	88.09	1763573.4	411635.9	58.106
8	CH4	6.74	0.48	42313.2	6573.5	0.928
9	CO	7.43	2.85	65484.7	13090.8	1.848
Total			98.88	3885923.0	708420.9	100.000

Figure B.12: Permanent gas GC results from glycerol decomposition (30W N_2)

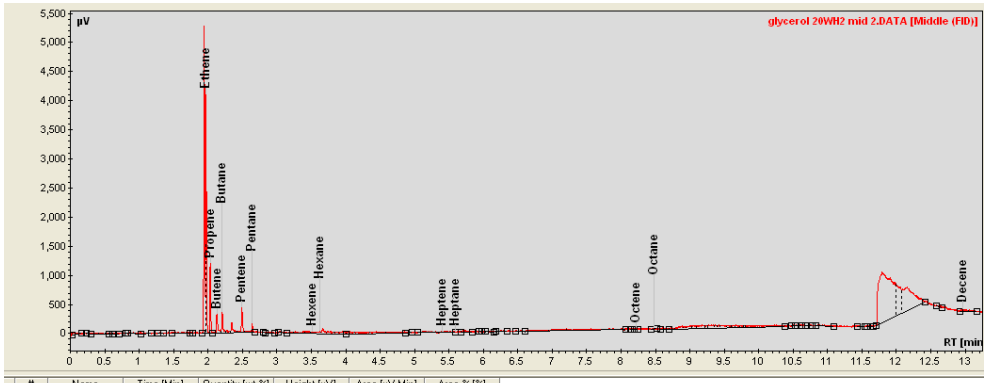

#	Name	Time [Min]	Quantity [wt %]	Height [µV]	Area [µV.Min]	Area % [%]
22	Ethene	1.97	0.05	4092.2	52.0	8.500
0	Ethane	1.99	N.D.	N.D.	N.D.	N.D.
23	Propene	2.03	0.00	1198.3	16.4	2.679
0	Propane	2.04	N.D.	N.D.	N.D.	N.D.
24	Butene	2.13	0.00	327.3	8.3	1.355
25	Butane	2.21	0.00	355.4	6.8	1.118
28	Pentene	2.49	0.00	422.3	9.1	1.493
30	Pentane	2.64	0.00	138.6	2.7	0.442
40	Hexene	3.52	0.00	24.6	1.1	0.187
41	Hexane	3.63	0.00	30.7	1.8	0.300
60	Heptene	5.40	0.00	11.4	0.6	0.094
62	Heptane	5.59	0.00	11.9	0.8	0.133
89	Octene	8.21	0.00	12.0	0.2	0.036
90	Octane	8.49	0.00	3.9	0.2	0.029
124	Decene	12.96	0.00	25.2	0.7	0.108
0	Decane	13.29	N.D.	N.D.	N.D.	N.D.
0	Dodecene	16.55	N.D.	N.D.	N.D.	N.D.
0	Dodecane	16.84	N.D.	N.D.	N.D.	N.D.
0	Tetradecene	19.43	N.D.	N.D.	N.D.	N.D.
0	Tetradecane	19.71	N.D.	N.D.	N.D.	N.D.
0	Hexadecene	21.92	N.D.	N.D.	N.D.	N.D.
0	Hexadecane	22.20	N.D.	N.D.	N.D.	N.D.
0	Octadecene	24.14	N.D.	N.D.	N.D.	N.D.
0	Octadecane	24.24	N.D.	N.D.	N.D.	N.D.
0	Eicosene	26.15	N.D.	N.D.	N.D.	N.D.
0	Eicosane	26.24	N.D.	N.D.	N.D.	N.D.
Total			0.06	16083.3	612.2	100.000

Figure B.13: Hydrocarbon GC results from glycerol decomposition (10W H_2)

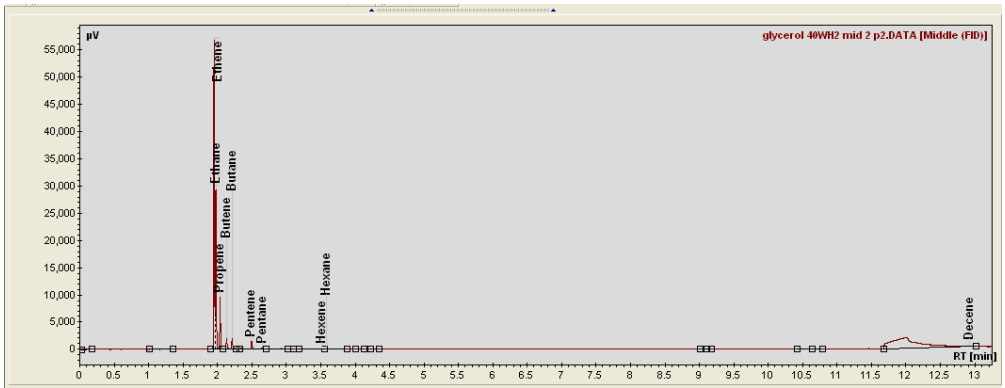

#	Name	Time [Min]	Quantity [wt %]	Height [µV]	Area [µV.Min]	Area % [%]
7	Ethene	1.95	0.54	56672.7	777.8	33.002
8	Ethane	1.98	0.46	29232.9	415.1	17.612
9	Propene	2.04	0.02	9500.0	126.8	5.379
0	Propane	2.04	N.D.	N.D.	N.D.	N.D.
10	Butene	2.13	0.01	1951.6	32.5	1.380
11	Butane	2.21	0.00	1941.8	32.3	1.371
13	Pentene	2.50	0.00	1510.0	29.8	1.265
15	Pentane	2.65	0.00	252.7	5.9	0.248
24	Hexene	3.51	0.00	14.5	0.6	0.026
25	Hexane	3.59	0.00	17.9	0.4	0.016
0	Heptene	5.40	N.D.	N.D.	N.D.	N.D.
0	Heptane	5.55	N.D.	N.D.	N.D.	N.D.
0	Octene	8.24	N.D.	N.D.	N.D.	N.D.
0	Octane	8.54	N.D.	N.D.	N.D.	N.D.
40	Decene	12.93	0.00	43.0	4.0	0.168
0	Decane	13.29	N.D.	N.D.	N.D.	N.D.
0	Dodecene	16.55	N.D.	N.D.	N.D.	N.D.
0	Dodecane	16.84	N.D.	N.D.	N.D.	N.D.
0	Tetradecene	19.43	N.D.	N.D.	N.D.	N.D.
0	Tetradecane	19.71	N.D.	N.D.	N.D.	N.D.
0	Hexadecene	21.92	N.D.	N.D.	N.D.	N.D.
0	Hexadecane	22.20	N.D.	N.D.	N.D.	N.D.
0	Octadecene	24.14	N.D.	N.D.	N.D.	N.D.
0	Octadecane	24.24	N.D.	N.D.	N.D.	N.D.
0	Eicosene	26.15	N.D.	N.D.	N.D.	N.D.
0	Eicosane	26.24	N.D.	N.D.	N.D.	N.D.
Total			1.04	104337.4	2357.0	100.000

Figure B.14: Hydrocarbon GC results from glycerol decomposition (30W H_2)

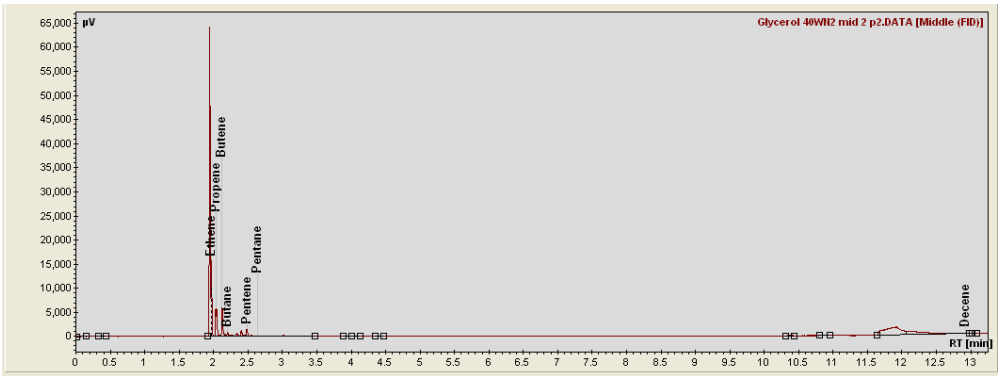

#	Name	Time [Min]	Quantity [wt %]	Height [µV]	Area [µV.Min]	Area % [%]
4	Ethene	1.97	0.14	15735.0	201.2	8.433
0	Ethane	1.99	N.D.	N.D.	N.D.	N.D.
5	Propene	2.03	0.03	5711.1	166.2	6.963
0	Propane	2.04	N.D.	N.D.	N.D.	N.D.
6	Butene	2.13	0.02	5999.6	120.7	5.059
7	Butane	2.20	0.01	946.4	36.6	1.535
10	Pentene	2.48	0.00	1542.0	36.6	1.536
12	Pentane	2.64	0.00	160.5	11.3	0.472
0	Hexene	3.55	N.D.	N.D.	N.D.	N.D.
0	Hexane	3.60	N.D.	N.D.	N.D.	N.D.
0	Heptene	5.40	N.D.	N.D.	N.D.	N.D.
0	Heptane	5.55	N.D.	N.D.	N.D.	N.D.
0	Octene	8.24	N.D.	N.D.	N.D.	N.D.
0	Octane	8.54	N.D.	N.D.	N.D.	N.D.
33	Decene	12.92	0.00	33.4	1.4	0.057
0	Decane	13.29	N.D.	N.D.	N.D.	N.D.
0	Dodecene	16.55	N.D.	N.D.	N.D.	N.D.
0	Dodecane	16.84	N.D.	N.D.	N.D.	N.D.
0	Tetradecene	19.43	N.D.	N.D.	N.D.	N.D.
0	Tetradecane	19.71	N.D.	N.D.	N.D.	N.D.
0	Hexadecene	21.92	N.D.	N.D.	N.D.	N.D.
0	Hexadecane	22.20	N.D.	N.D.	N.D.	N.D.
0	Octadecene	24.14	N.D.	N.D.	N.D.	N.D.
0	Octadecane	24.24	N.D.	N.D.	N.D.	N.D.
0	Eicosene	26.15	N.D.	N.D.	N.D.	N.D.
0	Eicosane	26.24	N.D.	N.D.	N.D.	N.D.
Total			0.20	100329.0	2386.4	100.000

Figure B.15: Hydrocarbon GC results from glycerol decomposition (30W N_2)

B.1.3: Waste glycerol

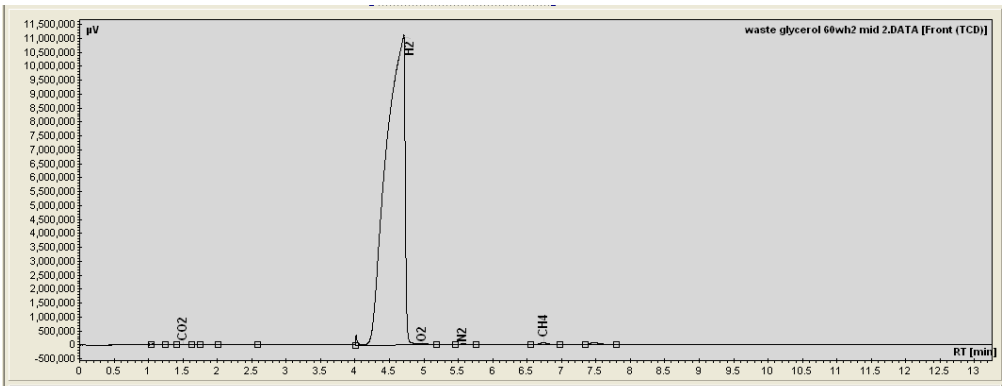

#	Name	Time [Min]	Quantity [%mol]	Height [µV]	Area [µV.Min]	Area % [%]
2	CO2	1.50	0.40	16697.8	1367.4	0.039
7	H2	4.71	67.71	11106216.7	3473573.3	98.550
8	O2	4.98	0.62	45407.6	4312.3	0.122
9	N2	5.57	0.69	32381.3	3215.3	0.091
10	CH4	6.74	0.82	77727.9	11315.9	0.321
0	CO	8.03	N.D.	N.D.	N.D.	N.D.
Total			70.24	11804209.6	3524693.8	100.000

Figure B.16: Permanent gas GC results from glycerol decomposition (50W H_2)

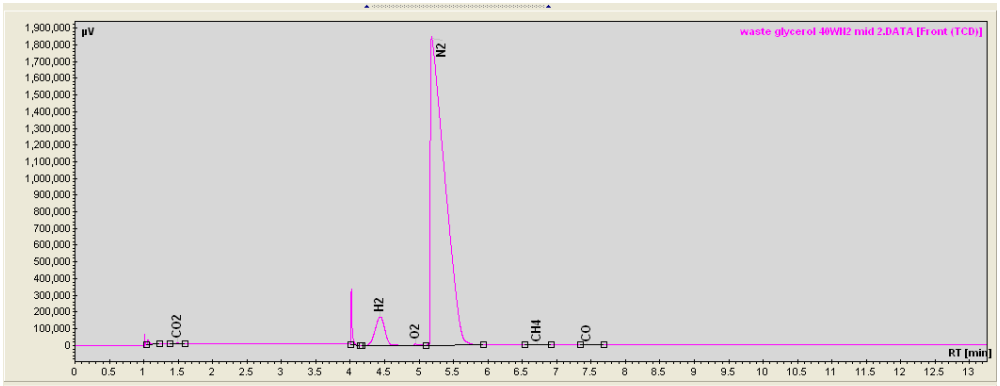

#	Name	Time [Min]	Quantity [%mol]	Height [µV]	Area [µV.Min]	Area % [%]
2	CO2	1.49	0.15	3659.6	312.7	0.065
4	H2	4.44	0.53	171235.2	27839.5	5.820
5	O2	4.95	0.07	7553.3	525.5	0.110
6	N2	5.18	94.59	1848339.8	442004.9	92.400
7	CH4	6.72	0.02	4010.3	601.3	0.126
8	CO	7.44	0.15	4393.4	707.2	0.148
Total			95.52	2400221.3	478359.1	100.000

Figure B.17: Permanent gas GC results from glycerol decomposition (30W N_2)

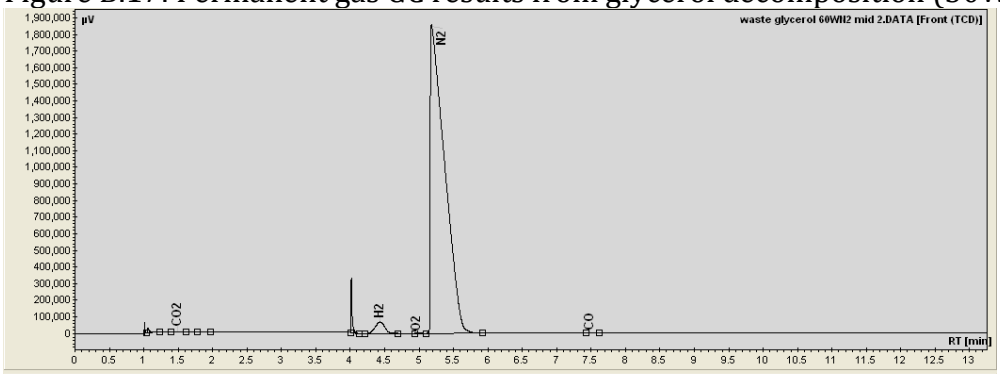

#	Name	Time [Min]	Quantity [%mol]	Height [µV]	Area [µV.Min]	Area % [%]
2	CO2	1.49	0.07	1630.6	137.3	0.030
5	H2	4.44	0.21	69426.3	11065.4	2.391
6	O2	4.96	0.03	4003.2	234.7	0.051
7	N2	5.18	95.22	1856658.0	444972.6	96.148
0	CH4	6.99	N.D.	N.D.	N.D.	N.D.
8	CO	7.48	0.02	1000.7	108.4	0.023
Total			95.56	2292340.7	462799.6	100.000

Figure B.18: Permanent gas GC results from glycerol decomposition (50W N_2)

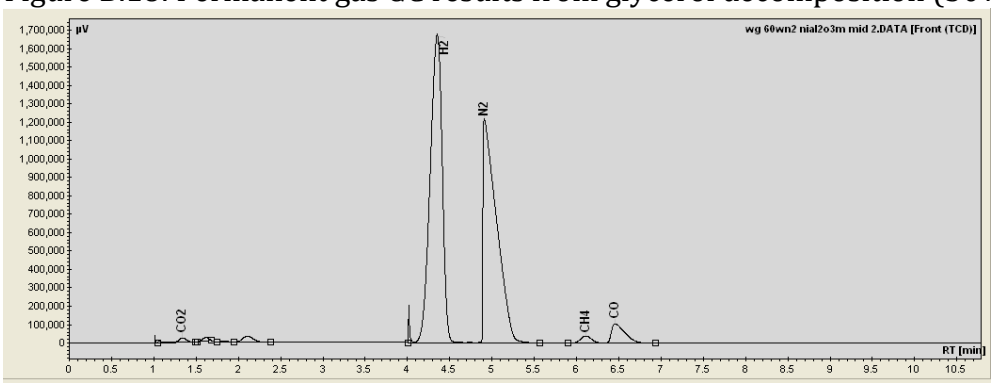

#	Name	Time [Min]	Quantity [mol]	Height [µV]	Area [µV.Min]	Area % [%]
2	CO2	1.34	0.89	23902.5	2407.7	0.443
7	H2	4.35	8.69	1678975.2	278567.8	51.223
9	N2	4.91	76.75	1220647.3	226771.1	41.699
10	CH4	6.11	0.61	39008.0	5905.7	1.086
11	CO	6.46	6.72	105785.8	19391.2	3.566
Total			93.66	3350837.7	543834.6	100.000

Figure B.19: Permanent gas GC results from glycerol decomposition (50W N_2 Ni/Al_2O_3)

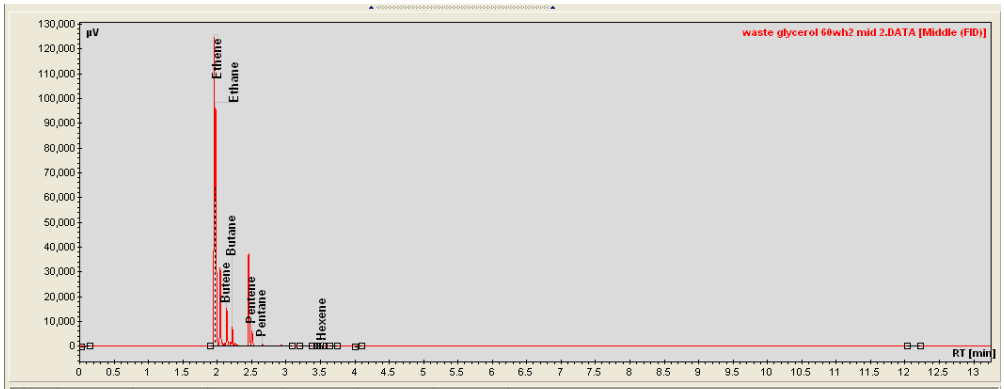

#	Name	Time [Min]	Quantity [wt %]	Height [µV]	Area [µV.Min]	Area % [%]
2	Ethene	1.96	0.63	124574.3	1578.8	29.075
3	Ethane	1.98	0.87	96419.9	2101.5	38.701
0	Propene	2.02	N.D.	N.D.	N.D.	N.D.
0	Propane	2.04	N.D.	N.D.	N.D.	N.D.
5	Butene	2.14	0.03	15502.3	247.8	4.563
6	Butane	2.22	0.23	7598.4	178.2	3.282
9	Pentene	2.51	0.01	6114.0	120.1	2.212
11	Pentane	2.66	0.00	744.6	18.7	0.344
18	Hexene	3.52	0.00	17.5	0.6	0.011
0	Hexane	3.60	N.D.	N.D.	N.D.	N.D.
0	Heptene	5.40	N.D.	N.D.	N.D.	N.D.
0	Heptane	5.55	N.D.	N.D.	N.D.	N.D.
0	Octene	8.24	N.D.	N.D.	N.D.	N.D.
0	Octane	8.54	N.D.	N.D.	N.D.	N.D.
0	Decene	12.98	N.D.	N.D.	N.D.	N.D.
0	Decane	13.29	N.D.	N.D.	N.D.	N.D.
0	Dodecene	16.55	N.D.	N.D.	N.D.	N.D.
0	Dodecane	16.84	N.D.	N.D.	N.D.	N.D.
0	Tetradecene	19.43	N.D.	N.D.	N.D.	N.D.
0	Tetradecane	19.71	N.D.	N.D.	N.D.	N.D.
0	Hexadecene	21.92	N.D.	N.D.	N.D.	N.D.
0	Hexadecane	22.20	N.D.	N.D.	N.D.	N.D.
0	Octadecene	24.14	N.D.	N.D.	N.D.	N.D.
0	Octadecane	24.24	N.D.	N.D.	N.D.	N.D.
0	Eicosene	26.15	N.D.	N.D.	N.D.	N.D.
0	Eicosane	26.24	N.D.	N.D.	N.D.	N.D.
Total			1.78	321928.1	5430.2	100.000

Figure B.20: Hydrocarbon GC results from glycerol decomposition (50W H_2)

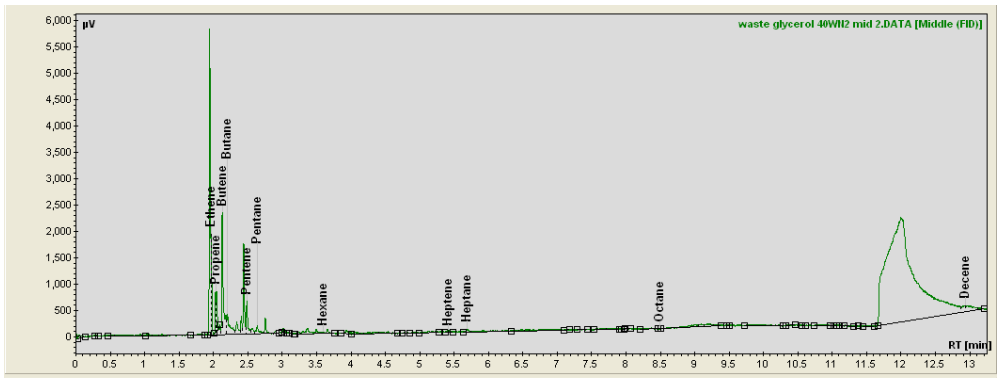

#	Name	Time [Min]	Quantity [wt %]	Height [µV]	Area [µV.Min]	Area % [%]
23	Ethene	1.96	0.03	1911.9	34.1	2.446
0	Ethane	1.99	N.D.	N.D.	N.D.	N.D.
110	Propene	2.03	0.00	779.9	11.4	0.822
0	Propane	2.04	N.D.	N.D.	N.D.	N.D.
24	Butene	2.13	0.01	2310.5	59.4	4.270
25	Butane	2.21	0.00	389.4	18.8	1.353
29	Pentene	2.49	0.00	623.7	16.2	1.160
31	Pentane	2.64	0.00	149.6	6.8	0.486
0	Hexene	3.55	N.D.	N.D.	N.D.	N.D.
40	Hexane	3.60	0.00	22.4	1.0	0.071
57	Heptene	5.42	0.00	34.3	1.4	0.099
58	Heptane	5.70	0.00	45.8	1.9	0.139
0	Octene	8.24	N.D.	N.D.	N.D.	N.D.
82	Octane	8.49	0.00	14.8	0.1	0.008
108	Decene	12.94	0.00	113.0	14.1	1.015
0	Decane	13.29	N.D.	N.D.	N.D.	N.D.
0	Dodecene	16.55	N.D.	N.D.	N.D.	N.D.
0	Dodecane	16.84	N.D.	N.D.	N.D.	N.D.
0	Tetradecene	19.43	N.D.	N.D.	N.D.	N.D.
0	Tetradecane	19.71	N.D.	N.D.	N.D.	N.D.
0	Hexadecene	21.92	N.D.	N.D.	N.D.	N.D.
0	Hexadecane	22.20	N.D.	N.D.	N.D.	N.D.
0	Octadecene	24.14	N.D.	N.D.	N.D.	N.D.
0	Octadecane	24.24	N.D.	N.D.	N.D.	N.D.
0	Eicosene	26.15	N.D.	N.D.	N.D.	N.D.
0	Eicosane	26.24	N.D.	N.D.	N.D.	N.D.
Total			0.05	19775.5	1392.1	100.000

Figure B.21: Hydrocarbon GC results from glycerol decomposition (30W N_2)

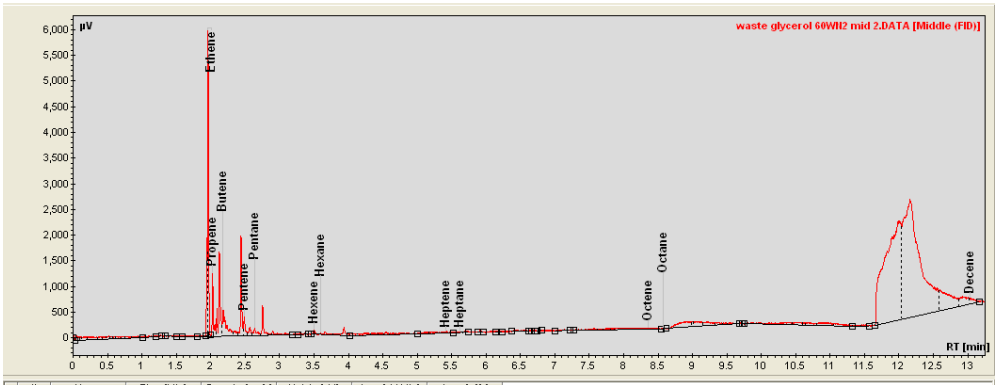

#	Name	Time [Min]	Quantity [wt %]	Height [µV]	Area [µV.Min]	Area % [%]
114	Ethene	1.96	0.09	5925.6	94.8	5.275
0	Ethane	1.99	N.D.	N.D.	N.D.	N.D.
27	Propene	2.03	0.01	1223.5	25.1	1.394
0	Propane	2.04	N.D.	N.D.	N.D.	N.D.
29	Butene	2.18	0.01	506.2	30.9	1.722
0	Butane	2.20	N.D.	N.D.	N.D.	N.D.
32	Pentene	2.49	0.00	356.4	10.5	0.585
34	Pentane	2.64	0.00	142.1	7.3	0.407
43	Hexene	3.50	0.00	77.4	2.0	0.114
44	Hexane	3.59	0.00	24.8	0.9	0.051
63	Heptene	5.42	0.00	28.3	1.4	0.079
65	Heptane	5.62	0.00	15.2	1.0	0.056
84	Octene	8.35	0.00	17.7	2.5	0.138
86	Octane	8.57	0.00	14.0	0.5	0.026
112	Decene	13.03	0.00	114.7	7.8	0.437
0	Decane	13.29	N.D.	N.D.	N.D.	N.D.
0	Dodecene	16.55	N.D.	N.D.	N.D.	N.D.
0	Dodecane	16.84	N.D.	N.D.	N.D.	N.D.
0	Tetradecene	19.43	N.D.	N.D.	N.D.	N.D.
0	Tetradecane	19.71	N.D.	N.D.	N.D.	N.D.
0	Hexadecene	21.92	N.D.	N.D.	N.D.	N.D.
0	Hexadecane	22.20	N.D.	N.D.	N.D.	N.D.
0	Octadecene	24.14	N.D.	N.D.	N.D.	N.D.
0	Octadecane	24.24	N.D.	N.D.	N.D.	N.D.
0	Eicosene	26.15	N.D.	N.D.	N.D.	N.D.
0	Eicosane	26.24	N.D.	N.D.	N.D.	N.D.
Total			0.11	22412.6	1796.6	100.000

Figure B.22: Hydrocarbon GC results from glycerol decomposition (50W N_2)

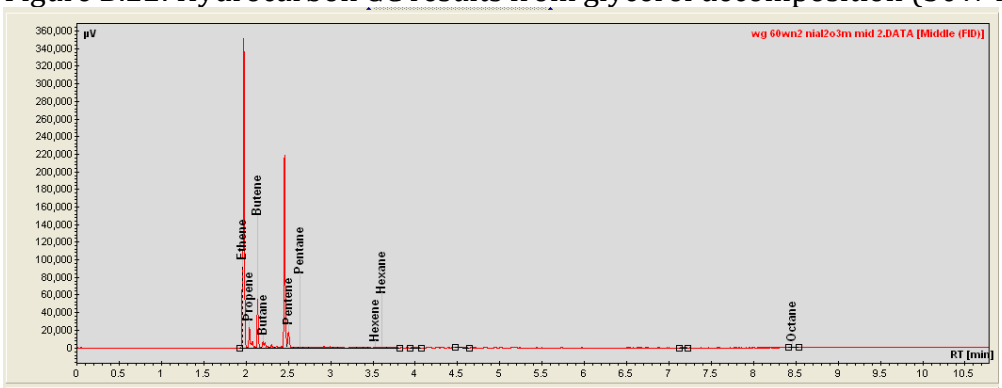

#	Name	Time [Min]	Quantity [wt %]	Height [µV]	Area [µV.Min]	Area % [%]
1	Ethene	1.96	0.74	91572.1	1118.5	9.227
0	Ethane	1.99	N.D.	N.D.	N.D.	N.D.
3	Propene	2.04	0.19	23409.3	536.8	4.429
0	Propane	2.04	N.D.	N.D.	N.D.	N.D.
4	Butene	2.14	0.21	55568.2	836.5	6.901
5	Butane	2.20	0.24	6892.5	255.9	2.111
9	Pentene	2.50	0.03	17774.3	451.6	3.726
11	Pentane	2.64	0.83	442.8	17.3	0.143
22	Hexene	3.53	0.00	114.3	4.4	0.037
23	Hexane	3.60	0.00	129.5	5.1	0.042
0	Heptene	5.40	N.D.	N.D.	N.D.	N.D.
0	Heptane	5.55	N.D.	N.D.	N.D.	N.D.
0	Octene	8.24	N.D.	N.D.	N.D.	N.D.
29	Octane	8.46	0.00	246.9	17.3	0.143
0	Decene	12.98	N.D.	N.D.	N.D.	N.D.
0	Decane	13.29	N.D.	N.D.	N.D.	N.D.
0	Dodecene	16.55	N.D.	N.D.	N.D.	N.D.
0	Dodecane	16.84	N.D.	N.D.	N.D.	N.D.
0	Tetradecene	19.43	N.D.	N.D.	N.D.	N.D.
0	Tetradecane	19.71	N.D.	N.D.	N.D.	N.D.
0	Hexadecene	21.92	N.D.	N.D.	N.D.	N.D.
0	Hexadecane	22.20	N.D.	N.D.	N.D.	N.D.
0	Octadecene	24.14	N.D.	N.D.	N.D.	N.D.
0	Octadecane	24.24	N.D.	N.D.	N.D.	N.D.
0	Eicosene	26.15	N.D.	N.D.	N.D.	N.D.
0	Eicosane	26.24	N.D.	N.D.	N.D.	N.D.
Total			2.25	779607.4	12121.6	100.000

Figure B.23: Hydrocarbon GC results from glycerol decomposition (50W N_2 Ni/Al_2O_3)

B.1.4:Triglycerides

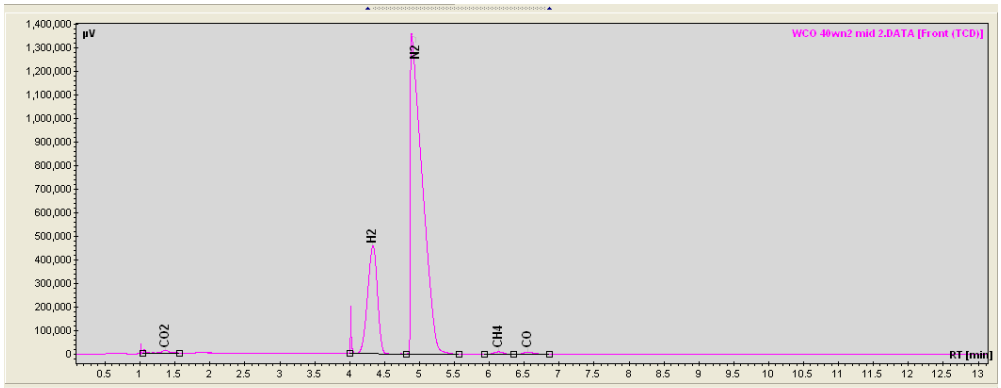

#	Name	Time [Min]	Quantity [mol]	Height [µV]	Area [µV.Min]	Area % [%]
2	CO2	1.36	0.58	12821.4	1571.2	0.451
4	H2	4.33	2.32	458125.6	74346.7	21.327
6	N2	4.89	90.06	1360605.0	266093.7	76.330
7	CH4	6.13	0.15	9823.5	1464.0	0.420
8	CO	6.55	0.59	9648.0	1702.2	0.488
Total			93.70	2070143.4	348611.3	100.000

Figure B.24: Permanent gas GC results from WCO decomposition (50W N_2)

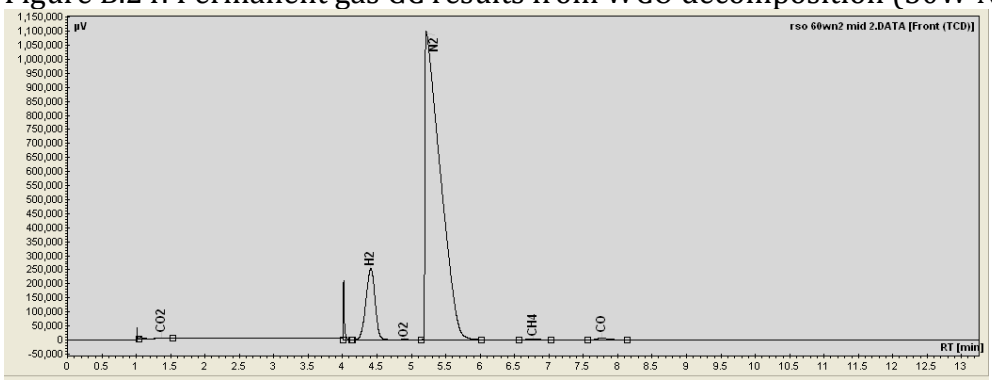

#	Name	Time [Min]	Quantity [%mol]	Height [µV]	Area [µV.Min]	Area % [%]
2	CO2	1.36	0.18	3688.7	499.9	0.153
4	H2	4.41	1.23	254021.0	39314.4	12.062
5	O2	4.90	0.07	3686.9	350.0	0.107
6	N2	5.22	94.76	1098721.7	279992.8	85.903
7	CH4	6.77	0.08	4565.6	798.0	0.245
8	CO	7.77	0.52	6386.4	1503.2	0.461
Total			96.84	1590251.2	325941.9	100.000

Figure B.25: Permanent gas GC results from RSO decomposition (50W N_2)

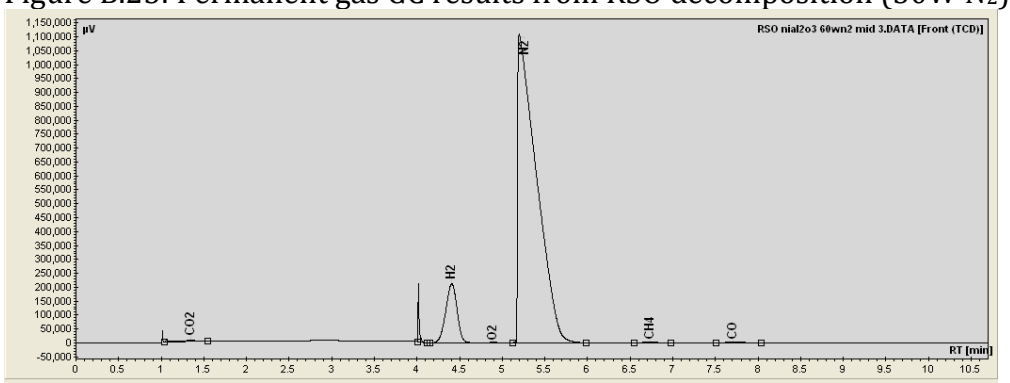

#	Name	Time [Min]	Quantity [%mol]	Height [µV]	Area [µV.Min]	Area % [%]
2	CO2	1.35	0.29	6484.9	797.0	0.249
4	H2	4.41	1.02	212521.2	32853.4	10.262
5	O2	4.90	0.06	3304.7	308.8	0.096
6	N2	5.20	95.08	1109227.4	280946.9	87.756
7	CH4	6.74	0.06	3655.7	624.3	0.195
8	CO	7.71	0.39	5048.0	1133.6	0.354
Total			96.92	1558139.1	320145.3	100.000

Figure B.26: Permanent gas GC results from RSOdecomposition (50W N_2 $BaTiO_3$)

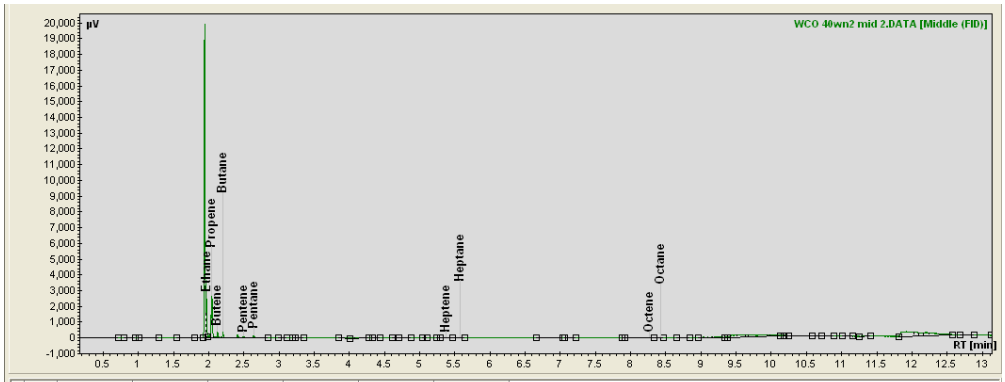

#	Name	Time [Min]	Quantity [wt %]	Height [µV]	Area [µV.Min]	Area % [%]
0	Ethene	1.96	N.D.	N.D.	N.D.	N.D.
195	Ethane	1.97	0.00	2382.7	33.6	1.282
0	Propene	2.04	N.D.	N.D.	N.D.	N.D.
193	Propene	2.04	0.00	2675.9	58.8	2.245
18	Butene	2.13	0.00	349.4	7.0	0.269
19	Butane	2.20	0.00	370.0	7.8	0.298
23	Pentene	2.49	0.00	96.3	2.5	0.096
25	Pentane	2.64	0.00	133.4	3.7	0.140
0	Hexene	3.55	N.D.	N.D.	N.D.	N.D.
0	Hexane	3.60	N.D.	N.D.	N.D.	N.D.
42	Heptene	5.38	0.00	15.7	1.4	0.055
44	Heptane	5.57	0.00	5.8	0.4	0.015
54	Octene	8.27	0.00	16.1	0.9	0.033
56	Octane	8.43	0.00	1.2	0.2	0.009
0	Decene	12.98	N.D.	N.D.	N.D.	N.D.
90	Decane	13.31	0.00	21.5	0.9	0.033
111	Dodecene	16.58	0.00	14.8	0.6	0.022
113	Dodecane	16.73	0.00	6.6	0.2	0.007
138	Tetradecene	19.28	0.00	16.6	0.5	0.020
0	Tetradecane	19.71	N.D.	N.D.	N.D.	N.D.
157	Hexadecene	21.91	0.00	124.6	6.7	0.255
159	Hexadecane	22.15	0.00	98.5	12.3	0.471
174	Octadecene	24.17	0.00	91.1	9.1	0.346
175	Octadecane	24.35	0.00	126.9	8.8	0.335
187	Eicosene	26.18	0.00	245.4	12.6	0.482
188	Eicosane	26.30	0.00	3377.2	197.0	7.516
Total			0.00	51030.7	2620.4	100.000

Figure B.27: Hydrocarbon GC results from WCO decomposition (50W N_2)

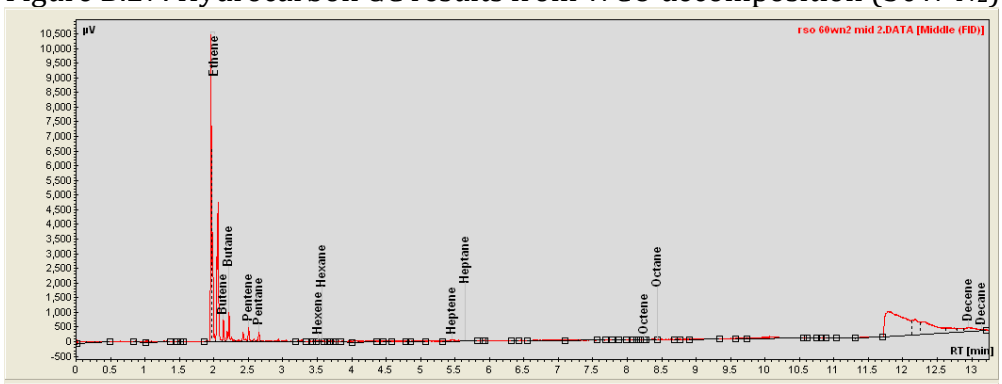

#	Name	Time [Min]	Quantity [wt %]	Height [µV]	Area [µV.Min]	Area % [%]
14	Ethene	1.96	0.94	10451.4	121.3	12.195
0	Ethane	1.99	N.D.	N.D.	N.D.	N.D.
0	Propene	2.02	N.D.	N.D.	N.D.	N.D.
0	Propane	2.04	N.D.	N.D.	N.D.	N.D.
17	Butene	2.14	0.00	734.7	11.7	1.174
18	Butane	2.22	0.00	985.8	25.0	2.513
21	Pentene	2.51	0.00	464.3	9.2	0.926
23	Pentane	2.65	0.00	330.5	7.4	0.740
33	Hexene	3.52	0.00	22.6	0.6	0.065
34	Hexane	3.58	0.00	8.5	0.3	0.031
47	Heptene	5.46	0.00	38.2	5.5	0.557
48	Heptane	5.65	0.00	16.3	0.4	0.045
67	Octene	8.24	0.00	7.2	0.1	0.011
69	Octane	8.44	0.00	10.6	0.3	0.031
97	Decene	12.95	0.00	125.6	20.2	2.034
98	Decane	13.14	0.00	35.8	1.5	0.147
0	Dodecene	16.55	N.D.	N.D.	N.D.	N.D.
0	Dodecane	16.84	N.D.	N.D.	N.D.	N.D.
0	Tetradecene	19.43	N.D.	N.D.	N.D.	N.D.
0	Tetradecane	19.71	N.D.	N.D.	N.D.	N.D.
0	Hexadecene	21.92	N.D.	N.D.	N.D.	N.D.
0	Hexadecane	22.20	N.D.	N.D.	N.D.	N.D.
0	Octadecene	24.14	N.D.	N.D.	N.D.	N.D.
0	Octadecane	24.24	N.D.	N.D.	N.D.	N.D.
0	Eicosene	26.15	N.D.	N.D.	N.D.	N.D.
0	Eicosane	26.24	N.D.	N.D.	N.D.	N.D.
Total			0.94	28744.6	995.1	100.000

Figure B.28: Permanent gas GC results from RSOdecomposition (50W N_2)

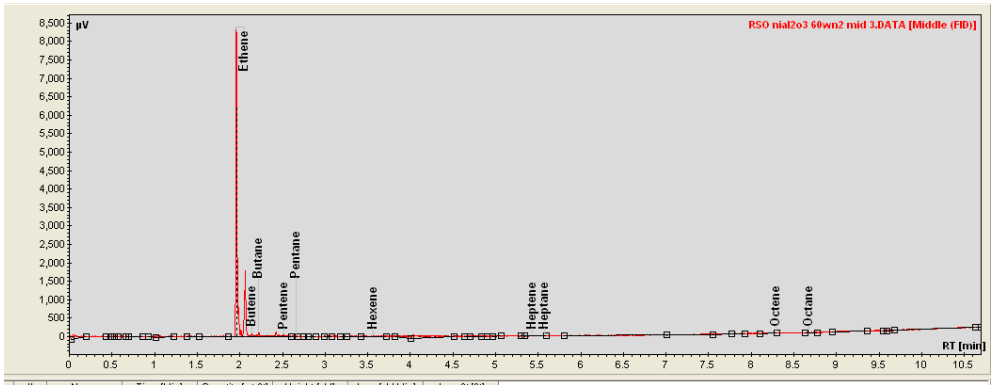

#	Name	Time [Min]	Quantity [wt %]	Height [µV]	Area [µV.Min]	Area % [%]
17	Ethene	1.96	0.69	8309.8	89.1	35.459
0	Ethane	1.99	N.D.	N.D.	N.D.	N.D.
0	Propene	2.02	N.D.	N.D.	N.D.	N.D.
0	Propane	2.04	N.D.	N.D.	N.D.	N.D.
20	Butene	2.14	0.00	64.9	1.7	0.668
21	Butane	2.22	0.00	105.5	3.4	1.370
26	Pentene	2.51	0.00	36.0	0.9	0.348
28	Pentane	2.66	0.00	46.4	1.1	0.451
36	Hexene	3.57	0.00	8.7	0.4	0.168
0	Hexane	3.60	N.D.	N.D.	N.D.	N.D.
52	Heptene	5.44	0.00	13.0	0.9	0.364
53	Heptane	5.58	0.00	16.3	0.5	0.189
75	Octene	8.29	0.00	16.7	0.8	0.308
76	Octane	8.67	0.00	12.2	0.2	0.091
0	Decene	12.98	N.D.	N.D.	N.D.	N.D.
0	Decane	13.29	N.D.	N.D.	N.D.	N.D.
0	Dodecene	16.55	N.D.	N.D.	N.D.	N.D.
0	Dodecane	16.84	N.D.	N.D.	N.D.	N.D.
0	Tetradecene	19.43	N.D.	N.D.	N.D.	N.D.
0	Tetradecane	19.71	N.D.	N.D.	N.D.	N.D.
0	Hexadecene	21.92	N.D.	N.D.	N.D.	N.D.
0	Hexadecane	22.20	N.D.	N.D.	N.D.	N.D.
0	Octadecene	24.14	N.D.	N.D.	N.D.	N.D.
0	Octadecane	24.24	N.D.	N.D.	N.D.	N.D.
0	Eicosene	26.15	N.D.	N.D.	N.D.	N.D.
0	Eicosane	26.24	N.D.	N.D.	N.D.	N.D.
Total			0.69	17995.3	251.4	100.000

Figure B.29: Hydrocarbon GC results from RSOdecomposition (50W N_2 $BaTiO_3$)

B.1.5: Glucose

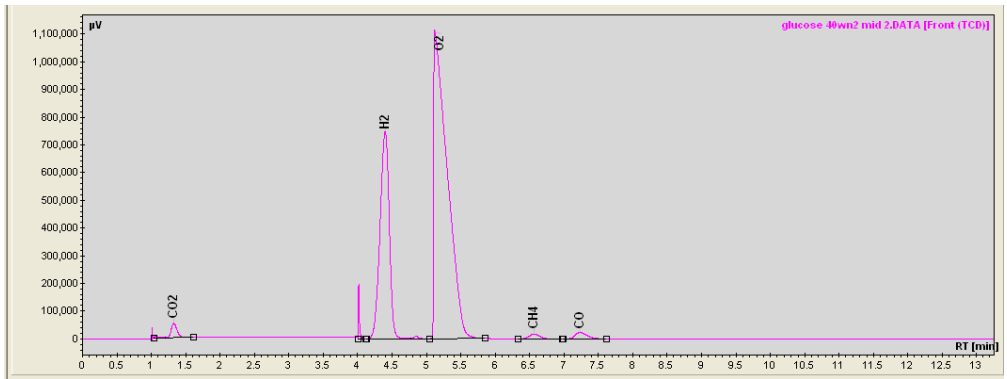

#	Name	Time [Min]	Quantity [%mol]	Height [µV]	Area [µV.Min]	Area % [%]
2	CO2	1.33	1.94	52188.1	5264.3	1.364
4	H2	4.40	3.64	749396.3	116578.6	30.214
6	O2	5.12	47.47	1113218.2	252482.2	65.437
0	N2	5.52	N.D.	N.D.	N.D.	N.D.
7	CH4	6.57	0.30	17152.1	2890.7	0.749
8	CO	7.23	1.61	23275.3	4649.5	1.205
Total			54.95	2169715.4	385842.6	100.000

Figure B.30: Permanent gas GC results from glucose decomposition (30W N_2)

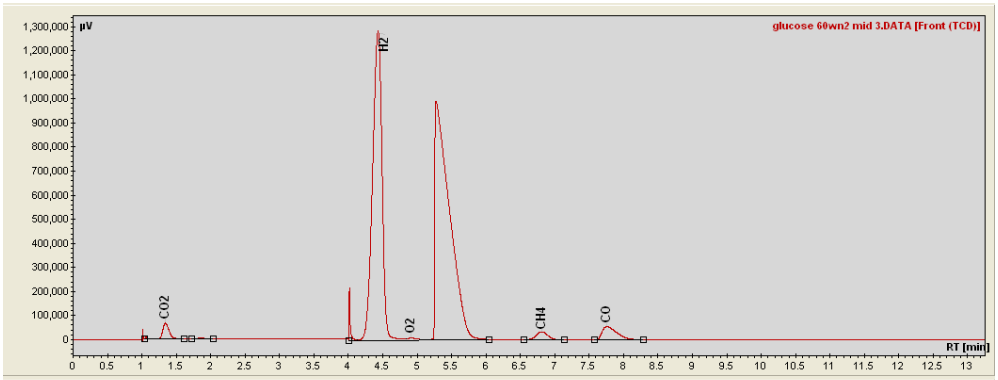

#	Name	Time [Min]	Quantity [%mol]	Height [µV]	Area [µV.Min]	Area % [%]
2	CO2	1.34	2.47	64749.0	6709.2	1.404
5	H2	4.43	6.35	1284198.9	203684.1	42.615
6	O2	4.92	0.24	9691.4	1294.2	0.271
0	N2	5.52	N.D.	N.D.	N.D.	N.D.
8	CH4	6.81	0.63	32531.2	6070.8	1.270
9	CO	7.76	4.67	54526.0	13484.0	2.821
Total			14.37	2665277.7	477965.6	100.000

Figure B.31: Permanent gas GC results from glucose decomposition (50W N_2)

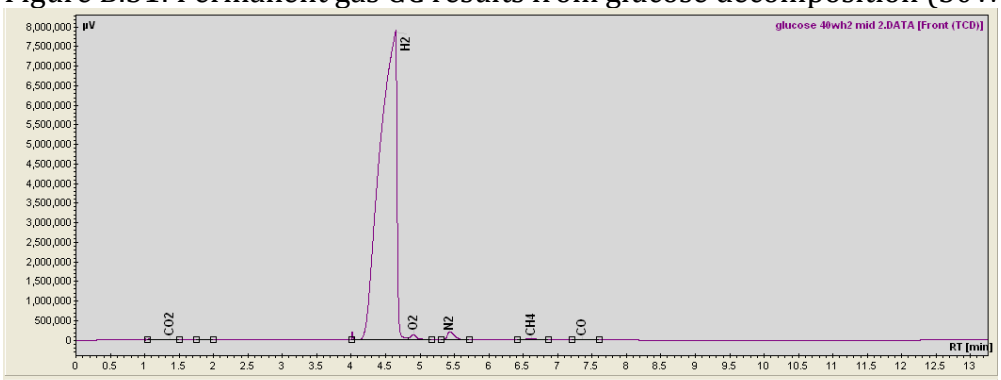

#	Name	Time [Min]	Quantity [%mol]	Height [µV]	Area [µV.Min]	Area % [%]
2	CO2	1.37	0.31	8045.9	854.7	0.037
5	H2	4.65	69.92	7899435.5	2242298.6	97.709
6	O2	4.91	2.52	129155.3	13419.4	0.585
7	N2	5.43	8.09	200016.0	23917.5	1.042
8	CH4	6.61	0.69	40460.2	6668.9	0.291
9	CO	7.37	1.02	16852.7	2939.4	0.128
Total			82.56	8534320.6	2294883.4	100.000

Figure B.32: Permanent gas GC results from glucose decomposition (30W H_2)

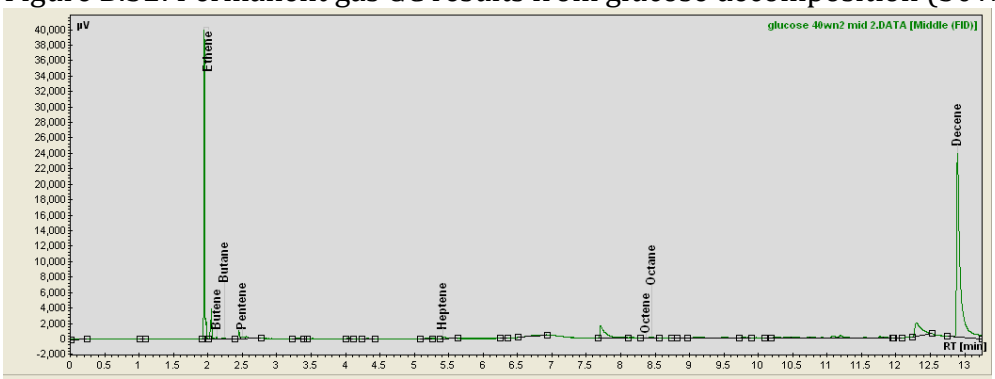

#	Name	Time [Min]	Quantity [wt %]	Height [µV]	Area [µV.Min]	Area % [%]
4	Ethene	1.95	4.64	39895.3	602.7	22.119
0	Ethane	1.99	N.D.	N.D.	N.D.	N.D.
0	Propene	2.02	N.D.	N.D.	N.D.	N.D.
0	Propane	2.04	N.D.	N.D.	N.D.	N.D.
6	Butene	2.13	0.00	221.3	3.8	0.141
7	Butane	2.24	0.00	145.7	5.3	0.193
10	Pentene	2.50	0.00	240.5	12.4	0.455
0	Pentane	2.63	N.D.	N.D.	N.D.	N.D.
0	Hexene	3.55	N.D.	N.D.	N.D.	N.D.
0	Hexane	3.60	N.D.	N.D.	N.D.	N.D.
17	Heptene	5.42	0.00	252.9	15.6	0.572
0	Heptane	5.55	N.D.	N.D.	N.D.	N.D.
21	Octene	8.37	0.00	24.8	1.3	0.046
22	Octane	8.45	0.00	55.4	4.9	0.178
46	Decene	12.90	0.00	23720.7	1428.1	52.415
0	Decane	13.29	N.D.	N.D.	N.D.	N.D.
0	Dodecene	16.55	N.D.	N.D.	N.D.	N.D.
0	Dodecane	16.84	N.D.	N.D.	N.D.	N.D.
0	Tetradecene	19.43	N.D.	N.D.	N.D.	N.D.
0	Tetradecane	19.71	N.D.	N.D.	N.D.	N.D.
0	Hexadecene	21.92	N.D.	N.D.	N.D.	N.D.
0	Hexadecane	22.20	N.D.	N.D.	N.D.	N.D.
0	Octadecene	24.14	N.D.	N.D.	N.D.	N.D.
0	Octadecane	24.24	N.D.	N.D.	N.D.	N.D.
0	Eicosene	26.15	N.D.	N.D.	N.D.	N.D.
0	Eicosane	26.24	N.D.	N.D.	N.D.	N.D.
Total			4.64	75470.5	2724.6	100.000

Figure B.33: Hydrocarbon GC results from glucose decomposition (30W N_2)

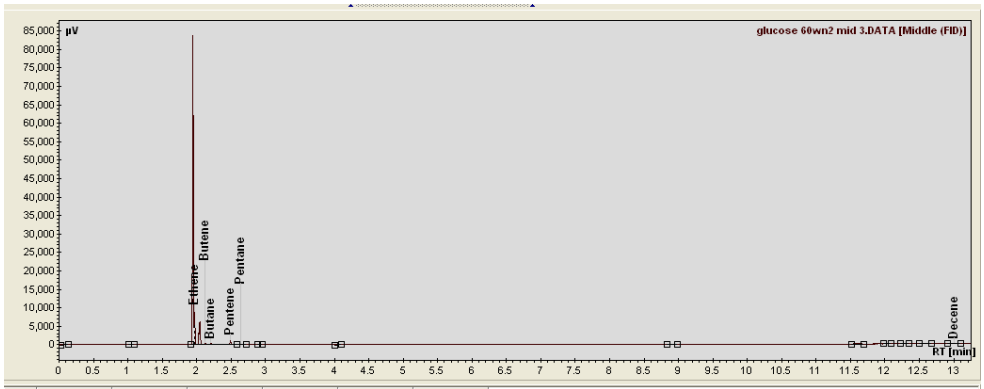

#	Name	Time [Min]	Quantity [wt %]	Height [µV]	Area [µV.Min]	Area % [%]
4	Ethene	1.97	0.86	8726.9	111.7	7.415
0	Ethane	1.99	N.D.	N.D.	N.D.	N.D.
0	Propene	2.02	N.D.	N.D.	N.D.	N.D.
0	Propane	2.04	N.D.	N.D.	N.D.	N.D.
6	Butene	2.13	0.00	348.2	5.6	0.371
7	Butane	2.20	0.00	404.3	6.9	0.456
11	Pentene	2.49	0.00	1134.8	20.7	1.371
13	Pentane	2.64	0.00	48.4	1.5	0.097
0	Hexene	3.55	N.D.	N.D.	N.D.	N.D.
0	Hexane	3.60	N.D.	N.D.	N.D.	N.D.
0	Heptene	5.40	N.D.	N.D.	N.D.	N.D.
0	Heptane	5.55	N.D.	N.D.	N.D.	N.D.
0	Octene	8.24	N.D.	N.D.	N.D.	N.D.
0	Octane	8.54	N.D.	N.D.	N.D.	N.D.
21	Decene	13.00	0.00	60.7	5.3	0.354
0	Decane	13.29	N.D.	N.D.	N.D.	N.D.
0	Dodecene	16.55	N.D.	N.D.	N.D.	N.D.
0	Dodecane	16.84	N.D.	N.D.	N.D.	N.D.
0	Tetradecene	19.43	N.D.	N.D.	N.D.	N.D.
0	Tetradecane	19.71	N.D.	N.D.	N.D.	N.D.
0	Hexadecene	21.92	N.D.	N.D.	N.D.	N.D.
0	Hexadecane	22.20	N.D.	N.D.	N.D.	N.D.
0	Octadecene	24.14	N.D.	N.D.	N.D.	N.D.
0	Octadecane	24.24	N.D.	N.D.	N.D.	N.D.
0	Eicosene	26.15	N.D.	N.D.	N.D.	N.D.
0	Eicosane	26.24	N.D.	N.D.	N.D.	N.D.
Total			0.86	101655.3	1506.2	100.000

Figure B.34: Hydrocarbon GC results from glucose decomposition (50W N_2)

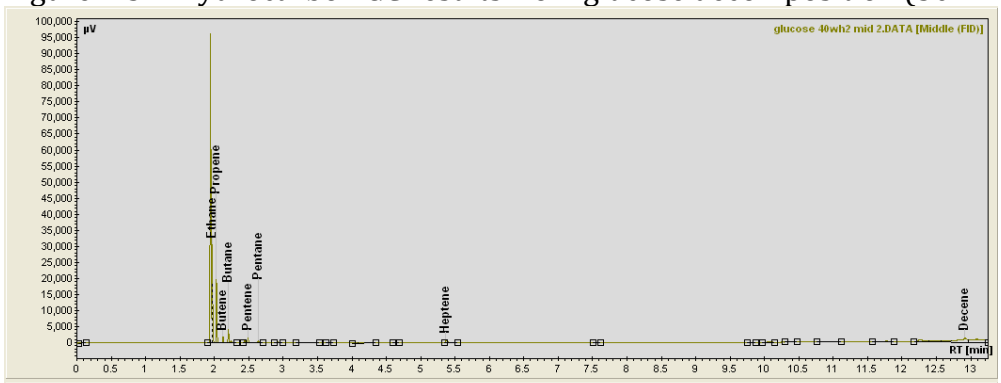

#	Name	Time [Min]	Quantity [wt %]	Height [µV]	Area [µV.Min]	Area % [%]
0	Ethene	1.96	N.D.	N.D.	N.D.	N.D.
2	Ethane	1.97	0.09	30460.5	351.5	22.776
3	Propene	2.03	0.09	19680.7	258.8	16.771
0	Propane	2.04	N.D.	N.D.	N.D.	N.D.
4	Butene	2.12	0.00	1991.9	32.4	2.096
5	Butane	2.20	0.01	4291.0	63.8	4.136
8	Pentene	2.49	0.00	1666.3	29.5	1.910
10	Pentane	2.64	0.00	774.0	14.5	0.942
0	Hexene	3.55	N.D.	N.D.	N.D.	N.D.
0	Hexane	3.60	N.D.	N.D.	N.D.	N.D.
22	Heptene	5.37	0.00	929.8	38.1	2.469
0	Heptane	5.55	N.D.	N.D.	N.D.	N.D.
0	Octene	8.24	N.D.	N.D.	N.D.	N.D.
0	Octane	8.54	N.D.	N.D.	N.D.	N.D.
35	Decene	12.92	0.00	1361.4	192.1	12.449
0	Decane	13.29	N.D.	N.D.	N.D.	N.D.
0	Dodecene	16.55	N.D.	N.D.	N.D.	N.D.
0	Dodecane	16.84	N.D.	N.D.	N.D.	N.D.
0	Tetradecene	19.43	N.D.	N.D.	N.D.	N.D.
0	Tetradecane	19.71	N.D.	N.D.	N.D.	N.D.
0	Hexadecene	21.92	N.D.	N.D.	N.D.	N.D.
0	Hexadecane	22.20	N.D.	N.D.	N.D.	N.D.
0	Octadecene	24.14	N.D.	N.D.	N.D.	N.D.
0	Octadecane	24.24	N.D.	N.D.	N.D.	N.D.
0	Eicosene	26.15	N.D.	N.D.	N.D.	N.D.
0	Eicosane	26.24	N.D.	N.D.	N.D.	N.D.
Total			0.19	66855.1	1543.2	100.000

Figure B.35: Hydrocarbon GC results from glucose decomposition (30W H_2)

B.1.6: Cellulose

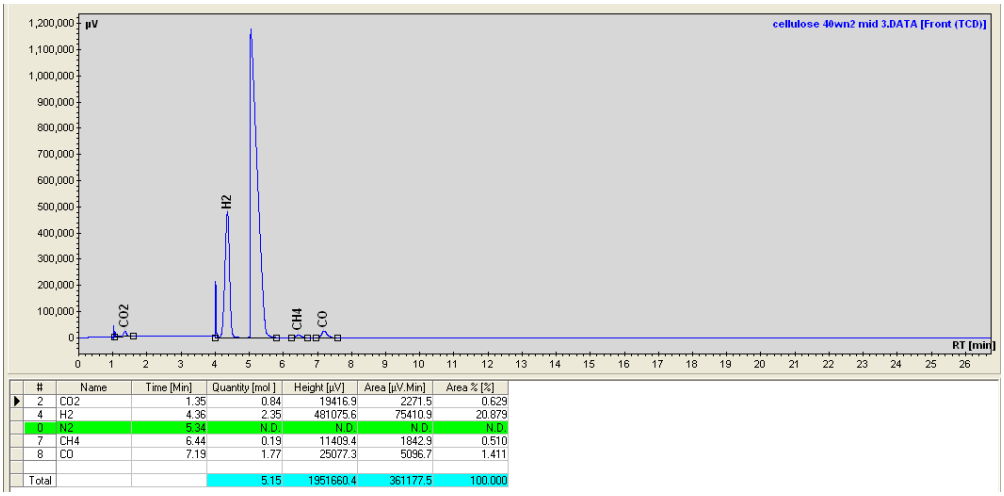

#	Name	Time [Min]	Quantity [mol]	Height [µV]	Area [µV.Min]	Area % [%]
2	CO2	1.35	0.84	19416.9	2271.5	0.629
4	H2	4.36	2.35	481075.6	75410.9	20.879
0	N2	5.34	N.D.	N.D.	N.D.	N.D.
7	CH4	6.44	0.19	11409.4	1842.9	0.510
8	CO	7.19	1.77	25077.3	5096.7	1.411
Total			5.15	1951660.4	361177.5	100.000

Figure B.36: Permanent gas GC results from cellulose decomposition (30W N_2)

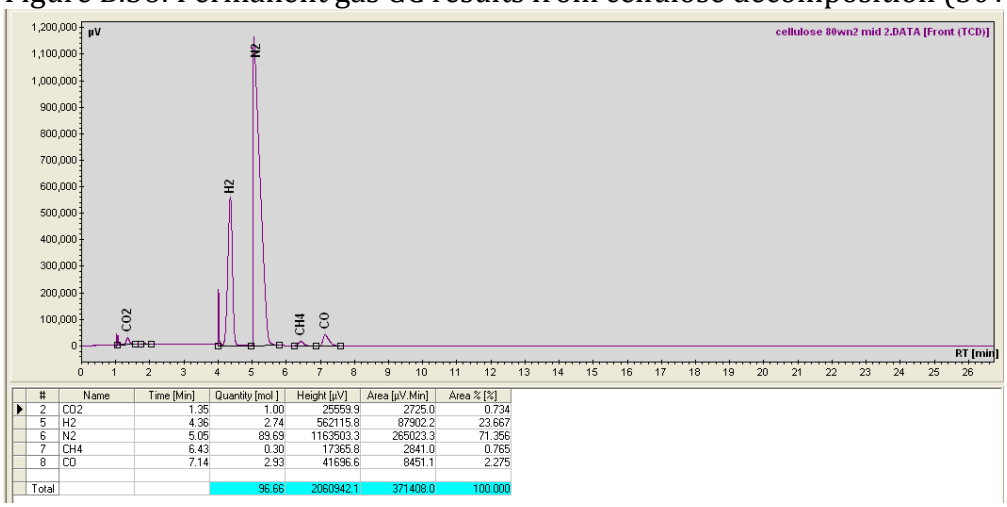

#	Name	Time [Min]	Quantity [mol]	Height [µV]	Area [µV.Min]	Area % [%]
2	CO2	1.35	1.00	25559.9	2725.0	0.734
5	H2	4.36	2.74	562115.8	87902.2	23.687
6	N2	5.05	89.69	1163503.3	265023.3	71.356
7	CH4	6.43	0.30	17365.8	2841.0	0.765
8	CO	7.14	2.93	41696.6	8451.1	2.275
Total			96.66	2060942.1	371408.0	100.000

Figure B.37: Permanent gas GC results from cellulose decomposition (70W N_2)

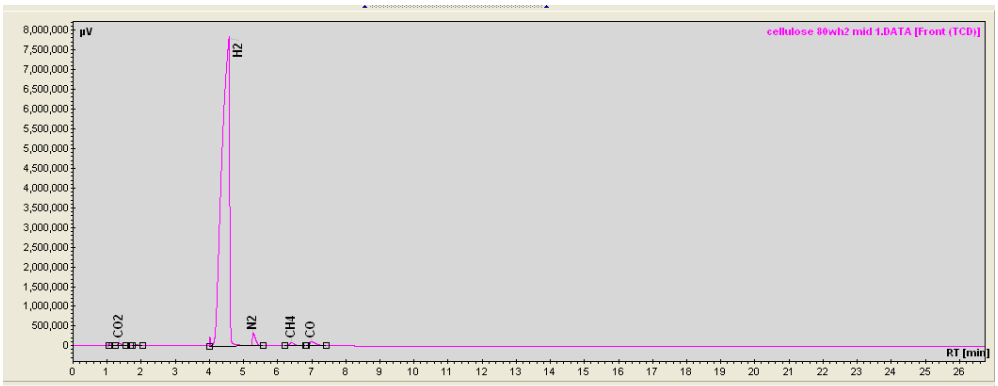

#	Name	Time [Min]	Quantity [mol]	Height [µV]	Area [µV.Min]	Area % [%]
2	CO2	1.35	2.55	67961.5	6918.7	0.324
6	H2	4.58	64.02	7823759.1	2053319.3	96.008
7	N2	5.28	11.78	317117.3	34798.5	1.627
8	CH4	6.41	1.30	77508.9	12483.4	0.584
9	CO	6.99	7.79	110020.7	22485.6	1.051
Total			87.44	8738971.6	2138685.5	100.000

Figure B.38: Permanent gas GC results from cellulose decomposition (70W H_2)

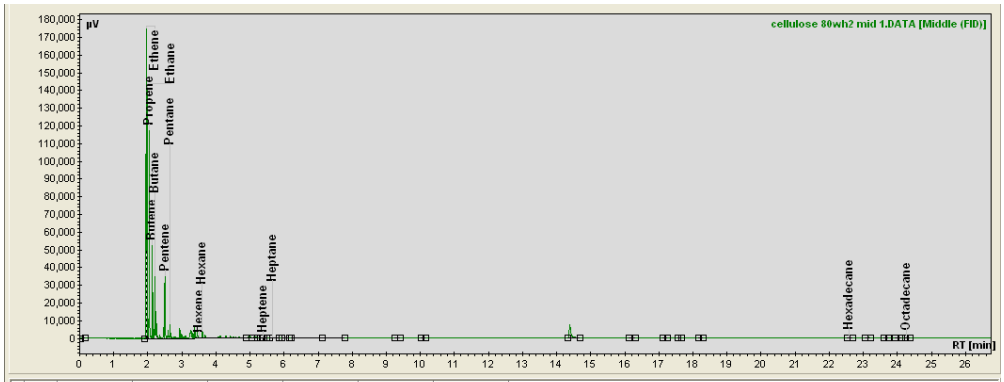

#	Name	Time [Min]	Quantity [wt %]	Height [µV]	Area [µV.Min]	Area % [%]
2	Ethene	1.95	1.36	174568.1	2423.7	21.559
3	Ethane	1.98	0.90	140274.1	2232.1	19.855
4	Propene	2.04	0.40	117312.7	1710.4	15.214
0	Propane	2.04	N.D.	N.D.	N.D.	N.D.
5	Butene	2.13	0.20	52564.1	762.3	6.781
6	Butane	2.21	0.30	34874.0	720.2	6.406
11	Pentene	2.50	0.05	34569.9	754.2	6.709
13	Pentane	2.65	0.86	7817.0	140.5	1.249
24	Hexene	3.52	0.00	366.7	13.2	0.118
25	Hexane	3.60	0.02	3749.5	101.5	0.903
46	Heptene	5.39	0.00	158.6	5.1	0.045
48	Heptane	5.65	0.00	425.4	20.8	0.185
0	Octene	8.24	N.D.	N.D.	N.D.	N.D.
0	Octane	8.54	N.D.	N.D.	N.D.	N.D.
0	Decene	12.98	N.D.	N.D.	N.D.	N.D.
0	Decane	13.29	N.D.	N.D.	N.D.	N.D.
0	Dodecene	16.55	N.D.	N.D.	N.D.	N.D.
0	Dodecane	16.84	N.D.	N.D.	N.D.	N.D.
0	Tetradecene	19.43	N.D.	N.D.	N.D.	N.D.
0	Tetradecane	19.71	N.D.	N.D.	N.D.	N.D.
0	Hexadecene	21.92	N.D.	N.D.	N.D.	N.D.
74	Hexadecane	22.59	0.00	82.8	4.6	0.041
0	Octadecene	24.14	N.D.	N.D.	N.D.	N.D.
78	Octadecane	24.26	0.00	52.4	4.1	0.036
0	Eicosene	26.15	N.D.	N.D.	N.D.	N.D.
0	Eicosane	26.24	N.D.	N.D.	N.D.	N.D.
	Total		4.09	634154.1	11242.2	100.000

Figure B.39: Hydrocarbon GC results from cellulose decomposition (70W H_2)

B.2: GC liquid analysis

B.2.1: Methanol

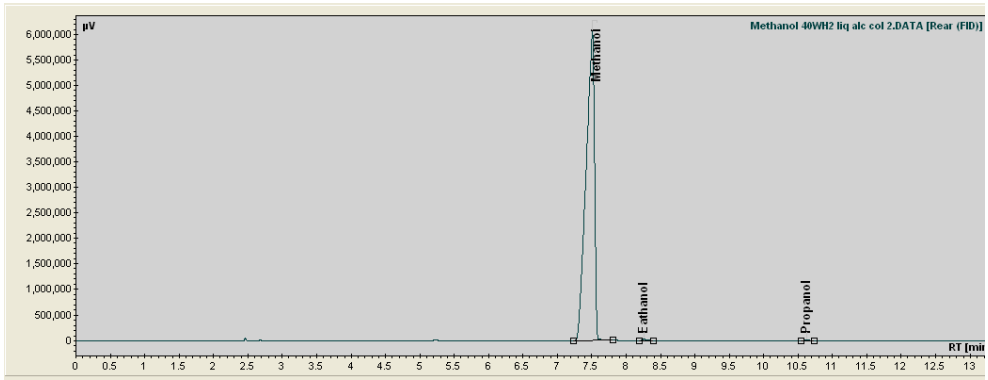

#	Name	Time [Min]	Quantity [wt%]	Height [µV]	Area [µV.Min]	Area % [%]
1	Methanol	7.51	131.89	6065668.4	855906.4	99.835
2	Ethanol	8.26	0.13	24948.9	1282.6	0.150
3	Propanol	10.63	0.01	2471.3	129.7	0.015
0	Butanol	13.12	N.D.	N.D.	N.D.	N.D.
0	Pentanol	15.04	N.D.	N.D.	N.D.	N.D.
0	Hexanol	16.69	N.D.	N.D.	N.D.	N.D.
0	Heptanol	18.18	N.D.	N.D.	N.D.	N.D.
0	Octanol	19.55	N.D.	N.D.	N.D.	N.D.
0	Nonanol	20.83	N.D.	N.D.	N.D.	N.D.
0	Decanol	22.03	N.D.	N.D.	N.D.	N.D.
	Total		132.03	6093088.7	857318.7	100.000

Figure B.40: Methanol liquid GC results (alcohol column)(30W H_2)

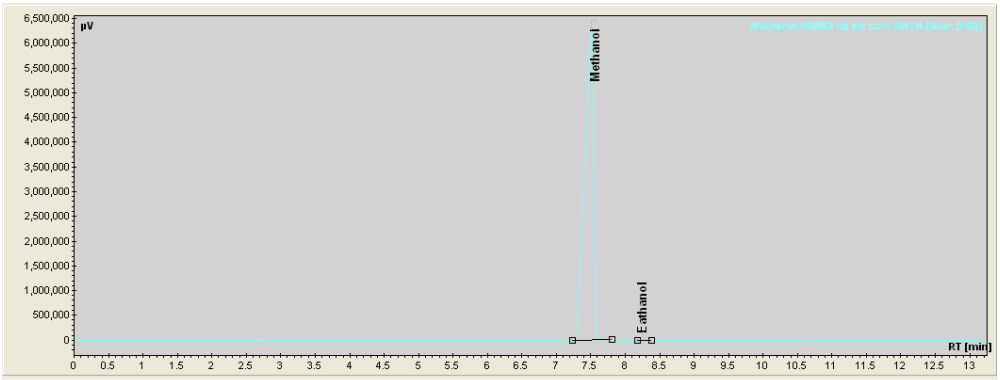

#	Name	Time [Min]	Quantity [wt%]	Height [µV]	Area [µV.Min]	Area % [%]
1	Methanol	7.51	144.53	6245679.4	937916.1	99.919
2	Eathanol	8.26	0.08	14592.5	758.8	0.081
0	Propanol	10.88	N.D.	N.D.	N.D.	N.D.
0	Butanol	13.12	N.D.	N.D.	N.D.	N.D.
0	Pentanol	15.04	N.D.	N.D.	N.D.	N.D.
0	Hexanol	16.69	N.D.	N.D.	N.D.	N.D.
0	Heptanol	18.18	N.D.	N.D.	N.D.	N.D.
0	Octanol	19.55	N.D.	N.D.	N.D.	N.D.
0	Nonanol	20.83	N.D.	N.D.	N.D.	N.D.
0	Decanol	22.03	N.D.	N.D.	N.D.	N.D.
Total			144.61	6260271.9	938674.8	100.000

Figure B.41: Methanol liquid GC results (alcohol column)(30W N_2)

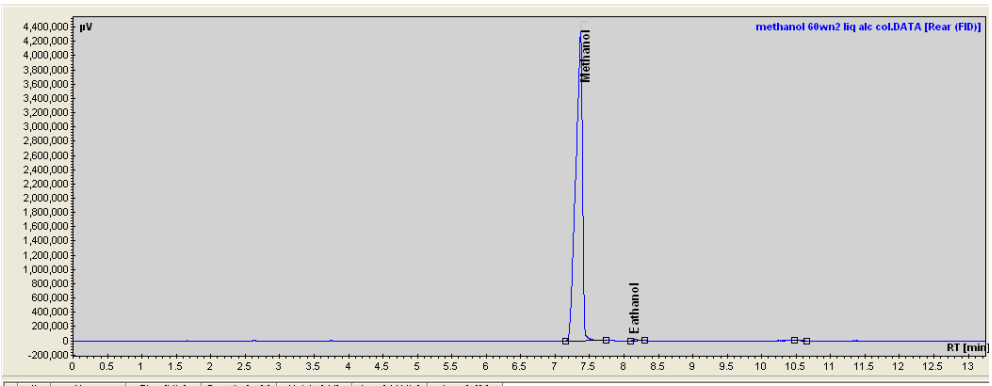

#	Name	Time [Min]	Quantity [wt%]	Height [µV]	Area [µV.Min]	Area % [%]
1	Methanol	7.37	75.50	4329118.2	489964.6	99.739
2	Eathanol	8.17	0.12	21957.8	1166.8	0.238
0	Propanol	10.88	N.D.	N.D.	N.D.	N.D.
0	Butanol	13.12	N.D.	N.D.	N.D.	N.D.
0	Pentanol	15.04	N.D.	N.D.	N.D.	N.D.
0	Hexanol	16.69	N.D.	N.D.	N.D.	N.D.
0	Heptanol	18.18	N.D.	N.D.	N.D.	N.D.
0	Octanol	19.55	N.D.	N.D.	N.D.	N.D.
0	Nonanol	20.83	N.D.	N.D.	N.D.	N.D.
0	Decanol	22.03	N.D.	N.D.	N.D.	N.D.
Total			75.62	4353286.0	491245.6	100.000

Figure B.42: Methanol liquid GC results (alcohol column)(50W N_2)

B.2.2: Waste Glycerol

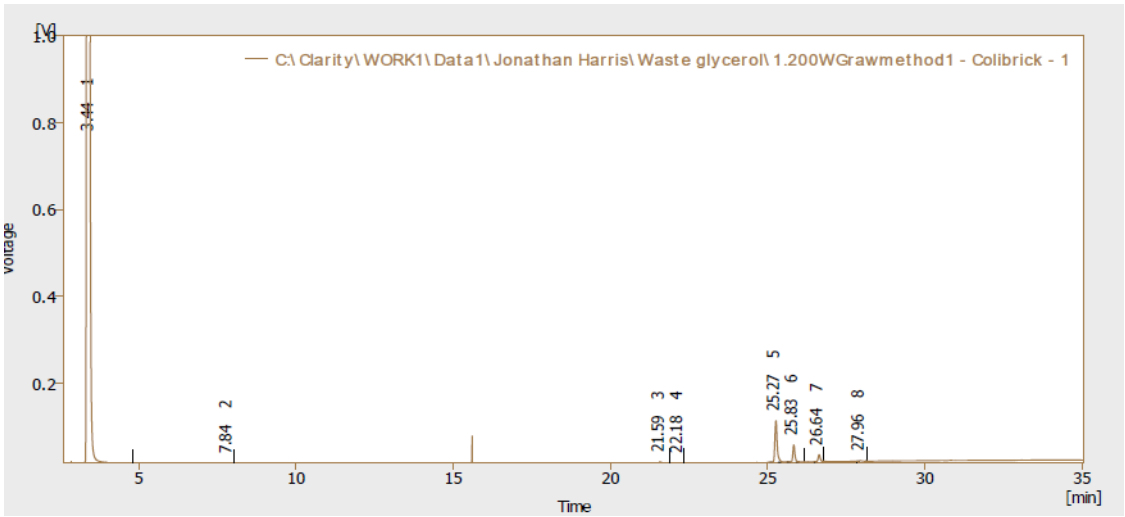

Figure B.43: Raw Waste glycerol GC analysis

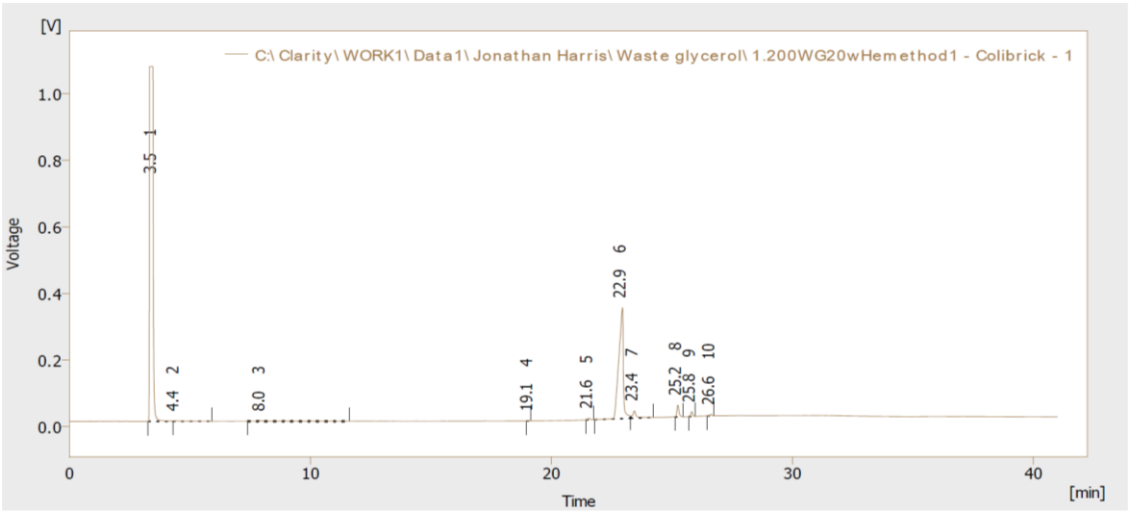

Figure B.44: 50W N_2 Waste glycerol GC analysis

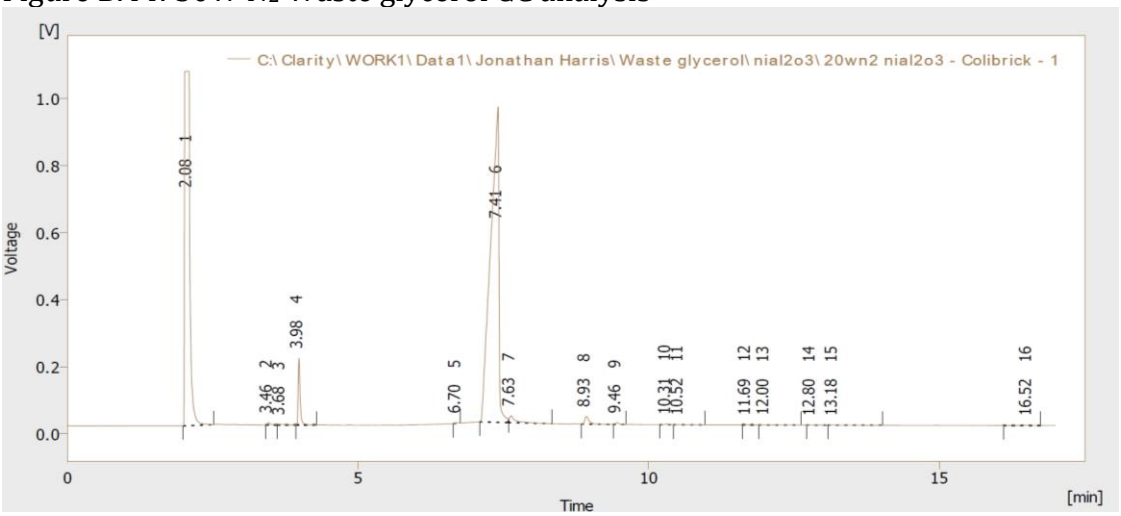

Figure B.45: 30W N_2 Ni/Al_2O_3 Waste glycerol GC analysis

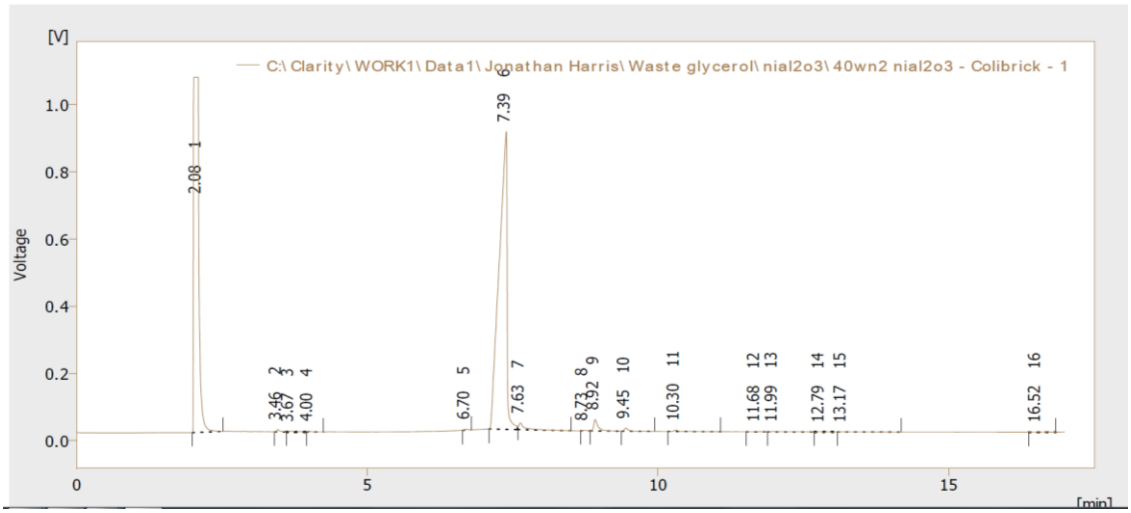

Figure B.46: 50W N_2 Ni/Al_2O_3 Waste glycerol GC analysis

B.2.3: Triglycerides

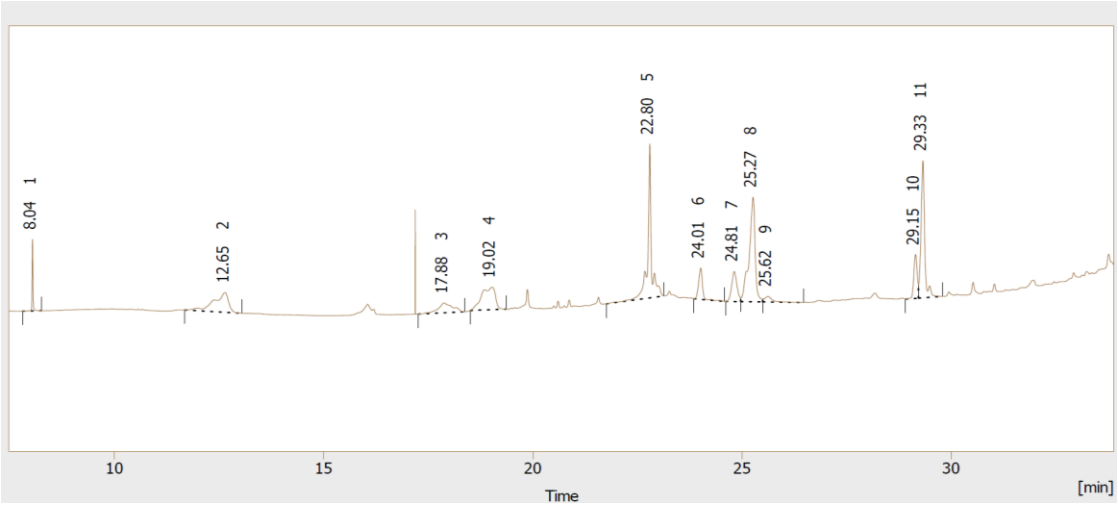

Figure B.47: Raw WCO GC analysis

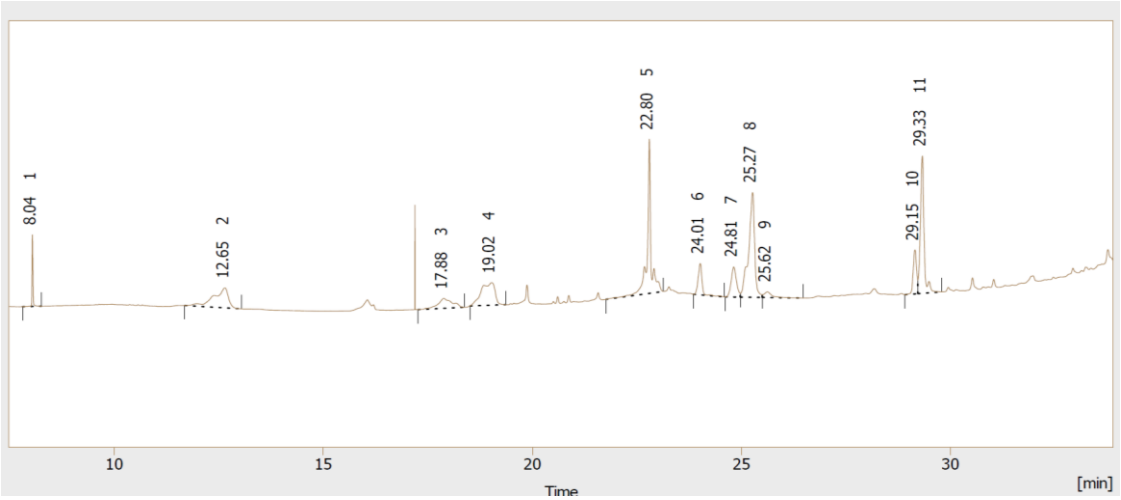

Figure B.48: 30W N_2 WCO GC analysis

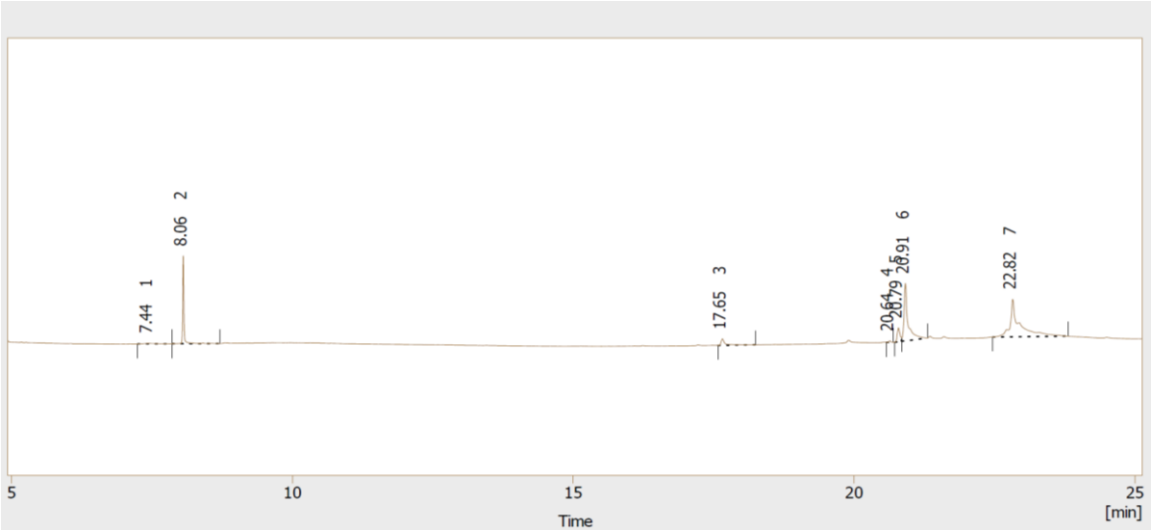

Figure B.49: 30W N_2 Ni/Al_2O_3 WCO GC analysis

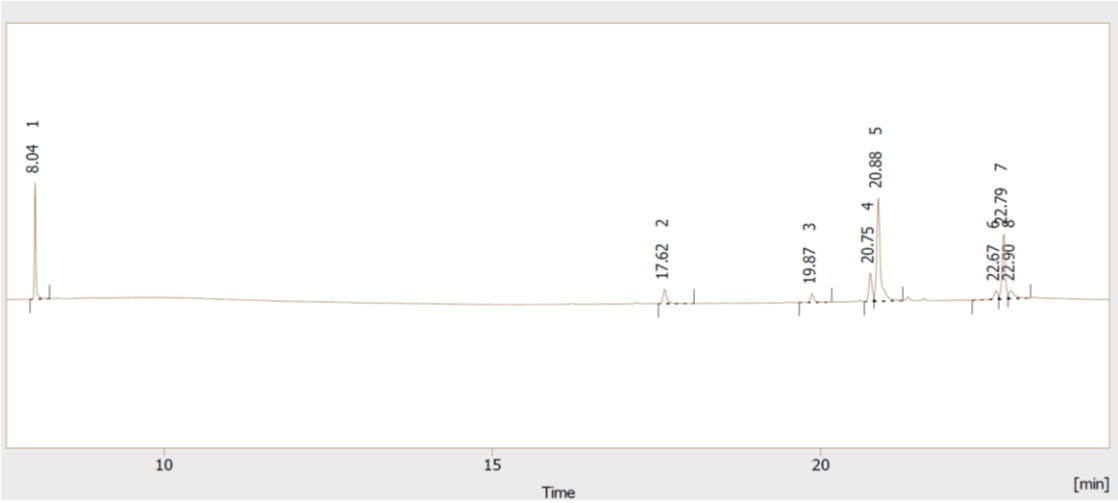

Figure B.50: 30W H_2 $BaTiO_3$ WCO GC analysis

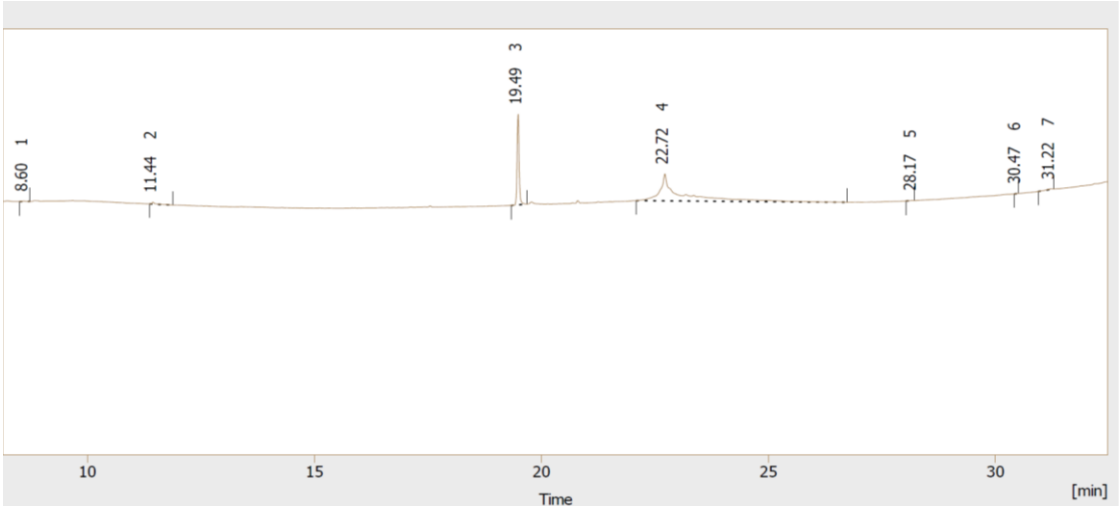

Figure B.51: 50W N_2 Ni/Al_2O_3 WCO FFA/FAME GC analysis

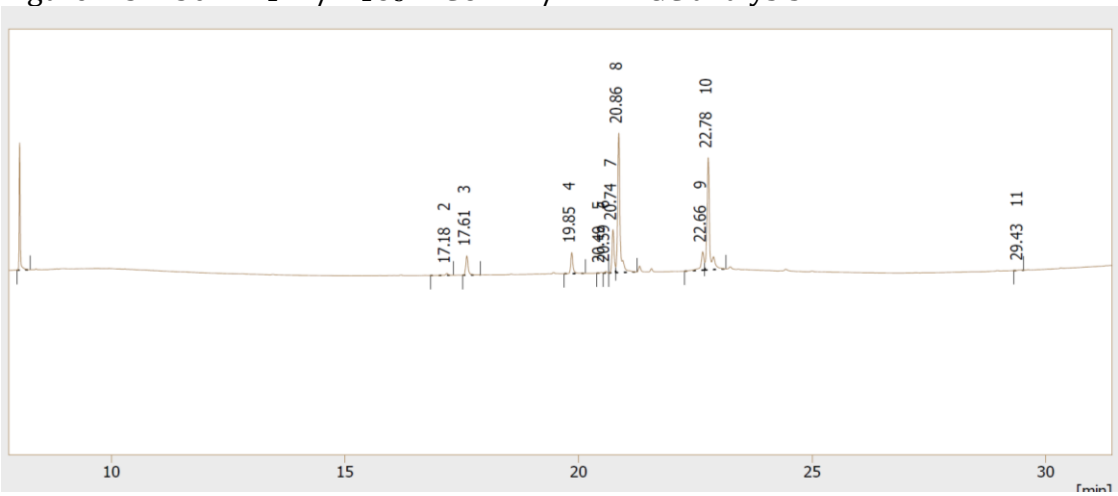

Figure B.52: 30W N_2 300C HZSM-5 WCO FFA/FAME GC analysis

B.2.4: Cellulose

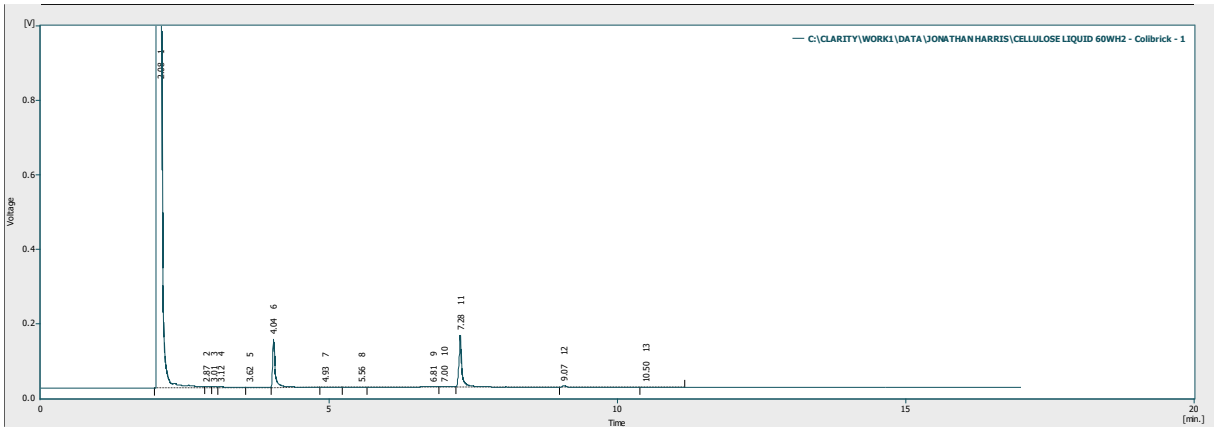

Figure B.53: 50W H_2 Cellulose liquid GC analysis

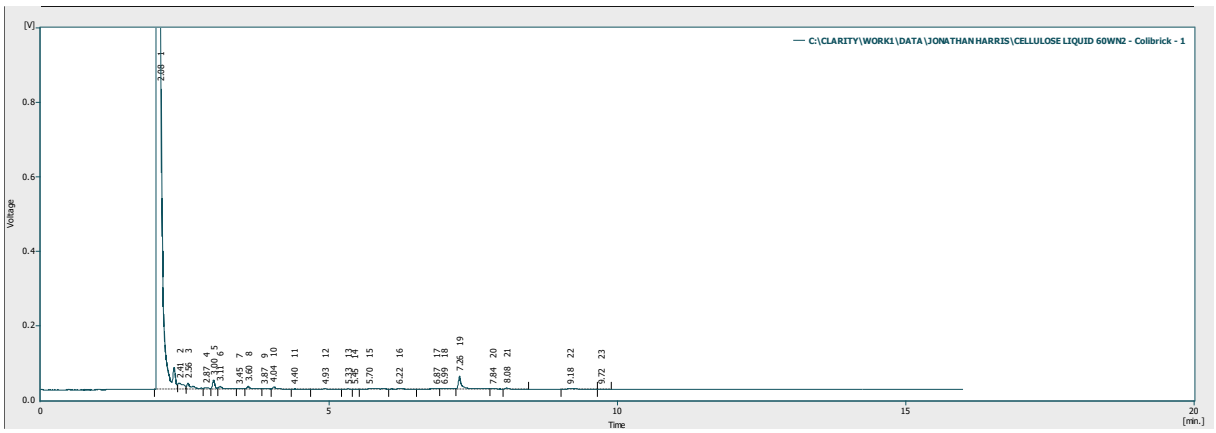

Figure B.54: 50W N_2 Cellulose liquid GC analysis

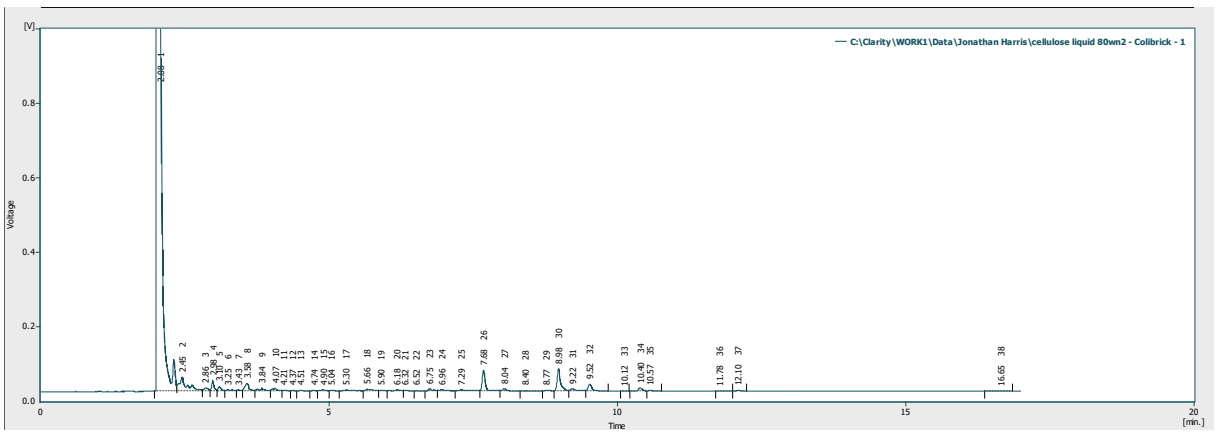

Figure B.55: 50W H_2 Cellulose liquid GC analysis